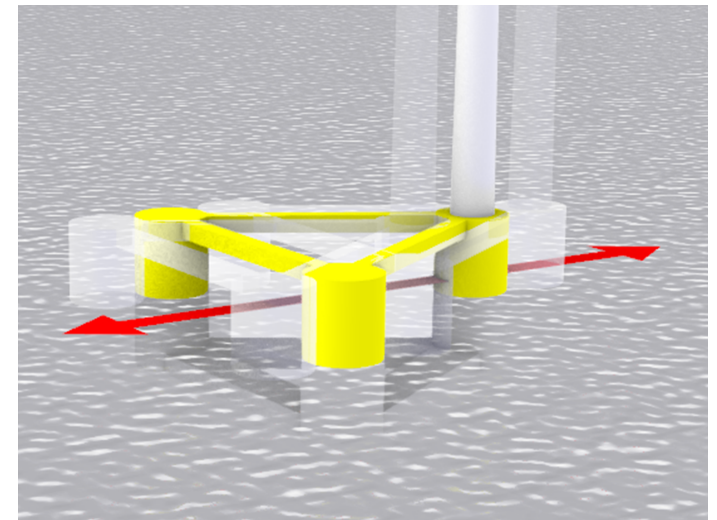


Peter Wiley

Low-Frequency Hydrodynamic Modeling of a 12 MW Semi- Submersible Wind Turbine

July 2021





Norwegian University of
Science and Technology

Low-Frequency Hydrodynamic Modeling of a 12 MW Semi-Submersible Wind Turbine

Peter Wiley

European Wind Energy Master

Submission date: July 2021

Supervisor: Erin Bachynski

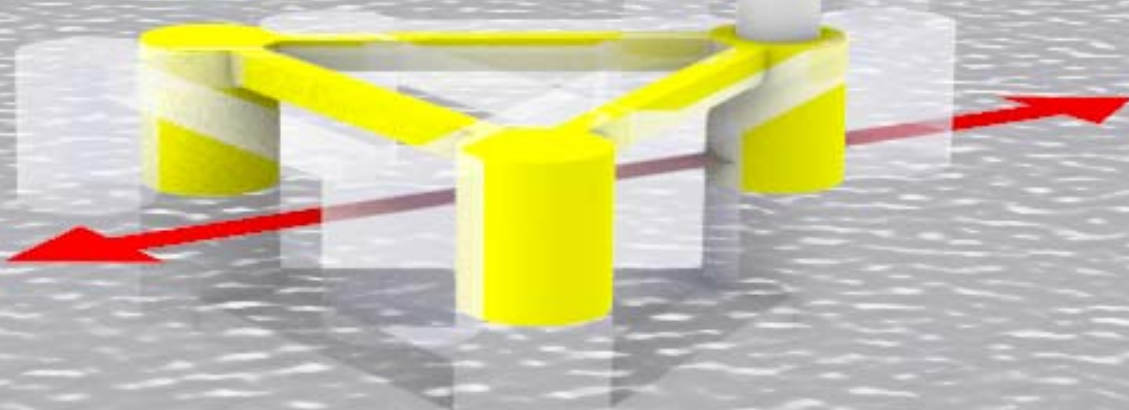
Co-supervisor: Axelle Viré

Norwegian University of Science and Technology
Department of Marine Technology

Low-Frequency Hydrodynamic Modeling of a 12 MW Semi-Submersible Wind Turbine

P. Will Wiley

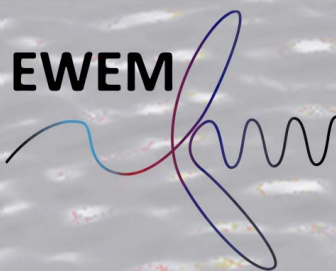
MSc Thesis



July 2021

Advisor: Erin Bachynski

Advisor: Axelle Viré



Acknowledgments

I would like to thank all of the professors from the Technical University of Denmark, Delft University of Technology, and the Norwegian University of Science and Technology who have impacted my studies during the European Wind Energy Master. I have greatly appreciated the opportunity to learn from their expertise in such an exciting field.

I would especially like to thank my two advisors for this thesis project, Erin Bachynski of NTNU and Axelle Viré of TU Delft. Erin Bachynski provided the inspiration for the project and was instrumental in all stages of the work throughout the year. She provided valuable insights and guidance every week and shared her expertise on the hydrodynamics of offshore wind platforms. Axelle Viré was also key to the success of the thesis. She gave very useful feedback and discussion all along the way and lent vast knowledge of computational fluid dynamics and floating wind energy. This work would not have been possible without the help of Erin and Axelle, and their passion for the subject has been very motivational.

I would also like to thank Andrei Metrikine for chairing my thesis committee and providing feedback on the presentation and organization of the project. I would like to thank Irene Rivera Arreba for help learning to use OpenFOAM and Trygve Kristiansen for valuable conversations about boundary layer hydrodynamics.

Finally I would like to thank SINTEF Ocean for the description of the platform and the model test data on which this project is based. In particular I would like to thank Petter Andreas Berthelsen, Andrea Califano, Nuno Fonseca, Carlos Eduardo Silva de Souza, and Maxime Thys for sharing their research and insights with me.

Abstract

The INO WINDMOOR platform is a semi-submersible designed to support a 12 MW wind turbine. Its natural frequencies in surge and pitch are below the frequencies of typical wave energy, and thus large resonant motions cannot be excited by first order loads. Large motions are critical for the design of the mooring system, and accurate predictions of the motions can help reduce the cost of wind energy. A new method of motion prediction is developed and tested, with a key focus on viscous flow effects.

A second order potential flow analysis is performed to predict excitation forces at the difference frequency of multiple waves through the use of a quadratic transfer function. First and second order potential flow coefficients with a constant value of critical damping are used to predict the six degree of freedom motions of the platform in wave only conditions. The predicted motions are compared to model test data for mono-chromatic, bi-chromatic, and irregular waves. The wave frequency motions are well predicted. The low frequency surge motion is under-predicted in short wave heights and is over-predicted in large wave heights. The discrepancies are attributed largely to a lack of accurate viscous effects.

When low-frequency resonance occurs, motions can become large, and viscous flow effects can become important. For the probable flows around the semi-submersible, it is predicted that the viscous flow effects are best described as a function of KC number. A computational fluid dynamics study was performed in OpenFOAM, including mono-chromatic and bi-chromatic forced oscillations over a range of KC numbers. A distributed model of the platform geometry was used with vertical divisions. From time series of the forces on each division, three coefficients were extracted: added mass, linear radiation damping, and quadratic viscous damping. The potential flow contributions were subtracted, removing the frequency dependency and leaving only viscous correction coefficients. The resulting functions of KC number were tested by predicting the forces of the combined oscillation cases.

The correction functions were implemented in the time domain motion prediction model. The functions were tested both with all three viscous correction coefficients included, and with only the quadratic damping coefficient included. The quadratic damping only model resulted in the most accurate motion predictions. It was concluded that the post-processing for forced oscillations is very sensitive, and it is difficult to remove the potential flow frequency dependence from the results. Because viscous changes to potential flow coefficients are so linked to frequency, it is more effective to neglect these for the KC number based functions, and only include the quadratic component. After analysis some changes would be made to the test procedure. However, it appears that the method of adding KC number based viscous corrections, from forced oscillation CFD simulations, can offer improved low-frequency motion predictions.

Contents

Table of Contents	ii
List of figures	v
List of tables	viii
1 Industry Context	1
1.1 Offshore Wind Energy	1
1.2 Floating Wind Turbine Platforms	2
1.3 Semi-submersible low frequency motions	3
2 Theory	6
2.1 Potential Flow	6
2.1.1 First Order Excitation	8
2.1.2 Second Order Excitation	8
2.2 Viscous Flow	9
2.2.1 Boundary Layers	10
2.2.2 Turbulent and Transitional Flow	12
2.2.3 Oscillatory Flow	14
2.3 Computational Fluid Dynamics	15
2.4 Signal Analysis	16
3 Previous Work	17
3.1 Potential Flow Projects	17
3.1.1 Roald, Jonkman, Robertson, and Chokani 2013	17
3.1.2 Chuang, Liu, and Lu 2020	17
3.2 Model Test Data Incorporation	18
3.2.1 Berthelsen, Bachynski, Karimirad, and Thys 2016	18
3.2.2 Silva de Souza, Fonseca, Berthelsen, and Thys 2021	19
3.2.3 Fonseca, Thys, and Berthelsen 2021	19
3.3 Computational Fluid Dynamics Projects	20
3.3.1 Rivera-Arreba 2017	20
3.3.2 Tran and Kim 2017	20
3.3.3 Burmester, Chen, Vaz, and Wang 2019	21
3.3.4 Burmester, Gueydon, Moctar, and Vaz 2020	21
3.3.5 Pinguet, Kanner, Benoit, and Molin 2020 and 2021	21
3.4 Conclusions and Research Gaps	22
4 WINDMOOR Model Test Data	24
4.1 Test Cases	24
4.2 Model Description	25
5 Potential Flow Study	27
5.1 First Order Potential Flow Study	27
5.2 Second Order Potential Flow Study	28
6 Model Test Comparisons	34
6.1 Time Series Construction	34
6.1.1 Excitation Force Time Series	34
6.1.2 Cummins Equation and Covolution Integral	35
6.1.3 Dynamic Response Calculation	37
7 Potential Flow Results	39
7.1 First Order	39
7.2 Second Order	39
7.3 Time Series Reconstruction Discussion	40
7.3.1 Mono-chromatic Waves	40
7.3.2 Bi-chromatic Waves	41
7.3.3 Irregular Waves	42

8	Computational Fluid Dynamics Study	43
8.1	CFD Model Setup	44
8.1.1	Computational Solvers	45
8.1.2	Turbulence Modeling	48
8.1.3	Mesh	52
8.1.4	Initial and Boundary Conditions	58
8.1.5	Parallel Processing	59
8.2	Test Matrix	60
9	Post-Processing	62
9.1	Single Forced Oscillations	64
9.2	Combined Forced Oscillations	71
9.2.1	Coefficient Extraction	71
9.2.2	Force Series Reconstruction	73
9.3	Directional Dependence	76
10	Time Domain Model Viscous Corrections	78
11	Conclusions	80
11.1	Recommended Future Work	81
A	First Order Potential Flow Results	84
B	Second Order Potential Flow Results	88
C	Mono-chromatic Time Series Reconstruction - Potential Flow Only	93
D	Bi-Chromatic Time Series Reconstruction - Potential Flow Only	102
E	Irregular Time Series Reconstruction - Potential Flow Only	113
F	Empirical Transfer Functions	120
F.0.1	First Order Empirical Coefficients	120
F.0.2	Second Order Empirical Coefficients	122
G	CFD Model Setup	124
G.1	Initial and Boundary Conditions	127
H	Single Forced Oscillation Post-Processing	128
I	Combined Forced Oscillations Post-Processing: Coefficient Extraction	144
J	Combined Forced Oscillations Post-Processing: Force Series Reconstruction	162
K	Time Series Reconstruction with Viscous Correction Functions	168
K.1	Mono-Chromatic Cases	168
K.2	Bi-Chromatic Cases	176
K.2.1	Direction Dependent Coefficients	187
K.3	Irregular Cases	188

List of Figures

1.1	Percentage of electrical power production from wind energy in the EU for 2019 [7]	1
1.2	Floating wind turbine foundation types [6]	3
1.3	Natural heave periods of typical offshore structures [9]	4
1.4	INO-WINDMOOR semi-submersible offshore wind turbine platform with full-scale dimensions in meters	5
2.1	Horizontal mean force contribution due to wetted surface difference; source: [9]	9
2.2	Boundary layer thickness, displacement thickness, and momentum thickness	11
2.3	Turbulent boundary layer; source: [14]	12
2.4	Transition to turbulence along a flat plate; adapted from [24]	13
2.5	Turbulent boundary layer; adapted from [30]	13
4.1	SINTEF Ocean model test configuration [29]	26
5.1	WINDMOOR panel model in HydroD user interface	27
5.2	Surge added mass coefficient with varying element length	28
5.3	Free surface mesh creation in HydroMesh	29
5.4	Absolute value of quadratic transfer function dependence on free surface model	29
5.5	Panel model with refinement zones	30
5.6	Absolute value of quadratic transfer function dependence on panel model	31
5.7	Surge force quadratic transfer function	32
5.8	Real surge force quadratic transfer function comparison: Newman's approximation shown in semi-transparent	33
5.9	Imaginary surge force quadratic transfer function comparison: Newman's approximation shown in semi-transparent	33
6.1	Rotated axes of integration on quadratic transfer function	35
6.2	Frequency dependent decomposition of added mass and damping	36
6.3	Radiation retardation function of surge	37
6.4	Bi-chromatic wave motion reconstructed time series	38
7.1	Potential flow surge added mass comparison: Wiley and Berthelsen et al.	39
7.2	Potential flow quadratic transfer function comparison: Wiley (a) and Fonseca (b)	40
8.1	Decomposed CFD platform geometry	45
8.2	Overset mesh motion cell types	46
8.3	$y+$ values used for Langtry-Menter transition turbulence model	50
8.4	Successful boundary layer cell wrapping around sharp corner	51
8.5	Intermittency of turbulence (γ) in steady flow	51
8.6	Outer domain mesh	53
8.7	Free surface zone cell matching	53
8.8	Mesh convergence study with distributed shortened force time series	55
8.9	Mesh convergence study with distributed drag coefficients	56
8.10	Mesh convergence study with total body drag coefficient	56
8.11	Velocity field with mesh density 5 (top) and 8 (bottom)	57
8.12		58
8.13	Time step convergence study using low KC number oscillation A [N-s ² /m]; B1 [N-s/m]; Bq [N-s ² /m ²]	58
8.14	Simple decomposition parallel processor arrangements	59
9.1	Coefficient extraction schematic	63
9.2	Added mass and radiation damping comparison between distributed results from WAMIT (red stars) and total body results from HydroD (blue and black lines)	63
9.3	Force coefficient functions found using the full force method cA [N-s ² /m]; cBl [N-s/m]; cBq [N-s ² /m ²]	65
9.4	Viscous correction coefficient functions found using the full force method cA [N-s ² /m]; cBl [N-s/m]; cBq [N-s ² /m ²]	66
9.5	Viscous correction coefficient functions found using the subtraction method cA [N-s ² /m]; cBl [N-s/m]; cBq [N-s ² /m ²]	67
9.6	Viscous correction coefficient functions found using the subtraction method and only linear or quadratic damping selection cA [N-s ² /m]; cBl [N-s/m]; cBq [N-s ² /m ²]	68
9.7	Boundary layer on the column in case <i>fo7</i> showing clear separation	69
9.8	Boundary layer on the column in case <i>fo1</i> showing no separation	70
9.9	Final selection of composite viscous correction functions cA [N-s ² /m]; cBl [N-s/m]; cBq [N-s ² /m ²]	71
9.10	Combined case coefficient comparison with chosen functions for case: <i>cf027</i> cA [N-s ² /m]; cBl [N-s/m]; cBq [N-s ² /m ²]	72
9.11	Reconstruction of case: <i>cf067</i>	75

9.12	Direction split viscous correction functions cA [N-s ² /m]; cBl [N-s/m]; cBq [N-s ² /m ²]	77
10.1	Time series reconstruction of bi-chromatic wave model test with viscous corrections	79
A.1	Added mass in surge, pitch, surge-pitch, and heave	84
A.2	Damping in surge, pitch, surge-pitch, and heave	85
A.3	Linear motion transfer function in surge, heave, and pitch	86
A.4	Linear excitation force in surge, heave, and pitch	87
B.1	Heave force quadratic transfer function	88
B.2	Pitch moment quadratic transfer function	89
B.3	Surge force quadratic transfer function diagonals	90
B.4	Heave force quadratic transfer function diagonals	91
B.5	Pitch moment quadratic transfer function diagonals	92
C.1	Test 1 mono-chromatic wave motion reconstruction	93
C.2	Test 2 mono-chromatic wave motion reconstruction	94
C.3	Test 3 mono-chromatic wave motion reconstruction	95
C.4	Test 4 mono-chromatic wave motion reconstruction	96
C.5	Test 5 mono-chromatic wave motion reconstruction	97
C.6	Test 6 mono-chromatic wave motion reconstruction	98
C.7	Test 7 mono-chromatic wave motion reconstruction	99
C.8	Test 8 mono-chromatic wave motion reconstruction	100
C.9	Test 9 mono-chromatic wave motion reconstruction	101
D.1	Test 1 bichromatic wave motion reconstruction	102
D.2	Test 2 bichromatic wave motion reconstruction	103
D.3	Test 3 bichromatic wave motion reconstruction	104
D.4	Test 4 bichromatic wave motion reconstruction	105
D.5	Test 5 bichromatic wave motion reconstruction	106
D.6	Test 6 bichromatic wave motion reconstruction	107
D.7	Test 7 bichromatic wave motion reconstruction	108
D.8	Test 8 bichromatic wave motion reconstruction	109
D.9	Test 9 bichromatic wave motion reconstruction	110
D.10	Test 10 bichromatic wave motion reconstruction	111
D.11	All bichromatic wave tests motion reconstruction for comparison	112
E.1	Group 1 irregular wave motion reconstruction	113
E.2	Group 2 irregular wave motion reconstruction	114
E.3	Group 3 irregular wave motion reconstruction	115
E.4	Group 4 irregular wave motion reconstruction	116
E.5	Group 5 irregular wave motion reconstruction	117
E.6	Group 6 irregular wave motion reconstruction	118
E.7	Group 7 irregular wave motion reconstruction	119
F.1	Empirical first order transfer functions and linear coherence from irregular wave tests	121
F.2	Potential flow first order transfer functions for comparison	121
F.3	Empirical and potential flow quadratic transfer function diagonal comparison	123
G.1	Mesh convergence study with distributed force full time series using varying mesh densities	124
G.2	Time step convergence study with distributed force time series using varying time steps	125
G.3	Symmetry plane validation with distributed force time series	126
H.1	Decomposed distributed force time series for case: <i>fo0</i>	128
H.2	Decomposed distributed force time series for case: <i>fo1</i>	129
H.3	Decomposed distributed force time series for case: <i>fo2</i>	130
H.4	Decomposed distributed force time series for case: <i>fo3</i>	131
H.5	Decomposed distributed force time series for case: <i>fo4</i>	132
H.6	Decomposed distributed force time series for case: <i>fo5</i>	133
H.7	Decomposed distributed force time series for case: <i>fo6</i>	134
H.8	Decomposed distributed force time series for case: <i>fo7</i>	135
H.9	Coefficient convergence with successive oscillations for case: <i>fo0</i> cA [N-s ² /m]; cBl [N-s/m]; cBq [N-s ² /m ²]	136
H.10	Coefficient convergence with successive oscillations for case: <i>fo1</i> cA [N-s ² /m]; cBl [N-s/m]; cBq [N-s ² /m ²]	137
H.11	Coefficient convergence with successive oscillations for case: <i>fo2</i> cA [N-s ² /m]; cBl [N-s/m]; cBq [N-s ² /m ²]	138
H.12	Coefficient convergence with successive oscillations for case: <i>fo3</i> cA [N-s ² /m]; cBl [N-s/m]; cBq [N-s ² /m ²]	139

H.13	Coefficient convergence with successive oscillations for case: <i>fo4</i> cA [N-s ² /m]; cBl [N-s/m]; cBq [N-s ² /m ²]	140
H.14	Coefficient convergence with successive oscillations for case: <i>fo5</i> cA [N-s ² /m]; cBl [N-s/m]; cBq [N-s ² /m ²]	141
H.15	Coefficient convergence with successive oscillations for case: <i>fo6</i> cA [N-s ² /m]; cBl [N-s/m]; cBq [N-s ² /m ²]	142
H.16	Coefficient convergence with successive oscillations for case: <i>fo7</i> cA [N-s ² /m]; cBl [N-s/m]; cBq [N-s ² /m ²]	143
I.1	Decomposed distributed force time series for case: <i>cf017</i>	144
I.2	Decomposed distributed force time series for case: <i>cf027</i>	145
I.3	Decomposed distributed force time series for case: <i>cf037</i>	146
I.4	Decomposed distributed force time series for case: <i>cf047</i>	147
I.5	Decomposed distributed force time series for case: <i>cf057</i>	148
I.6	Decomposed distributed force time series for case: <i>cf067</i>	149
I.7	Coefficient convergence with successive oscillations for case: <i>cf017</i> cA [N-s ² /m]; cBl [N-s/m]; cBq [N-s ² /m ²]	150
I.8	Coefficient convergence with successive oscillations for case: <i>cf027</i> cA [N-s ² /m]; cBl [N-s/m]; cBq [N-s ² /m ²]	151
I.9	Coefficient convergence with successive oscillations for case: <i>cf037</i> cA [N-s ² /m]; cBl [N-s/m]; cBq [N-s ² /m ²]	152
I.10	Coefficient convergence with successive oscillations for case: <i>cf047</i> cA [N-s ² /m]; cBl [N-s/m]; cBq [N-s ² /m ²]	153
I.11	Coefficient convergence with successive oscillations for case: <i>cf057</i> cA [N-s ² /m]; cBl [N-s/m]; cBq [N-s ² /m ²]	154
I.12	Coefficient convergence with successive oscillations for case: <i>cf067</i> cA [N-s ² /m]; cBl [N-s/m]; cBq [N-s ² /m ²]	155
I.13	Combined case coefficient comparison with chosen functions for case: <i>cf017</i> cA [N-s ² /m]; cBl [N-s/m]; cBq [N-s ² /m ²]	156
I.14	Combined case coefficient comparison with chosen functions for case: <i>cf027</i> cA [N-s ² /m]; cBl [N-s/m]; cBq [N-s ² /m ²]	157
I.15	Combined case coefficient comparison with chosen functions for case: <i>cf037</i> cA [N-s ² /m]; cBl [N-s/m]; cBq [N-s ² /m ²]	158
I.16	Combined case coefficient comparison with chosen functions for case: <i>cf047</i> cA [N-s ² /m]; cBl [N-s/m]; cBq [N-s ² /m ²]	159
I.17	Combined case coefficient comparison with chosen functions for case: <i>cf057</i> cA [N-s ² /m]; cBl [N-s/m]; cBq [N-s ² /m ²]	160
I.18	Combined case coefficient comparison with chosen functions for case: <i>cf067</i> cA [N-s ² /m]; cBl [N-s/m]; cBq [N-s ² /m ²]	161
J.1	Reconstruction of case: <i>cf017</i>	162
J.2	Reconstruction of case: <i>cf027</i>	163
J.3	Reconstruction of case: <i>cf037</i>	164
J.4	Reconstruction of case: <i>cf047</i>	165
J.5	Reconstruction of case: <i>cf057</i>	166
J.6	Reconstruction of case: <i>cf067</i>	167
K.1	Time series reconstruction of mono-chromatic test #1 with viscous corrections	168
K.2	Time series reconstruction of mono-chromatic test #2 with viscous corrections	169
K.3	Time series reconstruction of mono-chromatic test #3 with viscous corrections	170
K.4	Time series reconstruction of mono-chromatic test #4 with viscous corrections	171
K.5	Time series reconstruction of mono-chromatic test #5 with viscous corrections	172
K.6	Time series reconstruction of mono-chromatic test #6 with viscous corrections	173
K.7	Time series reconstruction of mono-chromatic test #7 with viscous corrections	174
K.8	Time series reconstruction of mono-chromatic test #8 with viscous corrections	175
K.9	Time series reconstruction of mono-chromatic test #9 with viscous corrections	176
K.10	Time series reconstruction of bi-chromatic test #1 with viscous corrections	177
K.11	Time series reconstruction of bi-chromatic test #2 with viscous corrections	178
K.12	Time series reconstruction of bi-chromatic test #3 with viscous corrections	179
K.13	Time series reconstruction of bi-chromatic test #4 with viscous corrections	180
K.14	Time series reconstruction of bi-chromatic test #5 with viscous corrections	181
K.15	Time series reconstruction of bi-chromatic test #6 with viscous corrections	182
K.16	Time series reconstruction of bi-chromatic test #7 with viscous corrections	183
K.17	Time series reconstruction of bi-chromatic test #8 with viscous corrections	184

K.18	Time series reconstruction of bi-chromatic test #9 with viscous corrections	185
K.19	Time series reconstruction of bi-chromatic test #10 with viscous corrections	186
K.20	Time series reconstruction of bi-chromatic wave model test with direction split viscous corrections	187
K.21	Time series reconstruction of irregular test #1 with viscous corrections	188
K.22	Time series reconstruction of irregular test #2 with viscous corrections	189
K.23	Time series reconstruction of irregular test #3 with viscous corrections	190
K.24	Time series reconstruction of irregular test #4 with viscous corrections	191
K.25	Time series reconstruction of irregular test #5 with viscous corrections	192
K.26	Time series reconstruction of irregular test #6 with viscous corrections	193
K.27	Time series reconstruction of irregular test #7 with viscous corrections	194

List of Tables

4.1	SINTEF mono-chromatic wave only test cases	24
4.2	SINTEF bi-chromatic wave only test cases	24
4.3	SINTEF irregular wave only test cases	25
5.1	First order panel model study computation times	28
8.1	Possible Reynolds and KC number ranges for model scale waves and motions	44
8.2	CFD model domain	52
8.3	Single forced oscillation CFD test matrix	60
8.4	Combined forced oscillation CFD test matrix	61
9.1	Single forced oscillation coefficient treatment selection	69
9.2	KC number selection methods	73
F.1	Empirical natural frequencies and damping ratios from model decay tests	122

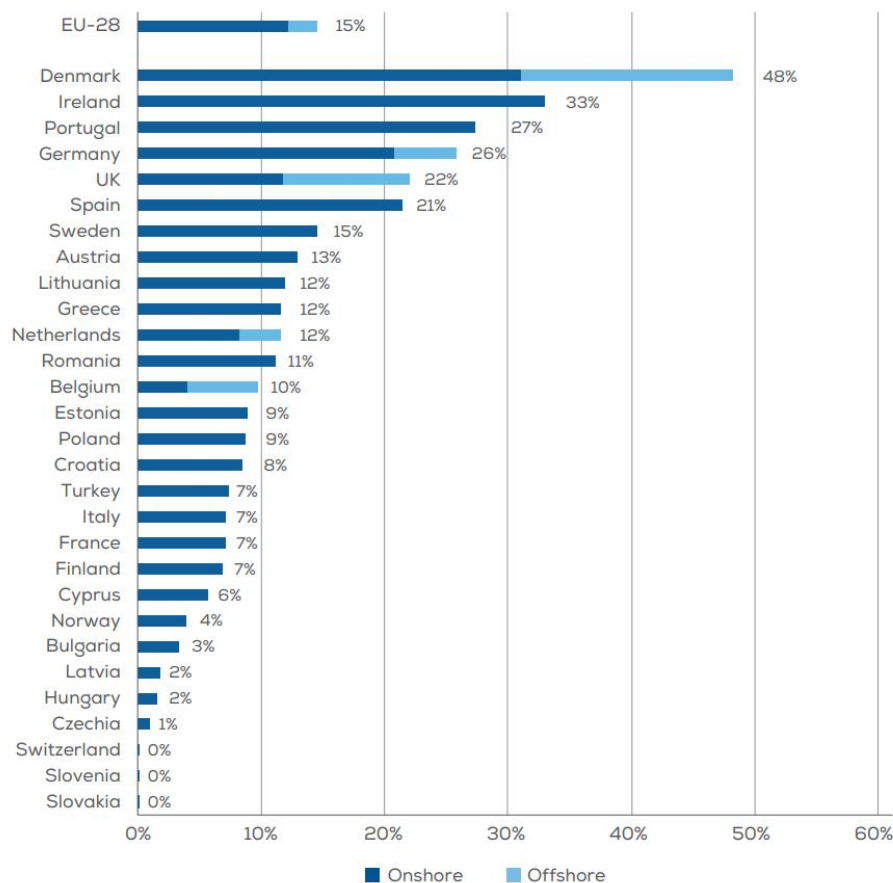
1 Industry Context

1.1 Offshore Wind Energy

With a growing world population that is increasingly mobile, the need for new energy sources will continue to grow. The dangerous effects of climate change make it clear that more renewable and sustainable energy production is necessary. Wind energy will likely need to play a significant role in this goal.

Before the discovery of electricity windmills had been used extensively in the Netherlands to pump water out of flooded low elevation lands. They were also used in various parts of the world to mill grain, leading to the term windmill. The first wind turbine to produce electricity was built by Charles Brush in Cleveland, Ohio in 1886. This first turbine had 144 blades and a diameter of 17.1 m, very different than the giant three bladed turbines of today [15]. In Europe most early wind turbine development occurred in Denmark, with Poul la Cour as a leading scientist in the field. It is estimated that by 1920 Denmark had 150 MW of installed wind power [15]. Much of the wind turbine development in the United States and in Denmark was fueled by a desire to bring electricity to rural agricultural areas. Before power plants and the electrical grid reached far from the cities, wind power was a way to bring the modern advances of electricity to more people.

Electricity generating wind turbines have advanced significantly over the last 130 years. Wind energy is now a large part of modern electricity production and is predicted to grow in significance in many places around the world. Europe had 205 GW of installed wind power as of the end of 2019. For the year of 2019 48% of the electrical consumption was provided by wind power in Denmark [7]. Figure 1.1 shows the percentage of power production provided by wind for countries of the European Union. These numbers have been growing and are predicted to continue to grow, especially the contribution of offshore wind farms. Large offshore wind installations are also planned for North America and Asia over the coming decade.



Source: WindEurope

Figure 1.1: Percentage of electrical power production from wind energy in the EU for 2019 [7]

Wind turbines were first placed on land, where the foundation is simpler, both from an engineering and financial point of view. There are some key challenges however with onshore wind turbines that can potentially be solved by moving the technology offshore. Wind on land is disturbed by topographical features, buildings, and vegetation. This results in wind with lower mean speeds and less consistency. Wind at sea can flow over a relatively flat surface which can be undisturbed for very long distances. This often results in winds with better

speed, consistency, and predictability.

Large population centers are often in cities near coastlines, where large open areas of land are difficult to find and very expensive. For many of these locations, open water is more accessible. By placing wind farms in the water, closer to users, less power is lost in transmission. Modern wind turbines are very large and can be seen from far away, and the vortices shed from the blades can also produce significant noise. The sight and sound of a wind turbine can disturb people who live nearby, and this can often prevent development near residential areas. When wind turbines are placed offshore, they can more easily be far enough away from any homes to not cause a disturbance. For these reasons, the technical and financial challenges of building offshore wind turbines are tackled increasingly often. It is also important to consider that while fewer people may be impacted by offshore wind turbines, they still can have impacts on marine life as well as maritime industries such as fishing and shipping. These subjects are studied in detail, and wind farms are designed to minimize any negative effects.

The first offshore wind turbines were installed in 1991 2.5 km off the coast of Vindeby, Denmark. This farm consisted of eleven 450 kW wind turbines, very small for today's standards [1]. In 2019 the average offshore wind turbine installed had a rated capacity of 7.2 MW [7]. The current largest constructed wind turbine is the GE Haliade-X which has drive train configurations for 12 or 13 MW. The levelized cost of energy from offshore wind has continued to decrease with advancements in turbine and foundation technology. The general trend is for turbines to become larger. Various economies of scale lead to lower costs of energy from bigger turbines.

There are several foundation types that have been used to support offshore wind turbines, and many concepts that have been proposed. The first offshore wind turbines were fixed to the seafloor. This type of design was easier for initial development, and has been successfully used in specific regions of the world. One particular region is the North Sea which benefits from strong winds and shallow water depths. Fixed bottom offshore wind turbines use several styles of foundations, including monopiles, jackets, and gravity based structures. Monopiles make up the largest portion of the installations. A monopile is a relatively simple steel cylinder that is driven into the seabed and supports the wind turbine tower. Monopiles have proven to be effective in water depths up to around 35 m. In deeper waters a monopile or jacket foundation is technically feasible, but becomes expensive to be an attractive financial decision. At some critical depth a floating wind turbine platform becomes more economically viable than a fixed bottom foundation.

1.2 Floating Wind Turbine Platforms

Floating wind turbines have a number of potential advantages over fixed bottom turbines. The first is the economic feasibility of installation in deep water locations. A second advantage is the difficulty and cost of installation. Fixed bottom foundations such as monopiles typically require large jack-up vessels for installation which are very costly. Adding to the cost of a fixed bottom installation, most parts of the operation take place on location at sea. After the foundation is in place, the tower, nacelle, and blades are typically installed in successive operations. Each step of the process requires large and expensive vessels. A floating wind turbine by contrast can be fully assembled in a port using less expensive land based cranes. Then the complete assembly can be brought to the wind farm location with smaller and more readily available tug boats. The mooring system can be installed in advance offering more potential weather windows, further reducing costs. A third advantage for floating wind turbine foundations is the potential for a more standardized construction. In a given fixed bottom wind farm each monopile for example may need to be built to different specifications based on the exact local bathymetry and soil composition. A single floating foundation design could be used in a larger number of situations. This means an entire wind farm could have identical foundations, and even identical foundations across multiple wind farms. This leads to reduced design, engineering, and construction costs.

Several types of floating foundations have been proposed and built. Four designs are shown by Wind Europe in Figure 1.2. The first two types shown, barge and semi-submersible both maintain their stability due to the waterplane area moment of inertia, which is dependent on the waterplane area. This stability is similar to a typical ship. If the platform is tilted in either heel or trim an increase in buoyant force on the low side and corresponding loss of buoyancy on the high side will create a righting moment. The third type shown, the spar buoy, is stable due to a very low center of gravity. The bottom of the spar is very deep and has a large mass, leading to a center of gravity much lower than the center of buoyancy, which keeps the platform stable. Due to their large draft, spar buoys require deeper water depths than the other styles, both for the farm location and the construction port. The fourth design shown is a tension leg platform, which achieves stability through the tension of the mooring system. The mooring lines of a tension leg platform are taut, and the floater's heel or trim is held in check by the tension.

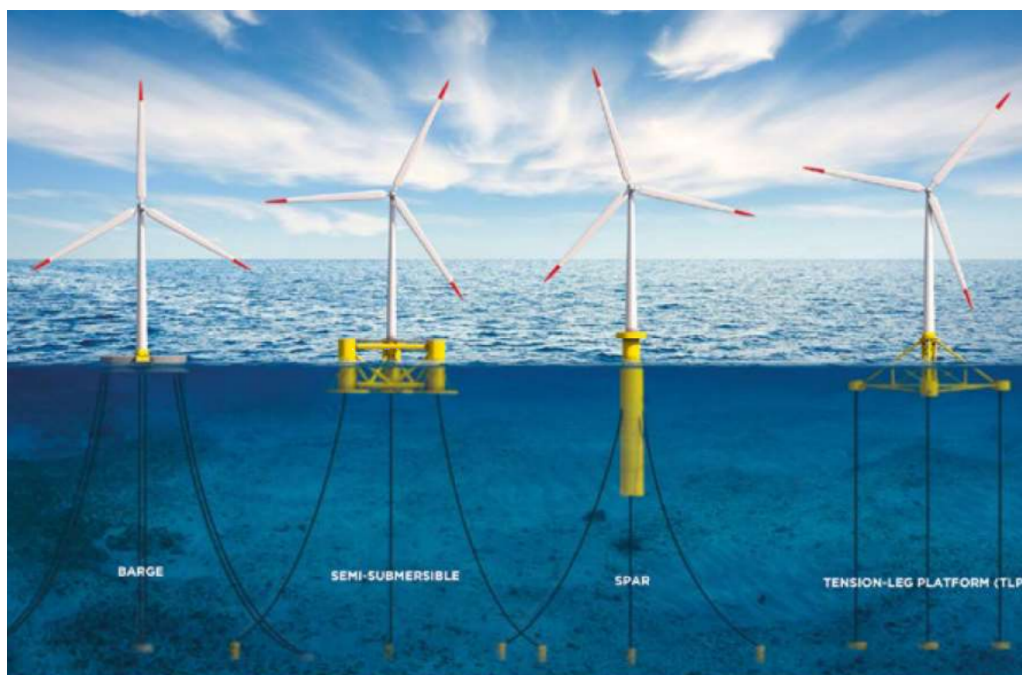


Figure 1.2: Floating wind turbine foundation types [6]


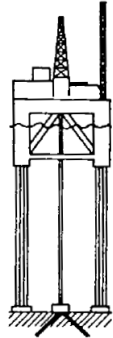

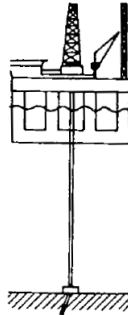
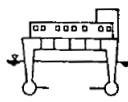
1.3 Semi-submersible low frequency motions

This project focuses on a semi-submersible platform. Semi-submersibles have been successfully commercially installed and the technology is thought to be proven and ready. A floating platform is subject to more motions than fixed bottom foundations. In order for a wind turbine to operate safely these motions need to be held below certain limits. The dynamics of the platform also lead to increased stresses which could lead to an ultimate limit state or a fatigue limit state failure. A conservative approach is to make the floating platform larger and stronger to ensure safe operations. This approach leads to more expensive and less environmentally friendly designs, which can make the option less profitable or viable. In order to reduce costs to a competitive price point, but maintain high confidence in the safety of the platform, it is important to make very accurate predictions of the motions that the platform will experience.

An offshore wind turbine experiences excitation loads due to wind, waves, and current. This project focuses only on the excitation due to waves. For an operating floating offshore wind turbine the interaction of the hydrodynamic and aerodynamic loads is important, but the wave loading is isolated here for better understanding. A floating platform encounters waves of many heights, frequencies, directions, and shapes. Different waves affect a semi-submersible differently, and the excitation from a particular wave can be described with varying levels of detail.

Typically the first type of wave excitation that is studied is first order potential flow excitation. A first order force is linearly proportional to the wave amplitude, and oscillates with a frequency equal to the frequency of the wave. The first order force is in most cases much higher in magnitude than any higher order forces, and in many cases it can be sufficient to only consider this. First order forces are easier and quicker to calculate than higher order forces, and thus if it is sufficient for the analysis, it is advantageous to stop the calculations there. For some problems, however, important information is lost with this limited approach.

Second order potential flow wave excitation forces are proportional to the square of the wave amplitude. Second order forces, unlike first order forces, can have mean values and can occur at frequencies above or below the incident wave frequencies. This is important to consider when determining if a structure will experience resonance. A simple example is a sea state of regular waves with a range of periods from 8 to 12 s. Figure 1.3 shows various common offshore structure types and their natural periods in heave. If the period of the force matches this period, even a small load can lead to very large motions which could be problematic. The first order load is not able to excite resonant heave behavior in the SES, TLP, or semi-submersible while it can for the displacement vessel and SWATH. Second order loads though can occur at a higher frequency and could excite large motions in the stiff TLP. They can also occur at a lower frequency and excite large motions in the semi-submersible. Even if the second order forces are orders of magnitude lower than the first order loads, they still can be governing for the design.

Vessel:					
Natural heave period:	<1 s	2–4 s	4–16 s ^a	>20 s	>20 s
Restoring force:	Air compressibility	Elasticity of tethers	Waterplane area	Waterplane area	Waterplane area
Dominating excitation mechanism around the natural heave period:	Linear wave forces due to high encounter frequency between ship and waves	Non-linear sum frequency wave forces	Linear wave forces	Swell (long waves)	Linear wave forces due to low encounter frequency between ship and waves
Important damping:	'Ride Control'	Viscous effects	Wave radiation	Viscous effects	Foil control

^a Rough estimate: $\sqrt{L/1.5}$, where L is ship length in metres.

Figure 1.3: Natural heave periods of typical offshore structures [9]

For different components of an offshore wind turbine platform, different motions are the most likely to contribute to a failure, and thus govern the design. For the mooring system, and its connections to the platform, the surge and pitch responses are critical. The natural period of surge and pitch for a wind turbine semi-submersible is typically larger than the periods of incident waves. For this reason, second order low-frequency hydrodynamic excitation loads are particularly important to understand.

The INO-WINDMOOR semi-submersible shown in Figure 1.4 is the particular subject of this project. The platform was designed by Inoceen and Equinor to support a 12 MW wind turbine [26]. The platform consists of three columns connected by pontoons at the baseline and deck beams at the top of the columns. The wind turbine tower is mounted on one of the three columns. In this figure the darker yellow represents the portion of the platform below the mean water line.

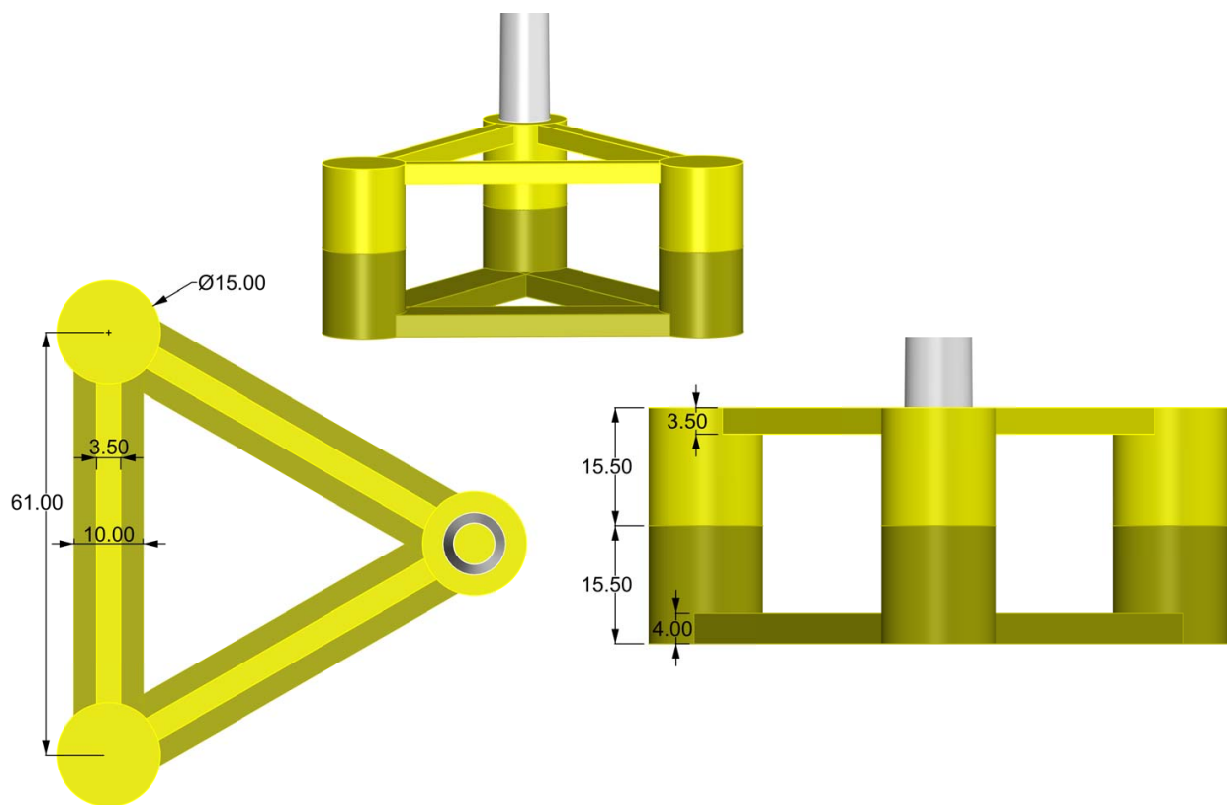


Figure 1.4: INO-WINDMOOR semi-submersible offshore wind turbine platform with full-scale dimensions in meters

Semi-submersibles used in offshore wind energy have relatively large volume components, which are typically well described by potential flow. However, when motions are large viscous flow effects can become important. A common first approach for the inclusion of viscous forces is the use of a constant critical damping value. This often does not lead to accurate motion predictions over a full range of environmental conditions. Higher fidelity numerical methods can be used to more accurately understand the effects of viscous flow.

This project focuses on understanding the loads that lead to low-frequency motions and finding accurate and efficient ways to predict them. An engineering model is first developed using potential flow coefficients. Then computational fluid dynamics is used to study viscous flow effects. The results of the more detailed and more expensive study are used to create efficient and broadly applicable corrections to the engineering model.

2 Theory

Some background theory is critical to understanding the choices made and analysis in the project. A relatively computationally inexpensive potential flow analysis is first performed. In many cases this approach provides adequate results. Potential flow theory however neglects some aspects of fluid flow which can be important. An overview of the potential flow concepts used in this work is given to understand what can be captured with the method. A description is then given of some important relevant viscous flow concepts. These ideas are important to understand as they lead to the choices made in the viscous corrections section of the work. A brief introduction to computational fluid dynamics and some signal analysis techniques is also given.

2.1 Potential Flow

Fluid flow is a complex problem and there are many types of approaches with varying complexity and accuracy to understanding and modeling it. When a fluid is assumed to be incompressible, Newtonian, and have a constant density and temperature, the flow can be described by the Navier-Stokes equations shown in Equation (1) and Equation (2) [30]. These are typical and reasonable assumptions for water in the scale observed in this project. Equation (1) describes the momentum of the fluid. The first term describes the material derivative of the velocity which includes both changes due to time and convection via velocity. The second term describes the gravitational body forces on the fluid. The third term describes the influence of the pressure on the fluid. The fourth and final term describes the viscous stresses on the fluid. Equation (2) is the continuity equation, and it requires that there is a conservation of mass in the fluid flow.

$$\rho \frac{d\mathbf{V}}{dt} = \rho \mathbf{g} - \nabla p + \mu \nabla^2 \mathbf{V} \quad (1)$$

$$\nabla \cdot \mathbf{V} = 0 \quad (2)$$

This set of equations should be able to describe all fluid flows with the stated assumptions. In practice these nonlinear equations are very difficult to solve analytically. There are very few simplified hydrodynamic problems with known solutions. For most more complex problems some simplifications or approximations need to be made in order to find meaningful knowledge about a flow.

One type of simplification with many practical uses is known as potential flow. A potential flow assumes that a flow is irrotational. This means that individual fluid particles do not rotate about their own axis. A viscous fluid can have an irrotational flow so long as the curl of the velocity is equal to zero, which is typically true in flow far from bodies and free shear layers. This means that a potential flow can be used for some applications of viscous flows. However it is more common that a potential flow assumes an inviscid fluid, which means the last term of Equation (1) is zero. Without viscous shear the flow will be irrotational everywhere, unless manually forced in a specific location. Irrotationality of a flow can be quantitatively described by the vorticity, ω , as shown in Equation (3). For a potential flow, this is equal to zero [16].

$$\omega = \nabla \times \mathbf{V} \quad (3)$$

This simplification allows the introduction of the velocity potential, ϕ , as described in (4).

$$\nabla \phi = \mathbf{V} \quad (4)$$

The velocity potential inherently satisfies that the flow is irrotational as shown in Equation (5), which combines Equation (3) and Equation (4).

$$\omega = \nabla \times \nabla \phi = \left\langle \frac{\partial \phi}{\partial x \partial y} - \frac{\partial \phi}{\partial y \partial x}, \frac{\partial \phi}{\partial y \partial z} - \frac{\partial \phi}{\partial z \partial y}, \frac{\partial \phi}{\partial z \partial x} - \frac{\partial \phi}{\partial x \partial z} \right\rangle = \langle 0, 0, 0 \rangle \quad (5)$$

The definition of the velocity potential can be incorporated into continuity, Equation (2), as shown in Equation (6). This is known as the Laplace equation, and is the governing partial differential equation to be used in potential flow analyses [16].

$$\frac{\partial^2 \phi}{\partial x^2} + \frac{\partial^2 \phi}{\partial y^2} + \frac{\partial^2 \phi}{\partial z^2} = 0 \quad (6)$$

From here, the Laplace equation can be used to express the pressure for an incompressible inviscid flow. Equation (7), is known as Bernoulli's equation, and assumes that gravity is only in the vertical z -direction [9].

$$p + \rho gz + \rho \frac{\partial \phi}{\partial t} + \frac{\rho}{2} \nabla \phi \cdot \nabla \phi = \text{Constant} \quad (7)$$

There are some important boundary conditions that are required to solve a potential flow problem. The first of these conditions is the body boundary condition. This requires that no flow can go through the surface of a body. Mathematically this is described by forcing the velocity of the fluid on the body surface to have a velocity with a component normal to the body surface, equal to the normal velocity of the body surface. This is described by Equation (8), where $\mathbf{U} \cdot \mathbf{n}$ is the normal component of the body surface velocity.

$$\frac{\partial \phi}{\partial n} = \mathbf{U} \cdot \mathbf{n} \quad (8)$$

This body boundary condition is similar to boundary condition on a wall on the bottom or any side of a fluid domain. For a typical marine application this could be the seafloor. The fluid cannot penetrate the seafloor, and thus the velocity on the bottom must have a normal component equal to the normal velocity of the seafloor, which would typically be zero.

For an analysis that includes a free surface, there are also two important boundary conditions on the free surface. The first is the kinematic free surface boundary condition. This condition requires that a fluid particle on the free surface must stay on the free surface. Similar to a particle touching the surface of a body, a particle touching the free surface must move with the free surface, and not through it. This is described by Equation (9) where ζ is the free surface elevation in the case that $z = \zeta(x, y, t)$.

$$\frac{D}{Dt}(z - \zeta(x, y, t)) = 0 \quad (9)$$

The dynamic free surface condition states that the pressure on the surface must be equal to the pressure of the atmosphere on the surface. If this were not true you would have accelerations of fluid particles through the surface, which would not be physical. The dynamic condition is described by Equation (10) [8]. This equation is valid on the surface where $z = \zeta(x, y, t)$

$$g\zeta + \frac{\partial \phi}{\partial t} + \frac{1}{2} \left(\frac{\partial \phi^2}{\partial x} + \frac{\partial \phi^2}{\partial y} + \frac{\partial \phi^2}{\partial z} \right) = 0 \quad (10)$$

The free surface can be described as flat with some perturbation which is the slope. The velocity potential can be divided into components which are dependent on the slope do different orders [13]. This can be done because the Laplace equation is linear, so superposition of velocity potentials is valid. This is described by Equation (11). The superscripts denote to which order of the slope the velocity potential is proportional to. The first term would be zero when observing a wave only environment.

$$\phi = \phi^{(0)} + \phi^{(1)} + \phi^{(2)} + \dots \quad (11)$$

This perturbation process allows for a linearization of the free surface boundary conditions. Using Taylor expansions the combined free surface condition and the body boundary condition can be described at the mean water level of $z = 0$ and the mean wetted surface of the body respectively. Each term will be proportional to the perturbation slope of some order. The terms linearly proportional to slope are part of the first order problem. The terms proportional to the square of the slope are part of the second order problem and so on [13]. When only the linear terms are considered the combined free surface condition is shown by Equation (12) at the elevation of $z = 0$ [9]. These simplifications are typically considered reasonable if the slope is small.

$$\frac{\partial^2 \phi}{\partial t^2} + g \frac{\partial \phi}{\partial z} = 0 \quad (12)$$

Regular sinusoidal propagating gravity waves are often used as a model for water waves. The velocity potential of this wave is given by Equation (13) [9]. In this equation ω is the wave frequency, ζ_a is the wave amplitude, k is the wave number, and h is the water depth.

$$\phi = \frac{g\zeta_a}{\omega} \frac{\cosh k(z+h)}{\cosh kh} \cos(\omega t - kx) \quad (13)$$

The linear dispersion, Equation (14), describes the relationship between the wave number and wave frequency of a progressive linear wave [13].

$$\omega^2 = gk \tanh kh \quad (14)$$

As long as a wave is not very steep a regular sinusoidal model is often a good representation of a realistic wave. The satisfaction of the free surface boundary conditions with the presence of gravity waves inherently links potential flow solutions to frequency when waves are possible.

2.1.1 First Order Excitation

When water flows past an object the object will disturb the flow. The resulting flow can be linearly broken into three components as shown by Equation (15). I signifies the incident flow, and would be the flow if no body was present. S signifies the scattering and is because of the disturbance from the body. These two components together make up D , called the diffraction potential. The final component, R , is the radiation component, and is the motion of the water due to the motions of the body [13]. Thanks to the Laplace equation and the concept of superposition each of these problems can be solved separately and the results can be added together.

$$\phi = \phi_I + \phi_S + \phi_R = \phi_D + \phi_R \quad (15)$$

Loads due to ϕ_I are known as Froude-Kriloff loads, loads due to ϕ_S are known as diffraction loads, and loads due to ϕ_R are known as radiation loads. Radiated waves will travel away from the body and eventually die out. The radiation condition states that the energy of radiated waves is carried away to the far field [13].

The resulting first order problem is a boundary value problem. Boundaries include the sea floor, the free surface, the body fluid interface, and the far field. The flow at the body can therefore be determined just based on the conditions at these boundaries. This makes the problem of determining the load on the body much simpler, as the conditions of the flow in all other positions is not required knowledge.

When the pressure due to the radiation potential is integrated on the body surface two forces are possible. One includes all terms proportional to the body acceleration, and one includes all terms proportional to the body velocity. The portion proportional to the acceleration is known as added mass and the portion proportional to velocity is known as damping. These terms are both a function of the frequency of motion [9].

The boundary value problem can be solved using a potential flow code like WAMIT. A panel code solves two integral equations one for the diffraction problem and one for the radiation problem. For the first order problem the integrals are both over the body surface, which is discretized into panels. It is assumed that the flow properties are constant over the area of the panel and are equal to the value at the geometric center of the panel. The integral equations are solved using Green functions which treat the potential problem as a problem of potential sources which create a flow that matches the boundary conditions [13].

When the velocity potential is known at each point on the body, the loads on the body can be calculated by integrating the corresponding pressure on the body. First order excitation will be proportional to the wave slope, which is also proportional to the wave height. First order excitation can only occur at the same frequency as the waves causing the excitation. First order excitation only has an oscillatory component and has a mean value of zero.

2.1.2 Second Order Excitation

Second order theory looks at the same conditions described in the first order theory but models them a little more accurately. In second order theory all terms that are proportional to the wave height or the wave height squared are kept. Rather than taking the free surface conditions at the mean water level and the body condition only at the mean wetted surface, in second order theory the changing elevation of the free surface and the motion of the body are included. Non-linearities in the fluid velocity are also taken into account [9]. Still higher than second order potential flow terms are neglected in in second order theory. Second order theory can result in mean excitation forces.

One source of the second order force is the inclusion of the body motions. Faltinsen describes that as the body moves and generates waves the relative body surface motion will result in an asymmetric time history of the wetted surface. Figure 2.1 shows an example of this where over the period of motion there will be a net force from left to right on the body. A potential flow code needs to first calculate the first order motions to use in second order calculations involving the changing position of the body.

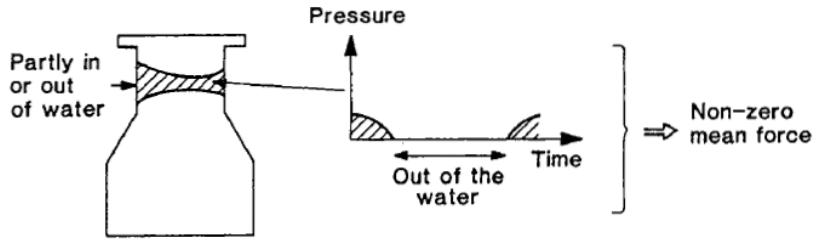


Figure 2.1: Horizontal mean force contribution due to wetted surface difference; source: [9]

Equation (7) and Equation (10) also contain squared terms. In first order theory these terms were neglected, but the second order components of these terms are included in second order theory. When waves of multiple frequencies are present the quadratic terms will lead to additional mean forces as well as forces that oscillate slowly with the difference in frequency and forces that oscillate quickly with the sum of the frequencies [9]. Interestingly when only terms up to the second order are kept, the second order velocity potential does not lead to any mean force. This means that if only the mean load is of interest only the first order velocity potential is needed, which makes calculations much quicker [9].

There are two common approaches to calculate the mean drift forces. The first is by using far field integration. This method is based on the conservation of momentum over a large domain. The load on the body will counter any changes in fluid momentum on the boundaries of the domain. The second approach is to use a direct pressure integration on the surface of the body. This method can have difficulties when implemented in a panel method if the panels are too large, due to the assumption that the flow is constant across the panel [9]. If forward speed or current are present, other second order terms become present as well. A more detailed compilation of the integrals needed to calculate the full second order excitation force can be found in [13].

The slowly varying second order excitation forces are of particular interest in this project. These forces occur at the difference frequency of two different waves. A quadratic transfer function will define the magnitude and phase of a difference frequency force given the input wave elevations and frequencies. For two waves of frequency f_n and f_m and heights ζ_{an} and ζ_{am} , the resulting force will be equal to: $H^2(f_n, f_m)\zeta_{an}\zeta_{am}$. The quadratic transfer function is complex valued which means that it will give information not only on the magnitude of the force, but also the phase relative to the input. The transfer function is used for calculations in the frequency domain.

Newman's approximation offers a simplification the difference frequency quadratic transfer function. Newman stated that the quadratic transfer function could be approximated only by the mean drift values, or the values along the zero difference frequency diagonal. The imaginary portion of the function is zero here, and the approximation says that it can be thought of as zero everywhere. The real component can be approximated based on the values along the center diagonal. Equations (16) and (17) explain this process [9].

$$\text{Re}\{H^{(2)}(f_n, f_m)\} = \frac{1}{2}(H^{(2)}(f_n, f_n) + H^{(2)}(f_m, f_m)) \quad (16)$$

$$\text{Im}\{H^{(2)}(f_n, f_m)\} = 0 \quad (17)$$

When zero current or forward speed is present, the values along the zero difference frequency diagonal are only a function of the first order velocity potential and not the second order velocity potential. This means that if Newman's approximation is used the necessary computations to calculate the slowly varying loads are significantly reduced. In cases that the approximation still provides good results, this can be very advantageous [9]. Often the quadratic transfer function is of interest if the natural frequencies of the response are much lower than the frequency of the incident waves. If the natural frequency of interest is very small and very close to the zero frequency diagonal, then Newman's approximation will likely yield good results, as the shape of the transfer function has not changed much over the short distance to this difference frequency. The semi-submersibles used in the oil and gas industry are often very large, and have very low natural surge and pitch frequencies. Because of this, Newman's approximation is often used.

2.2 Viscous Flow

A real fluid has a non-zero viscosity, which allows the fluid to impart shear stress on itself. This means that when two layers of fluid have a different velocity, there will be some resistance between the layers. The stress is dependent both on an intrinsic property of the fluid known as the viscosity, and the velocity profile of the flow. The stress can be calculated with Equation (18). In this equation μ is the dynamic viscosity. The kinematic

viscosity, ν , is also commonly used when describing viscous stress and is equal to the dynamic viscosity divided by the density ρ .

$$\tau = \mu \frac{\partial u}{\partial y} \quad (18)$$

Viscous flow near a body will result in a boundary layer. At the surface of a body the fluid cannot have any relative motion; this is known as the no-slip condition. This stationary fluid then imparts a shear stress on the fluid flowing outside of it, retarding its motion. This results in a boundary layer shape in the flow's velocity profile. Boundary layers are a very important topic of many practical flows. One important phenomenon that is dependent upon boundary layers is flow separation. Viscous flow cannot stay attached to a body when fighting against a strong adverse pressure gradient. This pressure gradient could be the result of flow around a blunt body such as a cylinder or a foil with a high angle of attack. When the flow cannot stay attached separation occurs which dramatically changes the pressure distribution on the body, and thus the forces. A real flow will always separate when a sharp corner is present. Viscous effects can significantly change the flow that is predicted by potential flow theory.

2.2.1 Boundary Layers

The boundary layer is the region where there is a significant gradient in velocity in the direction normal to the main flow. In this region there is important shear between layers of the flow, and the motion cannot be thought of as irrotational, thus making potential flow a bad model. A typical introduction to boundary layers studies the two-dimensional flow past a flat plate. On the plate the velocity is zero, and at the extent of the boundary layer the velocity has essentially asymptotically reached the outer velocity. Conventionally the end of the boundary layer is defined as the point when the velocity is equal to 99% of the outer velocity. The boundary layer thickness following this definition is called δ . The direction of the main flow is often called the x-direction and the direction normal to the plate is called the y-direction. Two assumptions are often made about boundary layer flows: the dimensions of the boundary layer are much larger in the x-direction than in the y-direction, and the changes in the flow are much larger in the y-direction than in the x-direction. These assumptions not only apply to a flat plate, but also to a curved surface or to a free shear layer, where again the x-direction would be associated with the direction of the main outer flow, and the y-direction would be normal to this [24].

These assumptions can be used to simplify the non-dimensional Navier Stokes equations for boundary layers using an order of magnitude method. It is found that the pressure gradient in the y-direction (normal to the outer flow) must be very small, and thus the pressure is said to be impressed through the boundary layer from the outer flow. Outside of the boundary layer, where the flow can be reasonably thought to be irrotational, potential flow often provides a good prediction. This means that for many cases the pressure throughout the boundary layer is very close to the pressure predicted by potential flow at the extent of the boundary layer. The result of the simplifications are the Prandtl boundary layer equations shown in Equations (19) and (20). In these equations a lowercase u represents the value of the velocity in the boundary layer, and the capital U represents the value in the outer flow [24].

$$\frac{\partial u}{\partial x} + \frac{\partial v}{\partial y} = 0 \quad (19)$$

$$\frac{\partial u}{\partial t} + u \frac{\partial u}{\partial x} + v \frac{\partial u}{\partial y} = \frac{\partial U}{\partial t} + U \frac{\partial U}{\partial x} + \nu \frac{\partial^2 u}{\partial y^2} \quad (20)$$

In the case of a steady flow with no pressure gradient, Equation (20) reduces to Equation (21).

$$u \frac{\partial u}{\partial x} + v \frac{\partial u}{\partial y} = \nu \frac{\partial^2 u}{\partial y^2} \quad (21)$$

This shows that the convective terms must be able to balance the viscous stress term. X derivatives are associated with a length in the x-direction which is proportional to some position X along the boundary layer, and y derivatives are associated with a length in the y-direction which is proportional to the boundary layer thickness δ . It is assumed that the velocity in the x-direction, u , is proportional to the outer flow U , and the velocity in the y-direction, v , is proportional to $u \frac{\delta}{X}$. From these assumptions, a proportionality for the boundary layer thickness is found as in Equation (22).

$$\delta \propto \sqrt{\frac{\nu X}{U}} \quad (22)$$

This shows that the boundary layer grows in thickness as it grows in length. It also shows that a more viscous fluid will result in a thicker boundary layer; this follows logically as the non-moving fluid at the start of the boundary layer will be able to impart more shear stress on the successive layers. It is also shown that the boundary layer becomes thinner with higher outer velocities, as the influence of the outer flow becomes more significant. This proportionality was derived with laminar flow in mind, but analogies can be drawn between the laminar viscosity and a so-called turbulent viscosity as well. It is important to note that if the boundary layer thickness changes more or less fluid is retarded, and thus to conserve mass some flow must occur in to or out of the boundary layer.

Two other useful descriptions of the boundary layer thickness are the displacement thickness and the momentum thickness. Both of these measures replace the viscous boundary layer with a slightly larger body and a flow that does not feel any viscous stress from the body (absence of the no-slip condition). The displacement thickness is the distance that the body would need to grow so that the loss in mass flow (assuming potential flow velocities) is equal to the loss in mass flow that occurs in the boundary layer. Similarly the momentum thickness is the distance that the body would need to grow so that the loss in momentum in the flow is equal to the loss in momentum that occurs in the boundary layer. These can be described mathematically by Equations (23) and (24) where δ_1 is the displacement thickness and δ_2 is the momentum thickness.

$$\delta_1 U_\infty = \int_0^\infty (U_\infty - u) dy \quad (23)$$

$$\delta_2 U_\infty^2 = \int_0^\infty u(U_\infty - u) dy \quad (24)$$

The momentum thickness is the smallest, followed by the displacement thickness, and then the boundary layer thickness as shown in Figure 2.2.

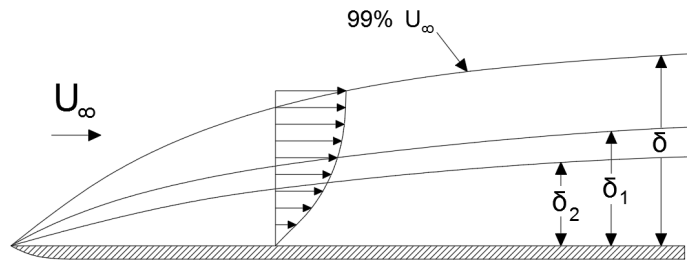


Figure 2.2: Boundary layer thickness, displacement thickness, and momentum thickness

The nature of the boundary layer will change when a pressure gradient is present in the outer flow. This is dictated by the terms in Equation (20) that contain a capital U . If the outer flow creates an adverse pressure gradient (the pressure increases in the direction of the outer flow) then the slowed fluid particles in the boundary layer will at some point not be able to continue forward. The fluid near the body will at some point actually start to flow opposite of the outer flow, following the local pressure gradient instead. At this point the boundary layer cannot stay attached to the body and will separate away into the free stream. The point where this occurs is called the separation point and will be some distance after the onset of the adverse pressure gradient, as the separation process takes some time. Separation is expected in flow around blunt bodies such as cylindrical shapes, and will always occur at sharp corners [24].

At the point of separation the direction of the flow directly above the body will switch. This means that at the separation point the derivative of the velocity, $\frac{\partial u}{\partial y}$, has a value of zero, leading to zero shear stress at the separation point. Flow past the separation point is often much more complex. Typically the value of the pressure in the separated region will be similar to the pressure at the point of separation [24].

The Reynolds number is a non-dimensional term that relates the relative importance of viscous forces to inertial forces and is given by Equation (25). The number can be defined in a number of ways with different ideas of a characteristic length and velocity. For very low Reynolds number flows the viscous forces are very dominant and separation may not occur even in the presence of an adverse pressure gradient. As the Reynolds number increases separation occurs, and the wake forms. The nature of the boundary layer before separation and the wake past separation varies with Reynolds number. Figure 2.3 shows rough regimes for a rigid cylinder in a steady flow based on experiments described by Lienhard in 1966. Many parameters including the presence of a free surface, three dimensional effects, roughness, and unsteadiness in the flow can change the corresponding

Reynolds number ranges for each regime, and the look of the flow in each regime. However the experiments still provide a good reference point for the progression of separation and the wake for a circular cylinder.

$$Re = \frac{Ul}{\nu} \quad (25)$$

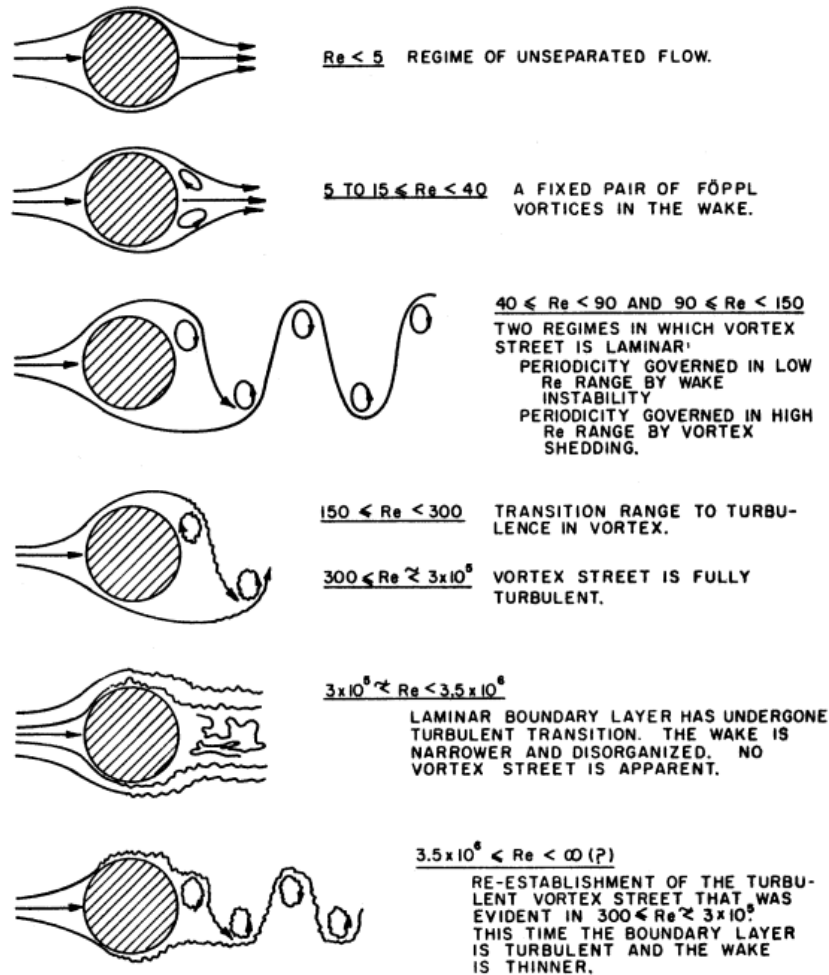


Figure 2.3: Turbulent boundary layer; source: [14]

2.2.2 Turbulent and Transitional Flow

The viscous flow described above is known as laminar flow. This type of flow has predictable smooth streamlines. Many real relevant flows are not laminar, but are turbulent, with random fluctuations in all directions. All real flows have some sort of tiny random fluctuations in them with a wide range of frequencies. In a laminar boundary layer the relative strength of the viscous shear overcomes these fluctuations and results in a stable flow where the perturbations die out. At some critical point a flow can become unstable and these perturbations will instead start to grow. For some time or distance after the point of instability the flow will contain laminar regions and turbulent regions. This region is known as the transition region, and the proportion that is turbulent will grow until there is no laminar flow left. At this point there is a fully turbulent boundary layer [24]. The transition region is shown in Figure 2.4.

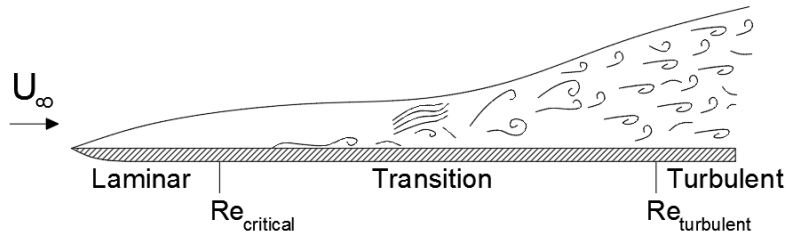


Figure 2.4: Transition to turbulence along a flat plate; adapted from [24]

The location of the point of instability can be predicted with the Orr-Sommerfeld equation. The equation shows that as the Reynolds number of the flow increases at some point instability will be triggered. This point is described by the critical Reynolds number. It also shows that this instability will happen sooner for a flow that contains an adverse pressure gradient [24].

Turbulence in a flow has some important impacts on the boundary layer. Random perturbations occur in every direction leading to mixing of fluid particles between layers. This means that there is some momentum transfer between layers of the boundary layer. This momentum transfer ties the layers together essentially creating a viscosity type effect. This increased virtual viscosity leads to a thicker boundary layer. The momentum transfer between the layers also impacts boundary layer separation for a turbulent flow. Because momentum can be fed into the boundary layer from the outer flow through the random perturbations, the boundary layer can withstand an adverse pressure gradient for a longer time or distance. This means that for the same outer pressure distribution and flow a turbulent boundary layer will separate later than a laminar boundary layer. This has a direct impact on the pressure distribution and forces on a body. The virtual added turbulent viscosity also impacts free shear layers such as wakes [24].

A fully developed turbulent boundary layer has a different profile as well as thickness and strength from a laminar boundary layer. When discussing a turbulent boundary layer a non-dimensional distance from the wall called y^+ is often used; this is calculated following Equation (26). In this equation v^* is the friction velocity, which is a function of the wall shear stress described by Equation (27).

$$y^+ = \frac{yv^*}{\nu} \quad (26)$$

$$v^* = \sqrt{\frac{\tau_w}{\rho}} \quad (27)$$

The turbulent boundary layer can be divided into three main sections as shown in Figure 2.5. The inner layer is dominated by viscous forces and the outer layer is dominated by turbulent forces. In the middle, or the overlap layer, both are important. The inner layer can be divided into two sections: the viscous sublayer with a linear velocity profile and extends to $y^+ = 5$ and the buffer layer with a logarithmic velocity profile which extends from $y^+ = 5$ to $y^+ = 30$. The outer layer starts at approximately $y^+ = 300$ and the profile is largely dependent on the pressure gradient of the outer flow. In the overlap layer the outer and inner solution need to match, and it is found that a logarithmic velocity profile allows this to happen [24].

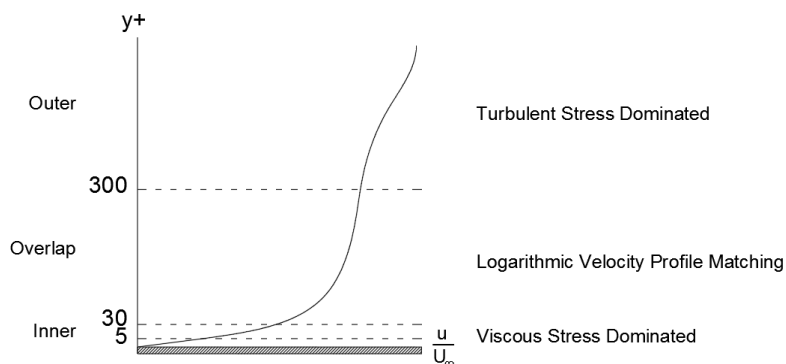


Figure 2.5: Turbulent boundary layer; adapted from [30]

Turbulent fluctuations can happen on many different scales. In a typical hydrodynamic application turbulence occurs on a very small scale. In a marine numerical simulation, resolving these very small turbulent

fluid motions is most often prohibitively computationally expensive. For this reason, many form of turbulence models are used instead. These will be described layer in further detail. In general a turbulence model attempts to capture the effects on the main flow from the turbulence, without directly calculating the intricacies of the turbulent flow.

2.2.3 Oscillatory Flow

Many of the important flows when considering the sea-keeping characteristics of a floating platform are oscillatory. Waves as previously described have circular water particle motions, and the velocities in a given direction thus vary sinusoidally. Motion in all six degrees of freedom for a moored platform are also periodic, resulting in relative oscillatory flows around the body. This results in problems where time derivatives are important. This is especially true for the potential flow solution which is very much dependent on the platform's and water's accelerations. It is also important for the nature of the viscous flow. The phenomena previously described such as boundary layer separation and transition to turbulence take time to develop. The relative importance of the terms of the boundary layer Equations ((19) and (20)) are also time dependent in an unsteady flow.

The Keulegan–Carpenter number is a non-dimensional number that describes how large a periodic motion is relative to a certain body. It is typically referred to as the KC number. It can be defined as shown in Equation (28), where A is the amplitude of the periodic motion and D is the characteristic diameter of the body. It is important to note that A is the amplitude of the relative motion between the body and a single particle of fluid; this does not correlate to a wavelength for a water wave, but is directly related to the wave height. A small KC number means that there is a small amplitude motion compared to the size of the body, and a high KC number means that there is a large amplitude motion compared to the size of the body.

$$KC = 2\pi \frac{A}{D} \quad (28)$$

The equation for the KC number is commonly expressed as Equation (29), where U_{max} is the maximum relative velocity between the fluid and the body, and f is the frequency of the motion.

$$KC = \frac{U_{max}}{fD} \quad (29)$$

Both separation and transition to turbulence take some time to develop, and thus may not occur for very small KC numbers. While transitioning to turbulent flow does take some time, it will occur at a lower critical Reynolds number for an oscillatory flow than a steady flow. The general unsteadiness of a periodic flow helps trigger instability at a lower Reynolds number. In addition to this, if there is separation and the development of a wake, the wake will become turbulent at a much lower Reynolds number than the boundary layer on the body. This is because in a wake there is an absence of the stronger viscous forces from the stationary fluid on the body which act to stabilize fluctuations at low Reynolds numbers. When the direction of the periodic flow reverses, the body will then travel through the previously generated wake. Moving through this more turbulent flow will also reduce the critical Reynolds number, and reduce the transition length to fully turbulent flow [24].

For very low KC number flows the time derivative terms are relatively much more dominant than the convective terms which again take time to develop. An analysis of successive approximations of the boundary layer equations can be done to predict the time of separation for a circular cylinder with an impulsive start up. The first order of approximation includes the time derivative terms and the viscous terms which are immediately important. The second order approximation includes convective terms which require that velocity has developed to be significant. Separation occurs when the velocity gradient ($\frac{\partial u}{\partial y}$) goes to zero at the body surface. It is found that this occurs at a time equal to 0.7 divided by the acceleration of the outer flow. The separation will occur first at the point where this acceleration is the greatest. It is found that for a circular cylinder this time occurs when the cylinder has traveled a distance equal to 18% of its diameter [24].

$$t_{separation} = \frac{0.7}{\partial U / \partial x} \quad (30)$$

$$x_{separation} = 0.18D \quad (31)$$

This means that if a cylinder does not move at least this far in an oscillation, separation cannot occur. Thus for very small amplitude oscillations, meaning very low KC numbers, there will not be any separation. For very low KC number motions accelerations are dominant, and potential flow can provide a very good prediction.

A successive approximations method can also be used for sinusoidal motions of a cylinder with a low KC number. Again the low KC number ($KC \ll 2\pi$) indicates that the convective terms are much smaller than the time derivative terms. For a circular cylinder it is found that the viscous contribution to the force (additional to the potential flow forces) comes in two parts. The first part is due to the wall shear force due to the viscous boundary layer. The second contribution is due to a change in the boundary conditions of the potential flow problem. When the original potential flow problem is solved a body boundary condition states that there can be no flow in or out of the surface. However when the boundary layer develops it has a varying thickness around the cylinder, which to satisfy mass continuity, requires inflow and outflow to the boundary layer. This slightly changes the potential flow solution for the outer flow. When the two contributions are added together it is found that the viscous force in a non-separated low KC number oscillation is linearly proportional to the velocity. This is different than the typical idea of a drag force, which is proportional to the velocity squared, which is true for a separated flow [24].

High KC oscillations start to more closely resemble steady flow. Phenomena such as turbulence, separation, and vortex shedding can have time to develop in a certain direction. Analogous to the potential flow concept of wave drift damping, when an oscillation is large compared to the size of the body, there is a section of the period which is similar to a quasi-steady motion. It is interesting to note that the wake generated from the previous direction's motion can still be present, and can effect the flow patterns. The presence of the wake will add turbulence and will also effect the relative velocity between the body and the fluid. Previously shed vortices will create on average a higher apparent velocity, increasing the drag forces [9].

The flow patterns for very low and very high KC numbers are somewhat predictable. For intermediate KC numbers there is more uncertainty. Three-dimensional effects also add to the complexity of the problem and make it more difficult to predict the appearance of the flow and the resulting forces on a body.

2.3 Computational Fluid Dynamics

Computational fluid dynamics (CFD) is a numerical method to predict flow. Typically this term is applied to codes that solve for a fully viscous flow. One common type of code uses the Reynolds averaged Navier Stokes (RANS) equations to describe a flow with turbulent velocity and pressure perturbations. Each velocity and pressure term in the Navier Stokes Equations ((1) (2)) is made of the sum of a time averaged value and a turbulent perturbation value. When the full equations are time averaged, many of the turbulent perturbations (any first order terms) disappear. However some second order turbulent terms called Reynolds stresses still remain, and act similarly to laminar viscous stresses. This forms the basis of the RANS equations, which are the base of some common CFD codes.

These codes include turbulence models to incorporate the effects of turbulence without fully solving for all turbulence. CFD typically refers to a time domain solution and can be used for steady or unsteady problems. For an unsteady simulation, the solution for velocity and pressure for a given time step is solved iteratively until some standard is achieved, then the solver proceeds to the next time step.

The finite volume method is the most widely used approach for CFD codes. A fluid domain is defined with specified boundaries and boundary conditions. This domain is then discretized into cells. Each cell has a value of velocity and pressure, as well as other variables depending on the types of models used. A cell center approach is common, where the value of a given variable for a cell is taken as the value of the variable at the centroid of the cell. Some initial conditions are given for the values of all variables in every cell. Each variable is calculated following the RANS equations and equations of other implemented models based on the values of the variables in the surrounding cells.

A good discretization of the domain is essential for physically accurate flow predictions. There are many ways to create and test the quality of a mesh, and different sizes and shapes of cells are useful in different locations in the domain. The temporal discretization of a simulation can also significantly effect the results, and care should be taken in selecting the time step. The Courant number is a useful indicator of the relative size of the time step. It is essentially the ratio of the distance traveled by a single fluid particle in a time step and the size of the cell. It is calculated following Equation (32), where the magnitude of the velocity in each i direction and the characteristic cell dimension in the i direction are used.

$$Co = \frac{|u_i| \cdot dt}{l_{celli}} \quad (32)$$

Many methods and models are used for different problems, and it is important to remember that no one method and model can provide good predictions for all problems. Attention must be given to make sure that the assumptions of each model fit the physics of the problem. Details on the specific models used in this project are described later, and the reasoning behind the selections are discussed.

2.4 Signal Analysis

Many engineering problems can be analyzed both in the time and frequency domain. Depending on the problem one or the other may be the advantageous choice. A continuous and periodic function can be transformed from the time domain to the frequency domain through a Fourier transform as shown in Equation (33). This function can then be transformed from the frequency domain back to the time domain through an inverse Fourier transform as shown in Equation (34) [27].

$$F(\omega) = \int_{-\infty}^{\infty} f(t)e^{-i\omega t} dt \quad (33)$$

$$f(t) = \frac{1}{2\pi} \int_{-\infty}^{\infty} F(\omega)e^{i\omega t} d\omega \quad (34)$$

When looking at measured data, summation forms of the previous two equations are used with discrete values. dt is replaced with the time step of the measurement system. The value of df used in the inverse Fourier transform is equal to $\frac{1}{T}$ meaning that $d\omega = \frac{2\pi}{T}$.

A transfer function quantifies an output signal from an input signal. An example of an input signal could be a time series of wave elevations which lead to an output of a hydrodynamic excitation force. A transfer function works in the frequency domain, so the signals may need to be converted by use of a Fourier transform. Given a certain frequency input a transfer function will give a corresponding frequency output. Two forms of a transfer function are a linear and a quadratic transfer function. For a given frequency a linear transfer function will quantify the direct relationship between input and output at that frequency, and a quadratic transfer function will quantify the second order relationship between the input and output at that frequency.

Throughout a time series of a signal the frequency of the data can change. A Fourier transform will provide information about the frequency and phase content of the entire time series, but does not pinpoint what the dominant frequency is at a given instant in time. It can be useful to quantify the instantaneous frequency of a signal. If a periodic signal is expressed in complex form, the phase of the signal at a given time will be equal to the frequency multiplied by the time, plus some phase difference. In theory if the instantaneous phase is differentiated with respect to time the result will be the instantaneous frequency. In practice for an irregular signal there is no way to know the function to differentiate. In 1995 Cohen described a method using the first moment of the local frequency, which is determined using a Gabor transform. The frequency is thus calculated following Equation (35) and Equation (36). The Gabor transform uses a Gaussian window to isolate the frequency information near the time of interest [4]. In reality the integration limits will be finite, and can be chosen along with the value of σ to give a certain level of significance at a certain time away from the time of interest.

$$f_{inst} = \frac{1}{\int |S_{Gabor}(t, f)|^2 df} \int f |S_{Gabor}(t, f)|^2 df \quad (35)$$

$$S_{Gabor} = \sigma^{1/4} \int_{-\infty}^{\infty} e^{-\sigma\pi(t-\tau)^2} e^{-i\omega\tau} f(\tau) d\tau \quad (36)$$

3 Previous Work

In order to make offshore wind energy increasingly cost competitive, accurate and efficient predictions of hydrodynamic loads and the resulting motions are needed. This has been the subject of many research projects. Some relevant previous approaches are described below. These works include the use of different types of numerical methods. Both potential flow calculations and viscous CFD have been used to try predict the motions of a semi-submersible wind turbine platform. Physical model tests have also been used in different ways to predict full scale results.

Successful components of these studies are considered when determining the test procedures of this project. This includes not only different ways of looking at the problem, but also incorporating effective practices for performing numerical calculations.

The potential flow study of this project is similar to previously performed studies, and similar shortcomings can be expected. The viscous correction study of this project is a unique approach to add accuracy to the model. The approach is based on problems identified in previous attempts to incorporate viscous flow effects.

3.1 Potential Flow Projects

Potential flow studies are relatively computationally inexpensive, and have been performed extensively. First order potential flow analyses are simpler but do not have the ability to predict any low-frequency wave excitation. Two studies are discussed below which incorporated second order potential flow calculations to model the difference frequency excitation effects.

3.1.1 Roald, Jonkman, Robertson, and Chokani 2013

In 2013 Roald, Jonkman, Robertson, and Chokani investigated the effects of second order excitation of both a spar buoy and tension leg platform floating offshore wind turbine. Both of these structures were designed to support the NREL 5 MW reference wind turbine [22]. At the time of publication most offshore wind turbine analyses were based on the empirical Morison's equation, which is best suited for slender structures. Most potential flow diffraction and radiation calculations only incorporated first order theory and excitation. Roald et al. conducted this study to determine the significance of sum and difference frequency forces on spar and tension leg platform wind turbines. While these structures have larger volume members than fixed bottom wind turbines, they are smaller than similar offshore structure for the oil and gas industry. Roald et al. compared their results with methodology typically used for oil and gas platforms [22]. Model tests performed at MARIN as a part of the DeepCWind project initiated interest in the second order effects on floating wind turbines.

Their analysis used the program FAST, where the frequency dependent hydrodynamic coefficients are solved for using WAMIT. FAST then models the coupled problem in the time domain which allows analysis of non-linear connections between the aerodynamic and hydrodynamic problems [22]. Roald et al. point out various limitations of looking at the turbine only in the frequency domain. The transient phase which can only be observed in the time domain, is important when looking at the effects of control theory, unsteady conditions, and viscous drag. The panel models used in the project utilized varying refinement with smaller elements near sharp corners and near the free surface. A convergence study was done to select the proper panel model. The project also looks at the effects of incorporating a flexible tower.

For the spar buoy the first order forces were found to be an order of magnitude larger than the second order forces. The difference frequency forcing however was found to cause a heave motion similar in magnitude to the first order forcing. For the tension leg platform sum frequency forcing was found to be similar in magnitude to the first order forces. The difference frequency forcing was found to cause larger pitch motions than the first order forcing, and much larger surge motions, and in the heave motion the sum frequency component was again equally significant. For the spar buoy the hydrodynamic mean drift force was also compared to the mean rotor thrust force of the operating wind turbine using FAST. At the rated wind speed, where thrust is at a maximum, the aerodynamic thrust was over 100 times larger. At most the hydrodynamic mean drift force was found to equal 15% of the aerodynamic thrust in extreme wind speeds. It was found that the low frequency motions due to hydrodynamic difference frequency forces were over an order of magnitude lower than those from the aerodynamic loads for the spar buoy supported turbine [22].

3.1.2 Chuang, Liu, and Lu 2020

In 2020 Chuang, Liu, and Lu from the Dalian Maritime University published a paper describing their work with the OC4 DeepCWind semi-submersible platform. The platform was also designed to support the NREL 5 MW wind turbine and was the subject of a large joint industry project. Chuang et al. analyzed the mean drift and slowly varying wave loading of the platform using two tools, FAST and SIMA. FAST was developed by the National Renewable Energy Laboratory and uses the WAMIT code to calculate the hydrodynamic coefficients

used for the time domain simulations. SIMA was developed by Sintef Ocean and uses WADAM for calculation of hydrodynamic coefficients, which is also based on the WAMIT code [31].

The OC4 semi-submersible is comprised of three large columns, one smaller column, and slender bracing. Chuang et al. modeled the three larger columns with a panel model and the smaller column and bracing as Morison elements. The panel model portion is used in the potential flow analysis, and the more slender Morison elements are modeled with Morison's equation, as the viscous load is more important for these members [31]. A convergence study with three refinement levels was conducted for the panel model. Both first and second order results were compared in the convergence test. It appears that the three models produce similar results in the majority of the frequency range, with varying results near the natural periods. Despite the dependence on the model resolution at the natural periods, the model with the middle refinement level was selected for efficiency. Both the far field and direct pressure integration methods for prediction of the mean drift force were also compared. After the model was chosen, a coupled aerodynamic and hydrodynamic time domain analysis was conducted in both FAST and SIMA. Three levels of hydrodynamic modeling were tested for three environmental conditions. The hydrodynamic models were: first order excitation only, first order and mean drift excitation, and first order and difference frequency excitation. The environmental conditions all included irregular head seas with a JONSWAP wave spectrum. Two environmental conditions included no wind, one with small wave conditions and the other with moderate wave conditions. Finally the moderate wave conditions were also tested in combination with a steady 18 m/s wind speed [31].

Chuang et al. found that the inclusion of the difference frequency excitation loads led to significantly higher mean surge values. This was true for both SIMA and FAST which provided similar results. The inclusion of the second order excitation loads did have slightly larger impact on the results produced in SIMA. The numerical results were only compared with each other, so there is not a way to validate which results are the most accurate. It was concluded that for the semi-submersible it is important to include the higher fidelity second order analysis. This was particularly true when observing surge motions and fairlead tension. The bending moment at the base of the wind turbine tower was not significantly effected. It was concluded that for the conditions tested this was strictly dominated by the wind conditions [31].

3.2 Model Test Data Incorporation

Model tests can be used to simply observe scaled motions in scaled environmental conditions. This is useful and interesting, but on its own only gives information about the response in one specific condition. Model test results can also be used in combination with potential flow analyses. Analysis of the model test data can be used to tune the potential flow based models or to fill in gaps in the potential flow theory. Different successful approaches to improving numerical models with the use of experimental data are described.

3.2.1 Berthelsen, Bachynski, Karimirad, and Thys 2016

Berthelsen, Bachynski, Karimirad, and Thys conducted a study of a braceless semi-submersible floating wind turbine in 2016. The platform was designed to support the NREL 5 MW reference turbine. The project aimed to calibrate and validate numerical predictions of motions based on the results of model tests performed in MARINTEK's ocean basin in 2015. The tests included both hydrodynamic and rotor loading. Due to the different scaling of the hydrodynamic and aerodynamic effects a true hybrid test is difficult to achieve with confidence in the results. To isolate the hydrodynamic study but still incorporate the coupling effects of the wind turbine an actuator method was applied in these tests. Catenary mooring lines are used in the tests scaled to match the weight properties of the real lines. Realistic irregular wind and wave spectra were used for the model tests. Decay tests and wind only and wave only tests were also conducted [2].

The numerical model to be calibrated to the model tests included potential flow coefficients and Morison elements. The potential flow coefficients were calculated using WAMIT and include frequency dependent added mass and damping as well as first order excitation transfer function and second order wave drift force transfer functions. Newman's approximation was used in the model to calculate difference frequency effects, so a full quadratic transfer function was not calculated. All components of the structure were assigned Morison drag coefficients which were selected to match the results of the model tests. The mooring lines were modeled by RIFLEX and also included Morison drag elements. The numerical model was designed to produce time series of motions and include the rotor loads that were applied to the actuator in the model tests. The wave elevations used in the numerical model are those measured in the model test [2].

The drag coefficients are selected based on an analysis of the model test decay tests. It was concluded that the quadratic drag coefficients are dominated and these are the only ones considered. The drag coefficients were iteratively adjusted for various components of the structure. Each iteration was evaluated by generating a numerical decay test to compare with the model test [2]. Berthelsen et al. state that these coefficients while applicable for calm water likely vary in wave conditions due to changes in the nature of the flow.

To test the selected coefficients the numerical model was used to generate time series for the wind and wave time series of the irregular model tests. It was found that the predictions for low frequency surge and pitch were significantly lower than the motions in the model test. To tune the model to match the data varying drag coefficients were introduced, with higher values closer to the free surface where the water velocities are the largest. This increases excitation force but not the damping, resulting in larger motions [2]. When comparing to simulations including no viscous drag terms it was concluded that for this platform the surge response is heavily dependent on viscous drag. It was also found that the wind thrust made the largest contribution to the surge response [2].

3.2.2 Silva de Souza, Fonseca, Berthelsen, and Thys 2021

Silva de Souza, Fonseca, Berthelsen, and Thys of SINTEF Ocean as a part of the WINDMOOR project used model test data to calibrate a time domain model. The low frequency motions of the semi-submersible are the focus of the work, where a numerical model is designed to recreate the experimental motions. Potential flow analysis was done using WAMIT to determine added mass, damping, and first and second order excitation. For the second order excitation only wave drift loads were calculated leading to the use of Newman's approximation to use as a quadratic transfer function. Drag coefficients for the model are made of a linear and a quadratic component. Both the linear and quadratic components are split into two parts, one part that corresponds to the calm water damping, and one part that corresponds to the damping in waves, which is sea state specific. The calm water coefficients are calculated using decay tests and the wave coefficients are calculated using wave model tests [25]. Once the coefficients were selected they were implemented using SIMA and RIFLEX to determine the resulting motions.

For each sea state tested the wave coefficients are calibrated so that the resulting motions match the model test motions as well as possible. The quadratic transfer function used in the time domain model also uses information from the model tests. An empirical transfer function is calculated from the tests as described by Fonseca [10]. This transfer function is blended with the numerically calculated function based on Newman's approximation. The empirical function takes precedence further from the zero difference frequency diagonal, and the numerical function takes precedence near zero difference frequency. This process is also sea state specific [25].

The results of the numerical model matched the experimental data well. The largest discrepancy occurred in the low frequency pitch motion. In general the empirical wave drift coefficients were higher than the coefficients found using WAMIT; this difference is more pronounced at the lower frequencies. The model test motions were compared with both the fully calibrated numerical model, and the numerical model which only used the potential flow results and the calm water damping values. The calibrated model performs well, and significantly better than the non-calibrated model for both small and large seastates at both the wave frequency and at low frequency [25].

3.2.3 Fonseca, Thys, and Berthelsen 2021

Fonseca et al. of SINTEF Ocean conducted a study on the INO WINDMOOR semi-submersible in 2021; they analyzed the same model test results used in this project. The analytical method of cross bi-spectral analysis described by Stansberg were used to find empirical quadratic transfer functions for the platform. The technique assumes that the measured signals are Gaussian distributed and requires statistical averaging and signal smoothing at multiple points of the process. Stansberg states that these can be difficult techniques to get correct and can take some experimentation. They are however critical to obtaining good results [27].

The analysis assumes that the low frequency motions can be considered uncoupled from the low frequency motion in the other degrees of freedom. A low frequency excitation force was calculated based on the filtered data assuming the form of a single degree of freedom damped oscillator [10]. The excitation force was used to calculate the quadratic transfer function through cross bi-spectral analysis. These functions were then used to reconstruct time series of surge which were compared to the data of the model tests. A considerable amount of iterative statistical averaging and changes to damping was needed to tune the quadratic transfer function. After this process Fonseca et al. found good agreement between the time series [10]. The project focuses on the low frequency surge and pitch response. Test cases for many irregular environmental conditions are studied. These include small, moderate, and severe sea states, as well as some cases with an added steady current. Most of the cases are with head seas, although some are also considered with beam seas [10].

They also calculated numeric predictions of the quadratic transfer function using a potential flow solver in the program Hydrostar. In the potential flow calculations the free surface integral is not included. These functions were compared to the empirical functions obtained from the model test analysis for verification. It was found that the potential flow solver and model tests had good agreement for small sea states over the entire frequency range. For larger sea states this agreement becomes much worse, particularly near the natural frequency. The potential flow predictions are even further from the model test data when current is included.

The discrepancies in high sea states and with current interaction are mostly attributed to viscous effects, as well as the possibility of higher than second order effects. Fonseca et al. also developed combined quadratic transfer functions that have influence from both the potential flow solution, and the model test empirical functions for a given environmental condition [10].

3.3 Computational Fluid Dynamics Projects

A number of studies have performed CFD analyses with semi-submersible wind turbine platforms. Each of these projects aimed to identify and evaluate the influence of viscous flow effects on the motions of a floating platform. In all cases it was found that the added computation cost of viscous calculations led to some new information about the body's motions.

Two types of tests are common: decay tests and freely floating tests with incident waves. Tests with wave excitation are interesting to observe. If performed at model scale these tests can serve as a strong method of validation with comparison to analogous model tests. If performed at full scale the Reynolds number effects of a real platform can be studied in a realistic environment. Decay tests are used to identify values of linear and quadratic damping. Some success has been found using this technique, however the damping coefficients are characteristic to the specific properties of the motion simulated in the decay test, and may not be effective when broadly applied.

Discussion of the numerical tools and solvers used and their effectiveness is also of interest for the CFD model setup used in this project.

3.3.1 Rivera-Arreba 2017

In 2017 Rivera-Arreba performed a computational study of the wave loads on floating structures including a test case of a cylinder and the DeepCWind semi-submersible floating offshore wind platform developed in the OC5 project. Like this project, the work was completed as the thesis of the European Wind Energy Master, and utilized OpenFOAM for the CFD analysis. The study was done in collaboration with Deltares. The waves2Foam tool, created by Jacobsen of Deltares, was used for the wave modeling and the for the mooring model. The numerical wave tank was tested to ensure that the waves generated matched the theory. Rivera-Arreba successfully validated the motions of the cylinder, and found improvements in the predictions of the motions of the semi-submersible when compared to potential flow predictions. In particular nonlinear motions were improved, and the ability to capture phenomenon such as wave run-up was gained in the CFD solver [21].

Rivera-Arreba used the solvers interDymFoam and waveDymFoam for the dynamic fluid structure interaction. The PIMPLE algorithm is was used for the pressure and velocity coupling. She used an adjustable time step where a maximum value is set for the Courant number. The dynamic meshing was handled using a mesh deformation solver which only deforms cells, and does not allow any topological changes in the mesh. In this method a certain region is defined where the cells are allowed to move and be deformed, and outside of this region the cells do not change. The flow in the CFD simulations was treated as laminar with no turbulence modeling [21].

3.3.2 Tran and Kim 2017

Tran and Kim from Gyeongsang National University in South Korea also did an analysis focusing on the OC4 DeepCWind semi-submersible. Their analysis included many coupled high fidelity models. Tran and Kim's goal was to develop a tool to replace model testing for floating offshore wind turbines. This goal was to reduce costs and increase accuracy. They mention the complexities of scaling for a model test, as Froude scaling is advantageous for the hydrodynamic testing, while the aerodynamic problem should be scaled by Reynolds number. By contrast their model is done in full scale. They also discuss how a potential flow based panel model cannot predict wave run-up or viscous flow separation. An unsteady CFD approach is performed using the commercial code Star-CCM+. This approach provides information about viscous effects as well as better modelling of the effects of the wake of upstream elements on downstream elements [28]. The project focuses on the effects of the coupling of the hydrodynamic and aerodynamic loads including the aerodynamic interactions of the rotating blades and the tower. A volume of fluid method and an overset mesh were used in the analysis. This allows for large efficient displacements of the structure while maintaining high fidelity modelling of the viscous flow around the structure. Within the overset mesh of the platform is a rotating domain around the rotor. A $k-\omega$ turbulence model is used. Tran and Kim compared the results of their simulations to those obtained for the same problem using the much more efficient program FAST [28]. The project only considered steady wind and mono-chromatic regular waves with no steady current.

This coupled model with many interacting high fidelity components resulted in very long computation times. Utilizing 40 CPUs operating in parallel a 10 minute time series took 24 days to calculate [28]. Some discrepancies were found in the aerodynamic loads from those predicted using FAST. Tran and Kim found that

one key contributor to this was the interaction of the wake with the tower. The hydrodynamic responses in pitch and heave were found to have good agreement. The predicted average surge motion however was almost 20% larger with the viscous CFD method [28]. Tran and Kim are next working on the incorporation of a more detailed mooring model that accounts for more realistic interaction with the seabed [28].

This study points to important effects of viscosity in the surge response of a semi-submersible. The effects of the hydrodynamic model however are difficult to isolate given the complexity of the model.

3.3.3 Burmester, Chen, Vaz, and Wang 2019

In 2019 Burmester, Chen, Vaz, and Wang performed a pitch decay study of semi-submersible floating wind turbine using CFD. The OC5 DeepCWind semi-submersible design was used in the project. The rotor and aerodynamic thrust were not considered, and the CFD model was made in 1/50 model scale. The results were compared to model tests performed by MARIN in the Netherlands, which were performed at this same model scale. The goal of the CFD was to numerically determine the pitch natural frequency and the linear and quadratic damping at this frequency. In addition more detailed knowledge of the flow characteristics was desired. ReFRESKO, the RANS solver developed by MARIN was used for the analysis. A deforming grid method was used to transfer the boundary mesh with the pitch motion of the structure. A KSKL ($k - \sqrt{kL}$) turbulence model was used [3]. A semi circular cylinder domain was used which included the same water depth as the model tank, and a radius 6 times larger than the characteristic radius of the platform. The cells in the wall boundary layer were generated to have a thickness corresponding to a $y+$ value of 1.5 [3]. Extra refinement was also applied to regions of geometric complexity like the connections of the bracing and sharp corners. Three grid refinement levels were tested and compared for convergence. The middle refinement level was selected for further simulations. A linear mooring restoring matrix was also included in the model.

The results of the simulations showed significant differences from the model tests. The natural period only varied by 1%, however the linear and quadratic damping coefficients were 12% and 59% lower respectively. Burmester et al. attributed these differences mostly to the added damping of a catenary mooring system, the added aerodynamic damping of the wind turbine, and the added damping of other coupled degrees of freedom which were not allowed in the CFD simulations [3]. The hydrodynamic pressure on the body was also studied at various phases of the pitch period. They also observed vortex shedding from the sharp corners of the heave plates. The project concluded that in future work it is important to model the viscous effects of the mooring lines, and to allow the platform to move in all six degrees of freedom.

3.3.4 Burmester, Gueydon, Moctar, and Vaz 2020

In 2020 Burmester and Vaz again worked together, this time with Gueydon and Moctar. This project examined the same DeepCWind semi-submersible platform, but this time with a focus on surge decay motions rather than pitch decay motions. A viscous CFD analysis was performed again using the MARIN code ReFRESKO. Similar simulation solvers and settings were used as were used for the pitch decay study.

The natural periods and linear and quadratic damping coefficients were extracted. This was done using two different methods; first a more classic PQ approach was used, and then a more robust least squares fitting method. Burmester et al. also focused on the uncertainty of their results. They state that for their study the discretization error is the only significant component compared with iterative uncertainty and statistical uncertainty. The most detailed model which allowed three degrees of freedom and included a free surface with quasi-static moorings resulted in significant differences from the model test results. The predicted natural period, linear damping, and quadratic damping were 2.4%, 15.9%, and 48.3% lower than measured respectively. The especially large error in the quadratic damping was attributed to a lack of quadratic drag from the mooring lines.

In their uncertainty analysis they identified a discretization uncertainty of 11.5% and 19.5% for the estimation of the amplitude and period of a decay oscillation. Difficulty in discretization was found to be particularly influenced by the complexity of the geometry near the connections of pontoons and braces. The team also found uncertainties with their methods of post processing the data. Damping coefficients found using the PQ approach and the least squares fitting approach varied by close to 10%.

3.3.5 Pinguet, Kanner, Benoit, and Molin 2020 and 2021

In 2020 Pinguet, Kanner, Benoit, and Molin used a CFD study to examine a the DeepCWind semi-submersible floating wind turbine designed by NREL. They used an overset mesh moving technique, which is a recent addition to the OpenFOAM code that they worked with. The overset mesh method uses two mesh domains, one larger outer stationary domain, and a smaller moving domain which contains the detailed mesh around the body. This method is different than other dynamic options such as mesh morphing. A simple vertical cylinder was tested first for validation against experimental data with the same geometry. The study focused on free decay tests in pitch, heave, and surge for the cylinder and free decay tests in pitch and heave for the

semi-submersible. Model basin decay tests were also performed for the semi-submersible geometry by MARIN providing a way to validate computational results [19].

In the simulations the bodies are free to move in all six degrees of freedom, and the equations of motion are calculated for the body in each time step, resulting in a new position for the body and its fitted mesh. The cylinder and semi-submersible were both modeled with a catenary mooring system using the waves2Foam add on. The mooring lines provide a more accurate catenary stiffness with lift-off from the seabed, but the hydrodynamic drag on the lines was not modeled [19]. For both the cylinder and the semi-submersible only one mesh density was tested. One important feature of the mesh was matching the cell sizes at the interface of the stationary and moving domains, including any refinement zones at the free surface. Refinement was also incorporated at locations with important geometry changes [19]. The selected mesh for the semi-submersible case had a total of 4.2 million cells. No symmetry plane was used in the simulations. No turbulence modeling was included in the simulations and the flow was treated as laminar [19].

The free decay tests for the cylinder had promising results for pitch, heave, and surge. The motions match the model test motions very closely, and significantly better than previous CFD tests performed in 2016 without the overset method. The natural periods and damping coefficients were calculated from both the experiments and the numerical simulations; only linear damping is considered. The calculated values match relatively well, with the largest discrepancy in the heave damping, which had an approximately 30% difference [19]. For the semi-submersible tests the natural periods were again accurately predicted in heave and pitch. In heave the CFD over-predicted the damping and in pitch the CFD under-predicted the damping. When comparing the results between the CFD performed with and without the overset method there are not significant differences. Pinguet et al. predict that some of the differences in damping could be explained by using too coarse of a mesh as well as the lack of a turbulence model which does not allow the accurate prediction of the effects of vortex shedding [19].

The same group continued their work with a paper in 2021. This work uses the same overset method in OpenFOAM for the DeepCWind platform, but looks at the response in waves instead of free decay. The tool waves2Foam is used to generate the wave field and handle absorption of the waves.

A more detailed mesh study was conducted in this project. The main mesh convergence study was done with only a two-dimensional domain. The two-dimensional body consisted of a section of a vertical column and a section of a rectangular pontoon below. This geometry was also tested in a physical experiment for comparisons. Three mesh densities are presented with time series of free surface elevation, platform heave, and platform pitch. It was found that the results with the coarsest mesh differed significantly, but the finer two meshes appeared to provide the same response. The middle density mesh was then selected to balance accuracy and computation cost [18]. It was previously mentioned that in the overset method the cells at the interface of the two domains should be similar in shape and size. Pinguet et al. tested three different styles of refinement around the inner moving domain, and found that the resulting platform motions were significantly tied to matching the domain interface cells. The group also looked at the importance of the time step. They used a variable time step and set a maximum allowable Courant number of 0.5, 1.0, and 2.0. They concluded that the effect of the Courant number was most significant in the transient phase compared with the stabilized motions and wave elevations. They stated that a, "Courant number of 2 can provide accurate enough solution when looking at global motion and wave elevation for this specific mesh" [18].

The insights from the two-dimensional study were used for the setup of the semi-submersible wave study. In these simulations a symmetry plane was used to cut computation time. Still the flow was treated as laminar with no turbulence modeling. It was found that the numerical model's predictions agreed well with the model test data. The group suggested again that a more refined mesh could align the results even better [18]. Overall it appears that Pinguet et al. found the overset tool in OpenFOAM to be a good method for modeling large motions of a semi-submersible platform.

3.4 Conclusions and Research Gaps

Potential flow studies have shown that second order calculations can result in low frequency excitation forces. These forces are much lower in magnitude than the corresponding first order forces, however they can still lead to significant motions due to the resonant frequencies of the platforms, even when also considering the aerodynamic loading.

Model tests have been proven to be effective for tuning engineering models based on potential flow coefficients. When extracting impacts of viscous flow effects it can be important to consider different parts of the body differently. It also was found that the sea state has important influence on the discrepancies from potential flow.

Using model test data to tune a model, and then comparing the model to results of model tests can be very successful, but has somewhat circular logic. It would be advantageous if accurate predictions could be made with fully numerical methods. CFD has been used to effectively predict platform motions both in decay tests and with wave excitation. These studies show promising results, but are specific to particular situations.

Viscous flow calculations are computationally very expensive, and it is not feasible to perform full CFD studies for long time series of many environmental conditions. A method of correcting potential flow based engineering models with limited CFD cases that can be broadly applied is missing.

4 WINDMOOR Model Test Data

Model tests were conducted by SINTEF Ocean with the INO WINDMOOR semi-submersible geometry. The tests were completed in March of 2020 in the Ocean Basin in Trondheim, Norway [29]. The results of the model tests are used in this project as a way to evaluate the accuracy of the numerical predictions, but they are not used to tune the numerical model.

4.1 Test Cases

Seven series of model tests were performed. These included wave only, wave and current, and wave, current, and wind tests. Decay tests and other system identification tests were also performed. Only the results of the system identification and wave only tests are used for comparison in this project. The wave only tests include regular mono-chromatic, bi-chromatic, and irregular with varying wave heights and periods. The specific wave only tests used in this project are given in Table 4.1, Table 4.2, and Table 4.3.

It should be noted that the regular wave tests include three different frequencies, each tested with a small, medium, and large wave height.

Test	SINTEF Test #	Wave Type	Wave Height [m]	f [Hz]
1	2010	Regular mono-chromatic	0.83	0.125
2	2020		1.57	0.091
3	2030		2.55	0.071
4	2040		3.33	0.125
5	2050		6.30	0.091
6	2060		10.20	0.071
7	2070		6.66	0.125
8	2080		12.59	0.091
9	2091		20.40	0.071

Table 4.1: SINTEF mono-chromatic wave only test cases

The bi-chromatic tests are particularly useful for isolating the difference frequency problem. The test wave frequencies were selected so that the difference in frequency matches the natural frequencies in surge and pitch as shown in table 4.2. The first three cases of each difference frequency represent a small or medium sea state; the final two cases of each difference frequency represent a large sea state.

Test	SINTEF Test #	Wave Type	Wave Height [m]		f [Hz]		$f_{difference}$ [Hz]	
1	3010	Bi-chromatic	0.64	0.75	0.143	0.132	0.0109	f_{n1}
2	3020		1.05	1.29	0.111	0.100	0.0109	
3	3030		1.57	2.03	0.091	0.080	0.0108	
4	3040		5.10	5.97	0.143	0.132	0.0109	
5	3050		8.43	10.36	0.111	0.100	0.0109	
6	3110	Bi-chromatic	0.64	1.11	0.143	0.108	0.0344	f_{n5}
7	3120		0.83	1.59	0.125	0.091	0.0344	
8	3130		1.05	2.21	0.111	0.077	0.0344	
9	3140		5.10	8.85	0.143	0.108	0.0344	
10	3150		6.66	12.69	0.125	0.091	0.0344	

Table 4.2: SINTEF bi-chromatic wave only test cases

43 irregular cases are considered in this project. These cases are grouped by their statistical peak frequencies and significant wave heights. Most of the groups contain multiple tests, some with different random seeds for the wave elevation series. This is advantageous for identification of empirical coefficients. Having more data, especially with different random seeds allows for better statistical averaging and data smoothing. It also reduces uncertainty in the results.

Group	Test	SINTEF Test #	Wave Type	Significant Wave Height [m]	Peak Frequency [Hz]
1	1	4210	Irregular	3.74	0.143
	2	4220			
	3	4225			
	4	5222			
	5	4223			
	6	4224			
2	7	4230	Irregular	6.19	0.111
	8	4240			
	9	4241			
	10	4242			
	11	4243			
	12	4244			
3	13	4270	Irregular	3.74	0.083
4	14	4290	Irregular	6.19	0.083
	15	4292			
5	16	4662	Irregular	11.0	0.083
	17	4670			
	18	4675			
	19	4677			
	20	4673			
	21	4674			
	22	4676			
	23	4686			
	24	4681			
	25	4682			
	26	4683			
	27	4684			
	28	4685			
	29	4687			
30	4688				
6	31	4510	Irregular	2.0	0.143
	32	4520			
	33	4521			
	34	4525			
	35	4523			
	36	4524			
7	37	4542	Irregular	3.74	0.111
	38	4550			
	39	4551			
	40	4552			
	41	4555			
	42	4554			
	43	4556			

Table 4.3: SINTEF irregular wave only test cases

4.2 Model Description

Froude scaling with a factor of 1:40 was used for the tests. The Ocean Basin used for the tests is 80 m long, 50 m wide, and 10 m deep with an adjustable floor [29]. The basin has the ability to generate waves with two wave makers and generate steady current. SINTEF reported all data in full scale dimensions. The full scale water depth of the tests was 150 m. The INO WINDMOOR semi-submersible was used as shown in Figure 1.4. The exterior of the model was made with painted aluminum. The mass and inertial properties were adjusted and tuned with solid weights to match the characteristics of the full scale design.

The full wind turbine was not modeled. Instead of aerodynamic loading of scaled blades an actuator method was used for the turbine loading which was built with six lines connected to the tower top in different directions. This avoids issues of Froude vs. Reynolds scaling, and means that the turbine loads are precisely known. The tests including turbine loading are not considered in this project. The mass and inertial properties of the turbine however are present for the tests.

The mooring system consisted of three horizontal lines. The fairlead connections were at the top of each of

the three columns, and the lines extended outward from the center of the model to the sides of the ocean basin. The fairlead height was 15.5 m above the mean water line, compared to 2.5 m above at the sides of the tank resulting in slight downward angle [29]. Force sensors and springs were built into the mooring lines to measure the loads and provide the desired stiffness. The configuration of the model, tank, and mooring system is shown in Figure 4.1.

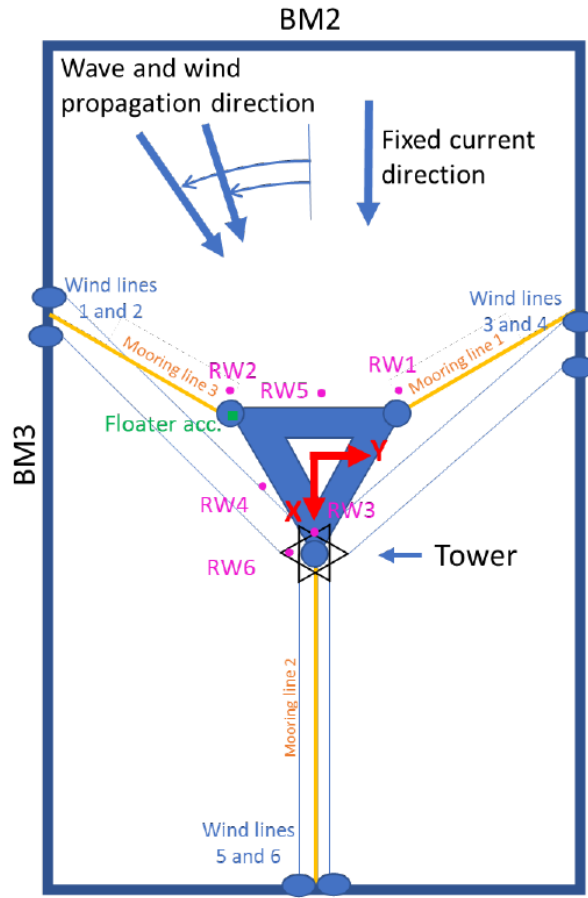


Figure 4.1: SINTEF Ocean model test configuration [29]

Sensors are used to collect data from the model tests. These include conductance type wave probes which are placed in various positions around the platform. The wave elevations used as input in the analyses of this project are from the sensor kept with the platform. The position of the floater in six degrees of freedom and the position of the top of the tower is recorded as well as the acceleration of the top of the tower. Tension in the fairleads is also measured.

5 Potential Flow Study

5.1 First Order Potential Flow Study

HydroD was used for most of the potential flow calculations. Specifically, version 4.10-01 was used. HydroD is a program developed by DNV-GL for hydrostatic and wave load and motion analyses. The program runs WADAM which utilizes the WAMIT code for its wave analyses. Both first and second order calculations can be done in the program, and both are used in this project. To begin a first order only model was used.

The first order analysis results in frequency dependent added mass and damping coefficients, linear excitation force transfer functions, and first order motions transfer functions. The analysis requires that the surface of the floating object is modeled by small panels. In this project the DNV-GL program Genie was used to generate the panel model. Genie is a program typically used for structural analysis of marine structures. The program offers a convenient interface for three-dimensional modeling and has built in functions to automatically generate mesh based on user defined limitations. These limitations can include the shape of elements, size of elements, number of elements in an area, number of elements along an edge, and the growth rate of element size. It is also possible to define different criteria for different sections of the model allowing simple generation of more refined zones where it is desired. The wetted surface of the model is also defined in Genie. A finite element mesh file is then exported from Genie and imported into a HydroD workspace for the hydrodynamic analysis. An example panel model of the WINDMOOR semi-submersible as shown in the HydroD user interface is shown in Figure 5.1.

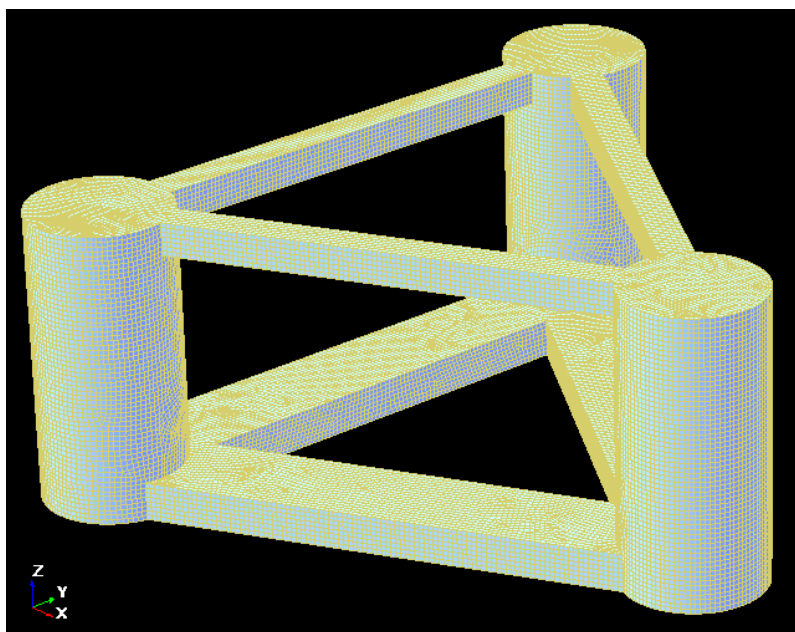


Figure 5.1: WINDMOOR panel model in HydroD user interface

A numerical model always requires a balance of efficiency and accuracy. Very large panel elements do not offer a very precise representation of the geometry of the body, or the variations in the fluid pressure throughout the element. Very small elements lead to an increase in the number of calculations that are needed in an analysis, increasing the computation cost and time. The goal is to find the model that is as efficient as possible that can provide the desired level of accuracy. Five different panel models were tested in the first order study, each with a constant element size on all surfaces of the model. The resulting added mass coefficients were used as the main method of comparison. Figure 5.2 shows a zoomed in region of the plot of surge added mass compared to period. The figure shows the results with the five different panel models, each with a different base element length.

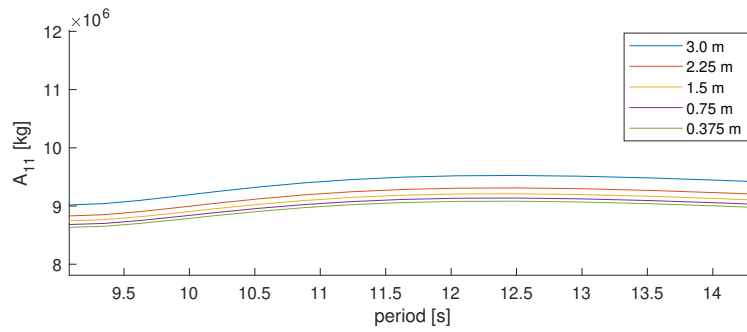


Figure 5.2: Surge added mass coefficient with varying element length

Given the results a desired level of accuracy needed to be balanced with the computation time. The first order run times for each of the original five panel models is shown in Table 5.1.

Element Size [m]	Number of Elements	Run Time [s]
0.375	39443	43315
0.75	9958	1101
1.50	4075	130
2.25	2623	51
3.00	1886	28

Table 5.1: First order panel model study computation times

The computation time does not increase linearly with the number of elements. This indicates that at a certain point an increase in refinement is not worth the added cost, particularly if the results with a coarser model are within a small margin of error.

The element size of 1.50 m was selected from the first order results. Full results of the first order analysis are shown in Appendix A.

5.2 Second Order Potential Flow Study

The second order potential flow study in this project was conducted to determine the difference frequency excitation quadratic transfer functions. This analysis is dependent on the results of the first order analysis, as the first order motions are an input into the second order forcing. The second order analysis uses the same panel model as used in the first order analysis, but also requires a model of the free surface.

The free surface mesh was constructed in the DNV-GL program HydroMesh. WADAM requires that the free surface mesh only consists of four sided elements, so the free surface needs to be split into four sided sections. The sections are split into elements based on the number of elements per edge. The elements can be manipulated so that they match up with the elements of the panel model at the waterplane. An example of the free surface mesh as created in HydroMesh is shown in Figure 5.3. The radius of the free surface mesh was made large enough to capture the largest wavelength tested, and the size of the largest elements was made small enough to capture the shortest wavelength tested.

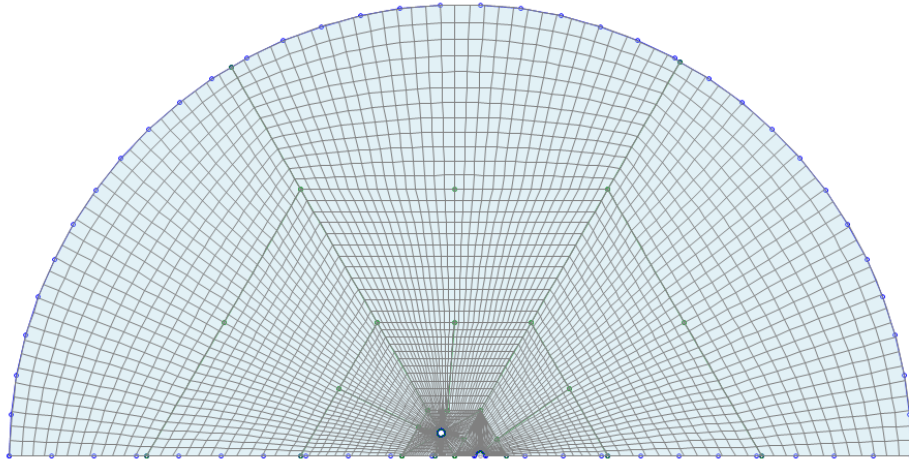


Figure 5.3: Free surface mesh creation in HydroMesh

Like the panel model, the results can be dependent upon the free surface mesh. Multiple free surface meshes were also tested to make sure that the selected model was refined enough to provide results independent of the mesh selection. Seven meshes were tested, and the dependence on the mesh was analyzed by comparing the diagonals of the quadratic transfer function. The results can be seen for five of the free surface models in Figure 5.4. The numbers in the legend indicate the total number of elements in the free surface model and the absolute value of the transfer function is shown. Each plot shows a diagonal cut of the quadratic transfer function. In order, the plots show the diagonals where: $f_{diff} = 0$, $f_{diff} = f_{n_{surge}}$, and $f_{diff} = f_{n_{pitch}}$.

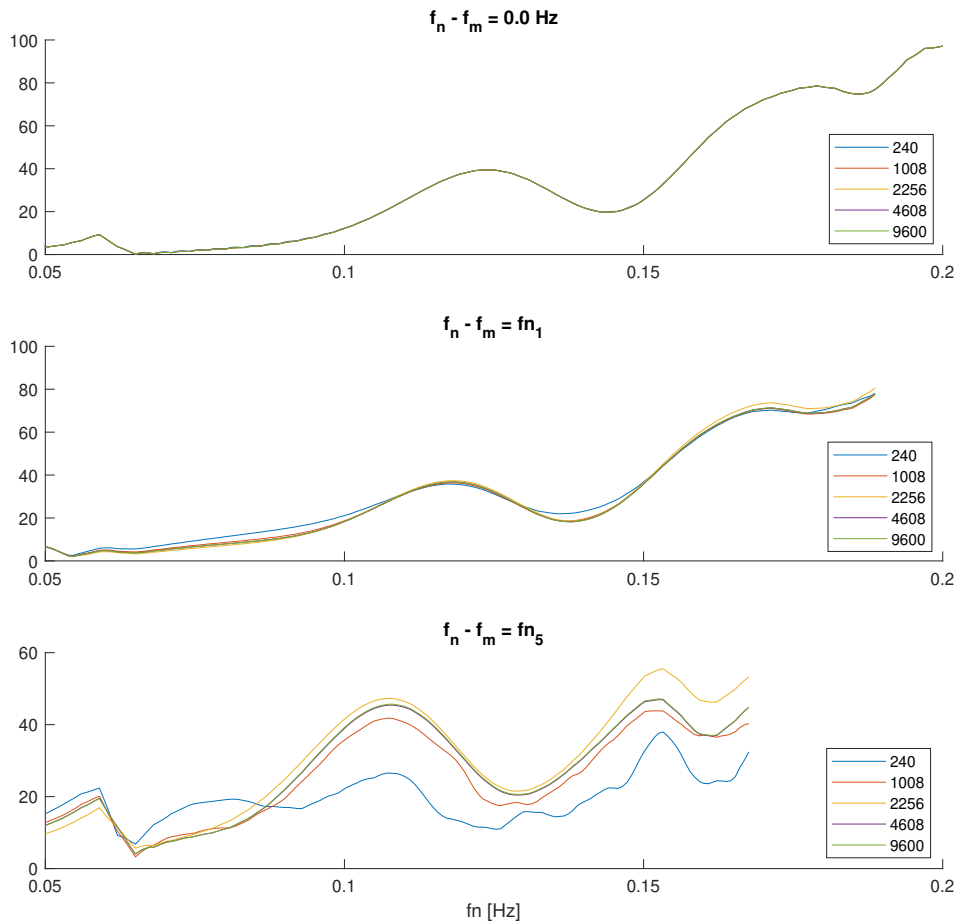


Figure 5.4: Absolute value of quadratic transfer function dependence on free surface model

As expected the diagonal of zero difference frequency shows no dependence on the free surface model. At a distance from the center diagonal of the surge natural frequency, all but the coarsest mesh appear to provide consistent results. Further from the mean drift load at the pitch natural frequency, the differences are larger, especially for the coarsest mesh. At this distance it appears that the second most refined mesh (4608 elements) offers the same results as the most refined mesh. This model with 4608 elements was selected for the rest of the project.

After selecting a free surface model further runs were done to make sure that the panel model was sufficiently refined. Even though the results appeared converged in the first order results, it appeared that the effect of the panel model was not yet converged for the second order results. The refinement was increased to the panel model with 9958 elements and the results still did not seem converged. The panel model with 39443 elements was tested next, but the second order simulation would not run on the computer used in the project. It was determined that this was not due to a problem with the model or a limit on the number of elements, but due to the necessary memory needed in the calculations. This memory exceeded the random access memory (RAM) of the available computer. Successive panel models were created with increasing panel size until the required memory was low enough for a successful simulation. The successful panel model had an element length of 0.6 m and 16641 total elements.

Certain regions of the model see larger variations in the flow, such as near the free surface and near the complex geometry of the column and pontoon connection. It is possible that the smaller elements can be used in these critical regions, and larger elements are used in other regions. This could potentially provide the same results as a more refined model with less memory and computation time required. This was tested by creating two panel models both which had the same 0.6 m elements as the best case homogeneous model in the refinement zones, but with larger base elements elsewhere. An example of this approach is shown in figure 5.5 where a corner and section of the waterline can be seen.

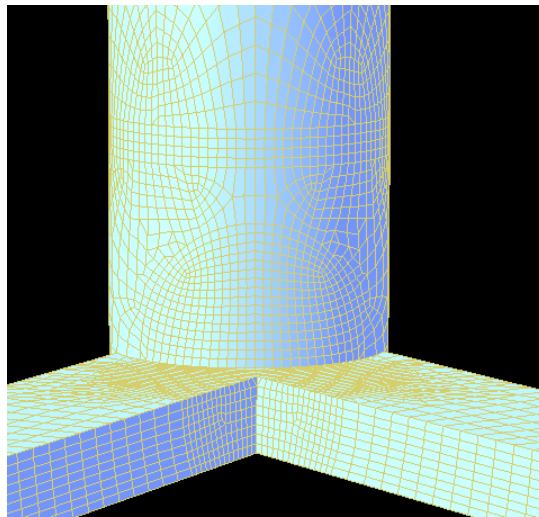


Figure 5.5: Panel model with refinement zones

If the second order results with these panel models was sufficiently similar to the results of the model with the homogeneous model with 0.6 m elements, the refinement zone approach would be used to find more converged results within the same memory limits. However it was found that the results with these models was proportionally between the two homogeneous models with both the larger and smaller element sizes. Thus it was determined that the approach would not lead to better results. Figure 5.6 shows cuts of the absolute value of the surge quadratic transfer function along a difference frequency of zero and of the surge natural frequency. It can be seen that the results have not converged with relation to the panel model. It can also be seen that the panel model with specific refinement zones did not more efficiently solve the problem. In the legend of the plots the panel model element size is shown. The lines with two numbers had a refined size of the first number, and a base size of the second larger number.

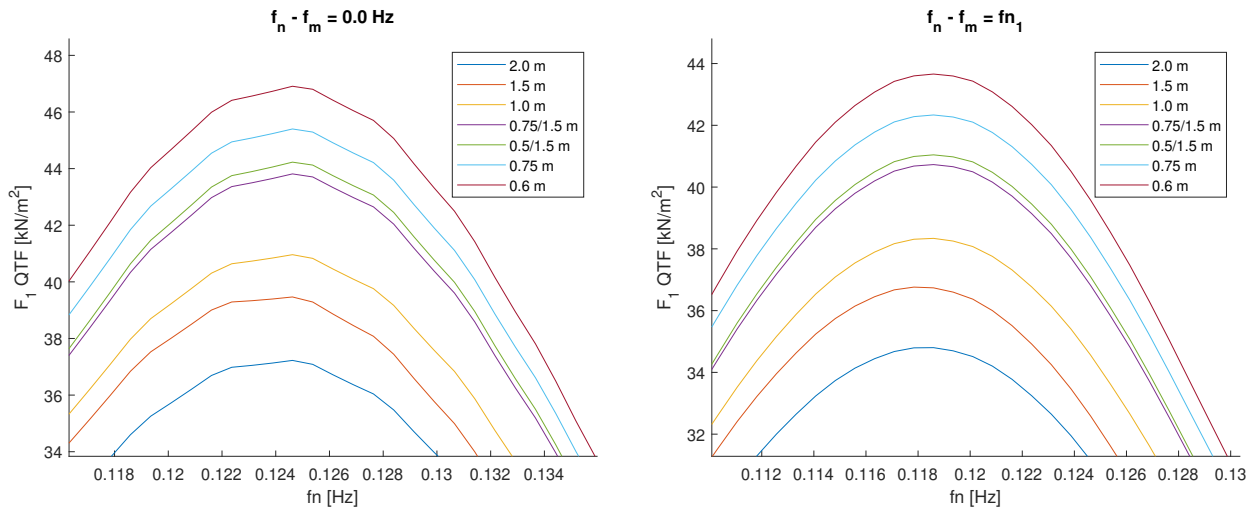


Figure 5.6: Absolute value of quadratic transfer function dependence on panel model

In future work a computer with more memory should be used to determine the panel model required for true converged results. For this project the results of the model with 16641 elements will be used in all further analyses.

Figure 5.7 shows surface plots for the quadratic transfer function of surge force. The top plot shows the real component, the middle plot the imaginary component, and the third plot the absolute value. As expected the real part is symmetric about the zero difference frequency diagonal while the imaginary part is anti-symmetric about this line. For these plots the function was trimmed at a difference frequency of 0.05 Hz. Similar plots are shown for the other two relevant degrees of freedom in Appendix B. The appendix also includes two dimensional plots of the diagonal cuts of the quadratic transfer functions for clearer numeric values.

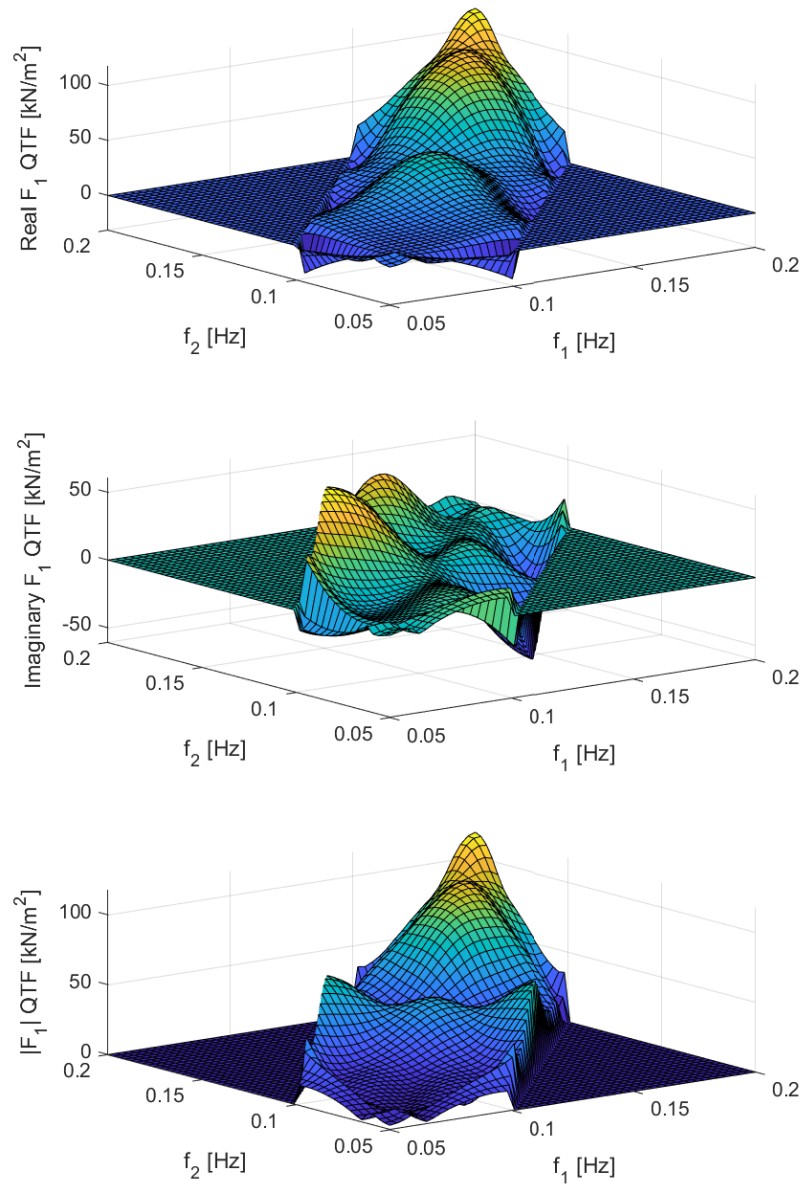


Figure 5.7: Surge force quadratic transfer function

It should be noted that second order excitation can be calculated with two methods, direct pressure integration and far field. In version 4.10-01 of HydroD it the ability to select the calculation method was not found in this project, however the option was found in version 4.6-03. The model with slight modifications was also run in this earlier version of HydroD with both calculation methods. No distinguishable difference was found in the results, indicating the results are not dependent on the method.

When comparing the results of the potential flow study to the model test data, time series were reconstructed. This process was done both with the full quadratic transfer function described in this section, as well as with an approximate quadratic transfer function based on Newman's approximation described in equation (16) and (17). It is interesting here to also compare the full and approximate transfer function with a surface plot. Figure 5.8 and 5.9 show the real and imaginary components of the surge force full quadratic transfer function and approximate transfer function. The solid surface is the full function, and the semi-transparent surface is the approximation. Note that by definition the approximation for the imaginary component is zero.

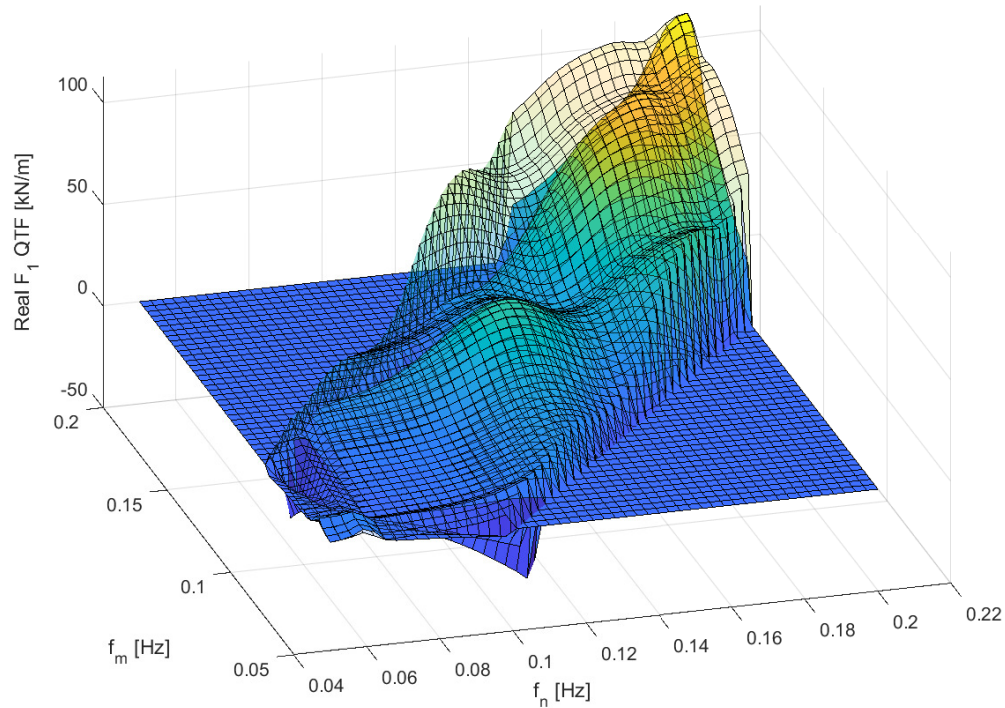


Figure 5.8: Real surge force quadratic transfer function comparison: Newman's approximation shown in semi-transparent

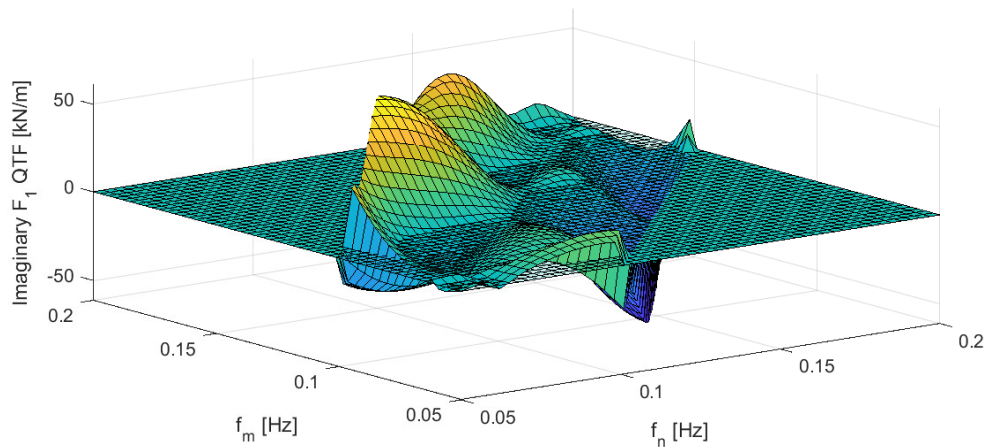


Figure 5.9: Imaginary surge force quadratic transfer function comparison: Newman's approximation shown in semi-transparent

Far from the zero difference frequency Newman's approximation significantly over predicts the in phase difference frequency force, and significantly under predicts the out of phase difference frequency force. The impact of this discrepancy for some potential sea conditions is examined in the following section.

6 Model Test Comparisons

6.1 Time Series Construction

One method to evaluate the results of the potential flow study, is to construct time series from the potential flow coefficients and compare them to the model test data. The time and free surface elevation measurements from a given model test are used as inputs to determine the hydrodynamic excitation force over the time span. This time series of hydrodynamic excitation forcing is then used to solve the equations of motion for the platform. The equations of motion are developed using the added mass and damping coefficients determined in the potential flow analysis.

The equation of motion in the frequency domain is given by Equation (37). Bold letters represent six by six matrices and the vector arrow signifies vectors of six components.

$$-\omega^2(\mathbf{M} + \mathbf{A}(\omega))\vec{X}(\omega) + i\omega\mathbf{B}(\omega)\vec{X}(\omega) + \mathbf{C}\vec{X}(\omega) = F_{exc}^{\vec{}}(\omega) \quad (37)$$

6.1.1 Excitation Force Time Series

In the equation of motion the excitation force is only based on the incident wave conditions and can then be calculated for the full time series prior to solving for the motions. The linear excitation force transfer function and quadratic excitation force transfer function from the potential flow calculations are used to find the excitation force in the frequency domain and then in the time domain.

The transfer functions are based on a coordinate system at the center of the waterplane area. Ideally the undisturbed wave elevation at this location would be used for calculations of the excitation force. Unfortunately the waves are disturbed by the platform, and no wave probe was placed at this longitudinal location. It was found that the wave probe that gave the best estimation was relative wave probe 5 as shown in Figure 4.1. This wave probe was attached to the platform, so the motions of the platform need to be added to the measured wave elevation for the absolute elevation. This was done by adding the instantaneous surge value and the sine of the pitch value multiplied by its distance from the center of the water plane.

The time series of the free surface elevation was made symmetric by mirroring it in time about the last data point. It was found that a symmetric wave time series gave a more realistic time series of the second order excitation force. This was particularly obvious when including a transient phase. After the excitation force was calculated the time series was then split to its original asymmetric original length. The free surface elevation was then brought to the frequency domain with a fast Fourier transform.

For calculation of the first order excitation force, the inverse fast Fourier transform of the product of the linear transfer function and the Fourier transform of the free surface elevation was taken. This is shown in Equation (38) and was described by Stansberg [27]. The equation shown is for a continuous function. Practically the discrete form of this equation is used instead, and the linear transfer function needs to be interpolated to the same frequency discretization as the free surface elevation. The limits of integration are also taken as finite frequencies. These frequencies are selected as the lower and upper limits of where there is significant wave energy. The cutoff of significance was defined as the lowest and highest frequency where at least 0.25% of the maximum wave energy is found.

$$\vec{f}_{exc}^{\vec{}}(t) = \int_{-\infty}^{\infty} H^{(1)}(f)\eta(f)e^{i2\pi ft} df \quad (38)$$

The second order force of concern is the difference frequency force. Here a double integration is needed over the two frequency ranges. The force is calculated using Equation (39), where * means complex conjugate. Again the equation shown is for a continuous function, while the discrete form is used in calculations.

$$\vec{f}_{exc}^{\vec{}}(t) = \int_{-\infty}^{\infty} \int_{-\infty}^{\infty} H^{(2)}(f_n, f_m)\eta^*(f_n)\eta(f_m)e^{i2\pi(f_m - f_n)t} df_n df_m \quad (39)$$

The double integration can be adjusted to a set of rotated axes. Instead of integrating over the two different frequencies, the first integration is done over lines of a constant difference frequency. The second integration is then done over lines of constant average frequency. Mathematically this is explained by Equation (40). The advantage of this rotation is that the exponential function is only a function of the difference frequency and can be pulled out of the inner integral. This allows a simpler inner integration, or numerically summation, followed by an inverse fast Fourier transform. This method is also described by Stansberg [27].

$$\vec{f}_{exc}^{\vec{}}(t) = \int_{-\infty}^{\infty} e^{i2\pi(f_m - f_n)t} \int_{-\infty}^{\infty} H^{(2)}(f_n, f_m)\eta^*(f_n)\eta(f_m) d\left(\frac{f_m + f_n}{2}\right) d(f_m - f_n) \quad (40)$$

Graphically this can more clearly be seen with the cuts of the quadratic transfer function shown in Figure 6.1. The red lines represent lines of constant difference frequency. The quadratic transfer function and corresponding frequency components of free surface elevation are integrated along each red line. Each of these integrals represent the frequency component of the second order difference frequency force that will occur with the given difference frequency. These values are then integrated along the direction of the blue lines of constant average frequency by use of an inverse fast Fourier transform.

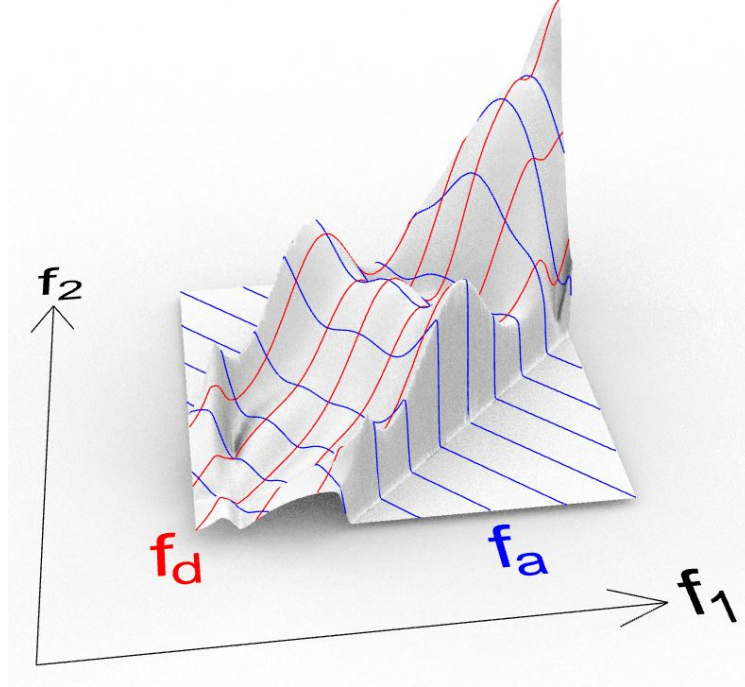


Figure 6.1: Rotated axes of integration on quadratic transfer function

The time series of the first and second order excitation forces are combined for the total excitation force to be used when solving the equations of motion. The above process is done for each of the six degrees of freedom; the resulting excitation force is a vector of six components (for the head seas considered, f_2 , f_4 , and f_6 are zero).

6.1.2 Cummins Equation and Covolution Integral

The added mass and damping are functions of the frequency and can be broken into two components, a constant value equal to the coefficient's value at infinite frequency, and a frequency dependent component as described by Taghipour, Perez, and Moan in 2007 [20]. This is described by Equations (41) and (42).

$$\mathbf{A}(\omega) = \mathbf{A}(\infty) + \mathbf{a}(\omega) \quad (41)$$

$$\mathbf{B}(\omega) = \mathbf{B}(\infty) + \mathbf{b}(\omega) \quad (42)$$

In potential flow theory the damping at infinite frequency should be zero, so the frequency dependent component is simply the entire function for the damping. In HydroD when a critical damping value is included, this critical damping value is added across all frequencies, and thus there is a value for $\mathbf{B}(\omega)$. The model used in this project includes critical damping values for heave, pitch, and roll. Each of these values were assigned 5% as described for the platform by Silva de Souza et al. [26]. It was found that the inclusion of surge critical damping was important as well. $B_{11}\infty$ was set to 8.3%; this value was chosen to match the model surge decay tests mentioned in Table F.1.

The components of the added mass and damping in surge are shown in Figure 6.2. The solid lines represent the full functions, while the dashed lines represent just the frequency dependent component with the constant infinite contribution removed. It is evident that both added mass and damping reach asymptotic values as the frequency tends to infinity. For the added mass this asymptotic value is substantial, while for the damping it is

relatively very small. The reason that it is not zero is that a critical surge damping value is included, however it should be noted that this critical damping value is small compared to the peak frequency dependent value.

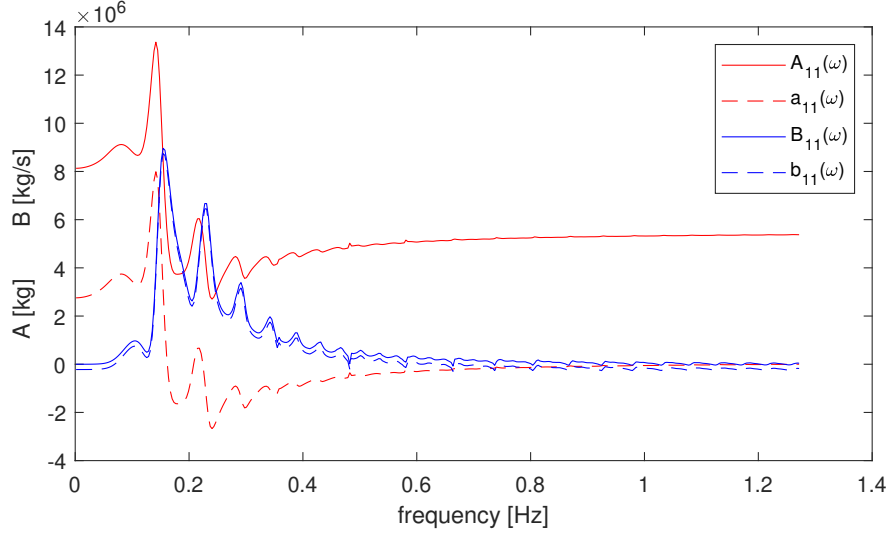


Figure 6.2: Frequency dependent decomposition of added mass and damping

In the following analysis it is important that the asymptotic values of the added mass and damping are known. The potential flow analysis to determine the linear and second order excitation transfer functions was conducted over a frequency range that covers typical wave energy (0.05 Hz - 0.20 Hz). This frequency range however does not provide information about the asymptotic values of A_∞ and B_∞ . In order to obtain this information another linear potential flow analysis was run over a range 0.0016 Hz to 1.27 Hz. In order to maintain good frequency resolution over this large range given HydroD's test limitations, the results from multiple frequency ranges were combined.

When the components of added mass and damping are separated the equations of motion can be rewritten as shown in Equation (43) [20]. Typically the fourth term containing B_∞ is not included as $B_\infty = 0$, however it is included here to incorporate the added critical damping matrix.

$$-\omega^2(\mathbf{M} + \mathbf{A}_\infty)\vec{X}(\omega) + (i\omega\mathbf{a}(\omega) + \mathbf{b}(\omega))i\omega\vec{X}(\omega) + i\omega\mathbf{B}_\infty\vec{X}(\omega) + \mathbf{C}\vec{X}(\omega) = \vec{F}_{exc}(\omega) \quad (43)$$

It should be noted now that only one term contains frequency dependent coefficients. The other terms can now more easily be brought into the time domain through an inverse Fourier transform. However in the second term, the frequency dependent coefficients cannot be brought outside of the frequency integral of the transform, and thus the integral remains. The resulting equation of motion in the time domain is as follows in Equation (44).

$$(\mathbf{M} + \mathbf{A}_\infty)\ddot{\vec{x}}(t) + \int_{-\infty}^{\infty} (i\omega\mathbf{a}(\omega) + \mathbf{b}(\omega))i\omega\vec{X}(\omega)e^{i\omega t} d\omega + \mathbf{B}_\infty\dot{\vec{x}}(t) + \mathbf{C}\vec{x}(t) = \vec{f}_{exc}(t) \quad (44)$$

This integral term incorporates the water's memory effect due to radiation. In 1962 W.E. Cummins established a method to solve for this term using a convolution integral [5]. The term is split into two functions, one containing the frequency dependent added mass and damping, and the other containing the response. This updated equation of motion is shown in Equation (45), where $\mathbf{k}(t - \tau)$ is called the retardation function, and is expressed by Equation (46). It should be noted that for a time series the time integral will start at some finite time rather than $-\infty$ (typically 0), and it will end at some finite time (the time being considered) rather than ∞ .

$$(\mathbf{M} + \mathbf{A}_\infty)\ddot{\vec{x}}(t) + \int_{-\infty}^{\infty} \mathbf{k}(t - \tau)\dot{\vec{x}}(\tau) d\tau + \mathbf{B}_\infty\dot{\vec{x}}(t) + \mathbf{C}\vec{x}(t) = \vec{f}_{exc}(t) \quad (45)$$

$$\mathbf{k}(\tau) = \frac{1}{2\pi} \int_{-\infty}^{\infty} (i\omega\mathbf{a}(\omega) + \mathbf{b}(\omega))e^{i\omega\tau} d\omega \quad (46)$$

The odd nature of the added mass term and the even nature of the damping term can be exploited to simplify the expression of the retardation function. This simplification, along with the fact that there will be no radiation effect before a time of $\tau = 0$ leads to the Kramers-Kronig relation, which is described in Equations (47) and (48). This relationship means that only the frequency dependent added mass, or frequency dependent damping is needed to determine the radiation memory effect [20].

$$\mathbf{k}(\tau) = -\frac{2}{\pi} \int_0^{\infty} \omega \mathbf{a}(\omega) \sin \omega \tau d\omega \quad (47)$$

$$\mathbf{k}(\tau) = \frac{2}{\pi} \int_0^{\infty} \mathbf{b}(\omega) \cos \omega \tau d\omega \quad (48)$$

This retardation function is shown for the platform over a time range of 70 s in Figure 6.3. The plot is shown for the surge component of the six by six matrix. The figure shows the function as found with three different methods. One based only on the damping, one based only on the added mass, and one based on the full combination. The Kramers-Kronig relation can be seen visually, with only small discrepancies between the three plots. In the functioning code the retardation function based on damping is used for calculations. It also becomes clear that as $t - \tau$ becomes large, the influence of the convolution integral will tend to zero. This means that the convolution integral can be evaluated for only a set length of time $t - \tau$ rather than all the way back to the start of the time series, and important information will not be lost. In this project a memory time of 70 s was selected based on analysis of the retardation function of each degree of freedom.

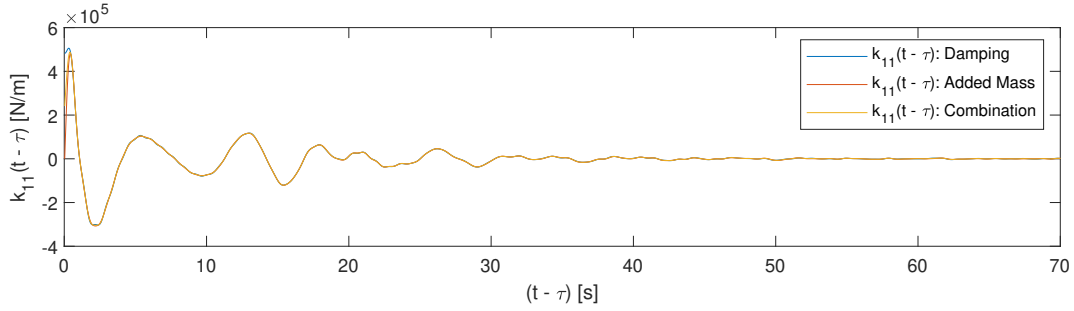


Figure 6.3: Radiation retardation function of surge

6.1.3 Dynamic Response Calculation

There are many methods for calculating the dynamic response from the differential equations of motion. Two different numerical integration methods were used in this project with similar results.

The first method used is the constant average acceleration method. This method says that the acceleration will be constant over the time step, and will be equal to the average of the acceleration at the start and end of the time step. The velocity for a succeeding time step and the position at a succeeding time step can be defined as in Equations (49) and (50).

$$\dot{x}_{i+1} = \dot{x}_i + \frac{1}{2}(\ddot{x}_i + \ddot{x}_{i+1})dt \quad (49)$$

$$x_{i+1} = x_i + \dot{x}_i dt + \frac{1}{4}(\ddot{x}_i + \ddot{x}_{i+1})dt^2 \quad (50)$$

This is an implicit method since the solution of the next time step contains other variables from the next time step. The method is unconditionally stable though [12].

This method can be used to solve Equation (45). First the value of \vec{x}_{i+1} is solved for as shown in Equation (51)

$$\vec{x}_{i+1} = \mathbf{C}^{-1}(f_{exc i+1}^{\vec{r}} - (\mathbf{M} + \mathbf{A}_{\infty})\ddot{\vec{x}}_{i+1} - \int_0^{t_{i+1}} \mathbf{k}(t - \tau)\dot{\vec{x}}(\tau) d\tau - \mathbf{B}_{\infty}\dot{\vec{x}}_{i+1}) \quad (51)$$

Next the convolution integral is split into an integral from $\tau = 0$ to $\tau = t_i$, and the value at $\tau = t_{i+1}$ multiplied by $d\tau$ as shown in Equation (52).

$$\vec{x}_{i+1} = \mathbf{C}^{-1}(f_{exc i+1}^{\vec{}} - (\mathbf{M} + \mathbf{A}_{\infty})\ddot{\vec{x}}_{i+1} - \int_0^{t_i} \mathbf{k}(t - \tau)\dot{\vec{x}}(\tau) d\tau - \mathbf{k}(t - t_{i+1})\dot{\vec{x}}(t_{i+1}) d\tau - \mathbf{B}_{\infty}\dot{\vec{x}}_{i+1}) \quad (52)$$

The constant average acceleration definition of $\dot{\vec{x}}(t_{i+1})$ can then be implemented as shown in Equation (53).

$$\vec{x}_{i+1} = \mathbf{C}^{-1}(f_{exc i+1}^{\vec{}} - (\mathbf{M} + \mathbf{A}_{\infty})\ddot{\vec{x}}_{i+1} - \int_0^{t_i} \mathbf{k}(t - \tau)\dot{\vec{x}}(\tau) d\tau - \mathbf{k}(t - t_{i+1})(\dot{\vec{x}}_i dt + (\ddot{\vec{x}}_i + \ddot{\vec{x}}_{i+1})\frac{dt^2}{2}) - \mathbf{B}_{\infty}(\dot{\vec{x}}_i + (\ddot{\vec{x}}_i + \ddot{\vec{x}}_{i+1})\frac{dt}{2})) \quad (53)$$

If this expression and Equation (50) are set equal to each other and solved for $\ddot{\vec{x}}_{i+1}$, the resulting equation for the succeeding time step's acceleration will be based only on values from the current time step, and can then be explicitly calculated. This is shown in Equation (54). With the acceleration of the next time step the velocity and position can then also be calculated using Equations (49) and (50).

$$\ddot{\vec{x}}_{i+1} = (\mathbf{I}_2 \frac{dt^2}{4} + \mathbf{C}^{-1}((\mathbf{M} + \mathbf{A}_{\infty}) + \mathbf{k}(t - t_{i+1})\frac{dt^2}{2} + \mathbf{B}_{\infty}\frac{dt}{2}))^{-1} (\mathbf{C}^{-1}(f_{exc i+1}^{\vec{}} - \int_0^{t_i} \mathbf{k}(t - \tau)\dot{\vec{x}}(\tau) d\tau - \mathbf{k}(t - t_{i+1})(\dot{\vec{x}}_i dt + \ddot{\vec{x}}_i \frac{dt^2}{2}) - \mathbf{B}_{\infty}(\dot{\vec{x}}_i + \ddot{\vec{x}}_i)\frac{dt}{2}) - \ddot{\vec{x}}_i - \dot{\vec{x}}_i dt - \ddot{\vec{x}}_i \frac{dt^2}{4}) \quad (54)$$

This is done iteratively for each time step of the time series. The response can then be compared to the data taken from the model tests as a validation of the results.

The process was performed for the mono-chromatic, bi-chromatic, and irregular wave tests. Full results of the time series and spectra of the results can be found in Appendix C, D, and E. The discrepancies of the results from the model tests are discussed in Section 7.

For a better understanding of the effect of the analysis type, time series were created for three different sets of excitation forces. One was based on the full quadratic transfer function described above. The second was using an approximate transfer function based on Newman's approximation. The third only included the first order excitation.

An example of the resulting time series is shown in Figure 6.4, with the time series on the left and the frequency spectra on the right.

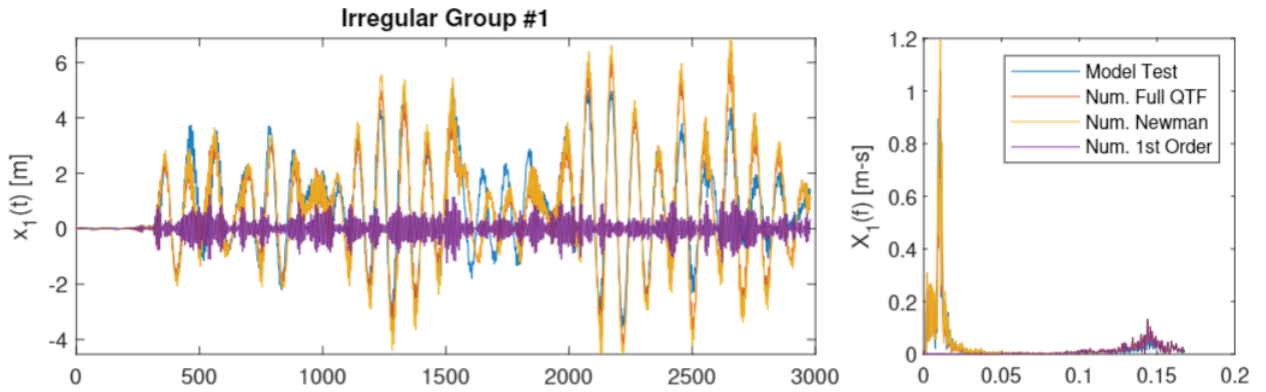


Figure 6.4: Bi-chromatic wave motion reconstructed time series

A fourth order Runge-Kutta method was also considered. This method is explicit, but it is only conditionally stable. In order to make the solver stable the time step needed to be reduced significantly resulting in much slower calculations. The resulting motions showed no noticeable difference, so the quicker constant average acceleration approach was selected.

7 Potential Flow Results

The results of the potential flow study found good agreement with other similar studies performed by SINTEF Ocean with the same body. The potential flow solutions also led to somewhat accurate predictions of platform motions, although there is still considerable room for improvement.

7.1 First Order

Silva de Souza et al. of SINTEF Ocean found first order potential flow coefficients of the INO WINDMOOR semi-submersible using WAMIT [26]. No difference can be seen when comparing the coefficients found in their work and in this project. As an example, a comparison of the surge added mass is shown in Figure 7.1. The plot on the left is from this project and the plot on the right shows the result used in the SIMA project. The first order coefficients here are plotted against time rather than frequency. This was done to match the plots of SINTEF for a better comparison.

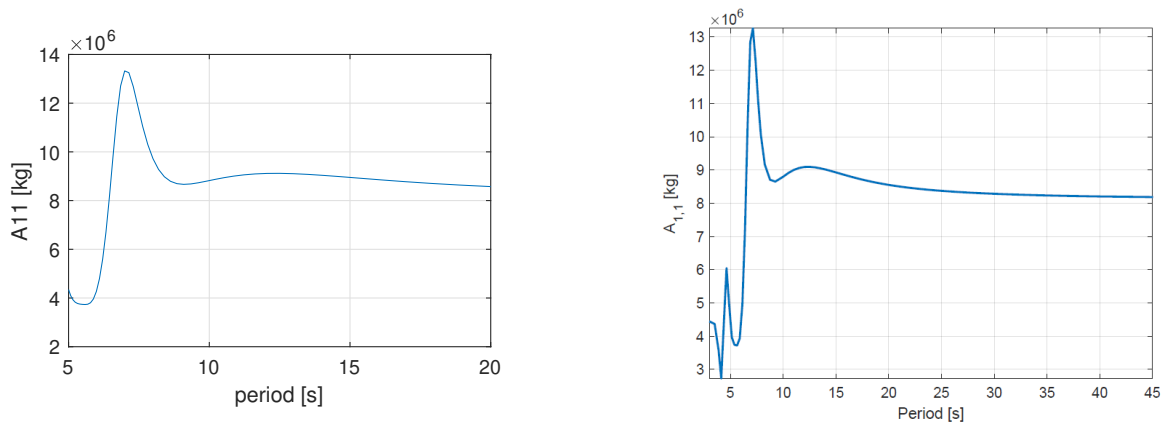


Figure 7.1: Potential flow surge added mass comparison: Wiley and Berthelsen et al.

Given the comparisons to the work performed by SINTEF and the results of the convergence study there is good confidence in the results of the first order potential flow study.

7.2 Second Order

The second order coefficients were also compared to work done by SINTEF. Fonseca found the difference frequency quadratic transfer function in surge both numerically and empirically [10]. Figure 7.2 shows diagonals along the zero difference frequency and roughly the surge natural frequency from both this project and from Fonseca's work. The plots on bottom are from Fonseca; the red line represents his numerical results and the yellow line represents the empirical results from one of the irregular wave model tests. When comparing the numerical results, the diagonals both follow the same trends and have roughly the same values. The diagonals from this project have slightly lower values than Fonseca found throughout the frequency range.

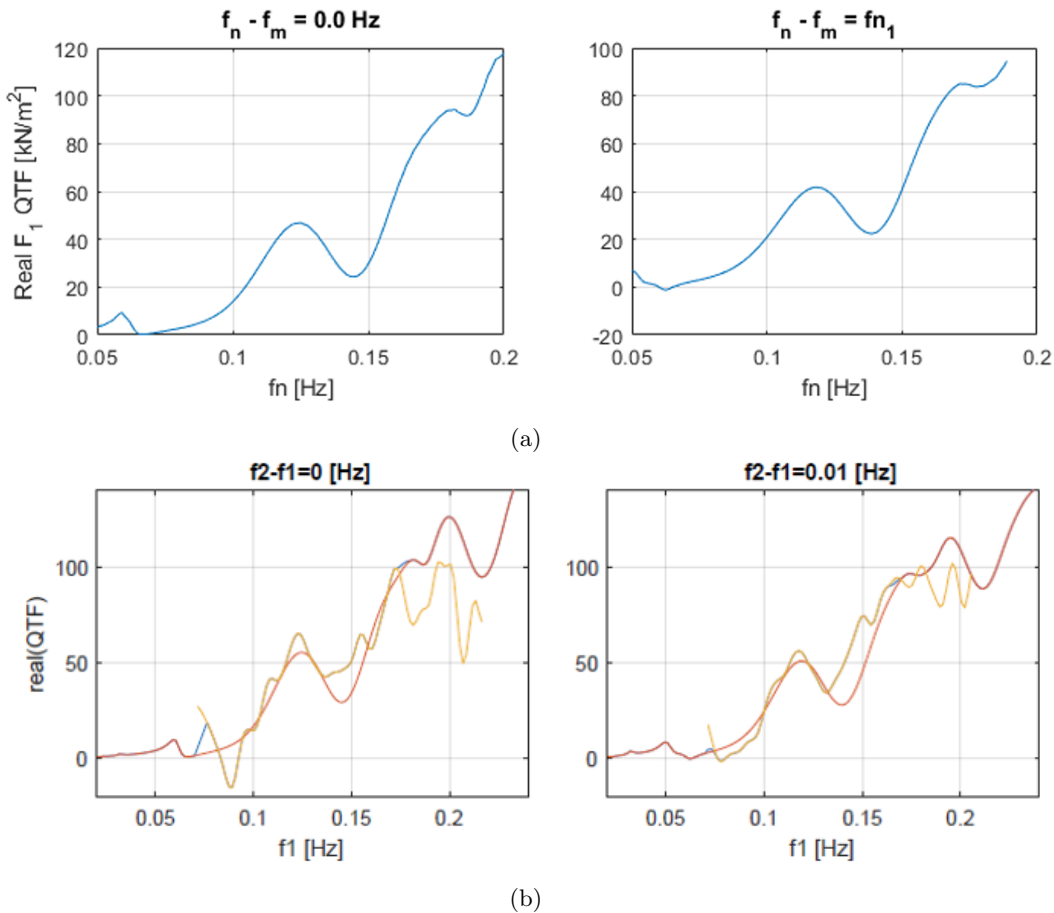


Figure 7.2: Potential flow quadratic transfer function comparison: Wiley (a) and Fonseca (b)

As discussed previously the computational resources in this project were a limiting factor for finding converged second order results. The trend observed was that each additional level of refinement brought small increases to the values of the quadratic transfer function. From the trend it is reasonable to believe that the results were converging towards similar values as found by Fonseca. In future work, this could be verified with more refined simulations until the results no longer appear to change.

7.3 Time Series Reconstruction Discussion

This discussion is mostly based on the plots found in Appendix C, D, and E. These plots demonstrate the ability to predict motions using only potential flow solutions.

7.3.1 Mono-chromatic Waves

As expected, a very little amount of slowly varying motion is present in the monochromatic wave series. The effect of the second order excitation force is apparent in the mean displacement however. The first order forcing only model was never able to predict a mean displacement in any of the degrees of freedom. It appears that for the mono-chromatic waves there is no discernible difference between the results found with the full quadratic transfer function and with Newman's approximation. This should be expected as Newman's approximation contains the full information along the zero difference frequency diagonal, which for a purely mono-chromatic wave set will be the only important information.

When a mean pitch displacement was present, the two second order methods were typically able to capture it well. The heave response was generally captured well, although the amplitude of oscillation was underpredicted for test case 6 and 9 correlating to the medium and large wave height of the lowest frequency.

The most interesting response is the surge. The mean surge displacement compared to its amplitude of oscillation was significantly larger for the highest frequency of 0.125 Hz. The higher frequency, and shorter waves, are more easily disturbed by the diameter of the columns, which results in a larger mean drift load. In these cases the numerical methods significantly over predict the mean offset and slightly over predict the amplitude of oscillation. This result is somewhat unexpected. The lack of viscous effects will likely both reduce the excitation force and reduce the damping. In this case where there is a mean offset but not large slowly

varying motion it would seem logical that the decrease in excitation force would be more important than the decrease in damping, leading to a lower mean offset; however, this was not the case.

It is also interesting to observe the model's ability to capture the transient phase. When the waves first hit the model and it gains a mean displacement there is naturally some low frequency oscillation in the model which gradually becomes more steady. This is true in the model test data, and also is predicted by the numerical methods. The numerical methods however over predict both the amplitude and the duration of these oscillations. This appears to indicate that the damping is too low, potentially due to a lack of viscous damping.

For the most part the frequency plots for the monochromatic cases do not provide any significant insights. The dominating energy of the response is at the wave frequency, with some energy at zero frequency.

7.3.2 Bi-chromatic Waves

The bi-chromatic wave series produce a significant amount of slowly varying motion in surge. As expected this was not captured at all by the first order only excitation model. The model using Newman's approximation did predict these motions; the method always predicted larger low frequency amplitudes than the full quadratic transfer function. In some cases this was a worse prediction compared to the model test data, but in some cases it was actually closer. In many cases the difference in results between the two second order methods was negligible.

The first five bi-chromatic cases featured a difference frequency equal to the surge natural frequency. These cases saw the most slowly varying motion. Test 3 however, which had medium wave heights did not see this same slowly varying motion in either the model test data or in the numerical predictions. Compared to the other tests of the first 5, the energy of the response of case 3 was not overly dominated by the low frequencies. Instead the response more follows the envelope shape of the wave series. Test 3 did feature the lowest frequency waves, which would place it lower on the surface of the quadratic transfer function, but the difference in the response compared to the other cases is more significant than expected.

When comparing test 1, 2, 4, and 5, which all saw the most slowly varying motion, there is a very noticeable difference between the small wave heights and the large wave heights. For the small wave heights the numerical methods slightly under predict the model motions (Newman was then a better predictor). For the large wave heights the numerical model largely over predicts the measured response (Newman was a slightly worse predictor). Berthelsen et al. discussed how a lack of viscous effects leads to two key problems, an under prediction of the excitation force and an under prediction of the damping. Depending on the characteristics of the flow and the body geometry one of these may have a larger impact than the other. It would seem that from these results the lack of damping dominates for the larger wave heights and the lack of excitation force dominates for the small wave heights. This could be reasonable since the damping is dependent on the body's motion, and the motion is an order of magnitude larger for the large wave heights tested. The impact of damping would especially grow with the size of oscillation for quadratic damping terms; separated flow due to viscous effects leads to a quadratic damping. The large slow oscillations also lead to something called wave drift damping. This is when the motion is large and slow enough that portions of the oscillation could be looked at as a quasi-steady case with incident waves and a forward speed. Forward speed and wave drift damping were not included in this project, and would play a more significant role for tests 4 and 5 which feature large wave heights and large surge motions.

Another point to note is that the impact of the transient phase of the bi-chromatic cases did not appear to be over or under predicted.

The heave response was generally well predicted by each of the three numerical models, and was dominated by wave frequency motion.

The pitch response was more impacted by low frequency motion for the second set of cases which featured a difference frequency that matched the pitch natural frequency. In four of the first five tests ($f_{diff} = fn_1$) the pitch response at the pitch natural frequency was under predicted, in test 5 though, with the largest wavelengths, the pitch response was over predicted significantly at this frequency. The same trend was found in the second set of tests ($f_{diff} = fn_5$). The pitch natural frequency response was under predicted for all cases except for the largest wave height.

The general trend for both the surge and pitch response is that the numerical model significantly over predicts the motion when the wave height is very large. Viscous effects become most important when the wave height is large compared to the structure's diameter. The linear regular wave model also starts to fall apart more when the wave becomes steeper, however this likely still is less important for the steepness of the waves tested. It seems from the bi-chromatic cases that viscous effects in large wave heights may lead to increased damping which is not properly captured in this model.

7.3.3 Irregular Waves

Although not as clean as in the bi-chromatic wave cases, the irregular wave cases also saw significant slowly varying motions. Again the surge and the pitch motions had the most interesting results.

In every case the first order excitation only model significantly under predicted the surge motion. There is some difference between the surge predictions with the full quadratic transfer function and with Newman's approximation, but the difference is never relatively large. In every case Newman's approximation predicts slightly larger low frequency motion; in some cases this more closely matches the model response, and in other cases it is further. It should be noted that even in the cases that Newman's approximation better predicts the motion, the reasoning behind the model is not more correct. It just so happens that the error in the approximation makes up for other error in the model. The key takeaway in comparing the full function and the approximation, is that for this semi-submersible and these wave conditions there is not a very large difference in the predictions. If more accuracy can be added to the model by incorporating viscous effects it is likely that the full quadratic transfer function would be the better selection.

When comparing the amplitudes of the slowly varying surge motion the same conclusions can be drawn as from the bi-chromatic wave tests. The second order model over predicts the motion for large wave heights, and under predicts the motion for small wave heights. The same influences of viscous damping and wave drift damping are likely of concern for the irregular wave cases as they were in the bi-chromatic cases.

The same trends are visible in the low frequency pitch response. Again the larger the wave height to more the second order models over predict the response, and the lower the wave height the more the models under predict the response. In general for the irregular wave cases the under prediction was worse for the pitch than for the surge.

8 Computational Fluid Dynamics Study

Viscous flow effects create some difference between potential flow predictions and the physical flow. This can create significant discrepancies between the predicted and measured motions of the platform for some types of motions. Reynolds averaged Navier Stokes solvers can offer insights into the importance more accurately predicting the viscous flow. CFD studies are typically orders of magnitude more computationally expensive than potential flow studies. It is not feasible to simulate long time series of every possible environmental condition that may be of interest for a platform. Instead knowledge must be gained from shorter specific cases, and this knowledge can be used to predict the effects for other scenarios.

As discussed in Section 3, decay tests are commonly used to quantify the damping of a platform in a certain degree of freedom. Post processing techniques can divide the damping into a linear and a quadratic component. While this provides a better description of the damping than a more arbitrary critical damping value, it still only describes effects for a specific scenario, and when applied to a wide range of wave and platform motions may not correctly predict the damping effects. Silva de Souza et al. used a method of tuning coefficients to recreate the motions of model tests. They performed this tuning for different sea states and determined that different tuned coefficients were needed to recreate the different motions in different wave conditions [25]. Berthelsen et al. also tuned drag coefficients to model test data. They found that using higher drag coefficients near the free surface and lower coefficients at deeper elevations improved the accuracy of the predictions [2].

The goal of the CFD in this project is to develop functions of viscous correction coefficients that only come from the numerical simulations and not from the model test data. Comparisons to experimental results are only made to assess the success of the method. If accurate predictions could be made without the need for model tests design iterations could be completed more quickly and with less cost. At this point however the physical experiments are crucial to validate the physicality of the predictions.

The ideal method is also not sea state specific. If different wave and motion conditions are experienced by the platform, the goal viscous correction method can adjust to accurately predict the viscous loads on the body.

As described in Section 2 viscous drag forces can take many different forms. The magnitude, phase, and proportionality of the viscous forces depend on the nature of the boundary layer, whether or not there is separation, and the unsteadiness of the flow among other factors. Potential flow coefficients are strictly functions of frequency. Viscous drag coefficients can vary drastically at a given frequency depending on the velocity and amplitude of relative motion. For a steady flow the velocity determines the Reynolds number which effects the relative importance of viscous and inertial forces, and determines the turbulence and attachment of the boundary layer. The amplitude determines the KC number which describes how developed a flow becomes in a certain direction, and the relative importance of time derivative terms. Both of these factors together effect whether or not separation will occur and where, when, and how separation will occur. Accurately predicting separation is essential to predicting the viscous forces.

Table 8.1 shows some possible Reynolds numbers and KC numbers that the WINDMOOR platform might experience in the model test environmental conditions (in model scale). This table lists the KC number and Reynolds number as if the particular wave or surge motion occurred in an isolated condition. In reality the flow will be a more complex combination of waves and platform motions. This simplification just gives a rough picture of what ranges might be possible. The nine regular waves of the mono-chromatic tests are given in the first section, the ten regular waves of the bi-chromatic tests in the second section, and the maximum experimental surge motions in the third section. The maximums and minimums over all three sections are highlighted in green and red respectively for the Reynolds numbers and KC numbers. The highest KC number occurs during the large amplitude low-frequency surge motion. The lowest KC number occurs from the wave with the shortest wave height. The Reynolds numbers shown are calculated based on the maximum particle velocity that occurs in a period of the wave. This maximum velocity is a function of both the wave height and the frequency. The maximum occurs in one of the mono-chromatic wave cases, and the minimum occurs in one of the bi-chromatic wave cases.

	f [Hz]	H [m]	Umax [m/s]	KC	Re
mono-chromatic	0.791	0.021	0.052	0.17	1.93E+04
	0.576	0.039	0.071	0.33	2.66E+04
	0.449	0.064	0.090	0.53	3.37E+04
	0.791	0.083	0.207	0.70	7.75E+04
	0.576	0.158	0.285	1.32	1.07E+05
	0.449	0.255	0.360	2.14	1.35E+05
	0.791	0.167	0.414	1.39	1.55E+05
	0.576	0.315	0.569	2.64	2.13E+05
	0.449	0.510	0.719	4.27	2.70E+05
	f [Hz]	H [m]	Umax [m/s]	KC	Re
bi-chromatic	1.107	0.016	0.045	0.13	1.7E+04
	0.834	0.019	0.049	0.16	1.8E+04
	0.703	0.026	0.058	0.22	2.2E+04
	0.634	0.032	0.064	0.27	2.4E+04
	0.575	0.039	0.071	0.33	2.7E+04
	0.506	0.051	0.081	0.43	3.0E+04
	0.904	0.128	0.362	1.07	1.4E+05
	0.834	0.149	0.391	1.25	1.5E+05
	0.703	0.211	0.465	1.77	1.7E+05
	0.634	0.259	0.516	2.17	1.9E+05
	f [Hz]	A [m]	Umax [m/s]	KC	Re
maximum surge	0.069	7.71	0.152	5.86	5.69E+04

Table 8.1: Possible Reynolds and KC number ranges for model scale waves and motions

Following the Reynolds regimes described in figure 2.3 for steady flow around a circular cylinder, the predicted range correlates to a laminar boundary layer with a fully turbulent vortex street. Given the unsteady flow it is likely that transition to turbulence in the boundary layer will occur at a lower Reynolds number than in steady flow. This means that the high end of the Reynolds number range predicted here could enter the regime with a turbulent boundary layer.

The minimum KC number of around 0.1 would predict non-separated flow. The maximum KC number of close to 6 would predict separated flow but most likely no established vortex street. It is hypothesized that the viscous effects on the forcing on the body are most strongly effected by the occurrence and nature of separation. For the waves and motions expected to be experienced by the platform, this will be most strongly dependent upon the KC number. Given the high computational costs of CFD there is not enough time in this project to run many simulations with many varying parameters. With the theoretically strong link between separation effects and the KC number, the viscous corrections are treated strictly as a function of KC number. Forced oscillations over the potential range of KC numbers are used to numerically quantify the viscous contributions to the body forcing. Only oscillations in the surge direction are considered. The surge motions are the dominant low-frequency motions, and are thought to be largely uncoupled from the other degrees of freedom. These surge oscillations are also used to approximate the viscous forces due to wave particle velocities in the surge direction. In reality the fluid in a wave moves in a circular pattern, which would involve potentially important three dimensional effects. However, a simplification is made, and the viscous contribution to wave excitation in the surge direction is approximated by purely surge direction oscillations.

8.1 CFD Model Setup

One key difference between the original potential flow study and the CFD study is the scale. The model test data was reported in full scale and the potential flow results were originally calculated to match this and to give a picture of what would occur for an actual floater and wind turbine. This can be done without negative consequence for potential flow coefficients which will scale correctly according to a constant Froude number. The viscous effects however are dependent on the Reynolds number which does not scale correctly. For this reason the CFD study was done at model scale, and the model test data was also converted back to model scale for comparisons.

The viscous flow effects are typically local phenomenon. Locations with varying geometry will see different flow patterns and different pressure distributions. Not only does the flow vary around the platform due to the shape of the platform, but due to the different water particle motions at different water depths. The wave particle velocities decay following a hyperbolic cosine function. Rotational motion of the platform also leads to

varying relative velocities and accelerations at different locations.

In the CFD study the platform is divided into elevation layers, and the forcing is measured separately for each layer. Viscous correction functions are thus found for each layer, and can be implemented based on the local conditions at that layer. In full scale the platform is divided in 1 m increments, corresponding to 31 elevation layers. In model scale this means that each layer is 1/40 m high. With a full scale mean water line of 15.5 m, this means that 16 elevation layers are of major importance. In following plots and discussion the elevation cuts are often referred to by a layer number. Layer 1 is at the keel and Layer 31 is at the deck. The mean waterline is at the mid-point of layer 16. A view of the decomposed platform is shown in Figure 8.1, the yellow layers and half of the blue layer are beneath the mean waterline, and thus are subject to the most important loading. Layers 1 through 4 make up the pontoon with a larger area and sharp corners. Layers 15 and 16 feel the most influence of free surface effects.

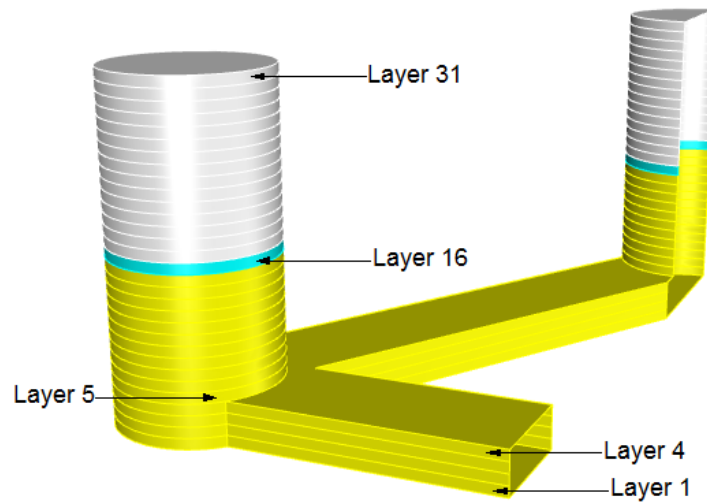


Figure 8.1: Decomposed CFD platform geometry

Because the upper braces are located well above the expected wet region of the platform, they are not included in the model. This saves the computational cost of additional cells needed to define the geometry of the braces. A symmetry plane is also used in the simulations. Similar to what was used in the potential flow analysis, the platform is only modeled in the positive Y direction, with a cut on the X-Z plane. The flow is predicted to be symmetrical for the forced oscillations at the KC numbers tested, so the use of a symmetry plane should not negatively affect the accuracy. Its use comes with a 50% reduction in cell count and thus computation time. Verification of this assumption is discussed when analyzing the flow patterns in the highest KC number motions.

8.1.1 Computational Solvers

In order for the fluid to understand the movement of the structure, the mesh needs to be adjusted in between time steps. This can be done in a number of ways. Two methods morph and distort the mesh with the body, and use the OpenFOAM *dynamicFvMesh* solver. One of these methods allows for topological changes in the mesh, meaning the actual cell arrangement can change, and the other maintains the mesh topology. The second method was used by Rivera-Arreba in her analysis of free decay and wave induced motions of a semi-submersible. She describes that her chosen method uses three defined regions. In the inner most region (containing the body) the mesh is rigid and fixed with respect to the body, meaning that the cells will not distort, but will move with the platform. In the outer most region the mesh is completely stationary. In the intermediate region the cells will deform and stretch to allow the motions of the inner most region, while still maintaining the same connections with the cells of the outer region [21].

A third method was introduced in OpenFOAM in 2017, known as the overset or Chimera method [17]. This method was used in the work of Pinguet et al. in 2020. Their work aimed to validate the use of the method again for free decay and wave induced motions of the same semi-submersible wind turbine platform studied by Rivera-Arreba. The overset method predicted motions with either equal or better agreement to model test data for the cases presented [19] [18].

An advantage of the overset method is that no cells in the mesh are distorted. If the mesh is generated in a particular way to capture particular flow effects, there can be confidence that the mesh will perform as intended. This can be particularly useful when the expected motions of the body are large, and distortion of cells could be expected to be significant for the *dynamicFvMesh* method. Highly distorted cells may influence

the results of the flow calculations. Because this work aims to accurately capture the differences between the body forces with viscous flow and with potential flow, it is important to accurately model the boundary layer and possible wake regions. This requires a complex and refined mesh, which is tested to ensure there is sufficient resolution. Given forced oscillations, the motions are known exactly before the simulations are run, and some of the motions are relatively large compared to the body geometry. In order to keep the quality of the tested mesh in the large amplitude motions, the overset method is used in this project. This choice is also influenced by the success of Pinguet et al. using the method.

Two different fluid domains are established in the overset method. There is a larger outer domain which is stationary and contains cells for every point in the domain. There is also a smaller inner domain which has a mesh that is fit to the shape of the body, and does not have any cells inside of the body. This inner domain moves inside of the outer domain with the motions of the body and is assigned an overset patch type. No cells in either domain distort in this method. The potentially complex and refined mesh around the body stays intact and simply translates and rotates with the object. It is also possible to have multiple separately moving bodies with the overset method. In this case there would be multiple body fitted dynamic meshes moving within the stationary outer domain.

At each time step cells are assigned one of three cell types. Hole cells are cells that lie inside of the body (only exist in the outer domain), and they are disregarded during that time step. The second type are calculated cells, in which the field values are calculated for the time step using the designated solvers. The third type are interpolated cells, in which the field values are interpolated from the neighboring cells [17]. Two main boundaries exist with interpolated cells. The first boundary is at the surface of the body. At this location the cells of the outer domain are interpolated based on the calculated donor cells of the inner overset domain. The second boundary is at the outer extents of the overset domain. At this location the cells of the inner overset domain are interpolated based on the calculated donor cells of the outer domain [19].

Figure 8.2 shows the cell types for the mesh of this project. The hole cells are in red; the calculated cells are in blue; the interpolated cells are in white. The view shows the mesh of both the outer and the overset domain with a wireframe on the edges of each; both domains are rectangular prisms. The plane in the foreground is the X-Z symmetry plane along the centerline of the platform, which cuts through one column and one pontoon. Touching the red hole cells of the platform are the white interpolated cells of the outer domain. The interpolated white cells forming a box around the platform are at the outer extents of the overset domain.

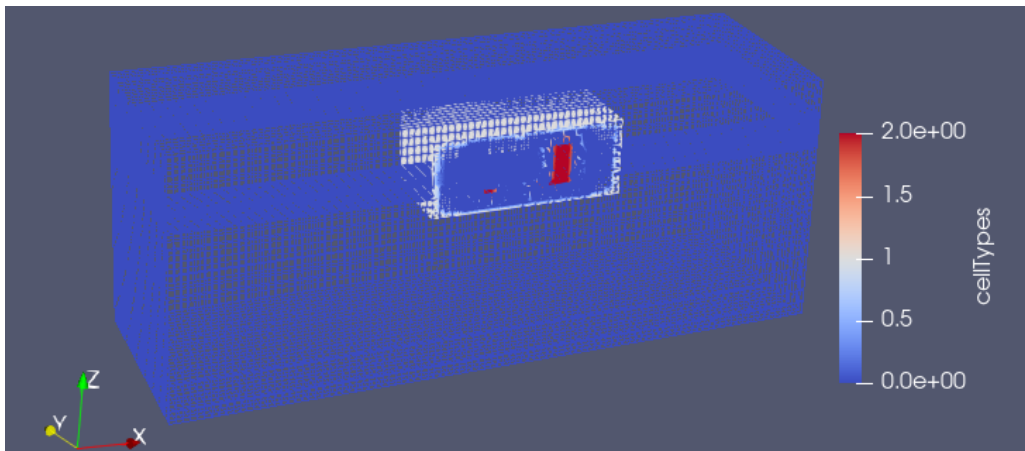


Figure 8.2: Overset mesh motion cell types

Note that one face of the overset domain, on the symmetry plane, does not have interpolated cells. If the other half of the domain was present, there would be no interface at this location, and the cells of the overset domain would be bordered by similar cells of the other side of the overset domain. If the cells on this face were interpolated, then the large cells of the outer domain would disturb the solution of the refined cells around the body, negatively affecting the accuracy of the flow predictions. The only consequence of this decision, and really a consequence of using a symmetry plane, is that no motion of the platform can occur in the y-direction. This reduces the possible degrees of freedom from six to three. Only surge motions are tested in the work, so this is not a problem.

In order to capture free surface effects, a two phase simulation is needed. This is done through the use of the volume of fluid, or VOF, method. In every cell there is a value, α , which states the percentage of the cell that is water. An α value of 0 is a cell filled fully with air, and an α value of 1 is a cell filled fully with water.

The value of α is updated in each time step using the transport equation given by Equation (55).

$$\frac{\partial \alpha}{\partial t} + \nabla \cdot u\alpha + \nabla \cdot u_r\alpha(1 - \alpha) = 0 \quad (55)$$

The first two terms are typical and simply relate the time rate of change of the volume fraction to the convection of the volume fraction with the velocity of the fluid. The third term is less physical, but is introduced to help keep a crisp free surface [21]. When a cell contains either only water or only air, the third term will disappear, so it only influences the cells that make up the free surface. In these cells a virtual velocity, u_r , is introduced with a magnitude proportional to the real velocity in the cell, and a direction that points into the water [21]. In every cell the properties of the fluid such as the density and viscosity are simply a weighted average of the properties of the two fluids based on the volume fraction.

The incompressible Navier-Stokes equations have four unknowns: the velocity in each of three directions and the pressure. There are also four equations to solve: the momentum equation in each of three directions and the continuity equation. The solvers of the finite volume method are based on an integration of the equations over each finite volume of a cell. In this integration process various schemes are used for the derivatives of the variables. These schemes can utilize the value of the cells from varying distances, various profile shapes, and can interpret the values between cells in different ways. For time derivatives, the Euler scheme is used, which is implicit and first order. Gaussian linear schemes with upwind approximation are used for spatial derivatives of each relevant variable [17].

With the selected schemes and the established grid, the governing equations can be written into a matrix form, where all coefficients of the velocity are grouped together. This results in a compact version of the momentum equations shown in Equation (56). The diagonal of the \mathbf{M} matrix corresponds to influence of the value in a cell on the value in the same cell for the next iteration. This diagonal can be extracted from the \mathbf{M} matrix to form a new purely diagonal \mathbf{A} matrix. The leftovers from the product of the off-diagonal terms of \mathbf{M} and the velocity vector are described by a matrix named \mathbf{H} . This decomposition of \mathbf{M} is described by Equation (57) [17].

$$\mathbf{M}\vec{u} = -\nabla \cdot \vec{p} \quad (56)$$

$$\mathbf{M}\vec{u} = \mathbf{A}\vec{u} - \mathbf{H} \quad (57)$$

These equations can be rearranged to solve for the velocity as shown in Equation (58). This can be solved using the velocity from a previous time step or iteration to give an approximation of the velocity. However, this velocity is not guaranteed to satisfy the fourth equation, the continuity equation [11].

$$\vec{u} = \mathbf{A}^{-1}\mathbf{H} - \mathbf{A}^{-1}\nabla \cdot \vec{p} \quad (58)$$

This expression can be inserted into the continuity equation in place of the velocity. The result is an equation for the divergence of pressure given by Equation (59). This is known as the Poisson equation of pressure for an incompressible flow. Due to the nature of a Poisson equation, the influence of the pressure in one location can be felt everywhere in the domain. The pressure to satisfy this equation is solved for; this is typically a critical step in terms of the speed of a CFD code [11].

$$\nabla \cdot (\mathbf{A}^{-1}\nabla \cdot \vec{p}) = \nabla \cdot \mathbf{A}^{-1}\mathbf{H} \quad (59)$$

This new pressure field will then satisfy the continuity equation for the approximated velocity field, however the velocity field was approximated using the old incorrect pressure. The velocity can then be updated using the new pressure. Through this iterative updating of the velocity and pressure, the solution will converge to a stable answer. This method is known as the pressure correction method and was first developed by Harlow and Welch in 1965 [11]. Various methods of iterating through the steps have been created, and are best suited for different kinds of analyses.

The SIMPLE algorithm was originally developed for steady flows and utilizes a form of under-relaxation to help with stability. The SIMPLE algorithm, or Semi-Implicit Method for Pressure Linked Equations, uses an iteration loop that includes all of the described calculations in each iteration. Because steady state problems lack time derivatives, they can have a relatively large \mathbf{H} matrix in comparison with the \mathbf{M} matrix, which can potentially lead to a less steady and slower convergence to a solution. In order to help this problem, the SIMPLE

algorithm uses under-relaxation, which dampens the changes between iterations, and aims to speed convergence [17].

The PISO algorithm, or Pressure Implicit with Splitting of Operators, was developed for unsteady flows. Unsteady flows are inherently more stable, and the under-relaxation of the SIMPLE method is not used. Without the under-relaxation, there is more risk of instability, and thus with the PISO method time steps should not be too large. The PISO algorithm does not loop through all steps of the pressure-correction method with every iteration. Instead only the velocity update and the pressure Poisson steps are iterated [17].

The PIMPLE algorithm is used in this study. The PIMPLE method combines some iterations of the SIMPLE method with the PISO method. This allows for a more stable solution, which then allows the use of a larger time step. The OpenFOAM settings, *nOuterCorrectors* and *nCorrectors*, refer to how many iterations are done of each loop [19]. In this project both of these numbers are set to two, which was also used by Pinguet et al. in their OpenFOAM overset method study.

The solution of the pressure correction step utilizes a preconditioned conjugate gradient solver and a diagonal incomplete-Cholesky preconditioner. These are typical choices for the matrix conditions of an overset mesh method [19].

8.1.2 Turbulence Modeling

As described in section 2 the presence of turbulence in the flow can have important effects on the resulting loads on a body. Important turbulence can occur at extremely small scales. To resolve these very small eddies, extremely fine resolution is needed. Directly resolving all eddies is not computationally feasible for most marine projects. Instead turbulence models are commonly used, which don't actually solve for turbulence, but instead model its influence on the mean flow.

Many turbulence models have been developed and some are better suited to different types of simulations. As a first option it is good to consider if modeling the flow as purely laminar, with no turbulence model, is suitable. This would be an accurate physical prediction for very low Reynolds numbers. It may also be the case that while the flow is not actually laminar, introducing a turbulence model does not give any more physical or accurate results, and only adds computational cost. Pinguet et al. and Rivera-Arreba both treated their flows as laminar in their semi-submersible OpenFOAM studies [19] [18] [21].

For the probable Reynolds numbers present in the CFD study, if in a steady flow, a laminar boundary layer with a turbulent wake would be expected. For an oscillatory flow, the critical Reynolds number will be lower, which means that transition to turbulence could occur in the boundary layer as well as in the wake [24]. The nature of the wake has added importance for an oscillating motion, as the body will travel through the wake of the previous oscillations. Three methods of turbulence modeling were tested in this project: laminar with no turbulence model, k-omega shear stress transport, and Langtry-Menter k-omega shear stress transport. Comparisons were made between the models with particular attention paid to the appearance of the boundary layer, the appearance of the wake, and the separation point. Turbulence can have a large impact on each of the these phenomenon.

In an oscillating motion, especially if the KC number is not very large ($KC \gg 2\pi$), the effects of the acceleration can dominate, and it can be difficult to focus on the qualities of the boundary layer, separation, and the wake. For this reason, the effect of the turbulence models was studied using a steady flow. The idea is that in a steady flow it is easier to identify if a model is able to capture certain flow patterns. Then when performing unsteady cases it is known what can possibly be predicted. The same approach is used and discussed when studying the required refinement of the mesh. In these tests the steady flow direction is in the positive x direction.

The k-omega shear stress transport, commonly called k-omega sst, is a two equation model. The model is a combination of two earlier models, k-epsilon and k-omega. K-epsilon is known to predict turbulence better far from any walls, and k-omega is known to predict turbulence better in the near wall region. K-omega sst then utilizes the k-omega model near the wall and the k-epsilon model far from the wall, with blending functions at the interface. The first k-epsilon model was introduced by Chien in 1982, and the first k-omega model was introduced by Wilcox in 1988 [23]. For each of the three models two additional variables are introduced, k , which is the turbulent kinetic energy, and either ϵ or ω , which give the dissipation rate of turbulence. ω is the specific dissipation rate while ϵ is the non-specific dissipation rate. ω is simply equal to ϵ divided by k and some constants.

The end goal of these turbulence models is to obtain a value of turbulent viscosity, ν_t , for each cell. This is a form of a virtual viscosity as discussed in section 2. In a turbulent flow the random fluctuations lead to a sharing of momentum between the mean layers in a flow. This transfer of momentum ties the layers together which is analogous to laminar viscosity. The end result is a virtually increased viscosity, often significantly, which impacts the mean flow. The value of ν_t can be calculated based on the value of k and either ϵ or ω . Equation (60) expresses the form used in the k-epsilon model. C_μ is called the model coefficient for turbulent

viscosity and has a standard value across the models [17].

$$\nu_t = C_\mu \frac{k^2}{\epsilon} \quad (60)$$

For each of these models the turbulent kinetic energy is calculated using a transport equation. The transport equation for the k-epsilon model is given by Equation (61) [17]. The equations for the other models contain the same general terms, but the variable names and constants used vary slightly.

$$\frac{D}{Dt}(\rho k) = \nabla \cdot (\rho D_k \nabla \cdot k) + P - \rho \epsilon \quad (61)$$

In this equation it should be noted that the first term is the full material derivative and thus contains both the time derivative and the convective term for the transport of k . The second term is for the diffusion of turbulent energy and the term D_k groups all coefficients which make up the diffusivity of k . The third term, P , is a source term for the production of k and is calculated based on the velocity field following Equation (62) [23].

$$P = \tau_{ij} \frac{\partial u_i}{\partial x_j} \quad (62)$$

The final term of Equation (61) is for the dissipation of k and is based on either ϵ or ω depending on the model.

The calculations of ϵ and ω are also done using a transport equation with a very similar form to the equation used for k . There is both convection and diffusion as well as production and dissipation of each variable in each time step [23]. Along with the two variables of each model the corresponding equations contain a number of coefficients which have been tuned to attempt to best recreate physical effects. Each of the three models also contain correction terms which adjust the transport of the variables in the near wall region [23].

The value of the variables in successive time steps is based on the transport equations and the values in the previous time step. At the start of the simulation though some initial conditions are needed in the domain. The OpenFOAM user manual provides some suggestions for the initial values based on a reference velocity, length scale, and turbulence intensity [17]. For this project the velocity used was the velocity at which the steady flow tests were conducted, the length scale used was the diameter of a column of the semi-submersible, and the initial turbulence intensity was set to 5%.

The k-omega sst model takes the strengths of the k-epsilon model in the free stream and the strengths of the k-omega model near the wall. It is a commonly used turbulence model in marine CFD applications especially for separated flows and thus was selected as a choice to test. A pitfall for the model is that it uses the same turbulent equations everywhere in the domain. When transition to turbulence is expected and expected to occur within a relatively short distance on a body, this is not a big problem. For the considered Reynolds numbers however, a laminar boundary layer may be more likely to occur, and even if transition to turbulence does occur, it likely will only be for a portion of the body. Treating the flow as purely laminar does not allow for turbulent effects in the wake, and also does not allow the potential for turbulence which may occur, but using the k-omega sst model most likely over-predicts the combined viscosity most of the time in the boundary layer.

For flow problems when transition to turbulence is of interest, transition models have been developed. One considered in this project is the Langtry-Menter transitional sst model. It is a four equation model and combines aspects of the k-omega sst model with aspects of a laminar solution. The first two variables and equations are the same k and ω used in the k-omega sst model. The second two new variables help to indicate when a transition to turbulence will occur, and are called γ and Re_θ . The first, γ , is called intermittency, and indicates what portion of time a flow would be turbulent. A value of zero indicates a fully laminar flow and a value of one indicates a fully turbulent flow. The equations used in each cell depend on this value of γ . Cells which have a value of one simply use the k-omega sst equations, and cells with a value of zero don't invoke any turbulence model. The cells with an intermittent value of intermittency use a form of a blending function to give appropriate strength to the corresponding equations [23].

Re_θ in this model is the transition Reynolds number. Instead of a Reynolds number based on a characteristic length of a body or a distance along a body, this Reynolds number is based on the momentum thickness of the boundary layer. In general the value of γ is one everywhere outside of the boundary layer, and the value starts at zero on the wall. γ can then be diffused into the boundary layer from the outer flow if the conditions allow for it. Re_{theta} is given some value at the boundaries which is based on an equation fit to experiments. The OpenFOAM user manual gives recommendations for this boundary condition based on the initial value of turbulent kinetic energy and the maximum velocity in the outer flow [17].

Both γ and Re_θ are calculated for successive time steps based on transport equations similar to described for k in Equation (61). The source term for production of intermittency in the γ transport equation is the most interesting. This term contains functions that determine when production will occur and they attempt to both predict when instability will be onset as well as how long transition should take. These are both functions of Re_θ [23].

The result is a model which is slightly more complicated and computationally expensive, but attempts to predict when transition will occur and then utilizes relevant models depending on the result. This model not only can predict transition, but adds the ability to treat a boundary layer as laminar but the wake as turbulent, if that is appropriate.

It should also be noted at this point that the mesh requirements vary depending on the turbulence model. In order for the models to behave as designed, special attention is given to the thickness of the cells that make the connection to a wall. The wall functions of the turbulence models assume different velocity profiles for the boundary layer, and the equations operate under the assumption that there is mesh resolution in different sections of the velocity profile. y^+ was defined in Section 2 and is a non-dimensional distance from a wall based on the shear stress on the wall. The velocity profile in a boundary layer changes depending on the value of y^+ . It is recommended that for a k-omega sst model with wall functions the first cell lands in the in the logarithmic portion of the boundary layer, which would indicate a y^+ value between 30 and 300. For the Langtry-Menter transition model, it is recommended to have the first cell land well within the linear portion of the viscous sublayer, specifically with a y^+ below 1. In order to gain the benefits of a good prediction of transition to turbulence, much thinner cells are needed in the boundary layer. This adds some additional computational cost. As well as adding to the number of cells, introducing thinner cells can effect the maximum Courant number in the simulation. Fortunately the velocities in the very near wall region where the cells are the thinnest are very small, but thinner cells still likely lead to a smaller maximum allowable time step.

The mesh generation process is described in detail below. As a starting point the thickness of the boundary layer cells was adjusted to match the desired y^+ value for the corresponding turbulence model. An iterative process is required for this since the wall shear quantities are not known prior to running a simulation. The resulting y^+ values for the mesh used with the Langtry-Menter transition turbulence model are shown in Figure 8.3.

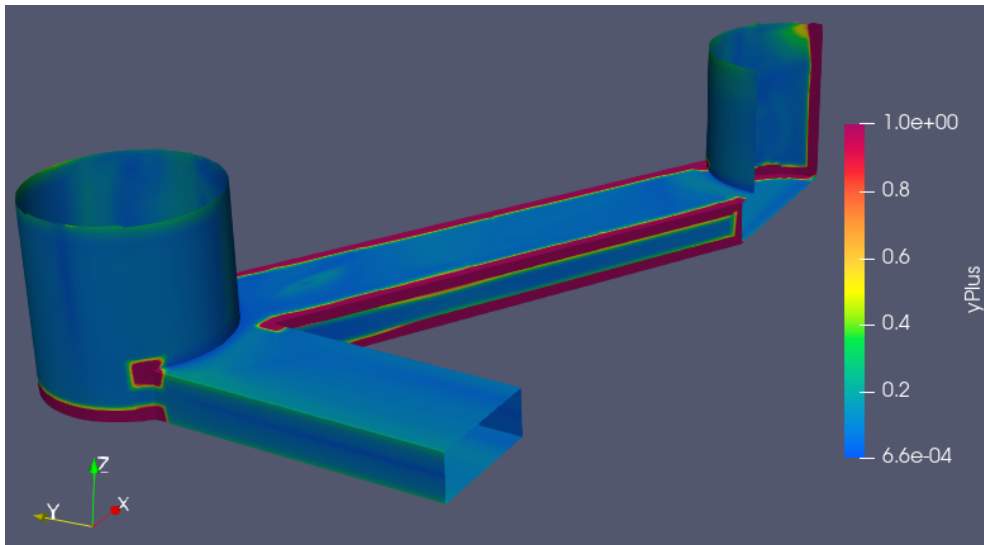


Figure 8.3: y^+ values used for Langtry-Menter transition turbulence model

The color scale is set with a maximum of $y^+ = 1$; any sections with a maroon color indicate a $y^+ > 1$. The aim for the transition model is to have all first boundary layer cells land beneath $y^+ = 1$, however there are some difficulties with the boundary layer cell generation. The meshing tool used in OpenFOAM can have difficulties continuously wrapping boundary layer cells around sharp corners. This is particularly true when the sharp corner does not lie along a principal axis. Figure 8.4 shows where the thin prism layer cells wrap around the corner well.

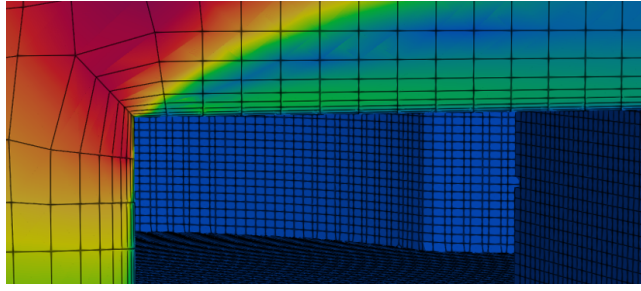


Figure 8.4: Successful boundary layer cell wrapping around sharp corner

This is a close view of the pontoon that runs along the y -axis (upstream pontoon in the steady current test). The coloring indicates velocity magnitude, and it is clear that the flow separates immediately at the sharp corner. The very thin cells along the body continue all the way through the corner. Because of this the y^+ value remains very low ($y^+ < 1$) as desired. Due to the hexahedral style used by the mesh generator wrapping very thin boundary layer cells around corners which run off-axis is difficult. Through experimentation with the settings of the meshing tool, it was found that when the first layer is thin enough to bring the y^+ value down below 1, the tool cannot wrap the cells on these corners. Instead the innermost layers gradually die out at the corner and the cells on the wall are thicker at these locations, leading to regions with higher values of y^+ . While it is not ideal, this should not cause significant problems. The flow will immediately separate at these corners whether or not the cells wrap as desired. The more important regions to capture the boundary layer are those along the extents of flat panel and particularly along the column where there is more uncertainty in the location of separation.

Figure 8.5 shows the resulting values for γ , the intermittency value for turbulence. For the majority of the structure the value is essentially zero, forcing the use of laminar equations in the near wall boundary layer region. This is as expected for the Reynolds number with a steady flow. The thin strips with a high value of γ correlate to the same locations where the layer cell wrapping failed on corners. Because of immediate separation at these points, it is expected that the effects on the flow field and body forces from the temporarily heightened γ are not important. A potentially more interesting region is the top of the pontoon in the foreground of the figure. There is a slightly white strip that runs along the plate and bends away near the column. This white strip roughly matches the position where the separated flow starts to reattach to the body. At this location some turbulence generated in the wake is brought back to the body, temporarily increasing the intermittency. The viscous forces near the body then stabilize this and the value of γ goes back towards zero.

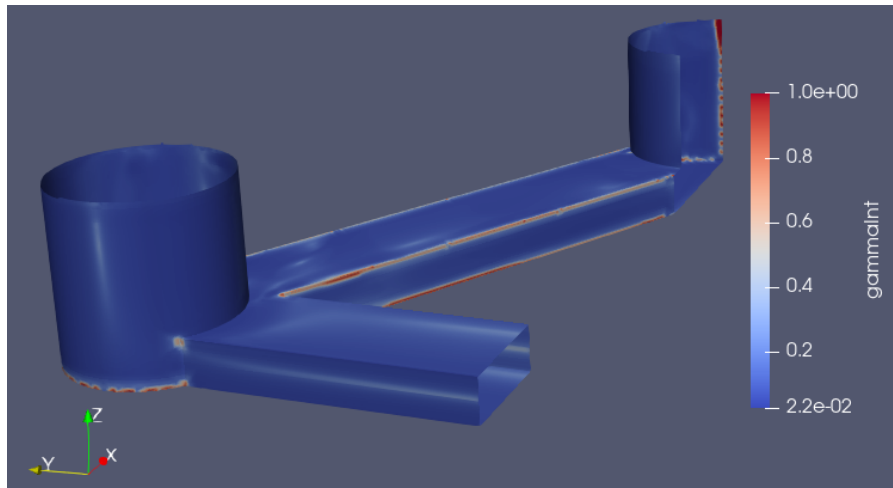


Figure 8.5: Intermittency of turbulence (γ) in steady flow

When comparing the flow predicted with the three turbulence modeling styles there are some key differences. The separation point on the column when using the k - ω sst model is noticeably later than that with either of the other two models. The boundary layer thickness is also noticeably larger than the other two models. Both of these qualities are expected for a turbulent boundary layer in comparison to a laminar boundary layer, which reflects the views of the models. There is also a difference in the pattern that the wake develops particularly between the laminar case and the two models which view the wake as turbulent.

After comparison the differences between the three models were deemed important enough to justify the use of the k - ω sst Langtry-Menter transition turbulence model. This model provides the ability to treat

the boundary layer as laminar and the wake as turbulent, which is expected for the flow based on experiments. The model also provides the ability to predict a transition to turbulent boundary layer which may be the case for an oscillating flow in this Reynolds number range.

8.1.3 Mesh

It is important that the fluid domain is large enough that the boundaries do not influence the results. Previous work with a similar body in forced oscillations was not found for a comparison. The possibility of reflected waves and other influence from the domain boundaries is expected to be similar to free decay tests. The outer domain extents are thus based on the relative domain size used by Pinguet et al., and are shown in Table 8.2 along with the extents of the inner overset domain. The extents of the overset domain are determined by the mesh refinement around the body. As mentioned by Pinguet et al. when using the overset mesh method it is important that the cells on the interface of the stationary and the moving domain are very similar in size and shape [18]. Surrounding the body are regions with various levels of added mesh refinement, to capture the more intricate flow near the platform. These levels of refinement taper off further from the body until they reach the base mesh of the larger outer domain. The key is to make the inner domain large enough that the mesh can gradually become more coarse to match the cells of the outer domain. In this study where motion of the inner domain is only in the surge direction, this is particularly important at the boundaries of the overset domain in the y-z plane.

Outer Domain Extents [m]			
	x	y	z
Minimum	-6.0	0.0	-3.75
Maximum	6.0	4.0	1.0

Inner Overset Domain Extents [m]			
	x	y	z
Minimum	-1.5	0.0	-0.7
Maximum	2.0	1.6	0.7

Table 8.2: CFD model domain

When using the overset method a separate OpenFOAM structure is set up for both the overset domain and the background domain. The background mesh contains only rectangular prism cells and was generated using only the *blockMesh* tool. The extents of a block are defined, and the number of divisions in each direction are given. Faces must match adjacent faces exactly in this tool, without divisions. The outer domain is made of eight different blocks, each covering a different range of elevations. The x and y discretization is the same among all of the blocks, but the thickness of the cells in the z direction varies. Near the seafloor, or model basin floor, the cells are very large as little to no important flow is expected here. The top of the domain where no water will be present also uses large cells. Both of these regions should not be important to the results so computational cost should be made as small as possible. In the majority of the water the cells are chosen to be as close to cubical as possible. Finally five blocks make up the region near the free surface. The finest z-direction refinement is exactly on the mean free surface, and it decays outward from there. The exact cell thicknesses and the extents of each block were chosen to match exactly with the free surface refinement zones of the inner overset mesh.

The full outer domain can be seen in figure 8.6. The region with the black cell divisions is the inner overset domain for reference, and the red cell divisions are in the outer domain.

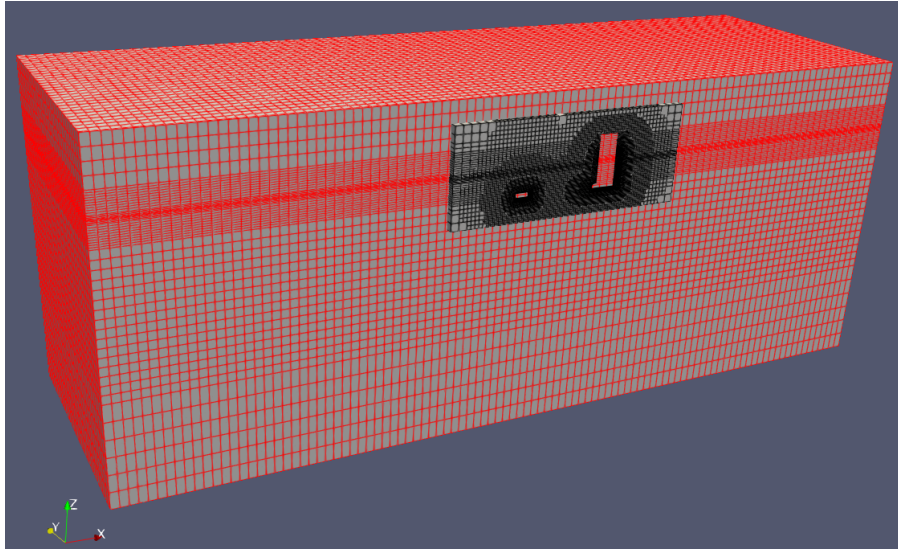


Figure 8.6: Outer domain mesh

The more complex inner mesh was generated using the *blockMesh*, *surfaceFeatureExtract*, and *snappyHexMesh* tools. The block mesh here consists of only one block, and the free surface z-direction refinement is instead achieved with features of the *snappyHexMesh* tool. The geometry of the platform, divided into elevation layers, was generated with the 3D modeling software Rhino, and saved for OpenFOAM implementation in the form of an STL file. The STL file is interpreted by the *surfaceFeatureExtract* function, which saves detailed information on the edges of the geometry to help with sharp and accurate fitting of the mesh to the body.

Finally most of the more complex features of the mesh are created with *snappyHexMesh*. First the STL files are used to locate the surfaces of the geometry, and the cells that are intersected by the surface are divided. Cells can be divided differently in what are called levels of refinement. Divisions always split the previous level. This means a level 1 split cuts each dimension in half, so one cell would turn into 8 cells ($2^3 = 8$). A level 2 split then would cut the level 1 cell in half, resulting in 64 cells to the original cell ($4^3 = 64$). For some refinement types it is also possible to have different levels of refinement in different directions. The first round of refinement occurs around the edges of the geometry defined by *surfaceFeatureExtract*. Level 4 refinement was selected for most of the wet edges, except for the edges of the sharp corners of the pontoons which received level 5 refinement. The next round of refinement is for the cells on each of the surfaces. Again level 4 was selected for most of the wet surfaces, and level 5 for the corners of the pontoons. The third round of refinement is for defined volumetric regions. This round of refinement was used to generate the free surface refinement. The free surface refinement was performed only in the z-direction. Level 4 is used at the mean waterline, and then two regions with level 3 and level 2 extend outward from there. These free surface zones match exactly with the free surface zones of the outer domain. It was found that if the matching was close, but not exact, at the free surface pressure spikes would form at the interface. The matching can be seen in figure 8.7, again with the outer domain cell divisions in red and the overset domain cell divisions in black.

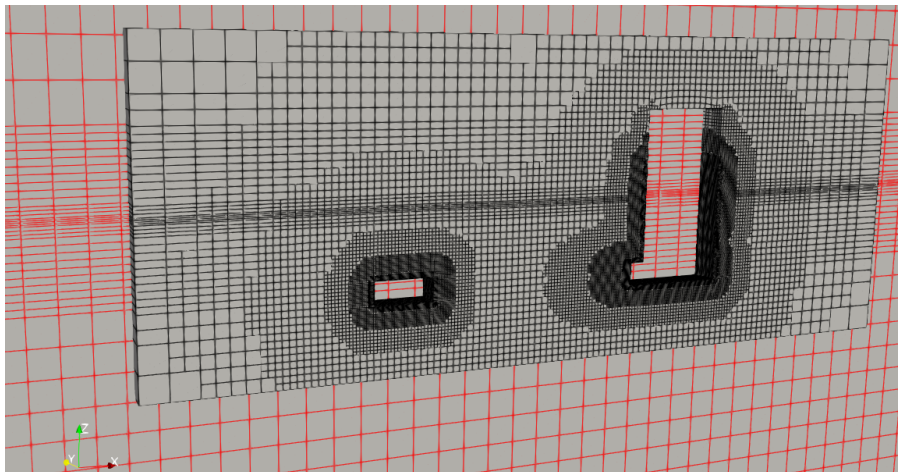


Figure 8.7: Free surface zone cell matching

Volumetric region refinements are also made based on distances to surfaces. For each elevation layer surface, specified distances from the surface are assigned varying levels of refinement. In figure 8.7 the refined zones are visible expanding around the surface of the platform. Note that very little refinement is used above the free surface. Also note that the changes in refinement level do not happen drastically. The refinement zones still have died out by the extents of the overset domain where the base cell size of the outer domain is reached.

The next step of the meshing process is removing the cells inside of the body. The tool can be used for both internal and external flow problems, so the user must indicate points inside the region that should be kept and points inside the region that should be deleted. After the internal cells are removed the cut surface of the mesh is snapped to the surface of the body to exactly model the geometry. Still the edges of the cells are flat faces, so good refinement is needed not only for flow calculations but also to accurately capture curved surfaces and complex angles.

The final step of the meshing process is adding in boundary layer cells. The requirements of these cells were mentioned in the turbulence modeling discussion. For each surface the number of layer cells is defined. The thickness of the inner most cell is prescribed along with an expansion ratio. Changes in cell size should not be dramatic, both between the layer cells and between the outermost layer cell and the normal mesh. The thickness of the inner most cell is selected to achieve a certain value of y^+ . For the selected transition turbulence model the inner most cell thickness is 0.00015 m. In order to have sufficient growth to blend smoothly into the outer mesh, 8 boundary layer cells are included with an expansion ratio of 1.5.

Finer mesh resolution typically leads to more accurate results, but comes with added computational cost. At a certain mesh resolution the idea is that the results are already accurate, and adding more cells will not improve the results, but only add to the cost. The goal is to find the point where the results can be deemed accurate enough but computational effort is not wasted. To find this ideal mesh, the resulting flow field and forces should be compared with varying mesh density. In this project 8 different mesh densities were tested. For every mesh the boundary layer cell settings were held constant to maintain the appropriate thicknesses for the turbulence model. The specified refinements were also kept the same; only the base cell size which the refinements are based on changes. The outer domain mesh is also updated to maintain matching of the free surface zone cells, and to keep the base cells as close to cubic as possible.

For this steady flow case the initial conditions are set so that the velocity everywhere in the domain is equal to the inflow velocity. It then takes some time for the flow to establish as it would actually occur in a steady flow. A purely steady flow result could also be achieved with a steady simulation using only iterations of the pressure and velocity coupling and no time steps. However the goal is set up the mesh so that it can capture unsteady phenomenon like the start of separation and the development of a wake. The simulation with each mesh is run to a time of 10 s, where the flow appears mostly established and stabilized. The pressures on the body are integrated for each elevation layer surface resulting in 31 different time series of forces on the body.

The full time series of forces are shown in figure G.1 in appendix G. This plot shows the forces normalized as a quadratic drag coefficient, based on the local area of the layer. It can be seen that the drag coefficients are roughly stabilized after 10 s. As only a form of a sanity check, the drag coefficient for layers only containing the columns roughly levels off to about 0.8, which is similar to found in experiment for a 2 dimensional flow around a smooth cylinder. When looking at the full time series it is difficult to discern the small differences between the results with the different mesh densities. Figure 8.8 shows only the last 3 s of the same time series. In this closer view it is a little easier to see some differences between the time series. The numbers in the legend correspond to increasing mesh density; 1 is the coarsest mesh, and 8 is the finest mesh. The first four meshes are marked with a dotted or dashed line and the finer four meshes are marked with a solid line to help identify them.

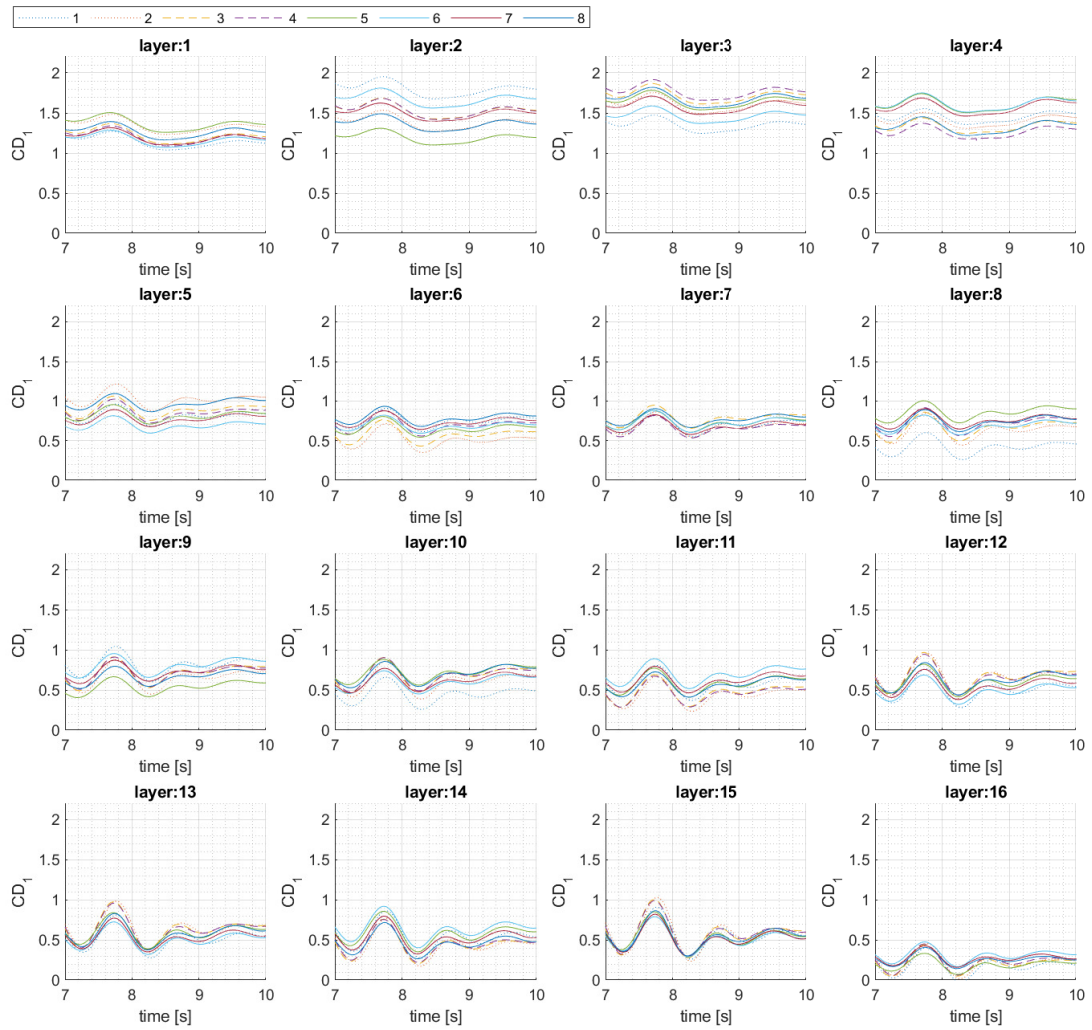


Figure 8.8: Mesh convergence study with distributed shortened force time series

Still it is hard to identify trends when looking at the time series. Figure 8.9 shows the final drag coefficients as a function of the number of cells for each elevation layer. To avoid amplifying the effects of a slight phase difference in the stabilizing drag, the coefficients are taken as the average value over the last 3 s of the time series.

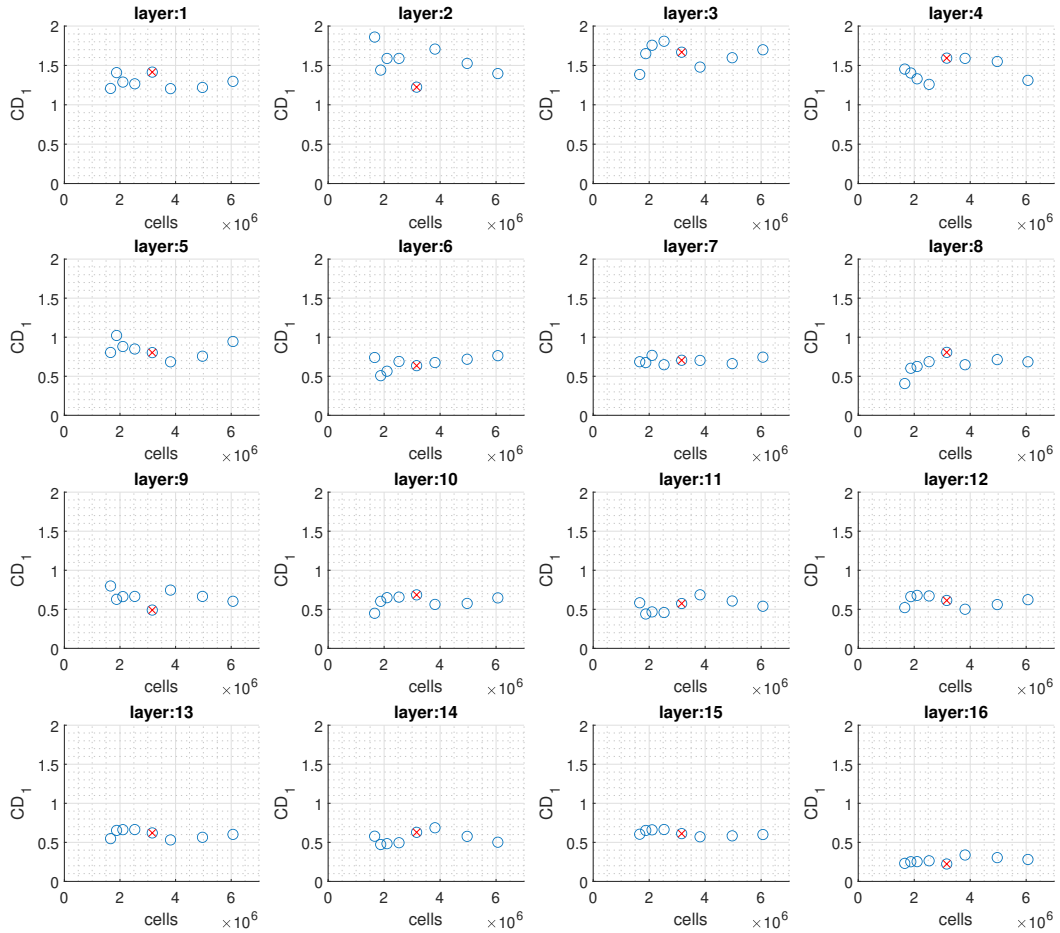


Figure 8.9: Mesh convergence study with distributed drag coefficients

In this figure it is evident that the desired converging trend with increased cell count does not appear. There is not a consistent trend among the different layers. It seems that the forces are slightly more consistent on the column (layer 5-16) than on the pontoon (layer 1-4). Still there is not a point where the forces seem to be independent of the mesh density.

Figure 8.10 shows again the final averaged drag as a function of cell count, but for the total body force and not distributed into elevation layers.

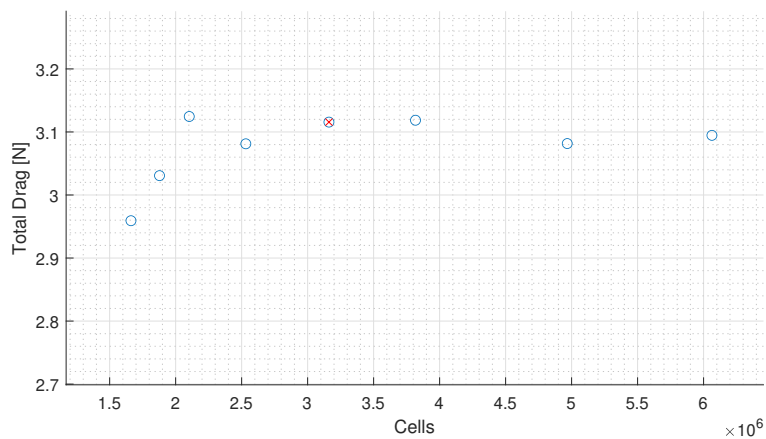


Figure 8.10: Mesh convergence study with total body drag coefficient

The total drag appears to converge slightly better than the distributed drag. In typical mesh convergence studies, the loads on an entire body are most often considered. The goal of this CFD study is to gain more detailed local information about the loads, so confidence in the convergence on the local level is desired. However, the computational and time constraints of the project mean that running meshes with even finer resolution than the 8 shown is not feasible. The trends of the total body drag are used to argue that the fifth mesh, with 3.16 million cells, best balances the benefits of added accuracy with costs of added cells. This mesh density was selected for use in the CFD study, and is marked with a red x in both figure 8.9 and 8.10.

While the mesh density does lead to some uncertainty in the exact drag forcing on the individual layers, the flow fields predicted by the different meshes qualitatively are very similar. Figure 8.11 shows the magnitude of the velocity in the x-z plane; the slice of the domain goes through the upstream pontoon on the left normal to the length of the pontoon, and through the downstream pontoon on the right at 60° to the normal. The top image is from the selected mesh with 3.16 million cells and the bottom image is from the finest mesh tested with 6.06 million cells.

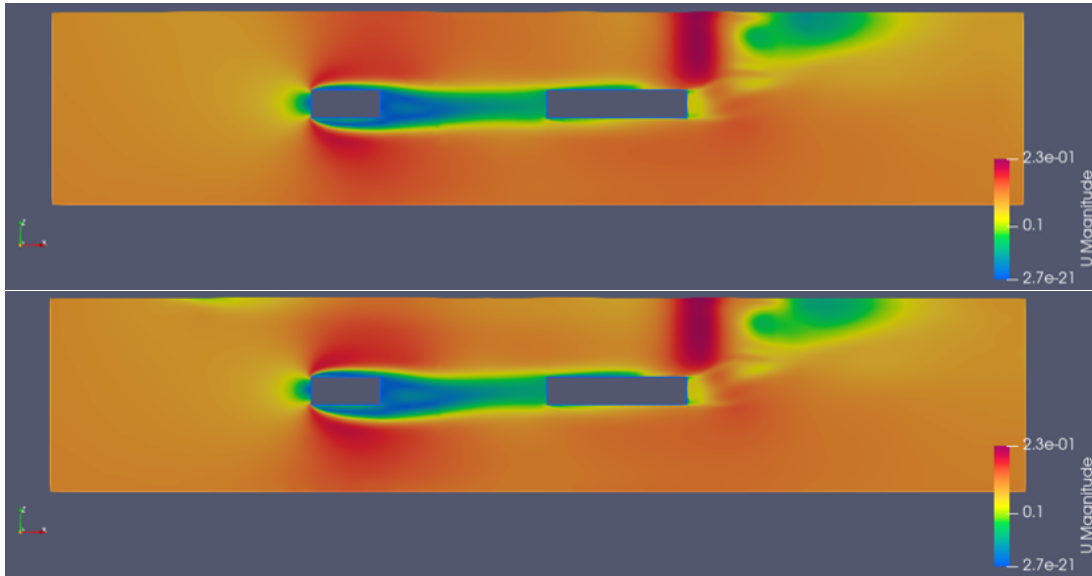


Figure 8.11: Velocity field with mesh density 5 (top) and 8 (bottom)

The flow fields look almost identical, and it appears that all features predicted by the finest mesh are also predicted by the coarser mesh. If there were isolated areas where a certain flow pattern changed depending on the mesh, then finer resolution could be added just in that location to efficiently improve the results. Through inspection of many x-z plane and x-y plane slices the patterns appear very similar between the two mesh resolutions, and the choice of mesh density 5 is confirmed.

Checks of two other modeling choices were also performed. These are the choice of the time step and the use of a symmetry plane. Both of these choices are better confirmed using unsteady oscillatory motion than with the steady flow used to analyze the turbulence modeling and mesh density.

The use of a symmetry plane was justified based on the range of KC numbers expected for the platform to encounter. The main possible asymmetrical flow pattern is the development of an oscillating vortex street. Experiments with circular cylinders show that this is not expected to start occurring for KC numbers as low as tested in this project. A larger amplitude motion relative to the size of the body is needed for these quasi-steady flow patterns to develop. In order to make sure that this choice is appropriate, tests were performed with the highest planned KC number (most likely to see alternating vortex shedding) with both the use of a symmetry plane, and with the full domain modeled. In order to reduce the computation time of this test, only a single column at the center of the domain was used.

Figure 8.12 shows the time series of the total force on the column for both the fully modeled and half modeled domains. For comparison the load on the half domain body is doubled. For more detail figure G.3 in appendix G shows the same time series but with the force distributed into elevation layers. Both in the total load and the distributed load the two domain choices show very good agreement. For a qualitative check as well, the flow field was inspected to check for any asymmetrical shed vortices. It is concluded that the assumption that a symmetry plane can be used is justified, which provides roughly a 50% reduction in computation cost.

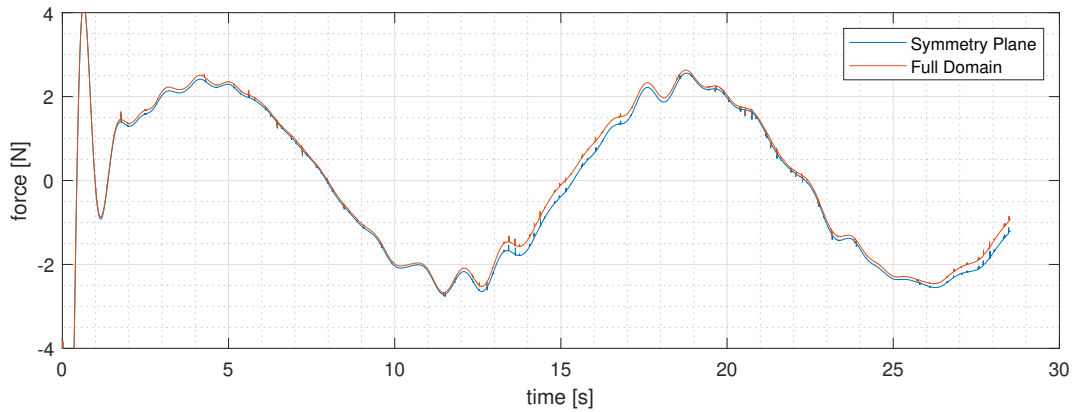


Figure 8.12

The time step was checked using the forced oscillation case with the highest accelerations. Both variable and constant time steps were tested. For the variable time step a desired maximum Courant number is set and a solver adjusts the time step based on the previous Courant numbers. It was found that the variable time step selection was somewhat unstable when the acceleration was high, and the constant time step was selected. Six time steps were tested ranging from 0.0005 s to 0.004 s. A first order implicit Euler time scheme is used, which has a first order error with time. An implicit time scheme allows the use of larger time steps without the risk of instability. The use of the PIMPLE pressure-velocity coupling which is also semi-implicit also allows for increased time steps potentially with Courant numbers greater than one.

Three different force coefficients are extracted from the force time series for the comparisons. The technique for extracting the coefficients is discussed in the post-processing section. One coefficient is for the force that is in phase with and linearly proportional to the acceleration. This is considered an added mass force, and the coefficient is labeled A . The second coefficient is in phase with and linearly proportional to the velocity. This is considered a linear damping force, and the coefficient is labeled Bl . The last coefficient is in phase with and quadratically proportional to the velocity (with an absolute value). This is considered a quadratic damping force and is labeled Bq .

Figure 8.13 shows how these coefficients vary for a particular forced oscillation based on the time step used. The added mass coefficient is very close to constant across all time steps. There is some slight variation in the linear damping coefficient, and a little more noticeable variation in the quadratic damping coefficient. Both damping terms seem to stabilize with a time step of 0.001 s. This time step correlates to a maximum Courant number of about 0.7.

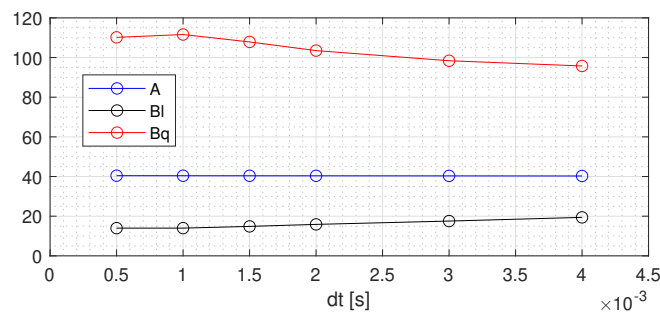


Figure 8.13: Time step convergence study using low KC number oscillation
 A [N-s²/m]; Bl [N-s/m]; Bq [N-s²/m²]

When examining the trends of the three coefficients on a distributed level for each elevation layer, there is less of a uniform pattern. In order to make run times feasible for the time frame of the project a time step of 0.002 s was used. This results in a maximum Courant number of about 1.3, which given the numerical schemes used should be acceptable. It does however likely add to the discretization error, and adds uncertainty to the results of the CFD study.

8.1.4 Initial and Boundary Conditions

The solutions for each variable for each time step are based on the solutions from the previous time step. At the start of a simulation each cell must be assigned an initial condition for each variable. In OpenFOAM these

initial conditions are dictated by files written in a time directory called “0”. When using the overset method there are two OpenFOAM directory structures, one for the overset domain and one for the background domain. The structure for the overset domain is only used to set up the mesh and cell assignments of the overset domain. After this has been completed the results are loaded into the background directory all necessary information about the simulation is accessed from this background structure. This is where the “0” directory is located.

The variables in cells are calculated not only based on the previous value in the same cell, but also based on the values of the neighboring cells. At the extends of the domain, or the boundaries, no neighbor cells exist outside of the model. At these locations boundary conditions are instead imposed, dictating conditions about the variable at the boundary. These boundary conditions are also implemented through the files in the “0” directory.

A brief description of the initial and boundary conditions for each required variable is provided in Appendix G.1.

8.1.5 Parallel Processing

The simulations are run in parallel on multiple processors to decrease computation time. There are a number of ways to decompose a simulation into a parallel task. Decomposition can either be structured, and defined by the used before the simulation, or unstructured. In this project a basic Simple decomposition was considered. For this method, three numbers are specified which dictate the number of partitions in each direction. The mesh is broken up prior to starting the fluids calculations, and certain cells are assigned to each processor. The processors then work at the same time reducing the total calculation time.

While sharing the work load reduces the computation time, there is some added cost of communication between the processors. When the number of processors is small the communication time is very small relative to the solution time, however as the number of processors grows this becomes more significant, and the added benefit of additional processors reaches some limit.

For different problems and meshes different partitioning of the domain may also be more effective. Different arrangements were tested for a short number of time steps to compare the efficiencies. Figure 8.14 shows the computation time per time step for ten different decomposition settings. The three numbers in the legend entries indicate the number of divisions in the x, y, and z directions respectively. The computation rates are then plotted against the total number of processors needed for each division. In general the greater the number of processors the lower the time, however with diminishing returns. For a given number of processors it was found that for this mesh two sections in the z direction and only one section in the y direction, with a larger number of divisions in the x direction was the most efficient approach.

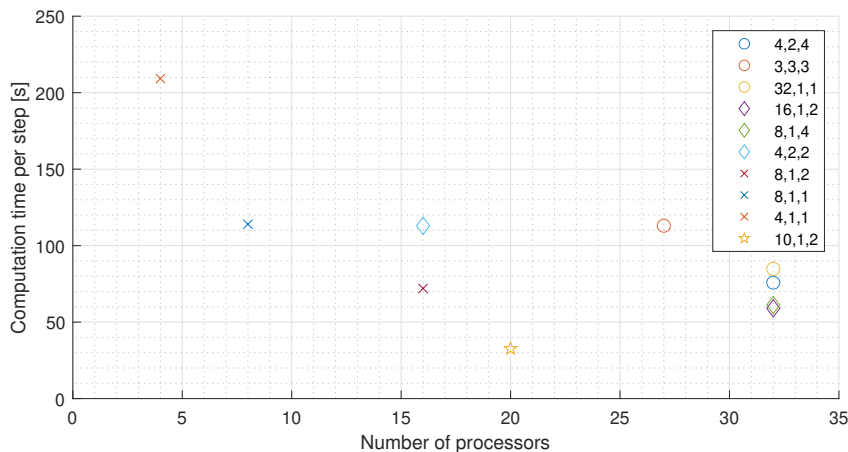


Figure 8.14: Simple decomposition parallel processor arrangements

The “10,1,2” division shown with the yellow star should not be compared with the other settings; it was run in the background while the others were run on an interactive node which gave it a small time advantage. The consensus from the other tests is to use a large number of x divisions with only one and two y and z divisions. The nodes which were the most readily available to use had a limit of 20 processors per job. Thus the “10,1,2” setting was selected, and its working speed is included on the plot for reference. More complicated decomposition techniques could be studied to further reduce computation time.

8.2 Test Matrix

As found in table 8.1 the potential KC numbers the platform will see range from 0.1 to 6.0. There are more expected KC numbers in the lower end of the range, so more resolution is desired there. The maximum KC number tested is 6.0, and there is an exponential pattern with a base of $\frac{1}{2}$. Originally seven cases were chosen with a minimum KC number of just below 0.1, but after setting up the time domain model one additional lower KC number case was added just below 0.05. The parameters of the forced oscillation cases can be seen in table 8.3. Each case uses a forced motion with a simple regular sinusoidal function.

Test Name	KC	A [m]	f [Hz]	Expected Separation	Expected Vortex Shedding
<i>fo0</i>	0.04688	0.00280	8.971	No	No
<i>fo1</i>	0.09375	0.00560	4.486	No	No
<i>fo2</i>	0.1875	0.0112	2.243	No	No
<i>fo3</i>	0.375	0.0224	1.121	No	No
<i>fo4</i>	0.75	0.0448	0.561	No	No
<i>fo5</i>	1.5	0.0895	0.280	Maybe	No
<i>fo6</i>	3.0	0.179	0.140	Yes	No
<i>fo7</i>	6.0	0.358	0.070	Yes	Unlikely

Table 8.3: Single forced oscillation CFD test matrix

For a given KC number only one amplitude is possible for a given body, but many combinations of frequency and maximum velocity are possible. Holding one of these variables constant while varying the other to achieve the desired KC number is a logical method. If the velocity is held constant then the maximum Reynolds number of the flow is the same for every case, which isolates the impact on the loads to the KC number, and not potential changes in the Reynolds number regime. If the frequency is held constant then the period will also remain constant, and the simulation time for a certain number of oscillations will be the same for each case. This could be advantageous as the frequency could be set high enough to avoid very long simulation times. If the frequency is constant it also means that the potential flow coefficients (added mass and linear damping) would be constant. This means that all differences in the resulting loads can be attributed to viscous effects and not potential flow.

A constant maximum velocity was selected to keep the maximum Reynolds number constant. This is predicted to be the best way to isolate the influence of the KC number. The potential flow solutions will be subtracted from the results either way, so using a constant frequency seems less important than a constant Reynolds number. The maximum velocity was selected so that the frequency of the largest KC number case (*fo7*) would be equal to the surge natural frequency of the platform. This results in a maximum velocity of 0.158 m/s.

Table 8.3 also shows some predictions about what flow phenomenon might be present in each case. Both the expected presence of separation and vortex shedding are based on the KC number. Separation would occur for steady flow, and is expected to occur for the larger KC number cases, where there will be periods of time with a somewhat quasi-steady type flow. It is expected that for the lower KC number cases the relative motion is not long enough the flow to separate. The effect of separation is expected to significantly change the nature of the forces on the body. An organized vortex street would not be expected for steady flow at this Reynolds number [14]. It is possible, however not expected, that the unsteadiness of the flow could lead to a more organized vortex shedding, as the critical Reynolds number and transition length are both reduced for an oscillatory motion. However even if the Reynolds number was higher, at a KC number of 6.0 it is still unlikely that a vortex shedding pattern could develop.

From these forced oscillation cases functions will be developed to determine what the viscous correction coefficients should be depending on the local KC number of the flow. In a real environment, as well as in the model tests and in the time domain model, there are typically flows with different KC numbers superimposed on each other at any given time. This could be due an irregular wave field with waves of different amplitudes as well as platform motions with various amplitudes. Likely many different waves and degrees of freedom of platform motion will occur at the same time.

Linear potential flow effects at various frequencies can be simply superimposed on each other. Viscous flow effects are more complicated, and a similar approach likely does not accurately predict the combined flow effects. If, for example, two flows occur at the same time, one with a KC number of 2.0 and one with a KC number of 5.0, it is not known whether the viscous correction coefficients resemble the coefficients associated with 2.0, 5.0, somewhere in between 2.0 and 5.0, or something different entirely.

A second set of CFD simulations are used to help determine this relationship. In an effort to isolate the effects of combining two different KC number flows, and not to introduce any other variables, the combined

cases are simply built out of the single forced oscillation cases. The low-frequency surge motions are the main point of interest, so all combined cases are a superposition of the largest KC number case and one other KC number case. The resulting test matrix is shown in table 8.4. For the test names, *cf* stands for combined forced oscillations, and the two numbers indicated which of the single forced oscillation cases have been combined. Predictions are again made for whether or not separation and or established vortex shedding can be expected. Since all cases include the large amplitude, 6.0 KC number, motions, separation is expected to occur for all cases. Again an organized vortex shedding pattern is very unlikely to form for any of the cases. It is even less likely than what was discussed for the single forced oscillation case, *fo7*, as the lower amplitude higher frequency motion will disturb patterns that take time to develop.

Test Name	KC ₁	A ₁ [m]	f ₁ [Hz]	KC ₂	A ₂ [m]	f ₂ [Hz]	Expected Separation	Expected Vortex Shedding
<i>cf017</i>	0.09375	0.00560	4.486	6.0	0.358	0.070	Yes	Unlikely
<i>cf027</i>	0.1875	0.0112	2.243	6.0	0.358	0.070	Yes	Unlikely
<i>cf037</i>	0.375	0.0224	1.121	6.0	0.358	0.070	Yes	Unlikely
<i>cf047</i>	0.75	0.0448	0.561	6.0	0.358	0.070	Yes	Unlikely
<i>cf057</i>	1.5	0.0895	0.280	6.0	0.358	0.070	Yes	Unlikely
<i>cf067</i>	3.0	0.179	0.140	6.0	0.358	0.070	Yes	Unlikely

Table 8.4: Combined forced oscillation CFD test matrix

Both oscillations are prescribed with no initial phase shift, and both oscillations follow a simple sinusoidal pattern. The result is a bichromatic wave pattern motion. The functions of viscous correction coefficients to be implemented in the time domain model come only from the single forced oscillation cases. The combined forced oscillation cases are used to determine how the functions should be implemented.

9 Post-Processing

The post-processing choices operate under the assumption that the forces on the body come in three forms. The first two are associated with the potential flow solution. There is a force which is in phase with and linearly proportional to the acceleration, called an added mass force. There is a force which is in phase with and linearly proportional to the velocity, called the linear damping force. While both of these forces are present in a potential flow solution, it is possible that viscous effects lead to some differences in them. The third force type is in phase with but quadratically proportional to the velocity, and is called a quadratic damping. This force correlates to the typical definition of a drag coefficient, which is multiplied by the square of the velocity for a steady flow, and is not present in a potential flow solution. Throughout the analysis the three forces are referenced with coefficients called cA , cBl , and cBq , for the added mass, linear damping, and quadratic damping respectively.

The dynamic motions in OpenFOAM are prescribed as positive sine waves with no phase offset. The velocity is then a positive cosine with no phase offset, and the acceleration is a negative sine with no phase offset. The forces on the body are due to the relative fluid motion and are thus in the opposite direction. The three viscous correction forces then follow Equations (63), (64), (65).

$$F_{cA} = cA \sin(\omega t) \quad (63)$$

$$F_{cBl} = -cBl \cos(\omega t) \quad (64)$$

$$F_{cBq} = -cBq \cos(\omega t) |\cos(\omega t)| \quad (65)$$

In the frequency domain, each of the forces appear differently, which enables them to be separated. A positive cosine wave in the time domain correlates to a positive real value in the frequency domain, and a positive sine wave in the time domain correlates to a negative imaginary value in the frequency domain. The forces in phase with the acceleration then have imaginary frequency components and the forces in phase with the velocity have real frequency components. This leads to the separation of the cA force from the other two forces, but does not help separate the two damping forces.

In order to dissect the damping force, Fourier series coefficients are used. The Fourier series shown by Equations (66), (67), and (68) approximates any function, $f(t)$, with pure sinusoidal signals.

$$f(t) = \frac{a_0}{2} + \sum_{n=1}^{\infty} (a_n \cos(\omega n t) + b_n \sin(\omega n t)) \quad (66)$$

$$a_n = \frac{\omega}{\pi} + \int_0^{\frac{2\pi}{\omega}} f(t) \cos(\omega n t) dt \quad (67)$$

$$b_n = \frac{\omega}{\pi} + \int_0^{\frac{2\pi}{\omega}} f(t) \sin(\omega n t) dt \quad (68)$$

For the linear forces (cA and cBl) this simply results in exactly Equations (63) and (64), with oscillations only at the original frequency of ω . The quadratic damping force however can be expressed by a series of linear components with higher frequencies. For this force all values of B_n are equal to zero (there is still no part in phase with acceleration). All A_n values with an even number of n also are zero, but each value of A_n with an odd numbered n has a non-zero coefficient. The first four non-zero coefficients are: $A_1 = \frac{8}{3\pi}$, $A_3 = \frac{8}{15\pi}$, $A_5 = \frac{-8}{105\pi}$, and $A_7 = \frac{8}{315\pi}$. When looking at the forces in the frequency domain, these higher frequency components of the quadratic force can be used to separate the linear and quadratic damping.

A fast Fourier transform is used to find the frequency spectrum. The real and imaginary parts are split for the velocity and acceleration dependent forces respectively. Next both real and imaginary parts are filtered by frequency with a simple band-pass filter. The bandwidth used for the filter is equal to one quarter of the oscillation frequency. The imaginary part is only filtered only for the oscillation frequency, while the real part is filtered for the first, third, and fifth multiples of the oscillation frequency. The proportion of the force which is filtered out with this process is of interest. If a large amount of the frequency spectrum is not at these expected frequencies, it indicates that the chosen description of the forces is not accurate. To capture this quantity the

integral of the filtered spectrum is divided by the integral of the unfiltered spectrum. This percentage is stored for each elevation layer and each period to measure the fit.

The first multiple of the oscillation frequency contains input from both the linear and the quadratic forces, but the third and fifth multiples theoretically only contain input from the quadratic force. The expected ratios of A_1 , A_3 , and A_5 are used to calculate the quadratic contribution to the first multiple based on the values of the third and fifth multiples. The two estimates are then averaged, with more weight on the estimate from the third multiple, as it is less subject to noise with a larger amplitude. The remaining portion of the first multiple is then associated with the linear damping force. The frequency components are then grouped by which force they are associated with, and brought back to the time domain with an inverse fast Fourier transform.

The amplitudes of the three separated forces are normalized by either the acceleration, velocity, or velocity squared resulting in the desired coefficients. Figure 9.1 shows a simplified flow chart of the coefficient extraction.

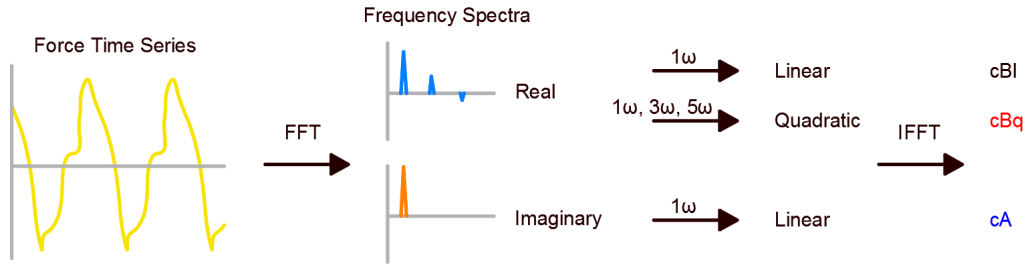


Figure 9.1: Coefficient extraction schematic

The force time series recorded from the CFD contain the potential flow radiation forces as well as the viscous correction forces. The potential flow force is a function of frequency. The hypothesis of this project is that the viscous correction forces should be thought of as a function of KC number and not of frequency. There is no way for the potential flow components to not appear in an oscillatory flow CFD simulation, so they need to be subtracted from the force to determine the viscous component dependent on the KC number.

The viscous correction forces are calculated separately for each elevation layer. In order to subtract only the potential flow force corresponding to a particular layer, the potential flow solution is needed for the distributed model. The simulations originally performed in HydroD only looked at the body as a whole. To determine the distributed properties for each elevation layer a separate analysis was performed.

A new panel model was built with the same parameters as previously used, except with clean divisions at the intersections of the elevation layers (no panels are a part of multiple layers). The pressures from all panels in a given layer are then integrated to determine the combined force for the layer. Only the pressures from radiation are relevant for the still water forced oscillations. WAMIT (version 6.4) was used for the calculations since it gives the ability to look separately at the radiation pressures. Only a first order analysis was performed, and only the frequencies present in the forced oscillation cases were considered.

To verify that the results of the distributed analysis agree with the original potential flow results, the added mass and linear damping for all layers are summed and compared with the original HydroD coefficients. Figure 9.2 shows the summations from WAMIT with red stars on top of the previously found functions.

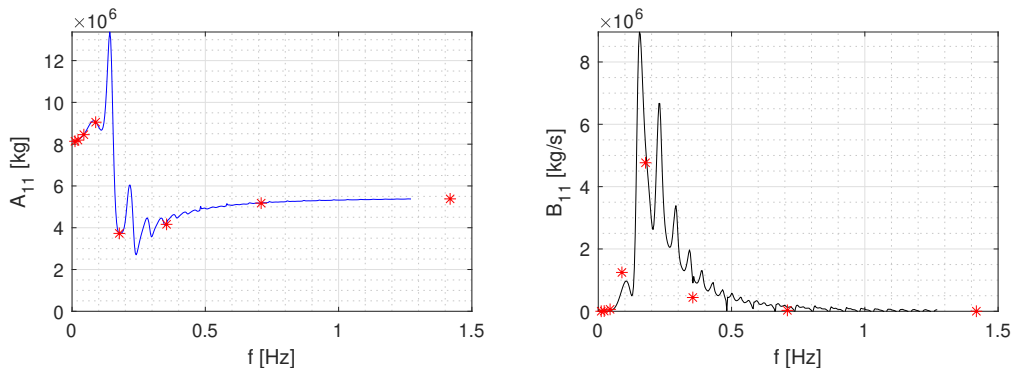


Figure 9.2: Added mass and radiation damping comparison between distributed results from WAMIT (red stars) and total body results from HydroD (blue and black lines)

The added mass shows very good agreement between the two sets of results. The radiation damping has significant differences, notably at the frequencies correlating to cases $fo2$ and $fo4$. The reason for the difference in

the results has not been found. It is expected that this could contribute significant error in the post-processing. Even small differences in the potential flow coefficients could wrongly appear as large viscous flow effects.

9.1 Single Forced Oscillations

An established flow field takes some time to develop in each simulation. It may take many oscillations for the flow pattern to stabilize, and thus for the force coefficients to stabilize. To determine if enough oscillations have been run, the coefficients are calculated with each successive period, and compared from one period to the next. Since the motion is prescribed, the exact period is known, and the time series can easily be broken into separate time series for each period.

The final coefficients selected for a each KC number are the mean values of the last three oscillations. The standard deviation of these three values is also recorded as a measure of the uncertainty of the stability of the coefficient.

Two approaches can be used for the extraction of the viscous correction coefficients. The first approach takes the full force from OpenFOAM and calculates the three coefficients. Then the potential flow coefficients are subtracted, leaving the viscous correction coefficients, which are only dependent on KC number. These corrections include the quadratic damping, as well as some correction of the added mass and linear damping. This is called the full force method.

The second approach is to subtract the predicted potential flow force before extracting the coefficients. A force time series is calculated for each elevation layer based on the prescribed motions and the distributed potential flow values. The difference between the full force time series and this potential flow time series forms what is called the viscous correction force. The coefficients are then extracted only from this signal. This is called the subtraction method.

The full force method shows better agreement between the force signal and the three force type description. The percentage of the frequency spectra captured in the filtered spectra correlating to the three force coefficients is very high. This is because the potential flow estimates do a good job of capturing the force. The potential flow part of the force dominates, especially for the low KC number cases. This is good to see, and adds confidence to the results of the CFD study, however it covers up what the study is really interested in, which is the small differences from the potential flow force.

Figure 9.3 shows the three coefficients as a function of KC number when calculated using the full force method. The added mass is blue, the linear damping is black, and the quadratic damping is red. The plot shows the coefficients before the potential flow components are subtracted. The “o” marks are the coefficients calculated from the CFD results, and the “*” marks are the potential flow coefficients. Error bars are included on all of the calculated coefficients, and the size of the error bar is equal to the standard deviation of the coefficient over the last three oscillations. The y-axes are too small to fit the units of all three coefficients. For this plot and all similar following plots the units of cA are $[\text{N}\cdot\text{s}^2/\text{m}]$, the units of cBl are $[\text{N}\cdot\text{s}/\text{m}]$, and the units of cBq are $[\text{N}\cdot\text{s}^2/\text{m}^2]$.

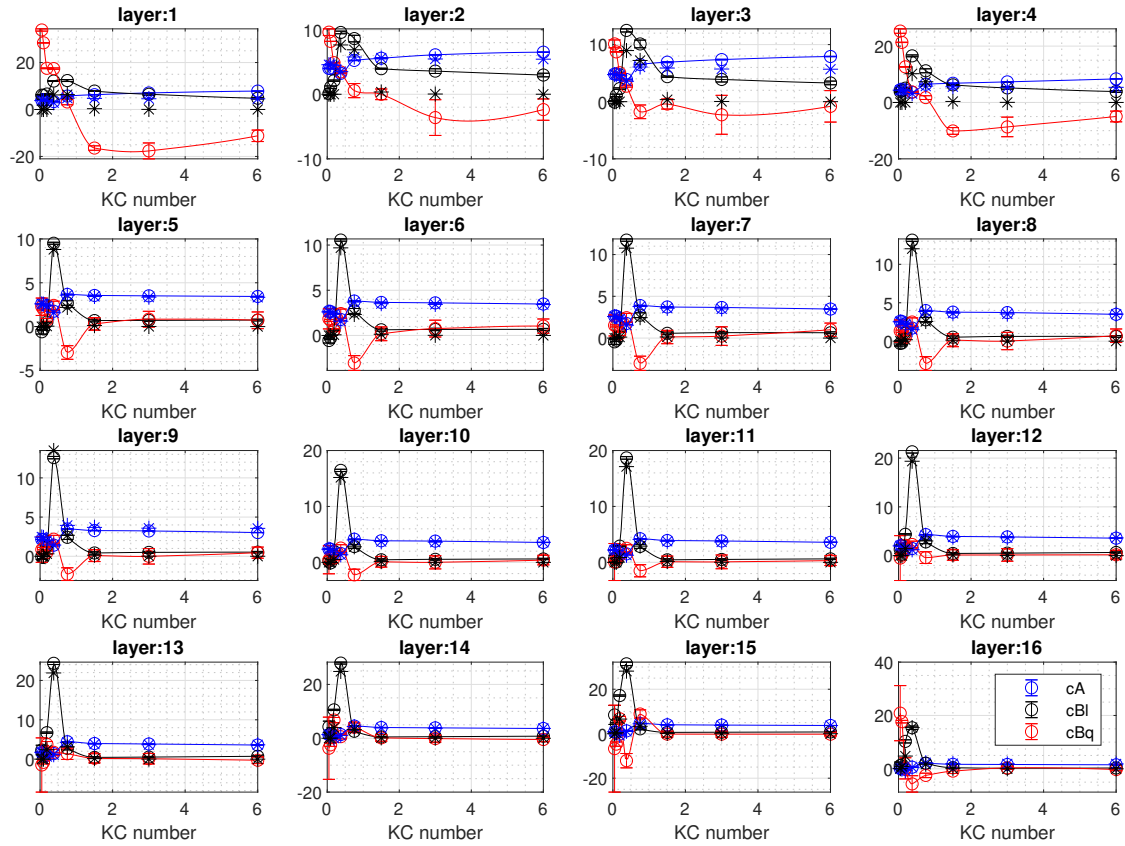


Figure 9.3: Force coefficient functions found using the full force method
 cA [$N\cdot s^2/m$]; cBl [$N\cdot s/m$]; cBq [$N\cdot s^2/m^2$]

Some interesting things to note are the generally good agreement between the potential flow coefficients and the values of cA and cBl found in layers 5-16. These layers make up the column, where separation does not occur for the lower KC numbers. The agreement in layers 1-4 which make up the pontoon is much worse. The sharp corners of the pontoon cause immediate separation and more drastic changes to the flow. It should also be noted that the quadratic damping is negative for a number of the high KC numbers on the pontoon, and for $fo4$ (Kc number = 0.75) on the column. The quadratic damping in theory is only due to separated drag and should always be positive. This negative value is likely not physical but due to the method of extraction. The quadratic damping sign and magnitude are determined based on the third and fifth multiples of the oscillation frequency in the frequency spectrum. The magnitudes of these values are much smaller than the value at the oscillation frequency, and are much more sensitive to noise in the data. When the quadratic damping value is determined to have some significant negative value, this also influences the calculated value of the linear damping. In order to balance the energy at the oscillation frequency, the linear damping will in turn be found to have a large positive value to counter the negative value of the quadratic damping. This is likely a contributing factor to why the value of cBl significantly exceeds the potential flow prediction for the high KC numbers on the pontoon.

Figure 9.4 shows viscous correction coefficients that would be determined from this method. This is the difference between the coefficients of the full force, and the potential flow coefficients (for the quadratic damping there is no potential force component).

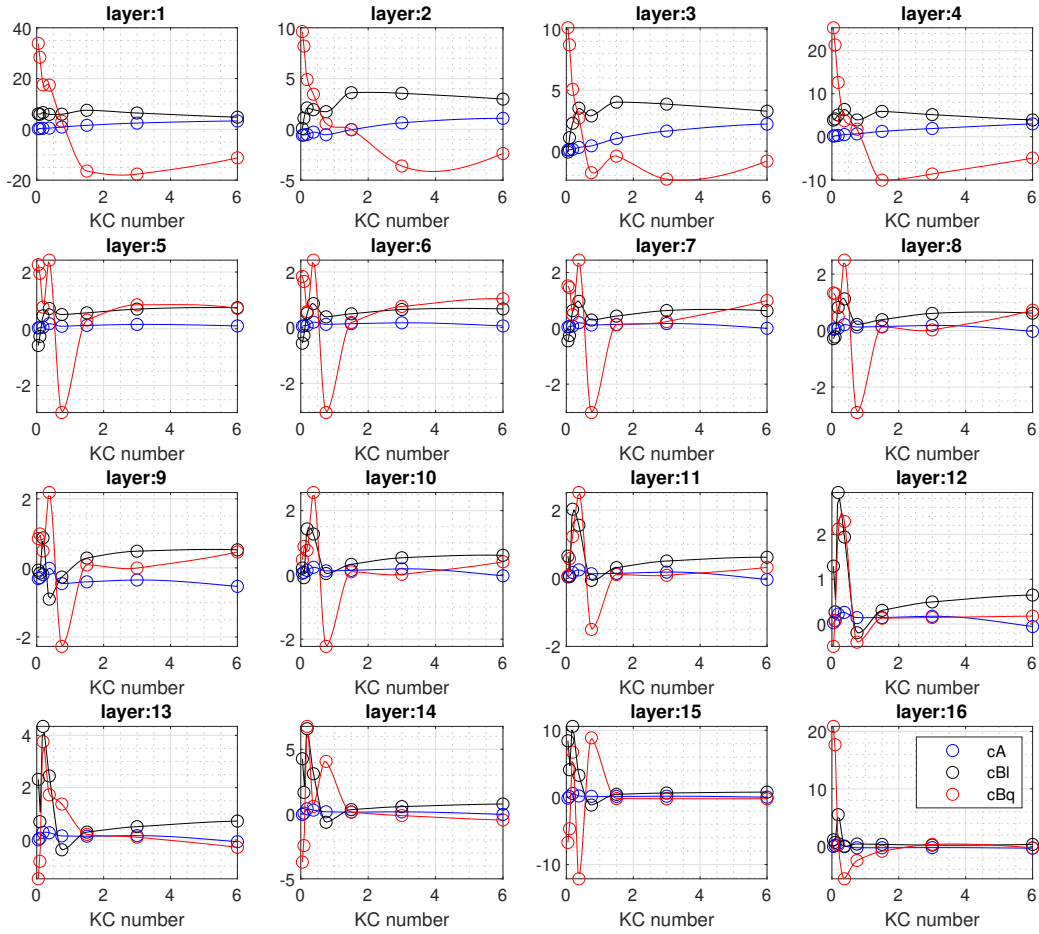


Figure 9.4: Viscous correction coefficient functions found using the full force method
 cA [$N\cdot s^2/m$]; cBl [$N\cdot s/m$]; cBq [$N\cdot s^2/m^2$]

Although the theory suggests that the forces in phase with the velocity will either be linearly or quadratically proportional to the velocity, other relationships are also looked for in the data. Unexpected spectral values at the third and fifth frequency indicate that the force signal is not made fully of the expected components. Forces which are in phase with the velocity should also depend on the direction of the velocity. Thus for any velocity proportionalities with an even numbered exponent an absolute value is included, as it is for the quadratic term.

A force that is proportional to the velocity to the power of three would have components only at the first and third multiples of the oscillation frequency. A force that is proportional to the velocity to the power of four would again have components at all odd numbered multiples of the oscillation frequency. The Fourier series coefficients were compared with the frequency spectra of the force in phase with velocity, and no force description seemed match the patterns better than quadratic.

It was determined that for some cases the method of splitting the linear and quadratic damping by means of the third and fifth frequencies is not reliable. When considering the full force, it is difficult to separate the two components in another way.

The subtraction method offers different possibilities. In the subtraction method the predicted potential flow force time series is subtracted before the coefficient extraction. Appendix H contains time series plots for each single forced oscillation case. The plots include the original full force recorded in OpenFOAM for each layer, the predicted potential flow force for each layer, and the difference between the two, the viscous correction. This difference time series provides good information prior to the coefficient extraction. The relative amplitude of the viscous correction is much larger for the high KC number cases than for the low KC number cases. The difference typically lags the potential flow signal, meaning that it is closer to in phase with the velocity and the potential flow signal is closer to in phase with the acceleration.

Figure 9.5 shows the correction coefficients found with this method. Comparing this figure with Figure 9.4 shows the results are almost identical to the results of the full force method. It does not matter whether the

potential flow component is subtracted before or after the extraction of the coefficients.

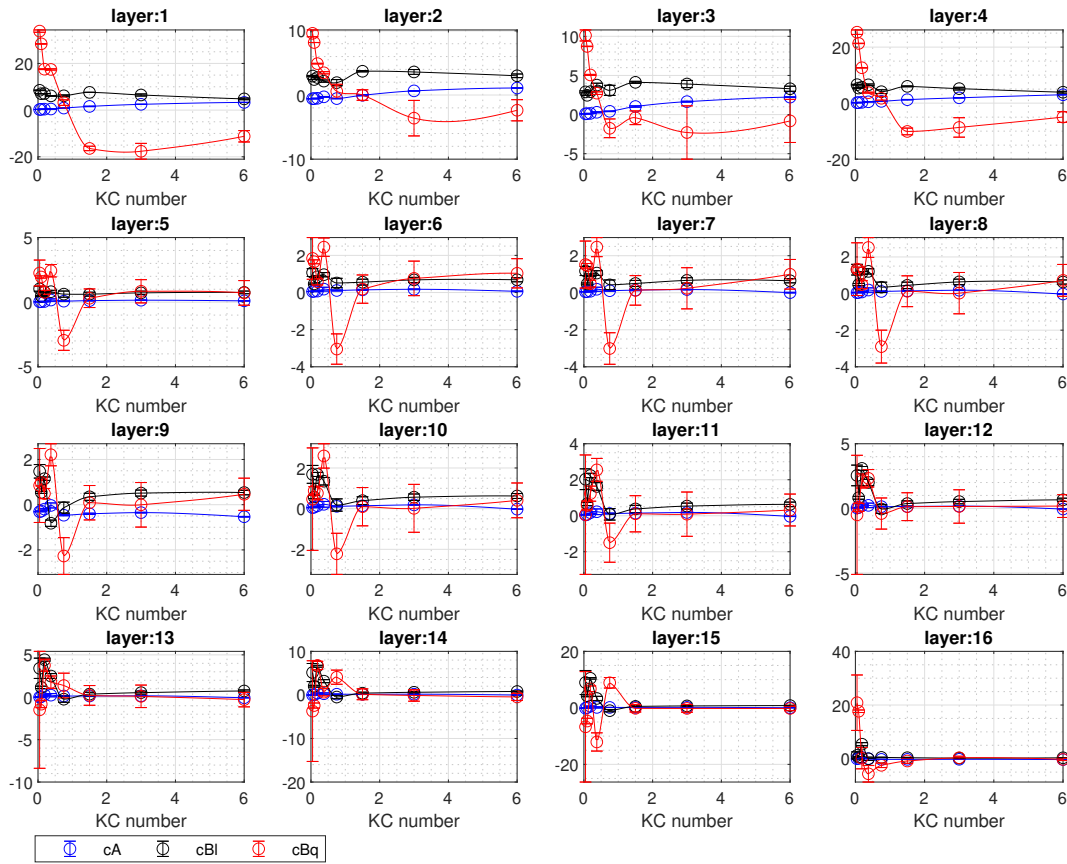


Figure 9.5: Viscous correction coefficient functions found using the subtraction method
 cA [$N\cdot s^2/m$]; cBl [$N\cdot s/m$]; cBq [$N\cdot s^2/m^2$]

Again the negative values of quadratic damping do not well represent the physics. Any negative value in phase with the velocity should likely be attributed to a difference in the linear damping from the potential flow coefficient.

When the potential flow components are subtracted first, the separation of the linear and quadratic damping can be approached differently. The signal used in the subtraction method is only the viscous correction signal. This could potentially be made of both a quadratic drag and also a viscous change to the linear damping, or it could be only one or the other. In the frequency domain the dominant value of the oscillation frequency could be fully attributed to either linear or quadratic damping. Figure 9.6 shows what the coefficients would be if all of the force in phase with velocity is considered only either linear or quadratic. This is referred to as the only linear or only quadratic selection method. The trends of the cBl_{Only} and cBq_{Only} coefficients are thus the same, but scaled by the maximum velocity, as their respective proportionalities are with the velocity and the velocity squared.

Appendix H contains coefficient convergence plots for each single oscillation case. The plots show the value calculated for each coefficient for each successive oscillation. These demonstrate how stabilized the solution is. Six coefficients are tracked. All coefficients come from the force subtraction method. The first three coefficients are the three coefficients calculated with the damping splitting technique using the third and fifth frequencies. The next three coefficients are calculated using this second approach where all damping is attributed to either linear or quadratic.

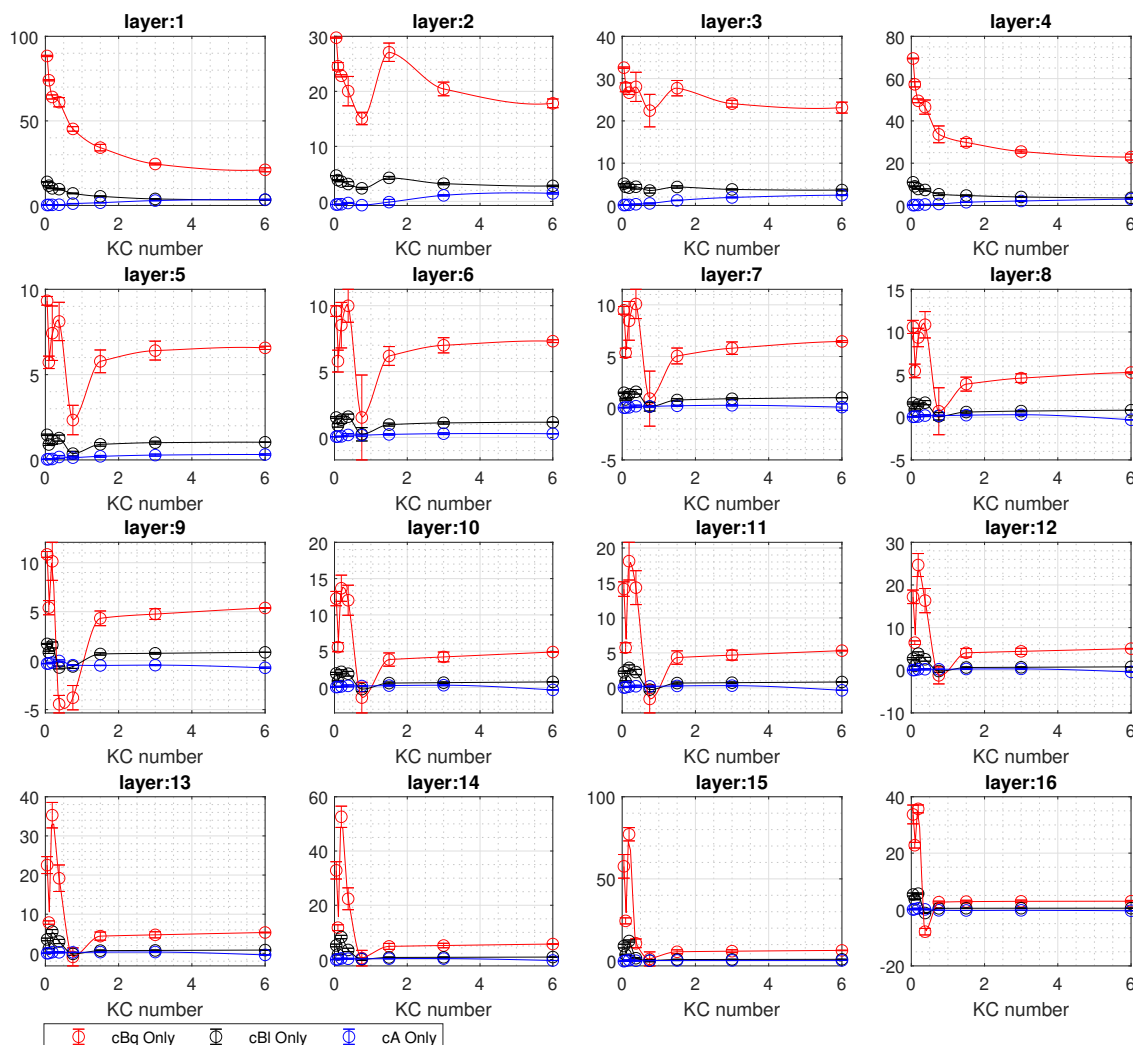


Figure 9.6: Viscous correction coefficient functions found using the subtraction method and only linear or quadratic damping selection
 cA [$N\cdot s^2/m$]; cBl [$N\cdot s/m$]; cBq [$N\cdot s^2/m^2$]

The trends using this method show clear distinction between the parts of the structure. The trends in layer 1 and layer 4, both the sharp corners of the pontoon are very similar. The trends in layer 2 and layer 3, both the walls of the pontoon, are also very similar. The trends in each of the layers of the column are also quite similar, with changes gradually appearing near the free surface. The value of $cBqOnly$ in the layers of the column starts to stabilize for KC numbers higher than 1.5. This is roughly when separation is expected to start to occur for the column.

Again for fo_4 with a KC number of 0.75 a negative value must come from either a linear or a quadratic damping. As a negative quadratic drag force is not physical this is best attributed fully to the linear coefficient.

The differences between the potential flow radiation damping found in the distributed analysis with WAMIT and the total body analysis with HydroD are possibly relevant. These differences were shown in Figure 9.2, and were most pronounced for the frequencies corresponding to fo_1 , fo_2 , fo_3 , and fo_4 . A more thorough convergence study was performed for the HydroD analysis, and more there is more confidence in these results, although they cannot be used on an elevation layer level. The negative viscous correction damping value found in fo_4 could be largely attributed to the underestimation of the radiation damping from the WAMIT analysis. The large positive viscous correction damping values found in fo_1 , fo_2 , and fo_3 could similarly be partially attributed to the overestimation of the radiation damping at these frequencies. Unfortunately it is not known whether the discrepancy in the potential flow damping term is spread over the whole body, or is only due to differences in a few elevation layers. It is however likely that the effect is most pronounced near the free surface, where the impact on radiated waves is the largest.

Where the possible error in the potential flow calculations is large, it is more logical to assume that the

damping correction should be assigned a linear relationship. While better than attributing this error to a quadratic drag force it is still not good. The goal of the analysis is to separate the KC number dependent forces (due to viscous effects) from the frequency dependent forces (due to potential flow effects). The linear damping viscous correction for these cases is likely more characteristic of the frequency of the oscillation and not of the KC number.

For the low KC number cases treating the damping as linear is theoretically not a bad choice for columns, where separation is not expected. On the pontoon however, separation is immediate, and quadratic drag should be present even at very low KC numbers. It is also likely that the viscous flow effects do change the predicted values of the linear damping as well for the pontoon. Thus some combination of the linear and quadratic damping viscous correction coefficients should be used. This is possible with the use of the original splitting method based on the third and fifth frequencies.

It was decided that some composite functions should be selected utilizing different techniques at different elevations for the different KC numbers. Table 9.1 explains some reasoning for the choices, and the final selection of how the coefficients will be treated. For each KC number the decision is made separately for the layers of the pontoon and the layers of the column. The decision is based on two factors: whether or not separation is evident when examining the flow field and how strong the spectral agreement is for the frequency method of splitting linear and quadratic components. If separation is evident then quadratic damping must be included. If the spectral agreement is strong, then it could be reasonable to use the frequency based splitting technique.

		$fo0$	$fo1$	$fo2$	$fo3$	$fo4$	$fo5$	$fo6$	$fo7$
KC number		0.047	0.094	0.188	0.375	0.75	1.5	3.0	6.0
Flow Field Separation	Pontoon	yes	yes	yes	yes	yes	yes	yes	yes
	Column	no	no	no	no	no	unclear	yes	yes
Spectral Agreement	Pontoon	yes	yes	yes	yes	no	no	no	no
	Column	no	no	no	no	no	no	no	no
Coefficient Treatment	Pontoon	0	0	0	0	2	2	2	2
	Column	1	1	1	1	1	2	2	2

Table 9.1: Single forced oscillation coefficient treatment selection

A “0” for the treatment means that the original frequency based splitting is used, a “1” for the treatment means that the linear only technique is used, and a “2” for the treatment means that the quadratic only technique is used.

Visualizing separation can be difficult at the onset. Separation begins at the location with the highest adverse pressure gradient, which for a cylinder is at the furthest downstream location. It then moves further upstream with time, and a wake region forms. Initially this can be hard to detect, and examining the boundary layer is the best way to be sure of separation. A separated boundary layer will have some region of reversed flow just above the surface. Figure 9.7 shows this for the clearly separated case of $fo7$.

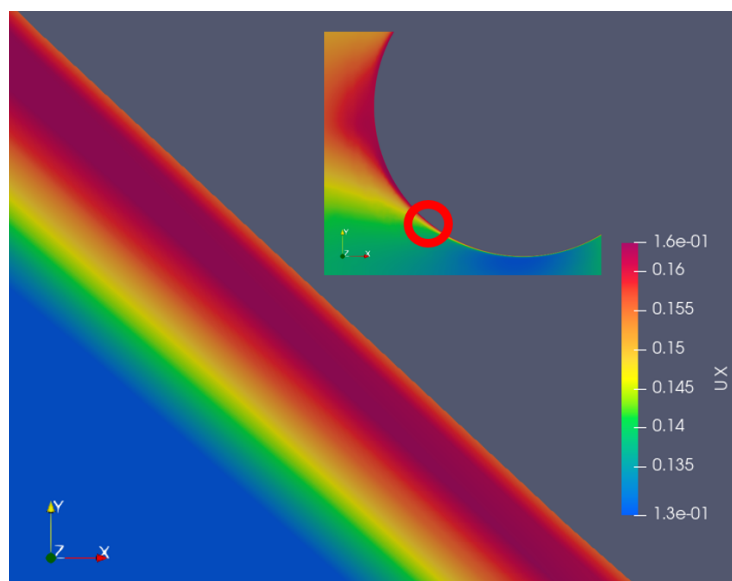


Figure 9.7: Boundary layer on the column in case $fo7$ showing clear separation

The red circle on the smaller image identifies the location of the larger zoomed image on the column. This

image is from the time of zero displacement and maximum velocity. Since the outer fluid is still and the body is moving, the velocity on the surface is not zero, but is equal to the velocity of the body, in this case 0.158 m/s in the positive x-direction (to the right in the image). The region of “reversed” flow, is then actually a region where the velocity is larger than the velocity of the body, or even further from the velocity of the outer flow than that of the body. This is evident by the band of darker purple in the image, indicating a higher velocity than the orange on the column surface.

In contrast the boundary layer is shown for the case *fo1* with a KC number of 0.09 in Figure 9.8. In this image it is shown that the velocity continually increases when approaching the column surface. This is a boundary layer with no region of reversed flow, indicating that no separation has occurred.

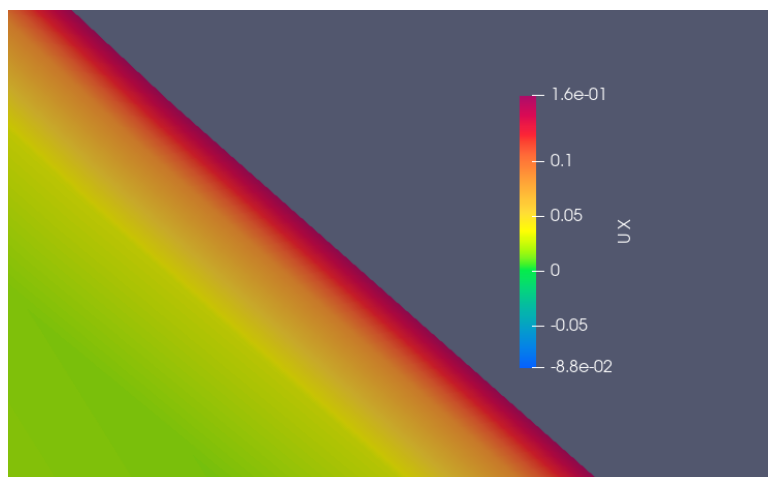


Figure 9.8: Boundary layer on the column in case *fo1* showing no separation

This approach is used to check for separation for each case. It is clear that the flow has separated for *fo7* and *fo6*. It appears that it probably has happened for *fo5*, but it is less definitive. No evidence of separation is found for any of the lower KC numbers.

The resulting composite viscous correction functions are shown in Figure 9.9. Note that for the low KC numbers the layers of the column have a value of zero for the quadratic damping, and that for the high KC numbers all layers have a value of zero for the linear damping correction.

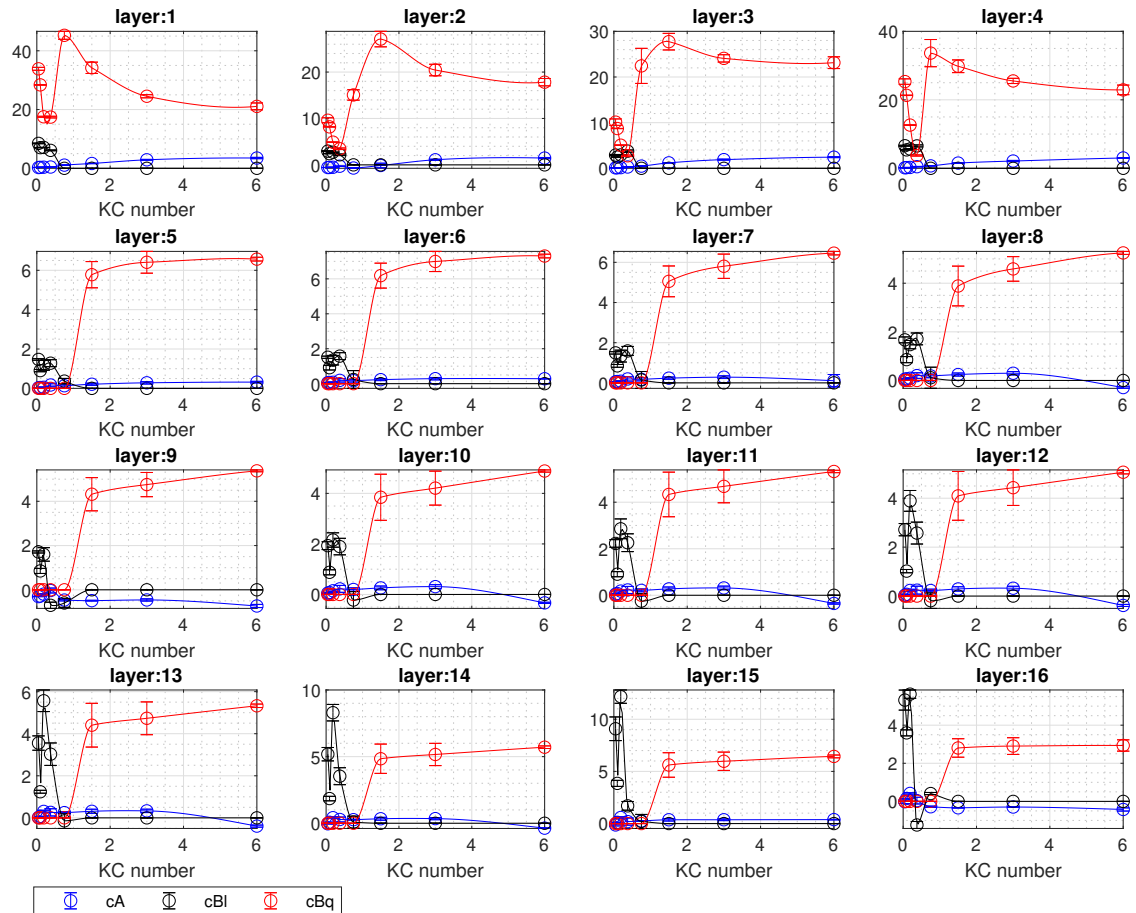


Figure 9.9: Final selection of composite viscous correction functions
 cA [$N \cdot s^2/m$]; cBl [$N \cdot s/m$]; cBq [$N \cdot s^2/m^2$]

9.2 Combined Forced Oscillations

Each of the six combined cases were run for four periods of the highest KC number oscillation. Especially for the cases with a low first KC number, this length of simulation should provide very stabilized results. Even for the higher KC number combinations such as *cf067* it appears that the results have stabilized after this number of oscillations, due to the added unsteadiness in the flow.

The results of the combined forced oscillations are not used to influence the coefficients in the viscous correction functions, but instead are used to influence how the coefficients are selected in a simulation. The combined cases are analyzed in two different ways, coefficient extraction, and force series reconstruction.

9.2.1 Coefficient Extraction

The first approach is similar to that used for the single forced oscillations. The three coefficients are extracted using the same techniques. Since the exact frequencies of the motion are known, the force can be split into a force associated with each KC number oscillation. This leads to the extraction of six coefficients, three for each component of the combination. Only the subtraction method, where the potential flow component is subtracted prior to coefficient extraction, is considered.

Appendix I contains the force time series for each of the six combined oscillation cases. The plots show the original full force as well as the decomposition into potential flow prediction and viscous correction force. The combinations with a very low KC number on top of the highest KC number are more difficult to visually analyze, as they have a very large number of the higher frequency oscillations. The large acceleration terms and low KC numbers also make the cases more closely captured by potential flow.

There are some interesting trends to note from visual inspection of the decomposed time series. When looking at *cf067* it is evident that viscous correction force is very asymmetric, with a mean offset. This is most likely due to the different drag forces in the different directions of travel, due to the asymmetric platform. The direction of motion of the larger KC number oscillation also appears to significantly impact the amplitude of the

drag force of the lower KC number oscillation. This indicates that separate coefficients for each direction may be important. In general it appears that the relative amplitude of the viscous correction force grows with the varying KC number of the combination. This is due partially to the fact that the overall forces are greater for the low KC number combinations with higher accelerations, and partially due to the fact that the viscous flow effects are more pronounced with the higher KC numbers. Other general trends are that the viscous correction force is relatively large near the free surface and on the pontoon.

The same two coefficient extraction techniques are applied in the frequency domain. The first technique splits the damping into linear and quadratic components by means of the higher frequencies. Conveniently the odd numbered multiples of the frequencies of the combined oscillations do not coincide with each other for any case. This means that the coefficients can be separately extracted for each of the two KC numbers in the combination. The second technique considers all damping to be either linear or quadratic. Appendix I also contains convergence plots of these coefficients with the successive periods. The plots track 12 different coefficients. Six are from each approach to the damping.

The third section of Appendix I shows the calculated coefficients from the combined cases in reference to the coefficients of the single force oscillation functions. Figure 9.10 below shows an example for *cfo27*. The lines show the selected composite functions from the single force oscillation post-processing. The star shaped markers show the values calculated with the splitting of the damping method, and the diamond shaped markers show the values calculated with the only linear or only quadratic damping method. The markers are placed according to the KC number that they correspond to in the combination.

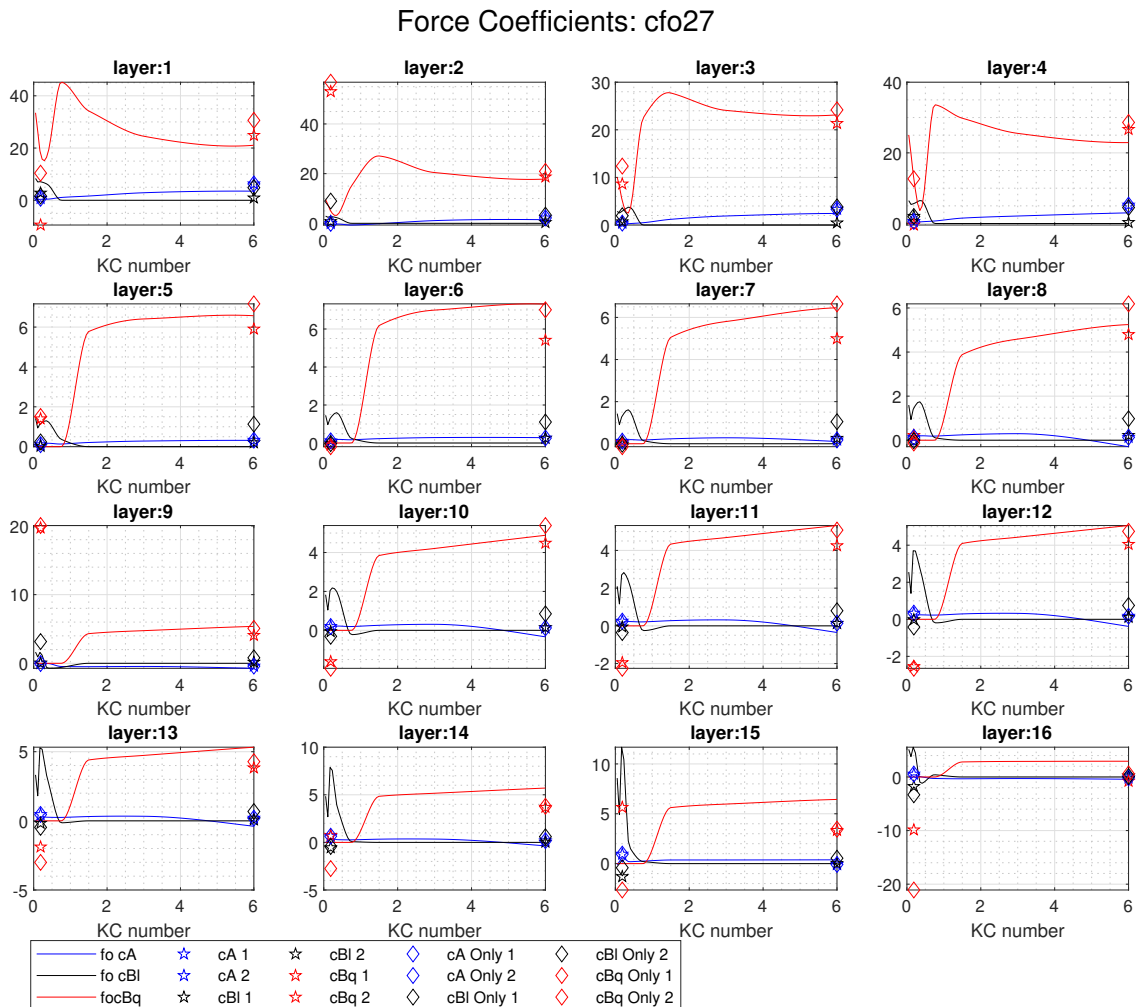


Figure 9.10: Combined case coefficient comparison with chosen functions for case: *cfo27*
 cA [N-s²/m]; cBl [N-s/m]; cBq [N-s²/m²]

The goal of these plots is to see how the addition of a second type of oscillation influences the viscous correction coefficients. This figure for *cfo27* for example shows that the coefficients of the high KC number of 6.0 are not significantly effected by the introduction of the smaller oscillation. It would be reasonable to believe that the smaller amplitude and higher frequency motions would break up the flow patterns that led to the drag

coefficients for the high KC number. However in this particular case it appears that the coefficients for the high KC number oscillation remain largely unchanged. In contrast the coefficients associated with the low KC number oscillation do appear to have significantly changed from those found with the single oscillation with the same parameters.

When comparing the plots from each of the combined oscillation cases it is difficult to detect a consistent pattern. The coefficients are not consistently similar to those of the single cases. They are also not consistently influenced by the other oscillation in a recognizable way. Similar to what was found with the single oscillation cases, it appears that quadratic coefficient at the low KC numbers is poorly predicted, and the linear damping only selection is probably more appropriate for the low end of the KC number range.

9.2.2 Force Series Reconstruction

The second approach to analyzing the results of the combined oscillation cases is to recreate the recorded force time series using the functions developed from the single oscillation cases. Different techniques of selecting the coefficients can be tested and tuned so that the predicted force best matches the CFD solution.

For this approach the known prescribed motions are used to calculate the predicted potential flow forces based on the values found in the first order HydroD analysis. The relative velocities and accelerations and velocities are already known, as the platform is moving in still water. The only thing needed to calculate the viscous correction contribution to the force is the correct coefficients to use. It would be simple to say that the motions contain two oscillations with two different KC numbers, and use these exact KC numbers to evaluate coefficients from the functions. However as found with the combined case coefficient extraction, the effects of a combined motion can change the corresponding coefficients. More importantly in the real time domain simulation, where the motions are predicted, the future motions of the platform are not known, and the past motions are more complex than a bichromatic sinusoidal oscillation. This means some method of deciding what the current KC number is at any given time step is needed. The combined oscillation cases provide good test cases for different approaches to selecting the instantaneous KC number and the viscous correction coefficients. Three methods are proposed and tested. The three methods are shown in Table 9.2 and are described in more detail below.

	IF	Spec	Amp
KC number	Single	Spectrum	Single
Dependence	Frequency Velocity	Frequency Velocity	Position
Coefficient Smoothness	Medium	High	Low
Computation Speed	Medium	Low	High

Table 9.2: KC number selection methods

The first method is called the instantaneous frequency, or “IF” method. The relative velocity is tracked throughout the time series, which in the case of the forced oscillation is only due to the velocity of the platform. The instantaneous frequency of the relative velocity is calculated using the Gabor transform method described in Section 2. This method essentially uses a fast Fourier transform to look at the frequency information of the previous signal. A Gaussian window is used to give more weight to the most recent time, and the width of this window is adjusted based on the desired significance at a certain time before the present time step. In this case it was chosen that there would be 1% significance given to the time 30 s before the current time. All times before this time are not considered in the Fourier transform to save computation cost, and they are considered irrelevant to the current instantaneous frequency. The length of this time window correlates to roughly two times the natural surge period of the platform, in order to make sure that the low frequency motions can be captured by the function. After the instantaneous frequency is known, the other component of the KC number is the maximum velocity of the current oscillation. Since the instantaneous frequency is now known, a period can be selected. The maximum relative velocity that occurred in the last period is chosen, and the instantaneous KC number is calculated. This method results in only one KC number, and the viscous correction coefficients are simply evaluated using this number and the correction functions.

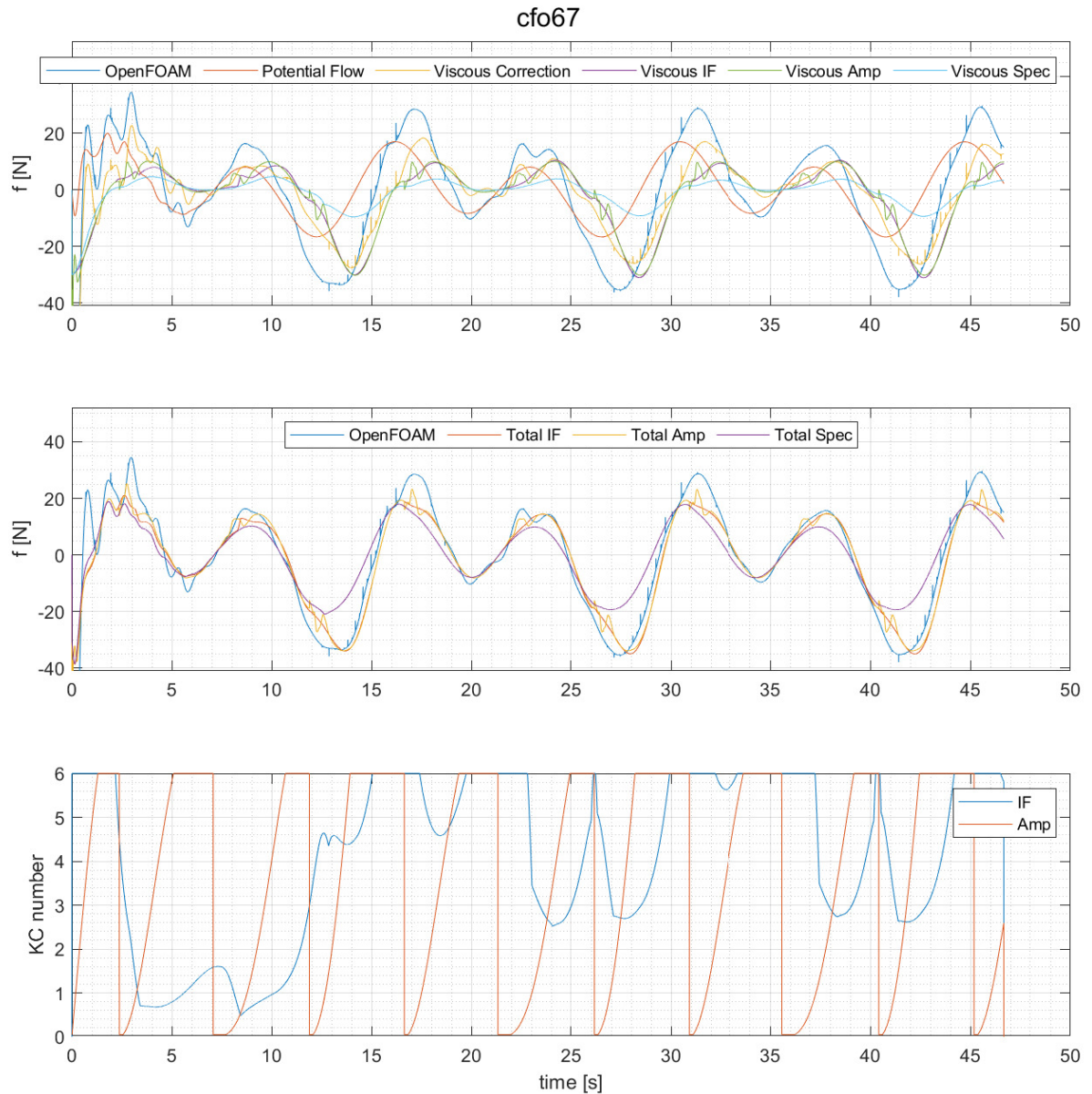
The second method is called the spectral method, or “Spec” method. This approach is to not think of a single KC number at a given time step, but to look at a spectrum of KC numbers. Then the viscous correction functions used as a sort of transfer function. The same relative velocity is tracked throughout the time series. The same Gabor transform is also used in this method to obtain a frequency spectrum weighted towards the current time. The difference is that a single frequency is not determined from this spectrum. Instead the frequency spectrum is converted to a KC number spectrum. The maximum velocity that occurred in the last period given each different frequency is used to calculate the corresponding KC number.

In this method the frequency spectrum is normalized so that the sum of the spectrum is equal to one. If the

normalized spectral value for a frequency meets a certain significance requirement (1% of the maximum value) then the coefficients are calculated for the corresponding KC number. The value of the coefficients multiplied by the normalized spectral values are summed for all frequencies. The end result is a summation for each coefficient where each contribution is weighted based on the strength of presence of a particular KC number. This method has the ability to capture more intricate changes in the viscous correction functions, since the KC numbers are not blended together into a single KC number. The method is considerably slower than the IF method. This is because the correction functions need to be evaluated potentially thousands of times for every time step.

The third method is called the amplitude method, or “Amp” method. This approach is the simplest and by far the quickest to operate. Similar to the first method it finds only a single KC number. The method uses the root of what a KC number is, simply the amplitude of the oscillation compared to the body size. The relative position is tracked for each time step. Again, for oscillations in still water, this is only based on the platform motions. The amplitude of the motion is taken as the distance traveled since the last direction change. The KC number is then calculated with this value, and the coefficients are selected. The consequence of this method is that the KC number is always considered low at the start of an oscillation. This could actually provide some added benefit. The viscous flow phenomenon that drive the differences between the forces at different KC numbers take time to develop. Therefore even for a larger oscillation, it may be reasonable to view the start of the oscillation with coefficients based on an oscillation with a small amplitude. The rapidly changing KC number does lead to less steady coefficients.

Each of the three methods of coefficient selection were tested with the motions of the combined force oscillation cases. All the resulting time series can be found in Appendix J. One example is shown below in Figure 9.11 for *cf067*. The top plot shows the full recorded time series from CFD in blue. The predicted potential flow force is shown in orange, and the true difference between these two, the viscous correction, is shown in yellow. The last three signals in the top plot show the predicted viscous correction force found with each of the three methods. The second plot in the figure shows the resulting total predicted force, by adding the potential flow and viscous correction components. The third plot in the figure shows how two of the three methods interpret the instantaneous KC number. This is only shown for the IF and Amp method, since the Spec method does not select a single KC number.

Figure 9.11: Reconstruction of case: *cfo67*

The instantaneous KC number changes rapidly for the Amp method as expected. The IF method finds a slightly smoother trend for the KC number, but it still has significant changes throughout the simulation. While the viscous force is slightly more erratic for the Amp method, it is still very similar to that predicted by the IF method. The Spec method in contrast predicts by far the smoothest viscous correction force, but appears to significantly under predict the force. Both the IF and Amp methods provide reasonably large improvements to the potential flow prediction.

Somewhat similar results are found for the other five combined oscillation cases. Each of the three methods lead to some slight over-prediction of the total force in the low KC number combinations. For example in *cfo27* the correct viscous correction appears as if it would come from a reduction in the added mass term, as the potential flow estimate is roughly correct in phase, but slightly too large in amplitude. The viscous correction force found by the three methods however do not fix this force in phase with acceleration, but instead add a very small force in phase with velocity. Overall the viscous correction force for the low KC number combinations should be small, and each method does add only a small contribution.

9.3 Directional Dependence

One interesting additional consideration is the importance of the direction of motion. The platform is not symmetric about the y-z plane. This means that when considering the surge motion, the platform looks different when traveling in positive and negative x-direction. The velocity dependent drag force can then be expected to be different for the two directions of travel.

In a frequency analysis of the force, this dependence on the direction of travel appears mostly as a mean offset, or a force with zero frequency. The time series of the viscous correction force found in Appendix H do show some mean offset supporting the presence of this effect. Because a force with zero frequency does not change, it is not possible to identify a phase for the force either. This means that from the signal analysis, it is not possible to say whether this mean force is in phase with the velocity or the acceleration, or some combination. If there was a difference in the added mass force between the two directions, the difference would likely be proportional to the acceleration. If there was a difference in the damping force between the two directions it would likely be proportional to either the velocity or the velocity squared. Since a phase cannot be identified from the signal, it must be chosen. It is predicted that the difference in direction would most strongly effect the quadratic damping force.

Mathematically, a mean offset is inherently even and thus considered fully real in a frequency analysis. However, the choice to consider position as a sine or cosine wave is arbitrary, and thus the real component could be selected to be in phase with velocity or acceleration.

The split direction coefficient extraction varies slightly from the normal procedure. The time series is split into half periods with breaks when the direction of motion changes. Each full period contains one half period for positive motion, and one half period for negative motion. Each half period is mirrored to create a full virtual period which resembles either only positive or negative motion. These virtual periods are put through the same coefficient extraction process as previously described. This procedure gives separate viscous correction functions for each direction of travel.

Figure 9.12 shows the resulting coefficients found in this analysis. Two functions are shown in red for the quadratic damping force. The red stars show the coefficients when the force is in the positive direction and the red x's show the coefficients when the force is in the negative direction.

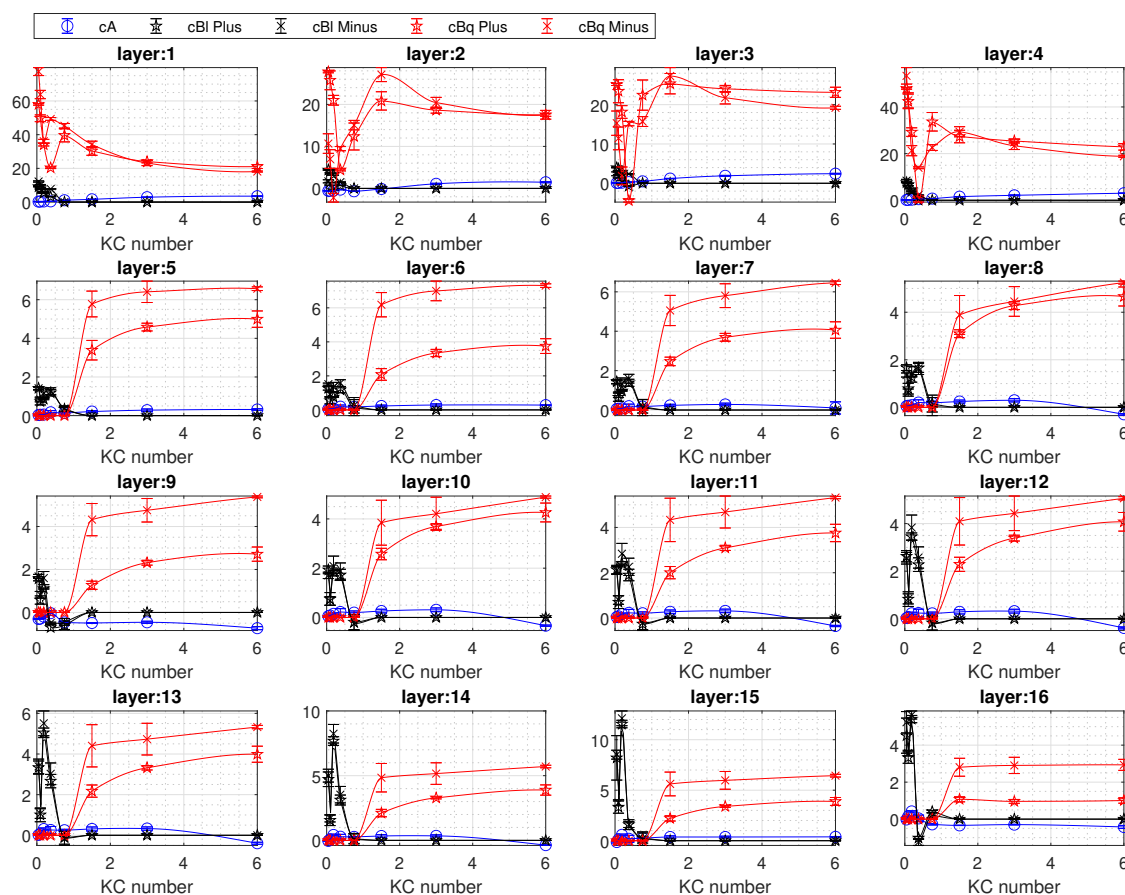


Figure 9.12: Direction split viscous correction functions
 cA [N-s²/m]; cBl [N-s/m]; cBq [N-s²/m²]

There is a significant difference in the coefficient between the two directions. The difference is small on the pontoon but much more pronounced on the column. This is interesting as the individual columns are symmetrical while the pontoons are not. One probable reason for the large difference on the columns is the presence of the wake from the pontoon. Since even the highest KC numbers are still relatively small, the columns are not influenced by the wakes of the other columns. However, the pontoons separate immediately, and directly adjacent to the columns. The separated flow from the pontoon influences the flow above it and thus effects the pressure distribution on the columns. This happens differently depending on the direction of travel.

10 Time Domain Model Viscous Corrections

The final goal and test of the viscous correction functions is to determine what kind of improvements can be made in the motion predictions. This is tested by implementing the functions into the time domain model discussed in Section 6.1, and comparing the predicted motions with the experimental model test results.

Of the three coefficient selection methods tested with the combined oscillation cases the IF and Amp methods provided the best results. The Amp method is significantly faster than the IF method and was thus selected for use in the final time domain model. While both methods produce very similar forces, the selected method is prone to predict slightly more erratic signals. This could be problematic if the platform was excited by high frequency forces. However, for the this semi-submersible, it is expected that there will be no impact of the small and quick fluctuations.

The time domain model operates almost exactly as described previously when only the potential flow coefficients were known. The only difference is in the addition of the viscous correction forces in the solution of the constant average acceleration solver.

The updated full equation of motion for the dynamic solver is given by Equation (69).

$$\begin{aligned}
 (\mathbf{M} + \mathbf{A}_\infty)\ddot{\vec{x}}_{i+1} + \mathbf{cA}(\ddot{\vec{x}}_{i+1} - u_{wavei+1}) + \int_0^{t_{i+1}} \mathbf{k}(t - \tau)\dot{\vec{x}}(\tau) d\tau + \mathbf{B}_\infty\dot{\vec{x}}_{i+1} + \mathbf{cBl}(\dot{\vec{x}}_{i+1} - u_{wavei+1}) + \\
 \mathbf{cBq}(\dot{\vec{x}}_{i+1} - u_{wavei+1})\left|\dot{\vec{x}}_{i+1} - u_{wavei+1}\right| + \mathbf{C}\vec{x}_{i+1} = \vec{f}_{exc_{i+1}}
 \end{aligned} \quad (69)$$

The viscous correction coefficients cA , cBl , and cBq are implemented as six by six matrices to work with the matrix equation, however the only non-zero values are at the surge surge location. The constant average acceleration approach is used to calculate the acceleration for each successive time step following Equation (70)

$$\begin{aligned}
 \ddot{\vec{x}}_{i+1} = (\mathbf{I}_2 \frac{dt^2}{4} + \mathbf{C}^{-1}((\mathbf{M} + \mathbf{A}_\infty + \mathbf{cA}) + \mathbf{k}(t - t_{i+1})\frac{dt^2}{2} \\
 + (\mathbf{B}_\infty + \mathbf{cBl})\frac{dt}{2}) + \mathbf{cBq}\frac{dt}{2}\left|\dot{\vec{x}}_i + \frac{dt}{2}\dot{\vec{x}}_i - u_{wavei}\right|^{-1} \\
 (\mathbf{C}^{-1}(\vec{f}_{exc_{i+1}} + \mathbf{cA}u_{wavei+1} + \mathbf{cBl}u_{wavei+1} - \int_0^{t_i} \mathbf{k}(t - \tau)\dot{\vec{x}}(\tau) d\tau - \mathbf{k}(t - t_{i+1})(\dot{\vec{x}}_i dt + \ddot{\vec{x}}_i \frac{dt^2}{2}) \\
 - (\mathbf{B}_\infty + \mathbf{cBl})(\dot{\vec{x}}_i + \ddot{\vec{x}}_i \frac{dt}{2}) - \mathbf{cBq}(\dot{\vec{x}}_{i+1} - u_{wavei+1})\left|\dot{\vec{x}}_{i+1} - u_{wavei+1}\right| - \vec{x}_i - \dot{\vec{x}}_i dt - \ddot{\vec{x}}_i \frac{dt^2}{4})
 \end{aligned} \quad (70)$$

The velocity and position vectors of the next time step are then calculated using the value of the acceleration. This new corrected model was used to predict the motions of all the wave cases previously considered with potential flow only.

The solution was calculated again using only the potential flow coefficients and constant critical damping value in order to gauge the improvements with the viscous correction functions. In addition to the use of the full viscous correction functions, the simulations were also run where the cBq coefficient stays the same, but the values of cA and cBl are set to zero. There is still large uncertainty in the error of the distributed potential flow analysis, which results in a lack of confidence in the corrections to the potential flow coefficients. This simulation checks to see the impact of only including the quadratic portion of the functions. In addition to the uncertainty in the distributed WAMIT solution, the changes to the potential flow coefficients are much more difficult to disconnect from their frequency dependency. The basis of this model is that the viscous corrections are functions of the KC number, and not the frequency. Small changes to the added mass and linear damping are expected due to viscous flow effects, and these changes are likely also linked to KC number. However when the base values of these coefficients vary so significantly with frequency, any tiny error is amplified by the value at the specific frequency tested, possibly masking the KC number dependency. The use of only the quadratic coefficient, while removing some effects, possibly strengthens the relationship to only the KC number.

Appendix K contains all of the reconstructed time series. For a quick comparison of the results, Figure 10.1 shows the surge motions for the first five bi-chromatic wave cases. These are the cases that have a difference frequency equal to the surge natural frequency, resulting in the largest low-frequency surge motions.

The viscous correction method only including the quadratic coefficient is consistently the best predictor of the model test results. The full viscous correction function consistently over-damps the motions. This implies that the linear damping contributions especially at the low KC numbers are too high. This could be explained by the under prediction of the distributed damping in the WAMIT analysis.

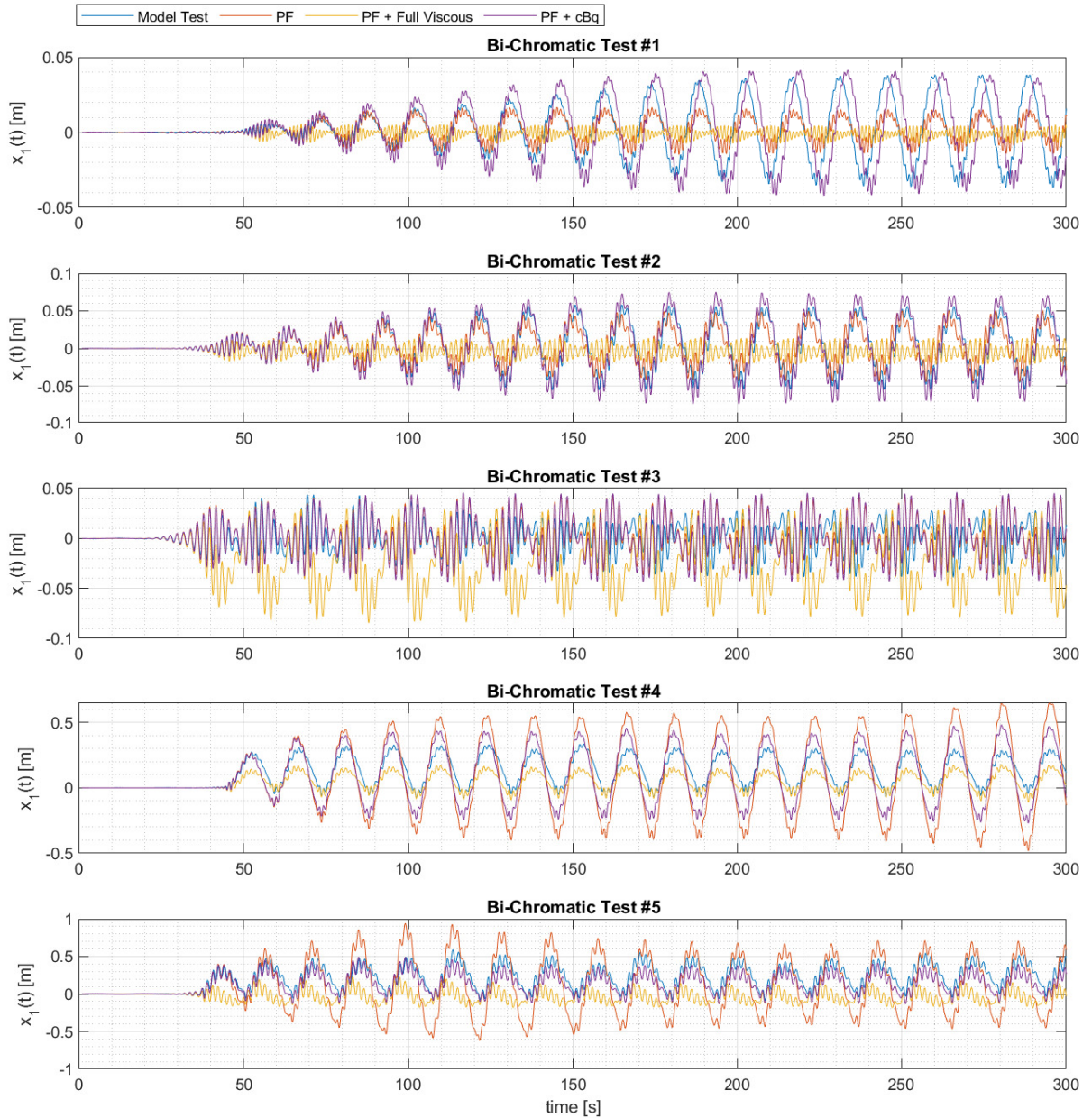


Figure 10.1: Time series reconstruction of bi-chromatic wave model test with viscous corrections

It is intriguing that the quadratic only viscous correction model is both effective at low wave height cases and at the high wave height cases. For the first bi-chromatic case the amplitude of the low-frequency oscillation is almost exactly correct, but there is some phase offset. The second case is similar with only a slight over prediction of the amplitude. The third case does not exhibit the same low-frequency surge motion as the other cases. The motions both predicted and measured more closely resemble simply the wave envelope. It seems that there was a slight error in the frequencies of the waves generated in the test, and the difference frequency did not exactly line up with the surge natural frequency. Still the quadratic only viscous correction method does a reasonable job of predicting the motions. The predictions from the method are the least accurate for the fourth case. The motions seem to be slightly under-damped resulting in somewhat larger amplitude motions than measured. The predictions for the fifth case are very close to the measured data both in amplitude and in phase.

The predicted motions were also calculated using the direction dependent coefficient functions. Figure K.20 in Appendix K shows the results for the first five bi-chromatic cases. The introduction of the direction dependence does not lead to significantly changed motion predictions.

11 Conclusions

A new method for predicting the low-frequency motions of a semi-submersible wind turbine platform was developed and tested. A first and second order potential flow analysis was performed and the results showed good agreement with similar previous work. The efficacy of the potential flow solution was tested with comparisons to model test data. Reconstructed time series showed the ability of the quadratic transfer function to predict low-frequency motions. While the model was able to predict when low-frequency surge would occur, the amplitudes of the oscillations showed some discrepancies from the measured values. It was predicted that this was largely due to the lack of viscous effects.

The quantification of viscous damping for semi-submersibles has been the subject of numerous projects. The most common approach to identifying it is the use of decay tests. The successive decay in the peaks of oscillation can be used to calculate linear and quadratic damping values. The post-processing for decay tests is robust, but the damping coefficients are only accurate for the conditions of the particular test. If a constant damping value is applied in all scenarios the predictions are not typically successful.

Other approaches that have been used include tuning coefficients to match the measured motions of model tests. This method has been proven as very effective by Silva de Souza et al. of SINTEF. The solution is found to be sea state dependent, and separate solutions are needed for each possible sea state. The result is a model that can effectively describe the system, but requires prior knowledge of the model tests. Previous work from numerous authors has also shown that it can be important to consider different damping effects for different regions of a body.

The guiding principle of the project is that viscous flow effects for an oscillatory motion are strongly linked to the KC number. This link to the KC number is likely why the solutions vary according to sea state. Different sea states lead to motions and relative flows with different KC numbers, which changes the nature of the drag forces. A benefit of using the KC number as the base parameter is that knowledge of wave conditions and the motions is not needed prior to a simulation. Even if the conditions change during a length of time, a KC number based model has the ability to adapt.

A CFD study was performed to quantify the relationship between KC number and viscous flow forces with some success. Forced oscillations were performed over a range of KC numbers with a constant maximum velocity and a varying frequency. The potential flow component of the total force is known to be frequency dependent, but the idea is that this frequency dependent portion can be subtracted, leaving only the KC number dependent portion. By holding the maximum velocity constant for each case, any effect of change in the Reynolds number is removed. In practice it was found that the subtraction of the potential flow component is difficult. Especially for low KC numbers, the potential flow portion is dominant, and even very small errors in the potential flow coefficients can drown out the viscous effect.

The post processing of forced oscillations is a very sensitive process. Any small numerical or discretization error can be easily confused with a viscous correction force. When decay tests are used to determine damping, there is a clear pattern found with the successive amplitudes of oscillation. Even if there is error on the order of 10% or more in the natural period or damping values, the same analysis techniques can be used. For oscillations that do not change, the method of extracting components of the force is very sensitive to small offsets in phase. It is thought that especially for the cases with the lowest KC numbers and the highest accelerations, the calculated coefficients could be very dependent on the time step used in the CFD simulation. Due to time constraints of the project a larger time step than desired had to be selected. This likely caused error in the prediction of the damping values for the low KC number cases.

The conclusions that can be drawn are also very sensitive to any error in the potential flow calculations. Because the value of added mass and radiation damping vary considerably with frequency, a small error at one frequency will appear very different than a small error at another frequency. The result is that when the potential flow components are subtracted, the small differences are heavily influenced by any error. This leads to apparent trends that are only caused of the frequency dependency of the potential flow portion. These trends can easily be confused for viscous flow effects.

Some key physical aspects are neglected by the study. One example is the influence of the three dimensional flow motion of waves. The study only considers relative fluid body motion in the surge direction. This relative motion could be made of motions of the platform, but also of the water particle motions due to waves. A wave is approximated as an oscillatory flow with a KC number that varies with wave height, but no motion in the z or y direction is considered. In reality waves create circular flow patterns and this three dimensional effect could impact the force on the body.

The viscous correction effects were only considered for surge motion, and these effects were treated as uncoupled from the other platform motions. This is an over-simplification of the problem. Pitch and surge in particular could have interesting coupling.

The low-frequency surge motions were best predicted when only including the quadratic damping coefficients. The coefficients came directly from the CFD solution, and no tuning was done to match the model tests, however, the final method still was largely forced. The choice to attribute the force in phase with velocity to either linear

damping, quadratic damping, or both was very manual, even if based on the results of the CFD and post-processing. It is plausible that if some of the identified shortcomings of the study were improved, the desired functions could be reached more organically.

Even with complications in the post processing and uncertainty in a number of the aspects of the CFD study, the method did lead to improved predictions of low-frequency surge motions. Particularly when only the quadratic drag coefficient was included, the solver was able to improve results both for short and large wave heights. At low KC numbers quadratic drag is only present on the pontoon and not on the column. This results in much lower total damping for the body. At high KC numbers quadratic drag is present on the entire body, and the damping is much larger. Tracking the KC number throughout a simulation allows the model to identify how to change the damping values in both time and location. This results in an approach that can be broadly applied to many different environmental conditions.

11.1 Recommended Future Work

It was found that separating the frequency dependence of the potential flow coefficients is very difficult. The viscous flow pattern can significantly deviate from potential flow predictions, and it is logical to guess that this would effect the added mass and radiation damping values. However, these viscous changes are so inherently linked to frequency, that treating them as a part of the KC number dependent functions is not effective.

It is recommended that future work done with this method fully removes any frequency dependence. This could be achieved by using a constant frequency and varying maximum velocity for the test matrix. This approach then would introduce unwanted influence of the Reynolds number. Instead it is suggested that the free surface is removed.

The link to frequency comes from the presence of radiated waves, which have different lengths with different frequencies. If there are no free surface waves, then the added mass term is constant and the linear damping term is zero. This would mean that the potential flow predicted coefficients would be the same for every KC number tested. It is expected that this technique could better isolate the influence of viscous flow effects. Any viscous effects in how waves form and potentially run up the structure would be lost, but the benefit of fully removing frequency dependence would likely be worth the loss.

In addition, it would be interesting to extend the viscous correction technique to other degrees of freedom. Pitch and roll motions are likely heavily influenced by viscous flow effects at the sharp corners on the bottom of the platform. Coupled viscous correction functions could also be developed for multiple degrees of freedom.

References

- [1] “Wind in our Sails - The coming of Europe’s offshore wind energy industry”. In: (2011). Ed. by European Wind Energy Association.
- [2] Karimirad Berthelsen Bachynski and Thys. *Real-time hybrid model tests of a braceless semi-submersible wind turbine part III: calibration of a numerical model*. Tech. rep. Busan, Korea: MARINTEK, 2016.
- [3] Vaz Burmester Chen and Wang. *CFD simulation of semi-submersible floating offshore wind turbine under pitch decay motion*. Tech. rep. St. Julians, Malta: University of Duisburg-Essen, MARIN, Texas AM University, 2019.
- [4] L. Cohen. *Time-frequency analysis*. Englewood Cliffs, New Jersey: Prentice Hall, 1995.
- [5] W.E. Cummins. *The Impulse Response Function and Ship Motions*. Tech. rep. Bethesda, Maryland: Department of the Navy: David Taylor Model Basin, 1962.
- [6] Wind Europe. “Floating Offshore Wind Energy - a Policy Blueprint for Europe”. In: (2017).
- [7] Wind Europe. “Wind energy in Europe in 2019”. In: (2020). Ed. by Colin Walsh.
- [8] O. M. Faltinsen. *Hydrodynamics of High-Speed Marine Vehicles*. Cambridge, UK: Cambridge University Press, 2005. ISBN: 0 521 84568-8.
- [9] O. M. Faltinsen. *Sea Loads on Ships and Offshore Structures*. Cambridge, UK: Cambridge University Press, 1998. ISBN: 0 521 45870 6.
- [10] Thys Fonseca and Berthelsen. *Identification of wave drift force QTFs for the INO WINDMOOR floating wind turbine based on model test data and comparison with potential flow predictions*. Tech. rep. under review. Trondheim, Norway: SINTEF Ocean AS, 2021.
- [11] Charles Hirsch. *Numerical Computation of Internal and External Flows*. 2nd ed. Butterworth-Heinemann, 2007. ISBN: 978-0-7506-6594-0.
- [12] R. Sigbjörnsson I. Langen. *Dynamisk Analyse Av Konstruksjoner*. Norway, 1979.
- [13] C.-H. Lee. *WAMIT Theory Manual*. Massachusetts Institute of Technology Department of Ocean Engineering, 1995.
- [14] John Lienhard. *Synopsis of lift, drag, vortex frequency data for rigid circular cylinders*. Tech. rep. Pullman, Washington: Washington State University, 1966.
- [15] P. Gipe M. Pasqualetti R. Righter. “History of Wind Energy”. In: (2004). Ed. by Encyclopedia of Energy.
- [16] J. N. Newman. *Marine Hydrodynamics*. 40th Anniversary ed. Cambridge, MA: The MIT Press, 2017. ISBN: 9780262534826.
- [17] *OpenFOAM: Manual Pages v2012*. OpenCFD Ltd. Creative Commons License BY-NC-ND, 2020.
- [18] Benoit Pinguet Kanner and Molin. *Modeling the dynamics of freely-floating offshore wind turbine subjected to waves with an open-source overset mesh method*. Tech. rep. 978-1-880653-84-5. Marseille, France: Aix Marseille Univ. and Principle Power Inc., 2020.
- [19] Benoit Pinguet Kanner and Molin. *Validation of open-source overset mesh method using free-decay tests of floating offshore wind turbine*. Tech. rep. IOWTC2021-3536. Marseille, France: Aix Marseille Univ. and Principle Power Inc., 2021.
- [20] T. Moan R. Taghipour T. Perez. *Hybrid Frequency-Time Domain Models for Dynamic Response Analysis of Marine Structures*. Tech. rep. Trondheim, Norway: Norwegian University of Science and Technology, 2007.
- [21] I. Rivera-Arreba. *Computation of nonlinear wave loads on floating structures*. Tech. rep. Trondheim, Norway: Norwegian University of Science and Technology, 2017.
- [22] Robertson Roald Jonkman and Chokani. *The effect of second-order hydrodynamics on floating offshore wind turbines*. Tech. rep. Trondheim, Norway: National Renewable Energy Laboratory, Laboratory of Energy Conversion, 2013.
- [23] Christopher Rumsey. “Langley Research Center: Turbulence Modeling Resource”. In: (2021).
- [24] Herman Schlichting. *Boundary-Layer Theory*. 7th ed. New York, NY: McGraw-Hill Book Company, 1979. ISBN: 0-07-055334-3.
- [25] Berthelsen Silva de Souza Fonseca and Thys. *Calibration of a time-domain hydrodynamic model for a 12 MW semi-submersible floating wind turbine*. Tech. rep. OMAE2021-62857. Trondheim, Norway: SINTEF Ocean AS, 2021.

-
- [26] Silva de Souza, Berthelsen, Eliassen, Bachynski, Engebretsen, and Haslum. *Definition of the INO WIND-MOOR 12 MW base case floating wind turbine*. Tech. rep. OC2020 A-044. Trondheim, Norway: SINTEF Ocean AS, NTNU, Inocean and Equinor, 2021.
- [27] Carl Trygve Stansberg. *Linear and Nonlinear System Identification in Model Testing*. Tech. rep. Trondheim, Norway: Norwegian Marine Technology Research Institute A/S, 1997.
- [28] D. Kim T. Tran. *A CFD study of coupled aerodynamic [U+2010]hydrodynamic loads on a semisubmersible floating offshore wind turbine*. Tech. rep. Gajwa [U+2010]dong, Jinju, South Korea: Gyeongsang National University, 2017.
- [29] Thys, Souza, Sauder, Fonseca, Berthelsen, Engebretsen, and Haslum. *Experimental investigation of the coupling between aero- and hydrodynamical loads on a 12 MW semi-submersible floating wind turbine*. Tech. rep. OMAE2021-62980. Trondheim, Norway: SINTEF Ocean AS, Inocean and Equinor, 2021.
- [30] Frank M. White. *Fluid Mechanics*. 8th ed. New York, NY: McGraw-Hill Education, 2016. ISBN: 978-0-07-339827-3.
- [31] Y. Lu Z. Chuang S. Liu. *Influence of second order wave excitation loads on coupled response of an offshore floating wind turbine*. Tech. rep. Dalian, China: Naval Architecture and Ocean Engineering College - Dalian Maritime University, 2020.

A First Order Potential Flow Results

The results of the first order potential flow analysis are shown for each of the five original panel models. The legends indicate the length of the base element in the panel model.

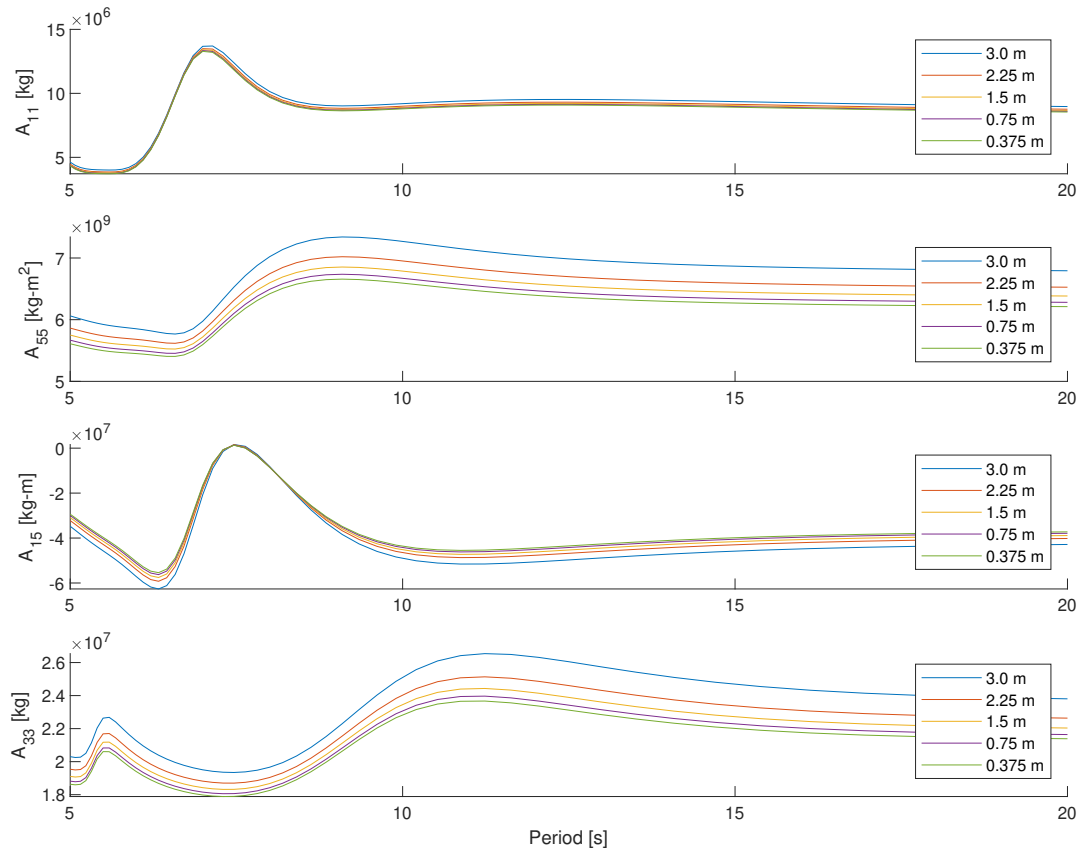


Figure A.1: Added mass in surge, pitch, surge-pitch, and heave

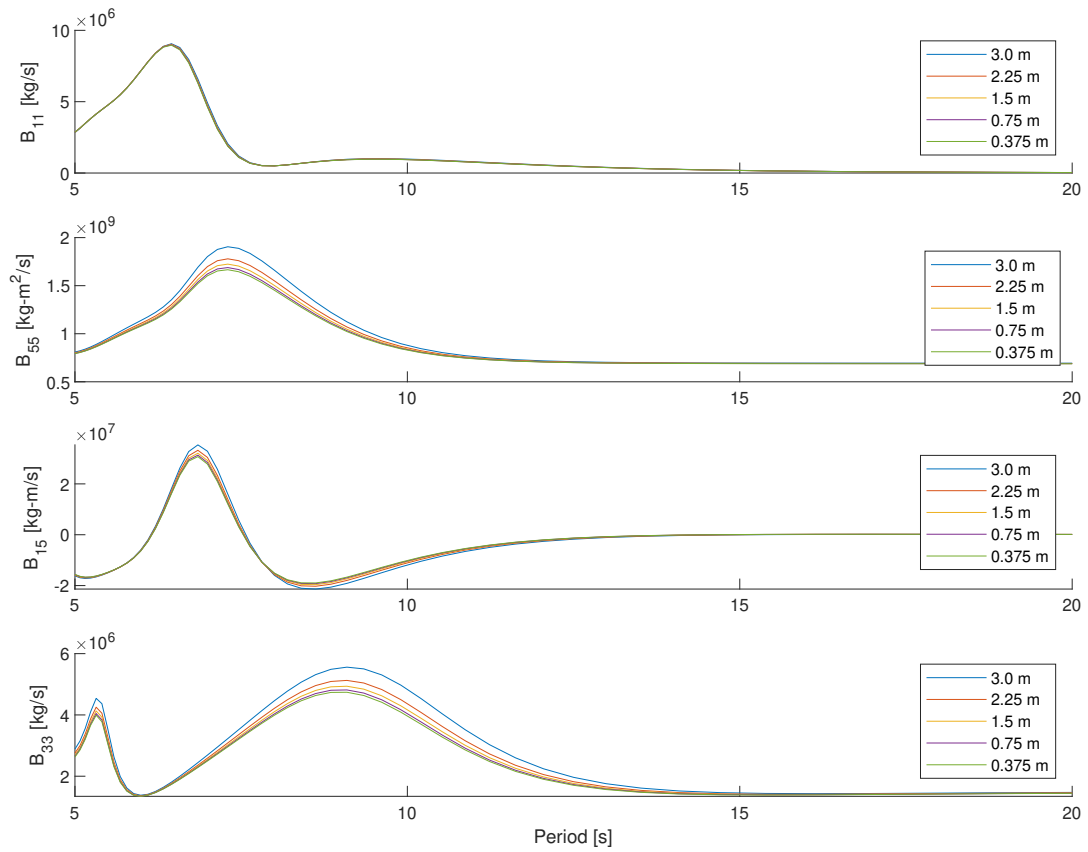


Figure A.2: Damping in surge, pitch, surge-pitch, and heave

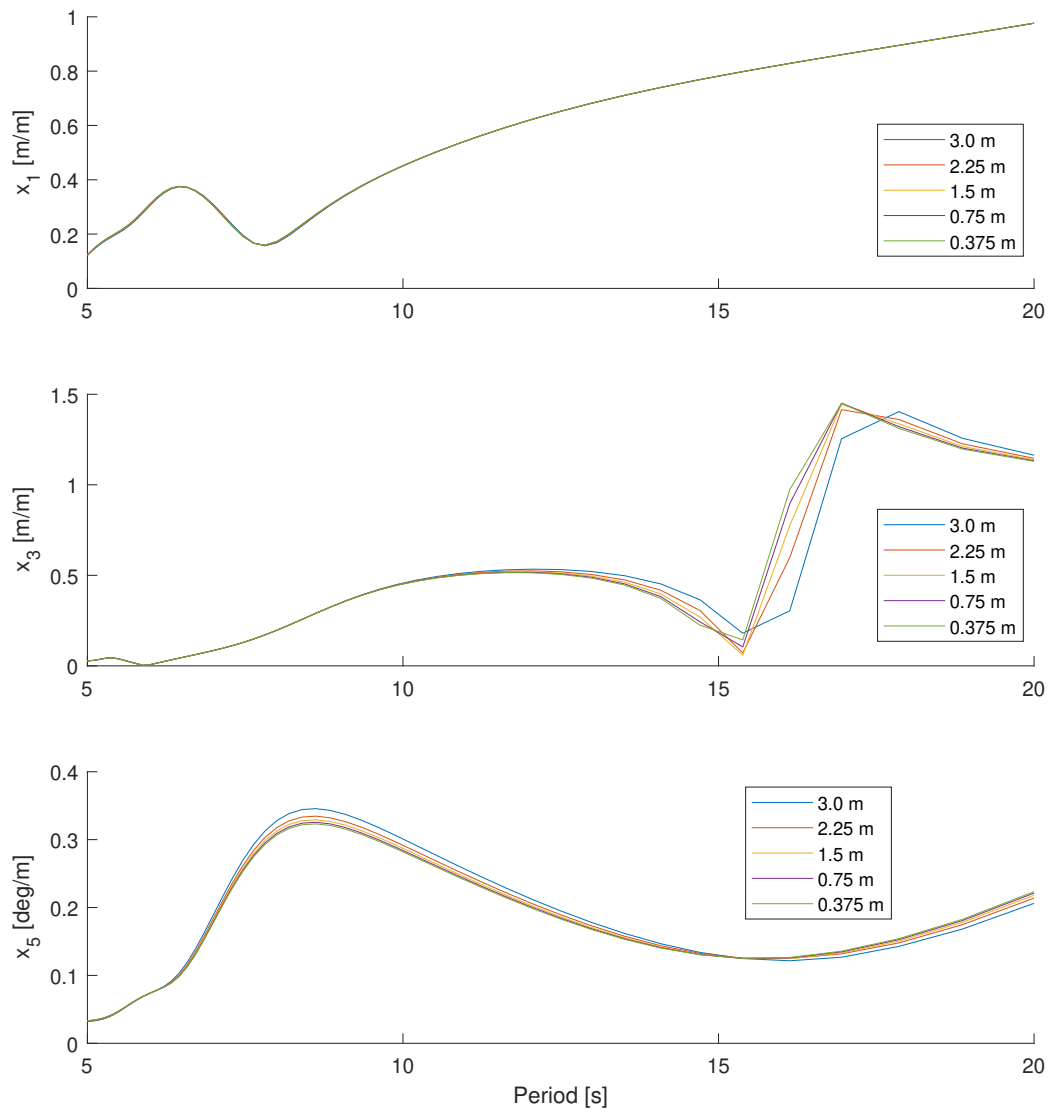


Figure A.3: Linear motion transfer function in surge, heave, and pitch

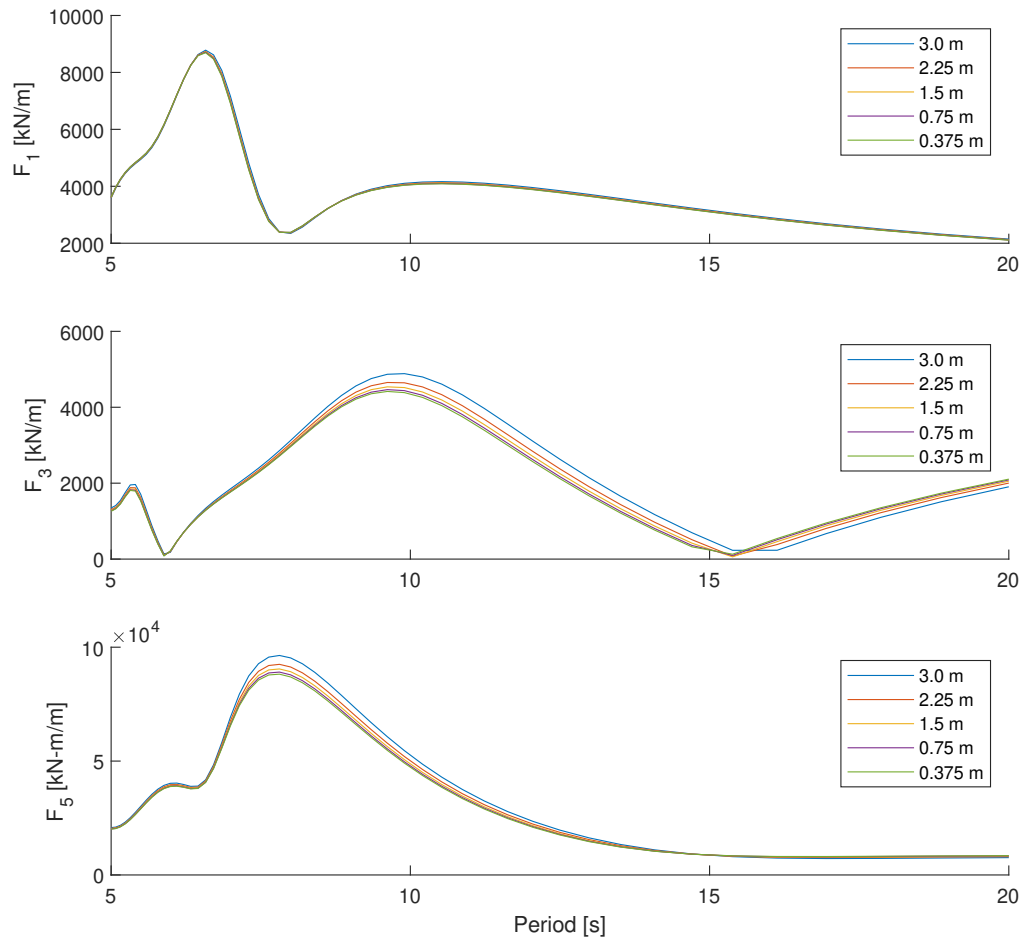


Figure A.4: Linear excitation force in surge, heave, and pitch

B Second Order Potential Flow Results

The difference frequency quadratic transfer functions of heave force and pitch moment are shown below. The surface plots include the real component, imaginary component, and absolute value. Again for head seas sway, roll, and yaw are irrelevant.

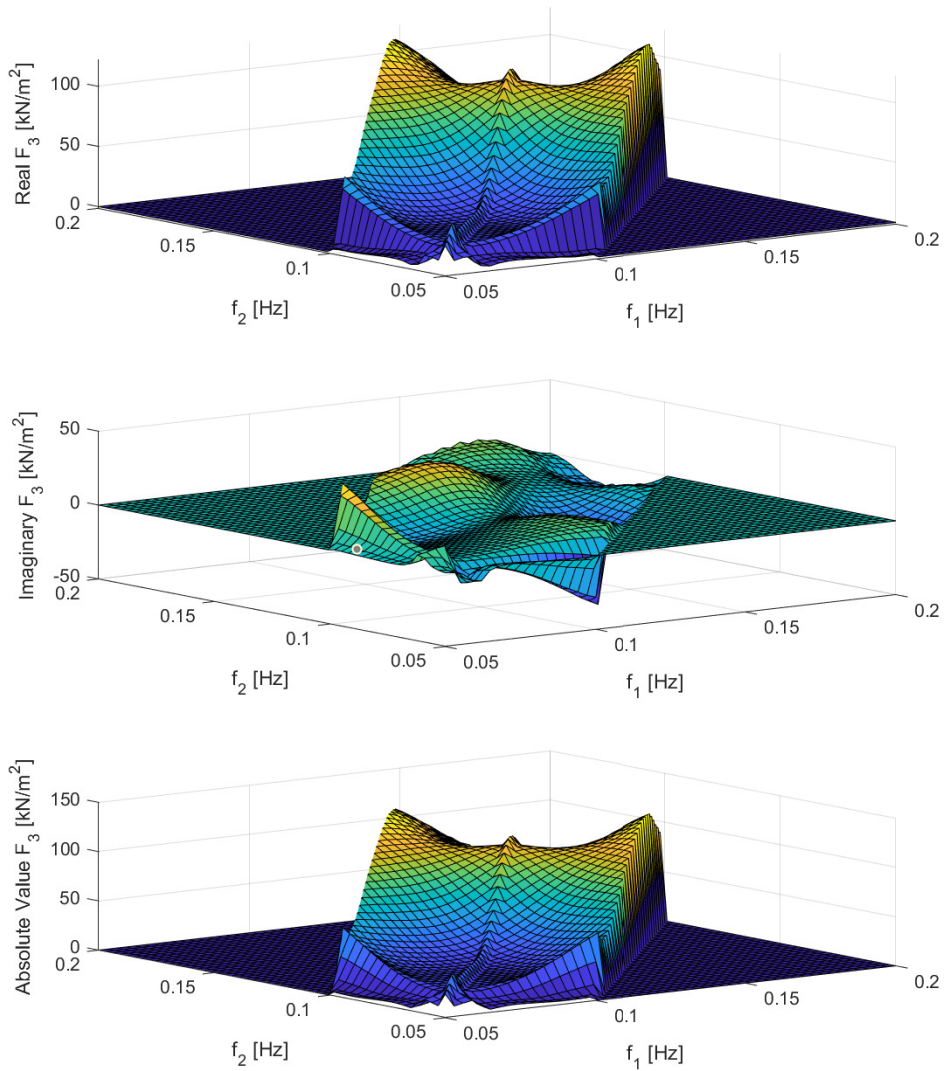


Figure B.1: Heave force quadratic transfer function

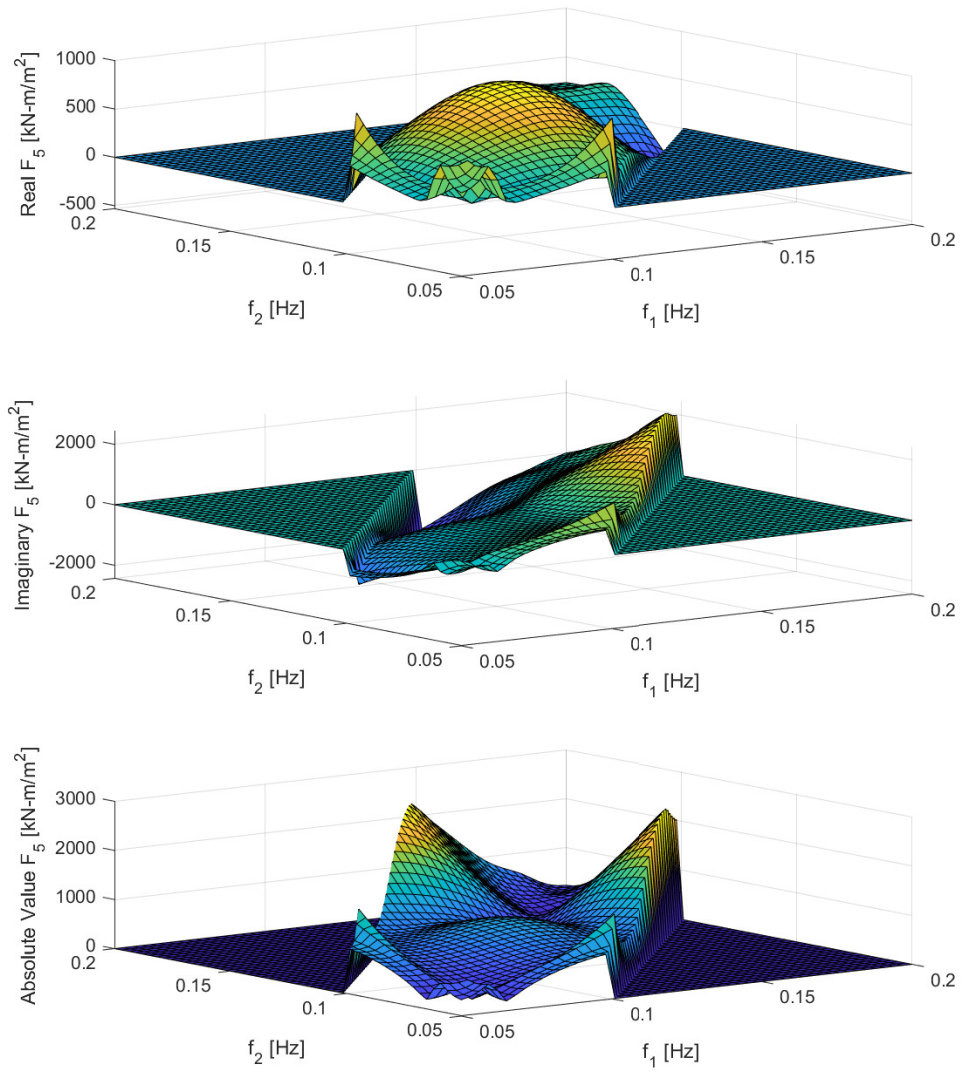


Figure B.2: Pitch moment quadratic transfer function

The difference frequency quadratic transfer functions of surge, heave, and pitch are also shown by means of diagonal cuts along lines of constant difference frequency. Again the real component, imaginary component, and absolute value are shown for each of the three diagonals shown. It should be noted that the imaginary component along the zero difference frequency diagonal is essentially zero for each plot, despite the noise shown by the small scale of the plot.

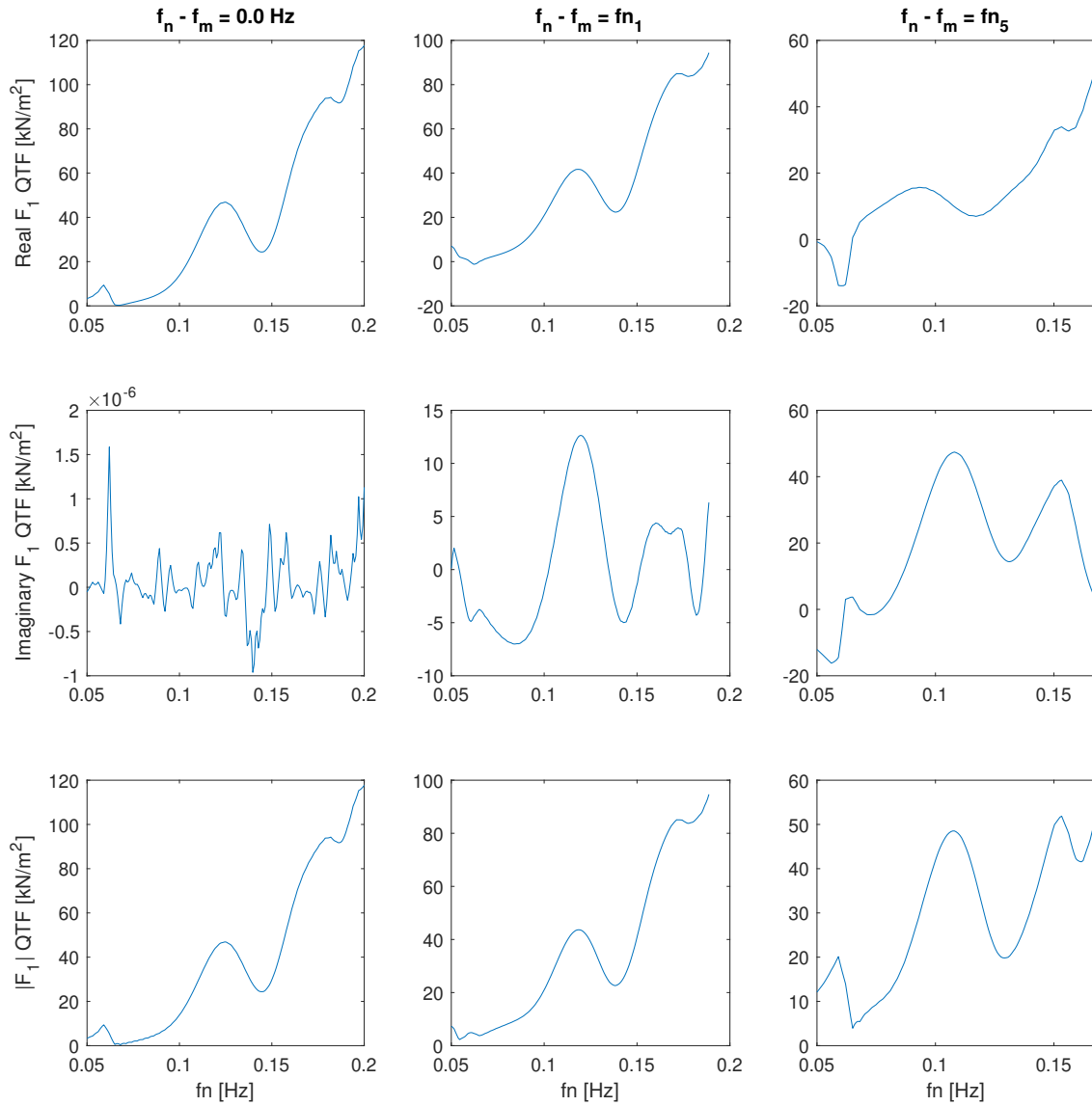


Figure B.3: Surge force quadratic transfer function diagonals

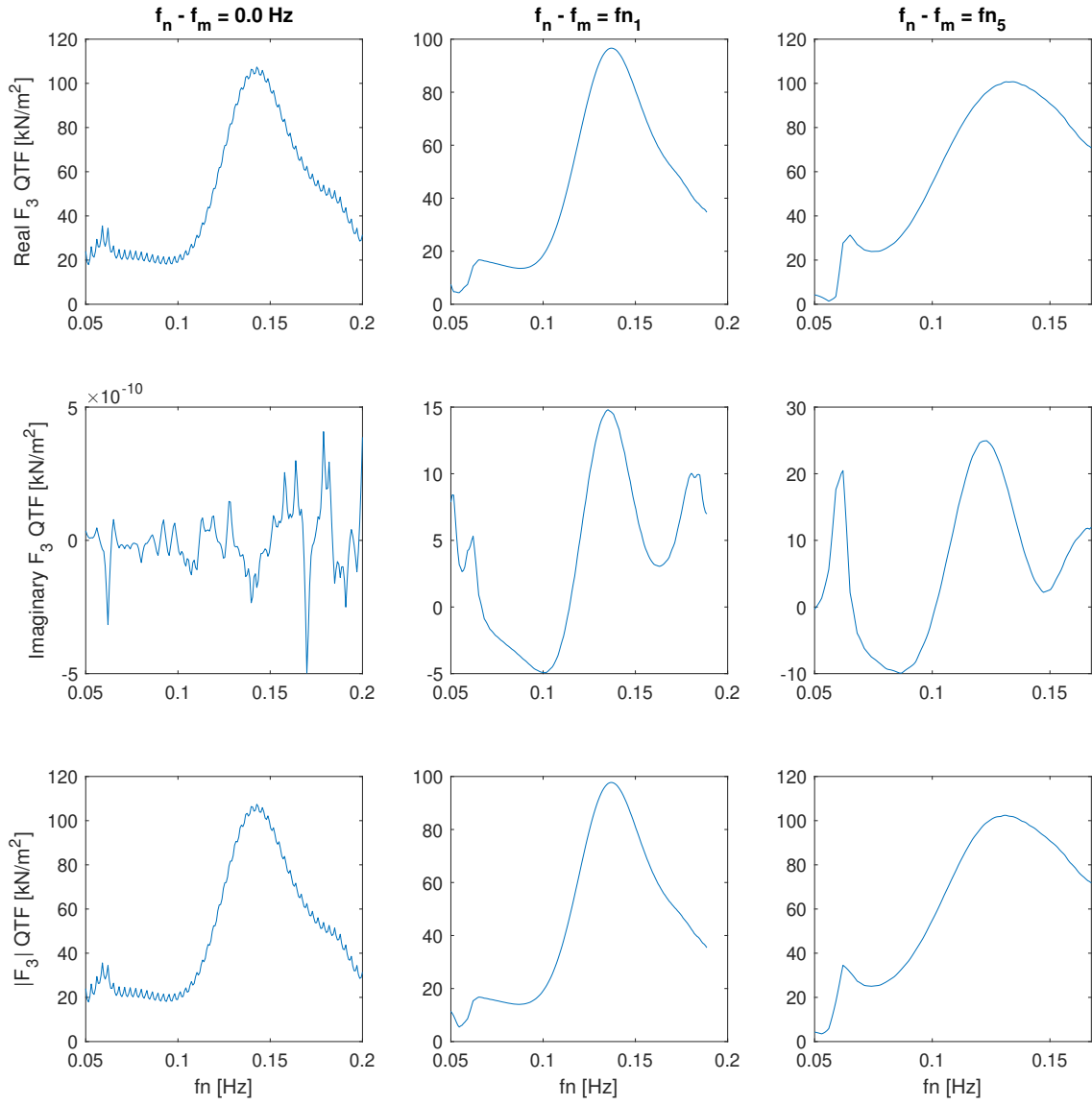


Figure B.4: Heave force quadratic transfer function diagonals

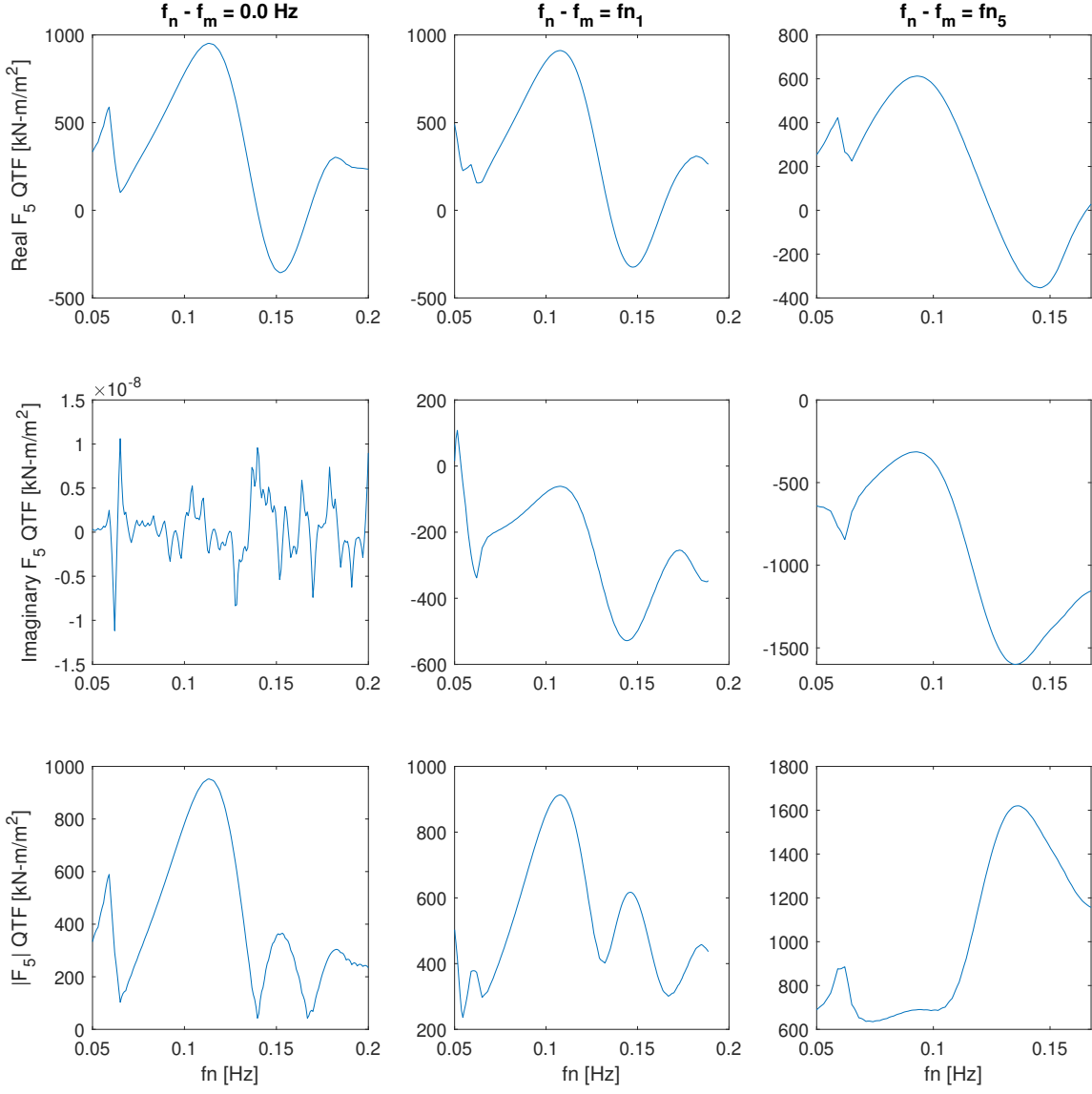


Figure B.5: Pitch moment quadratic transfer function diagonals

C Mono-chromatic Time Series Reconstruction - Potential Flow Only

The results of the numerical reconstruction are shown below for the mono-chromatic wave model tests. The test numbers correlate to the wave heights and frequencies referenced in table 4.1. For each test plots are shown for surge, heave, and pitch. The legend shows the four values that are compared: the measured data from model tests, the numerical results using the constant average acceleration method and the full QTF, the numerical results using Newman's approximation, and the numerical results including only the first order excitation. Both time domain and frequency domain plots are shown.

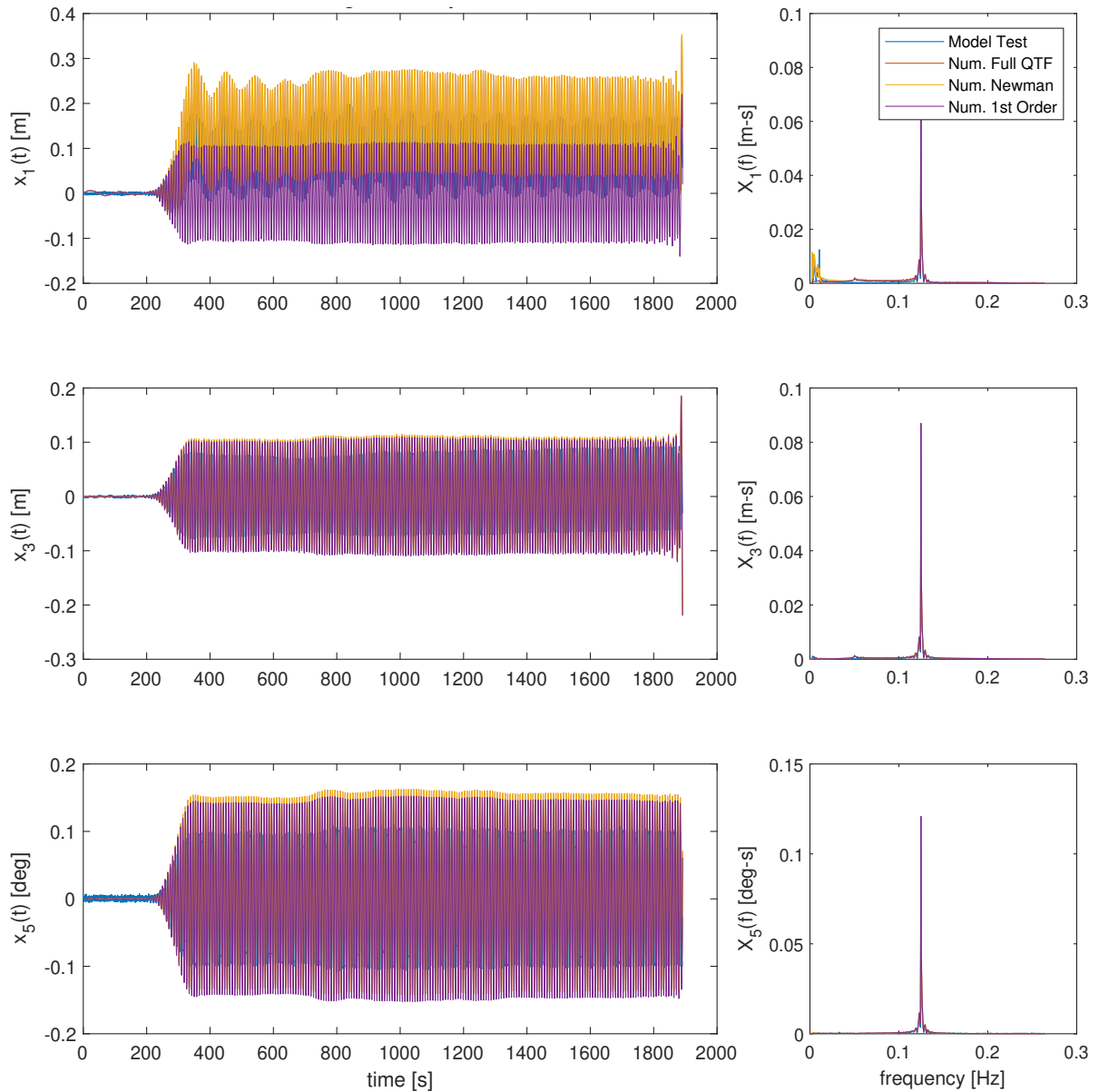


Figure C.1: Test 1 mono-chromatic wave motion reconstruction

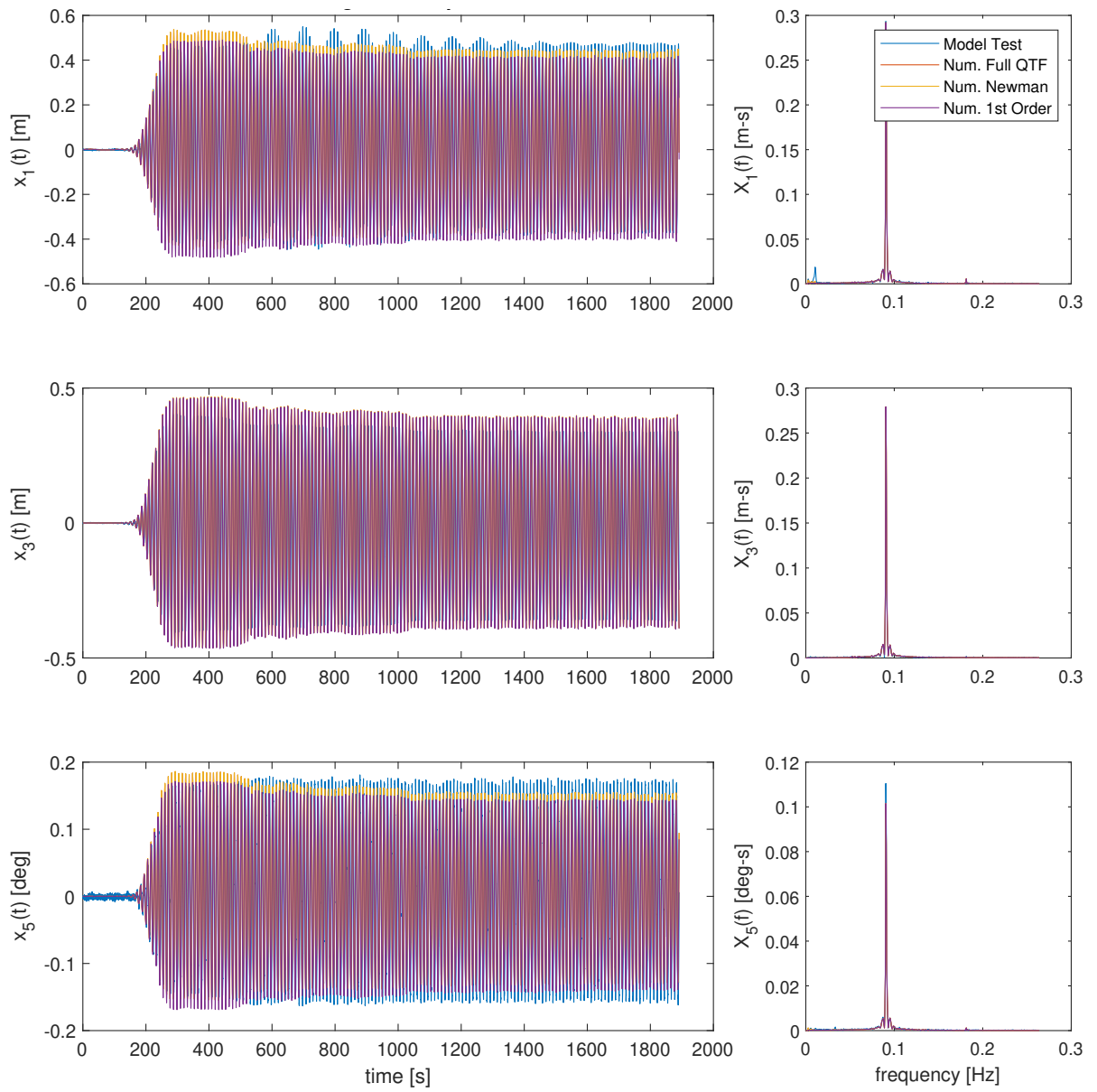


Figure C.2: Test 2 mono-chromatic wave motion reconstruction

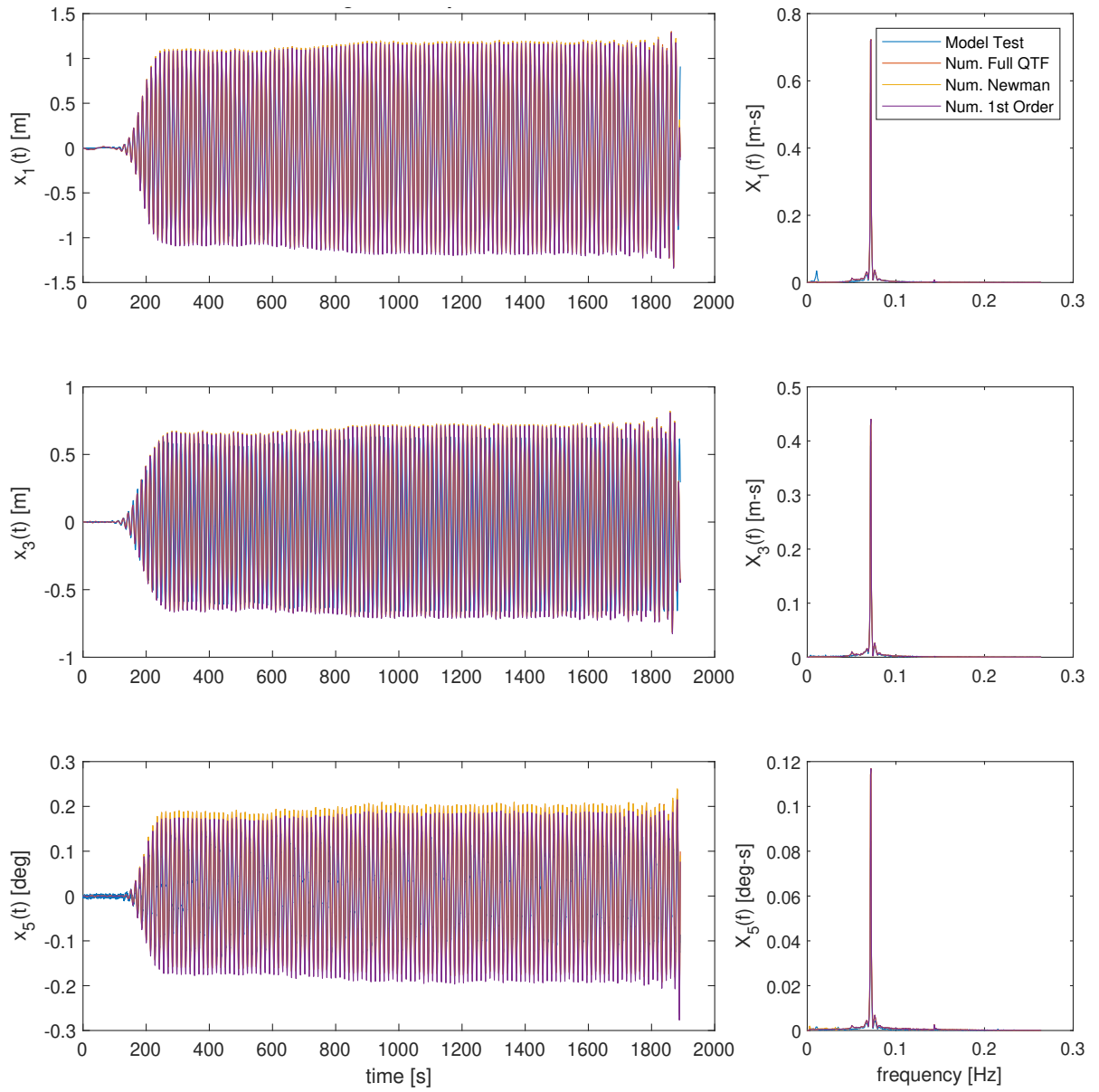


Figure C.3: Test 3 mono-chromatic wave motion reconstruction

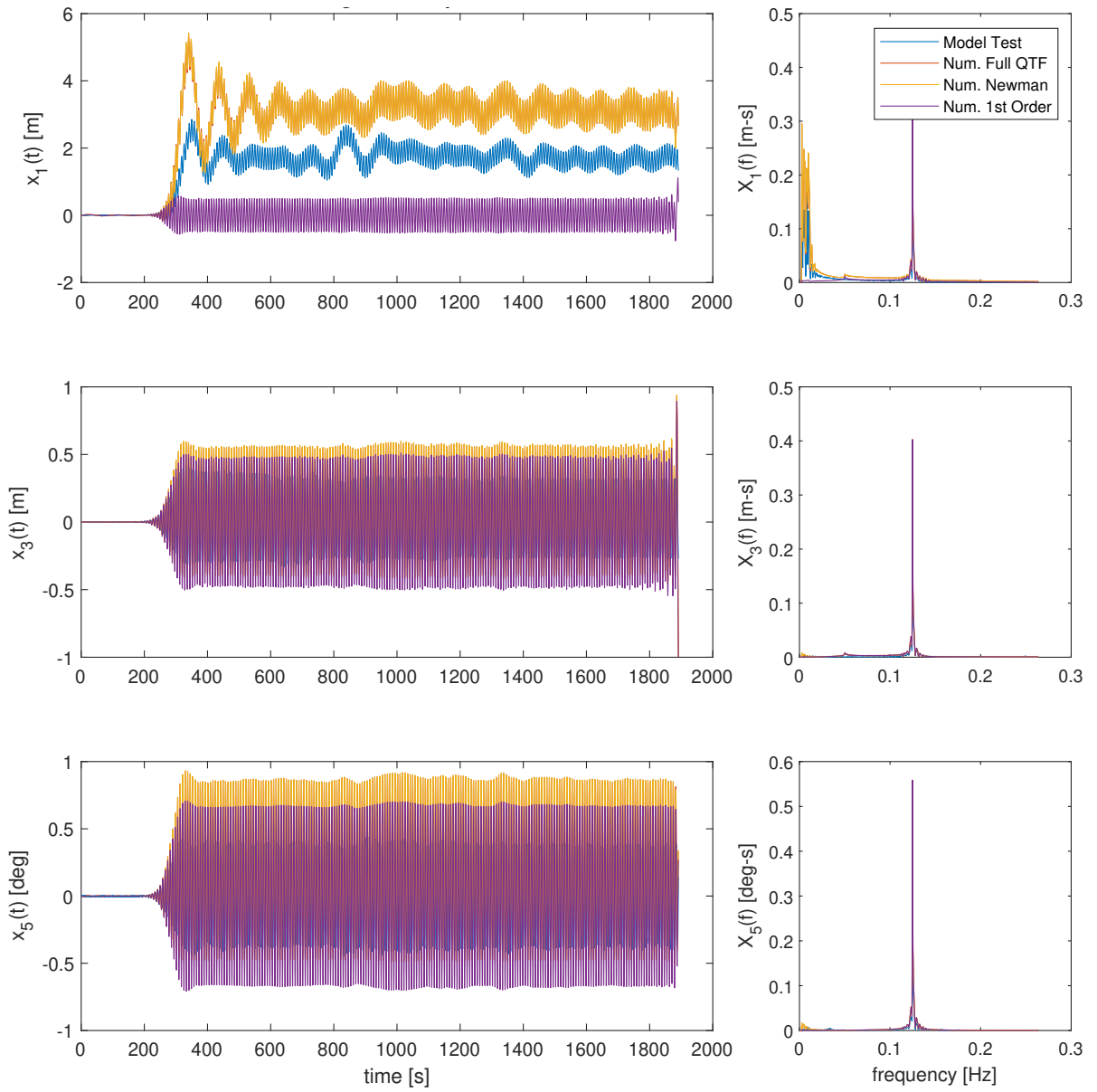


Figure C.4: Test 4 mono-chromatic wave motion reconstruction

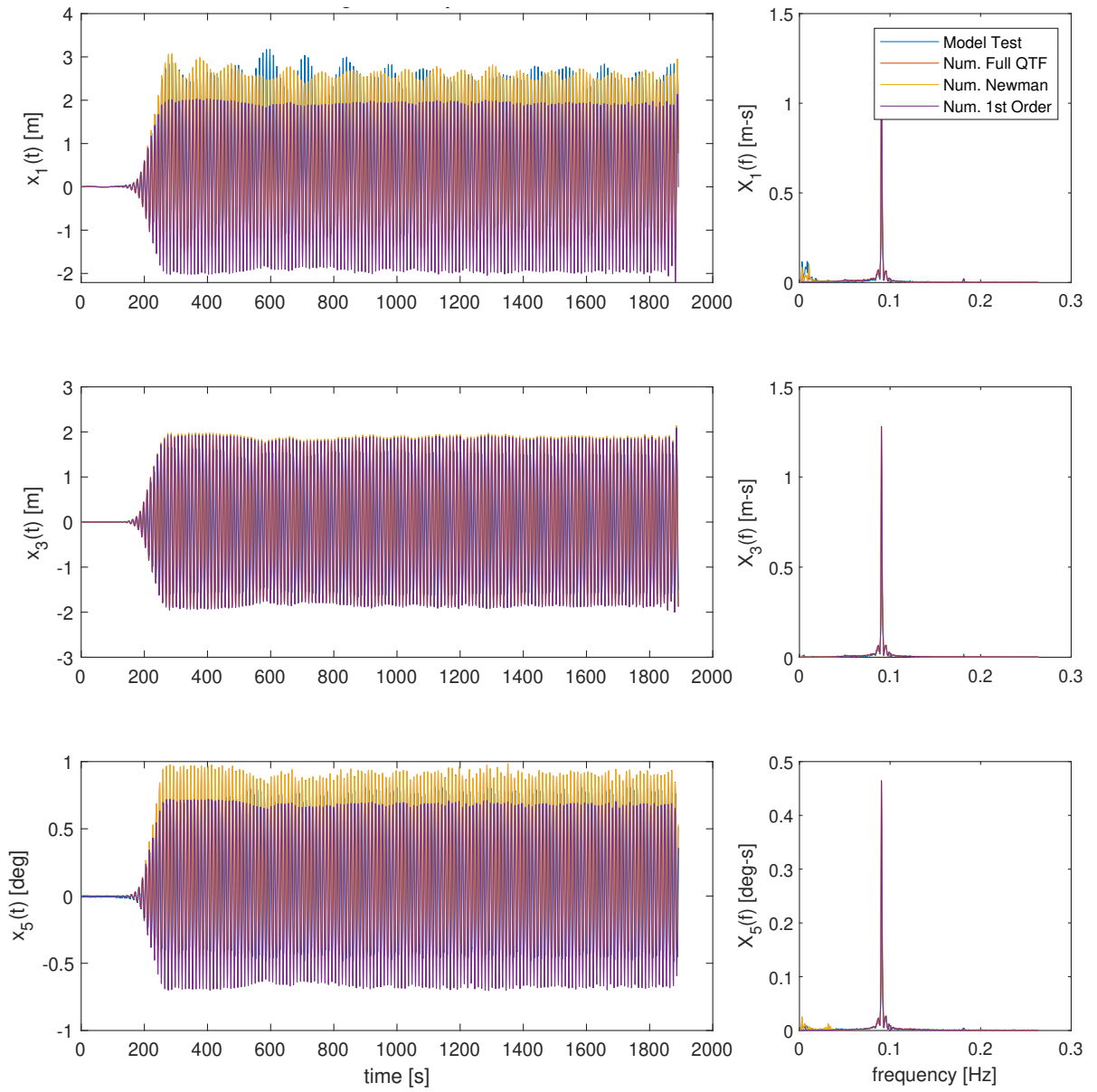


Figure C.5: Test 5 mono-chromatic wave motion reconstruction

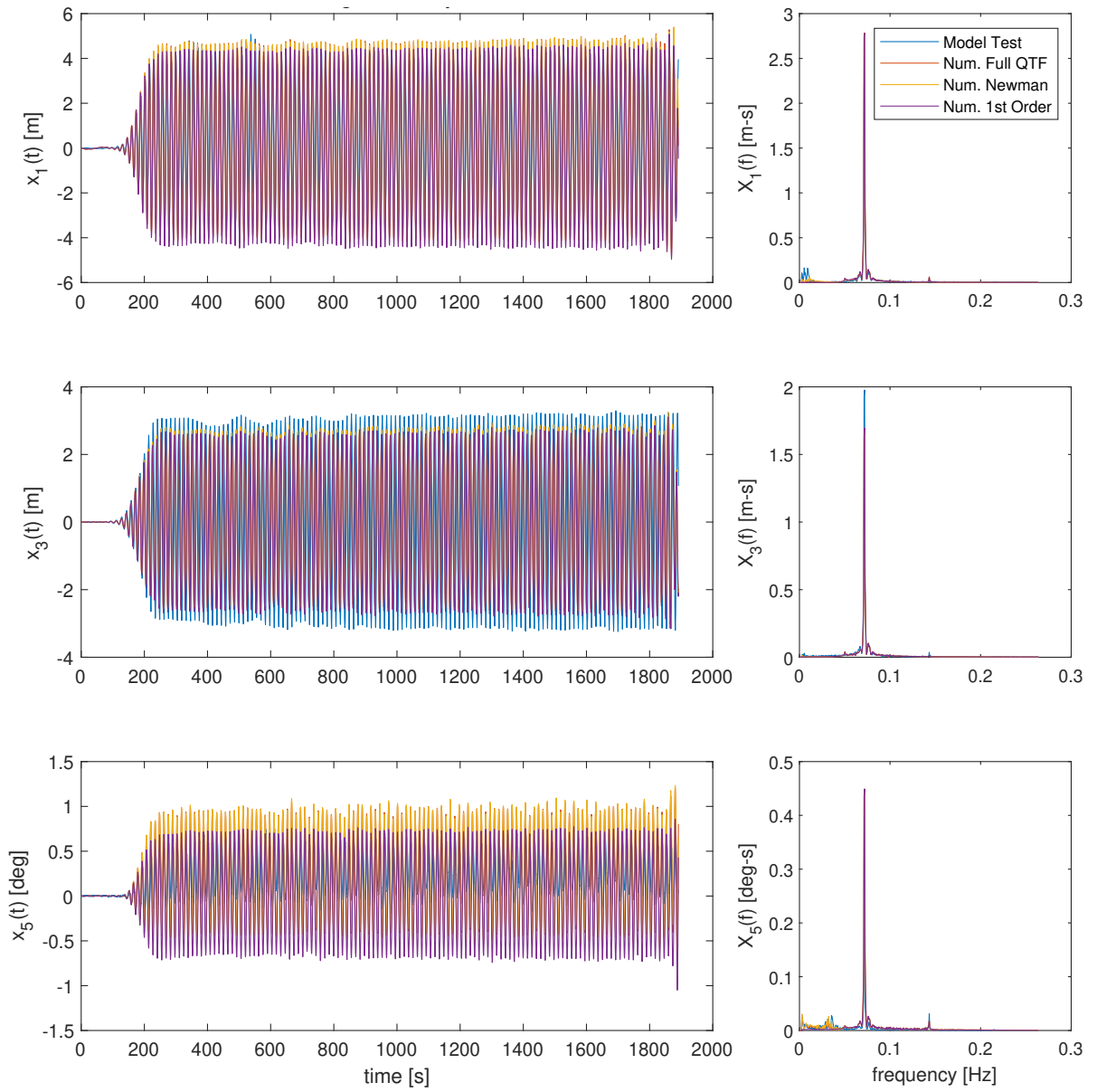


Figure C.6: Test 6 mono-chromatic wave motion reconstruction

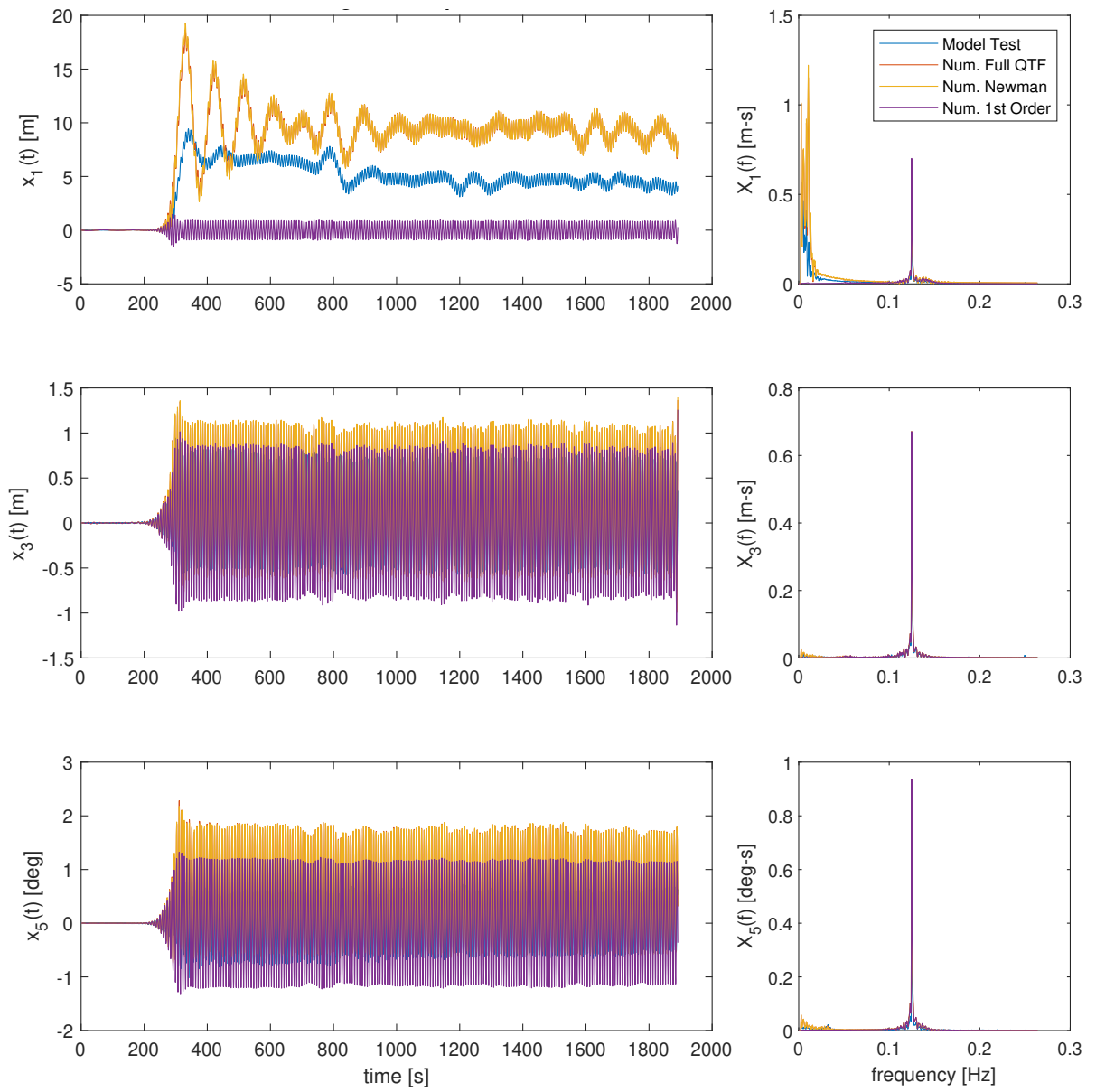


Figure C.7: Test 7 mono-chromatic wave motion reconstruction

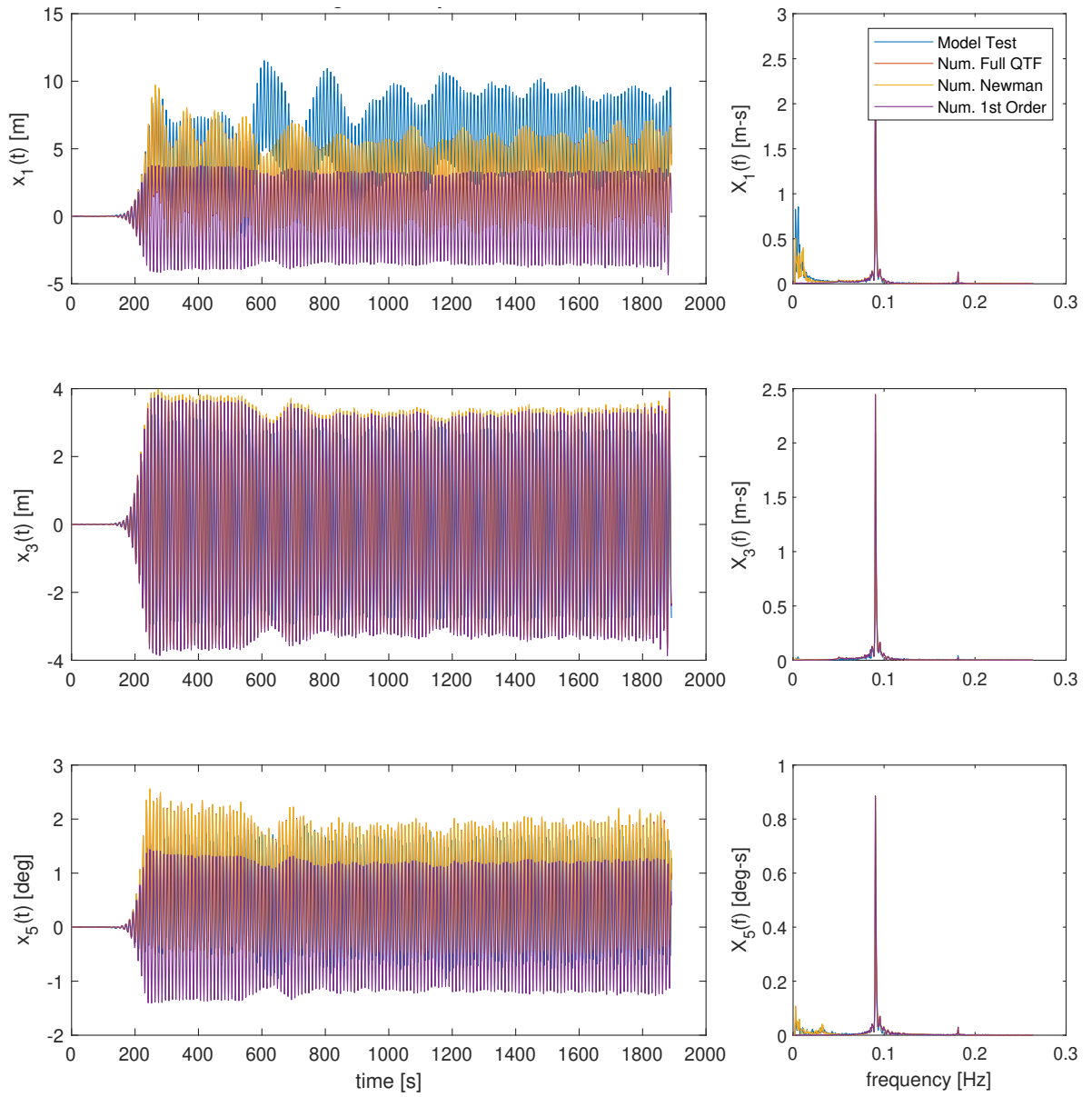


Figure C.8: Test 8 mono-chromatic wave motion reconstruction

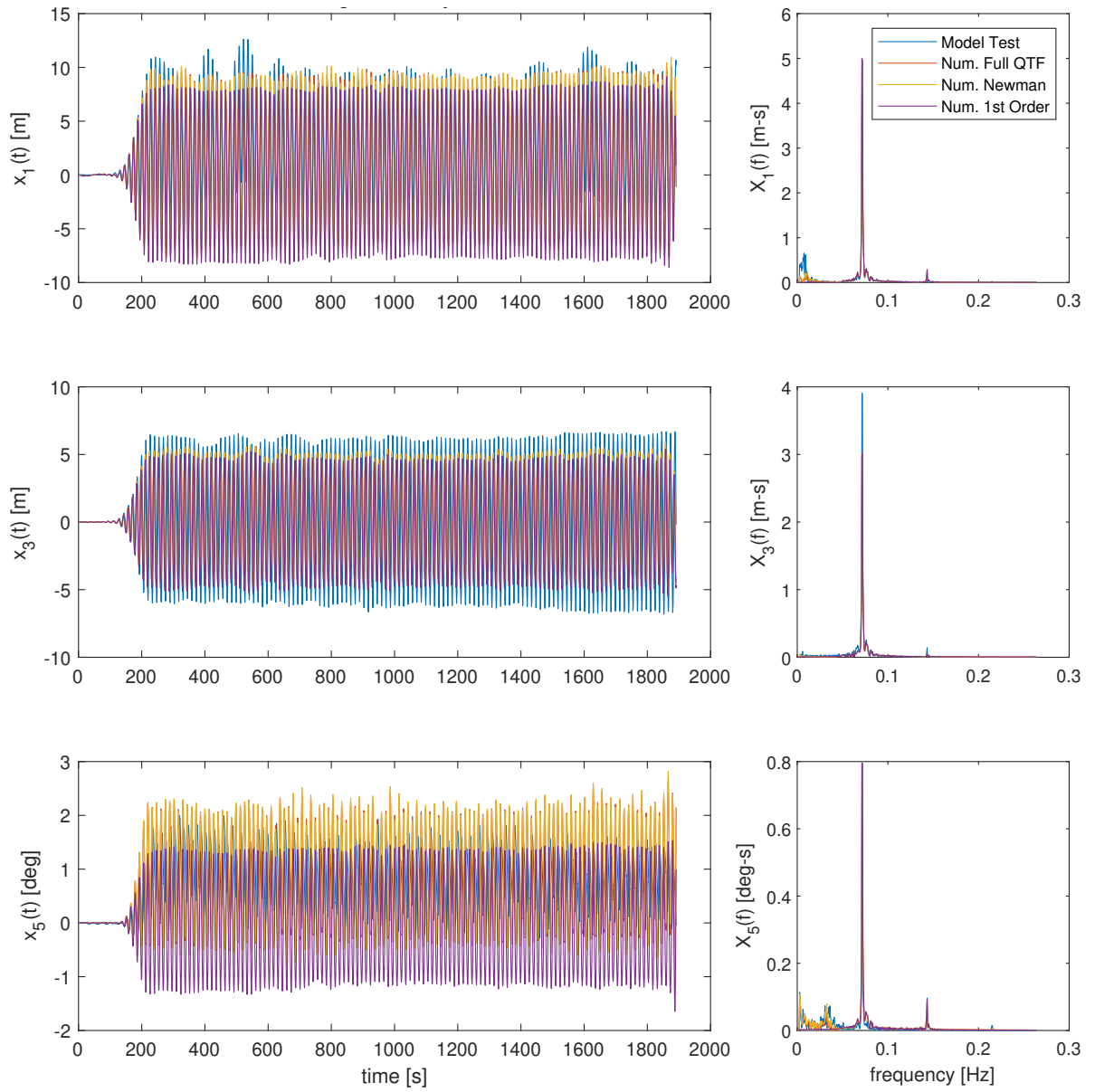


Figure C.9: Test 9 mono-chromatic wave motion reconstruction

D Bi-Chromatic Time Series Reconstruction - Potential Flow Only

The results of the numerical reconstruction are shown below for the bi-chromatic wave model tests. The test numbers correlate to the wave heights and frequencies referenced in table 4.2. For each test plots are shown for surge, heave, and pitch. The legend shows the four values that are compared: the measured data from model tests, the numerical results using the constant average acceleration method and the full QTF, the numerical results using Newman's approximation, and the numerical results including only the first order excitation. Both time domain and frequency domain plots are shown.

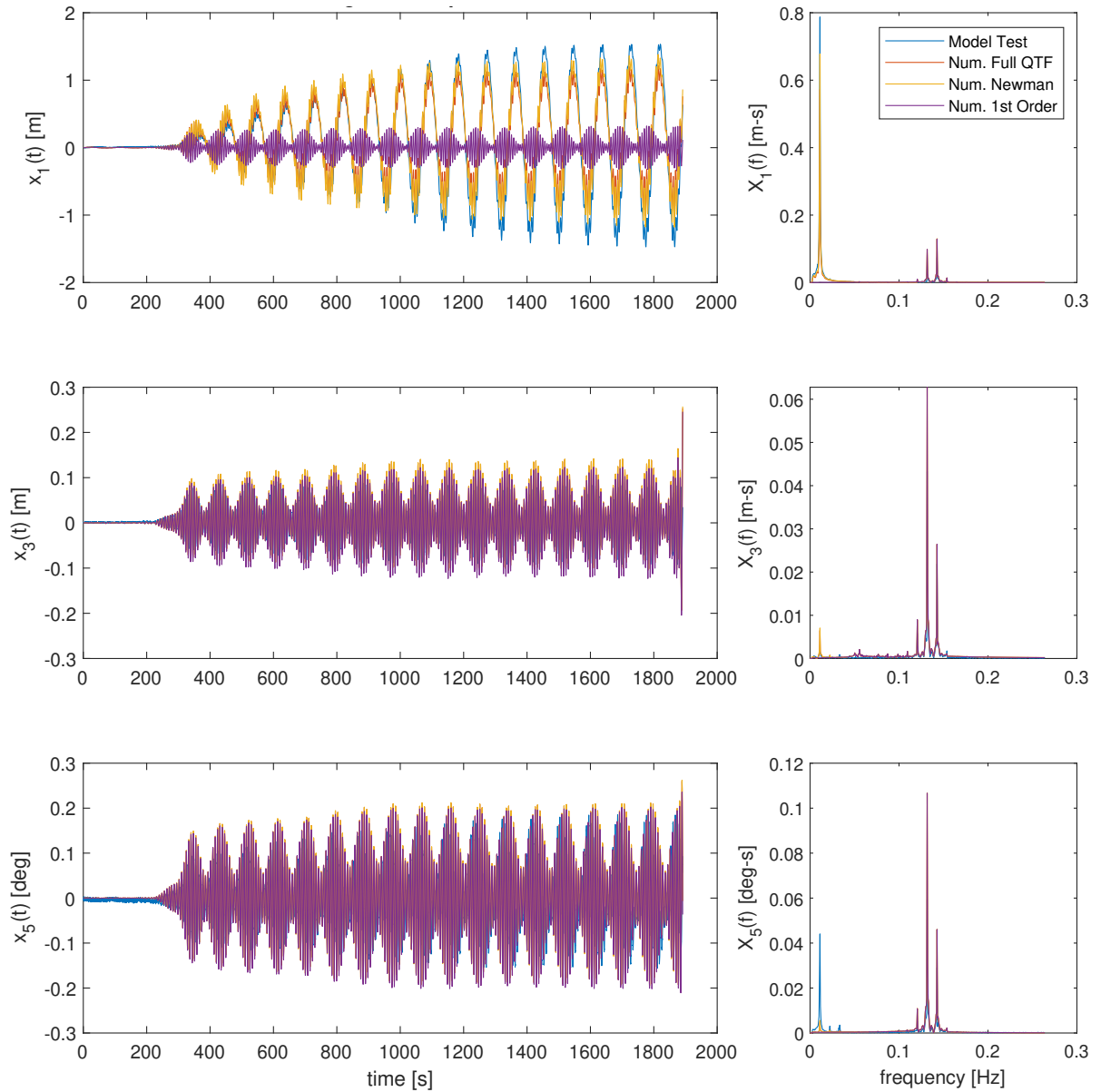


Figure D.1: Test 1 bichromatic wave motion reconstruction

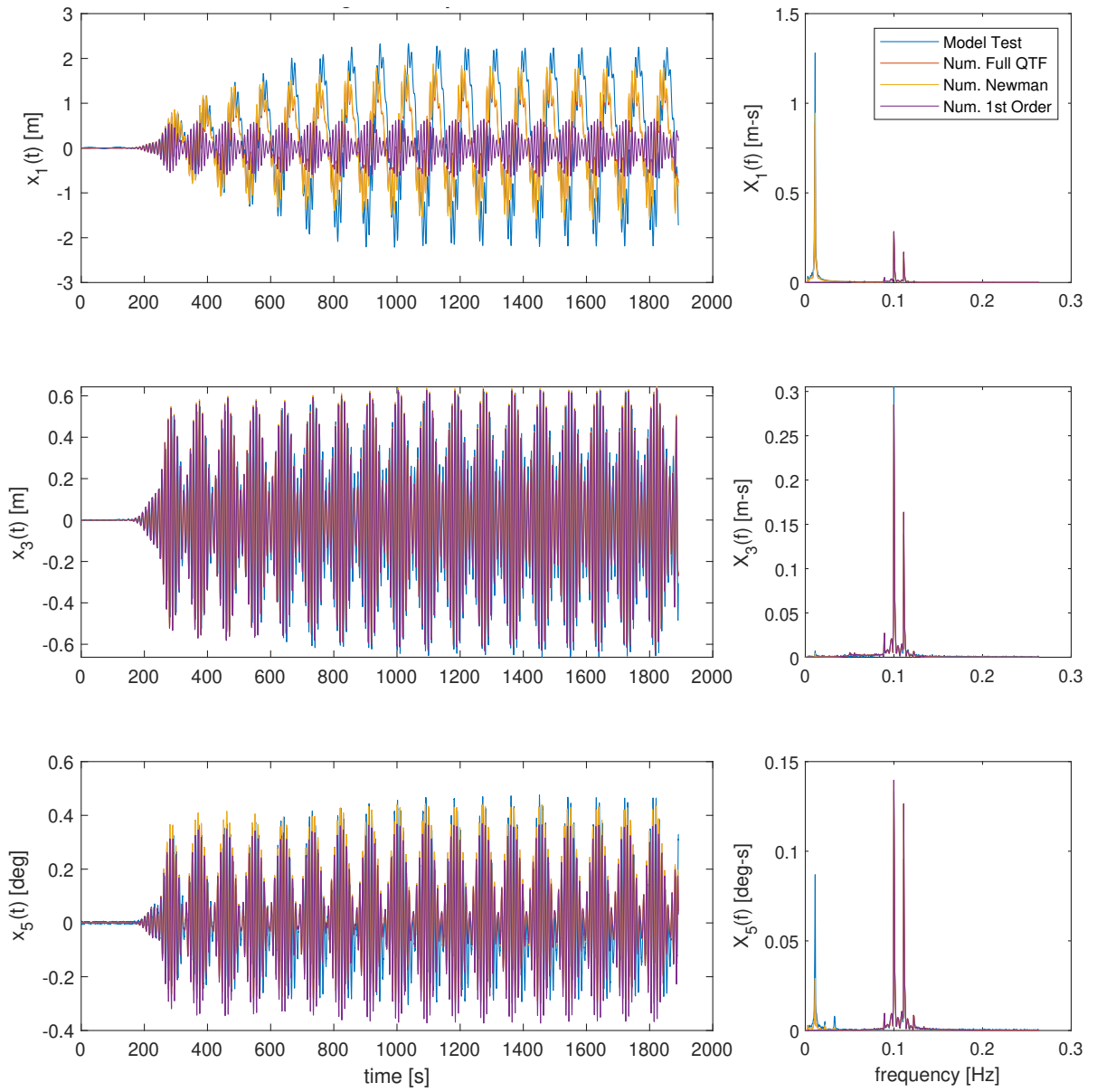


Figure D.2: Test 2 bichromatic wave motion reconstruction

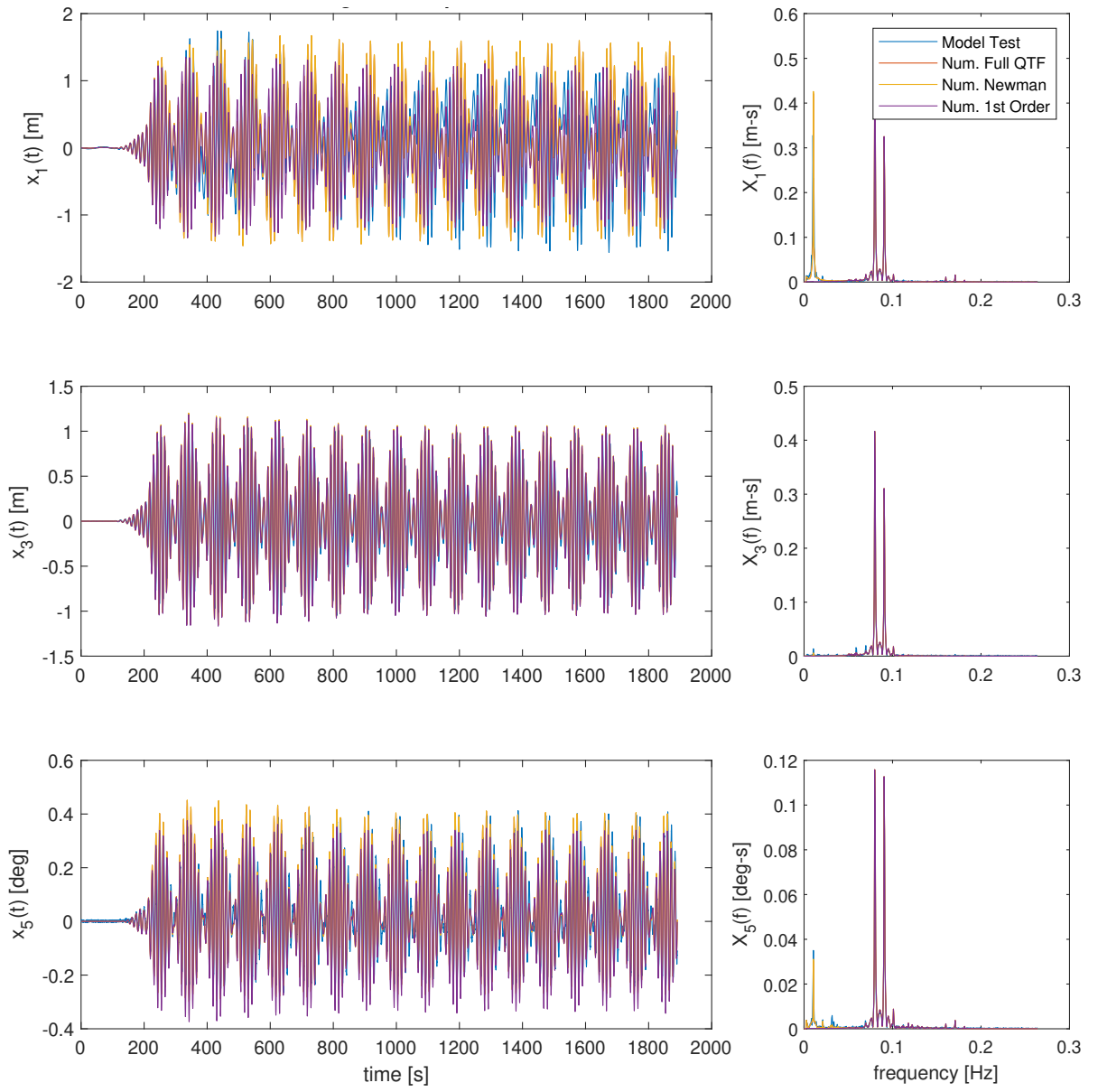


Figure D.3: Test 3 bichromatic wave motion reconstruction

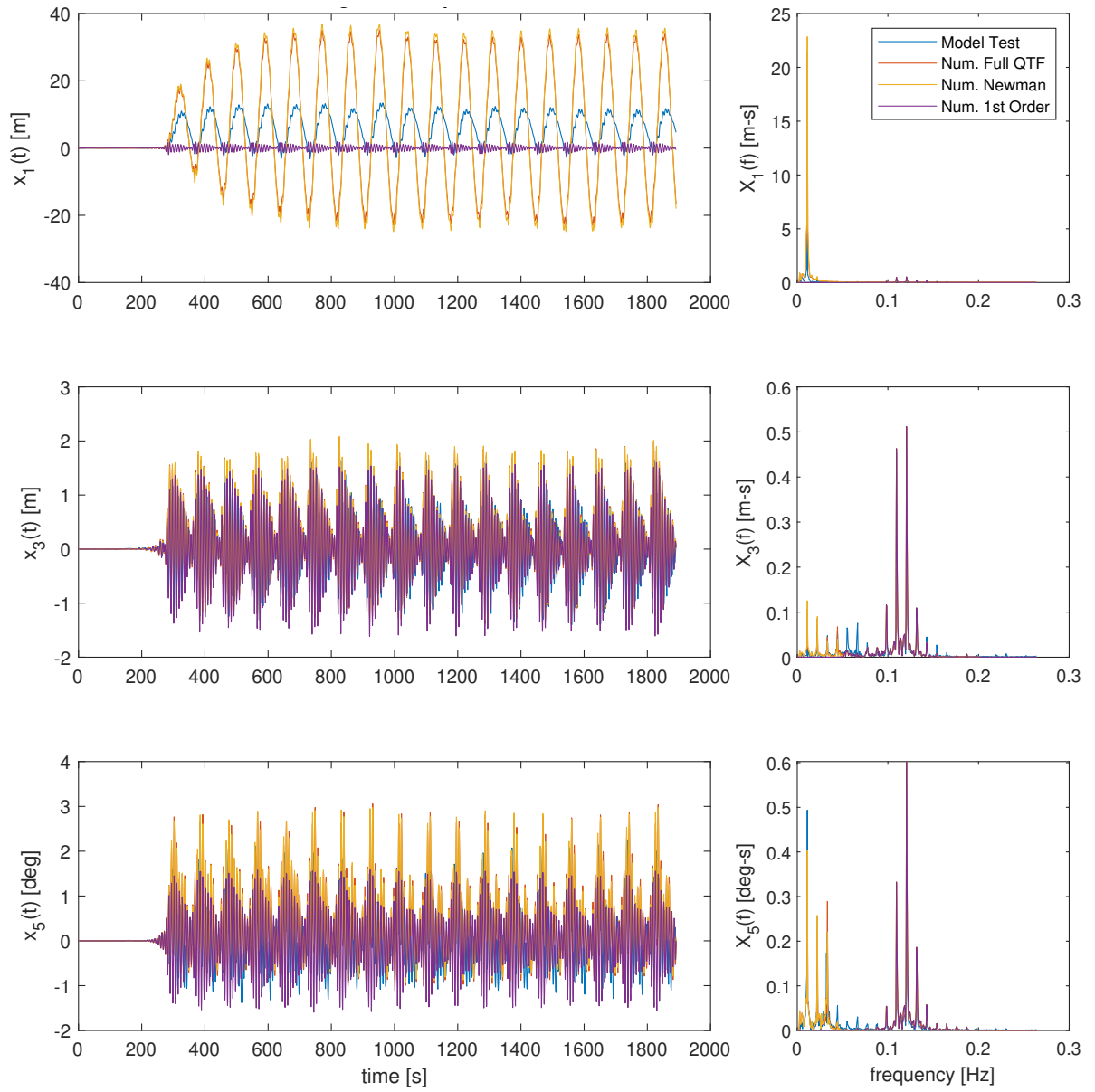


Figure D.4: Test 4 bichromatic wave motion reconstruction

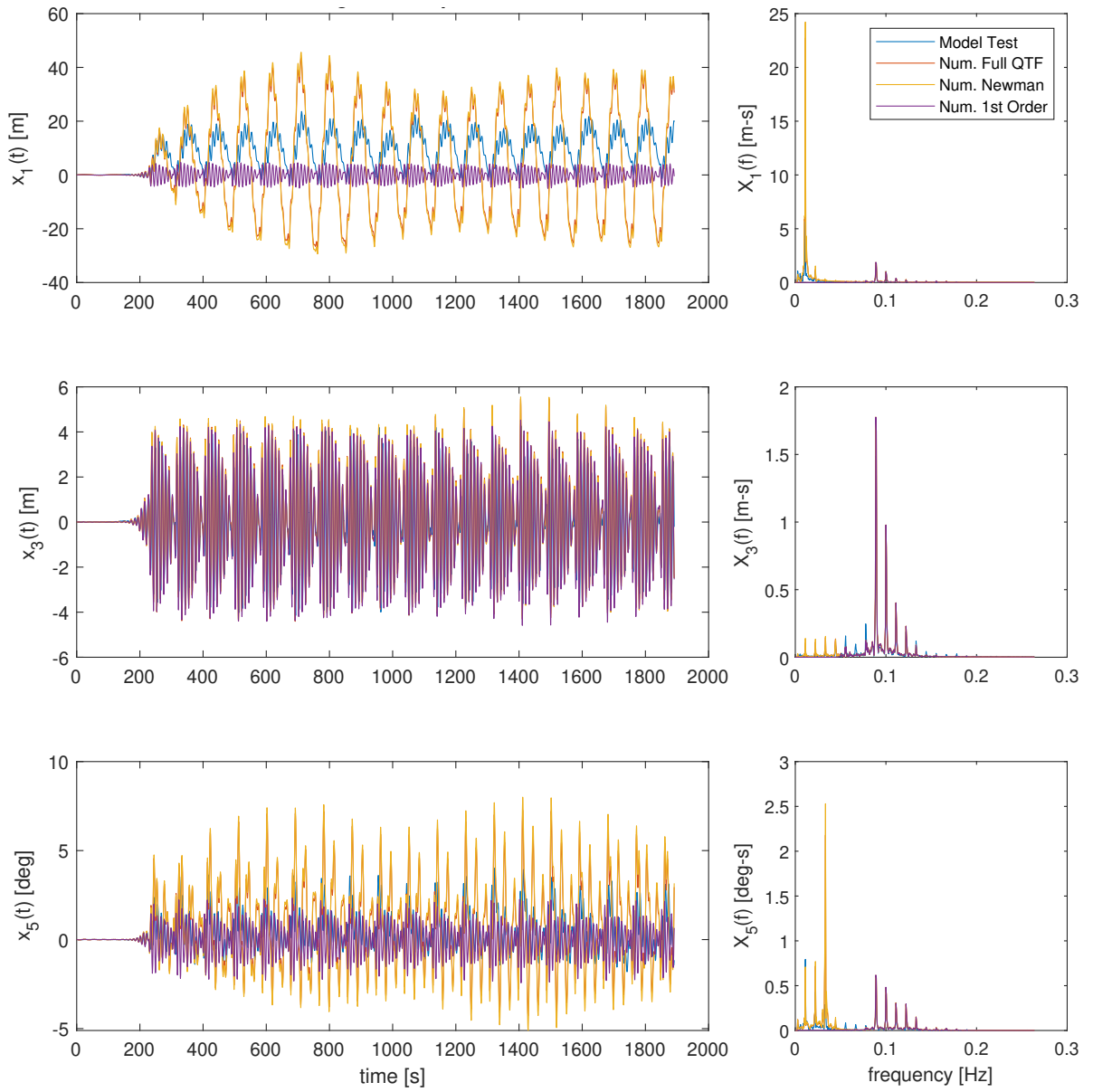


Figure D.5: Test 5 bichromatic wave motion reconstruction

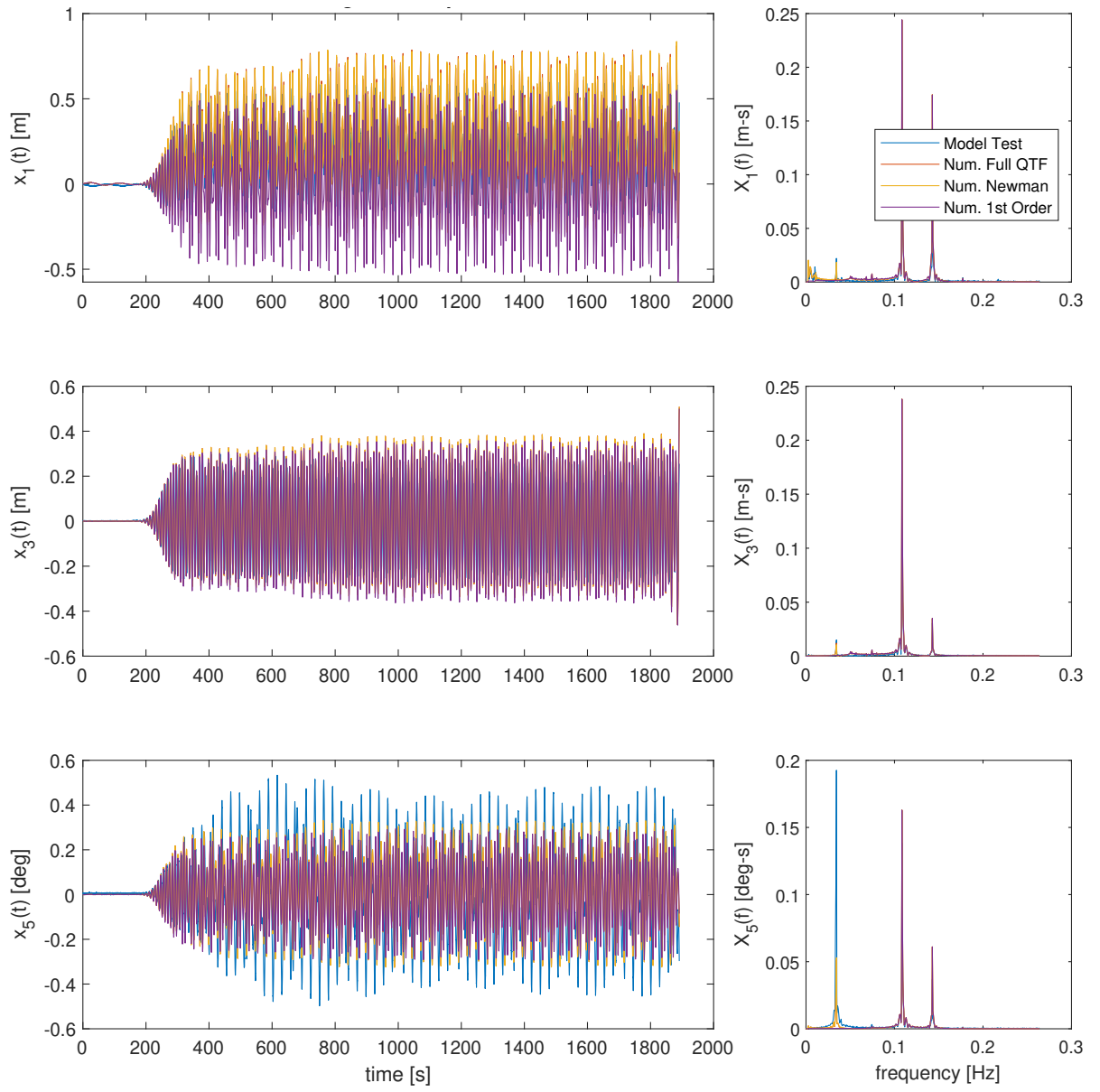


Figure D.6: Test 6 bichromatic wave motion reconstruction

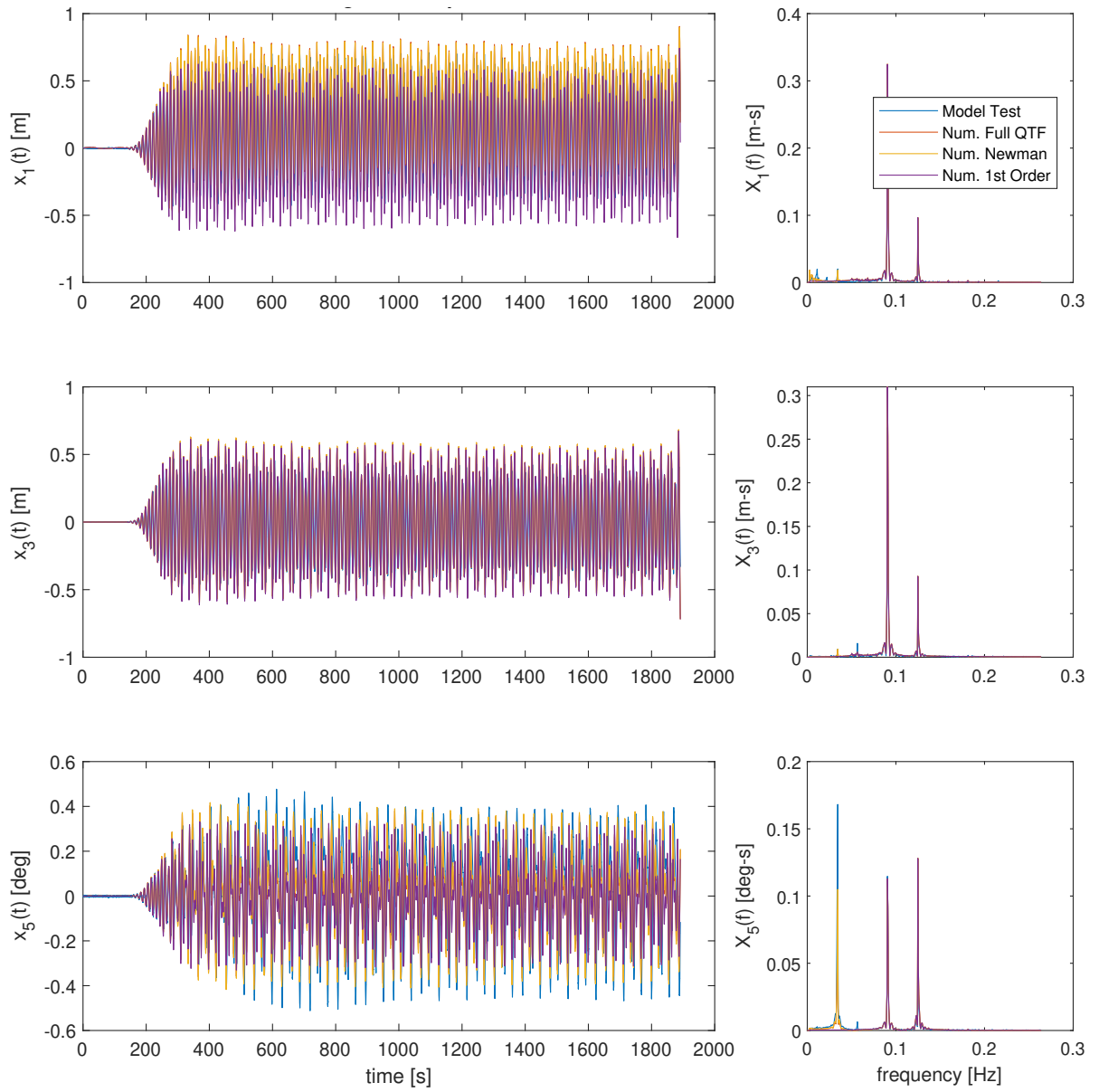


Figure D.7: Test 7 bichromatic wave motion reconstruction

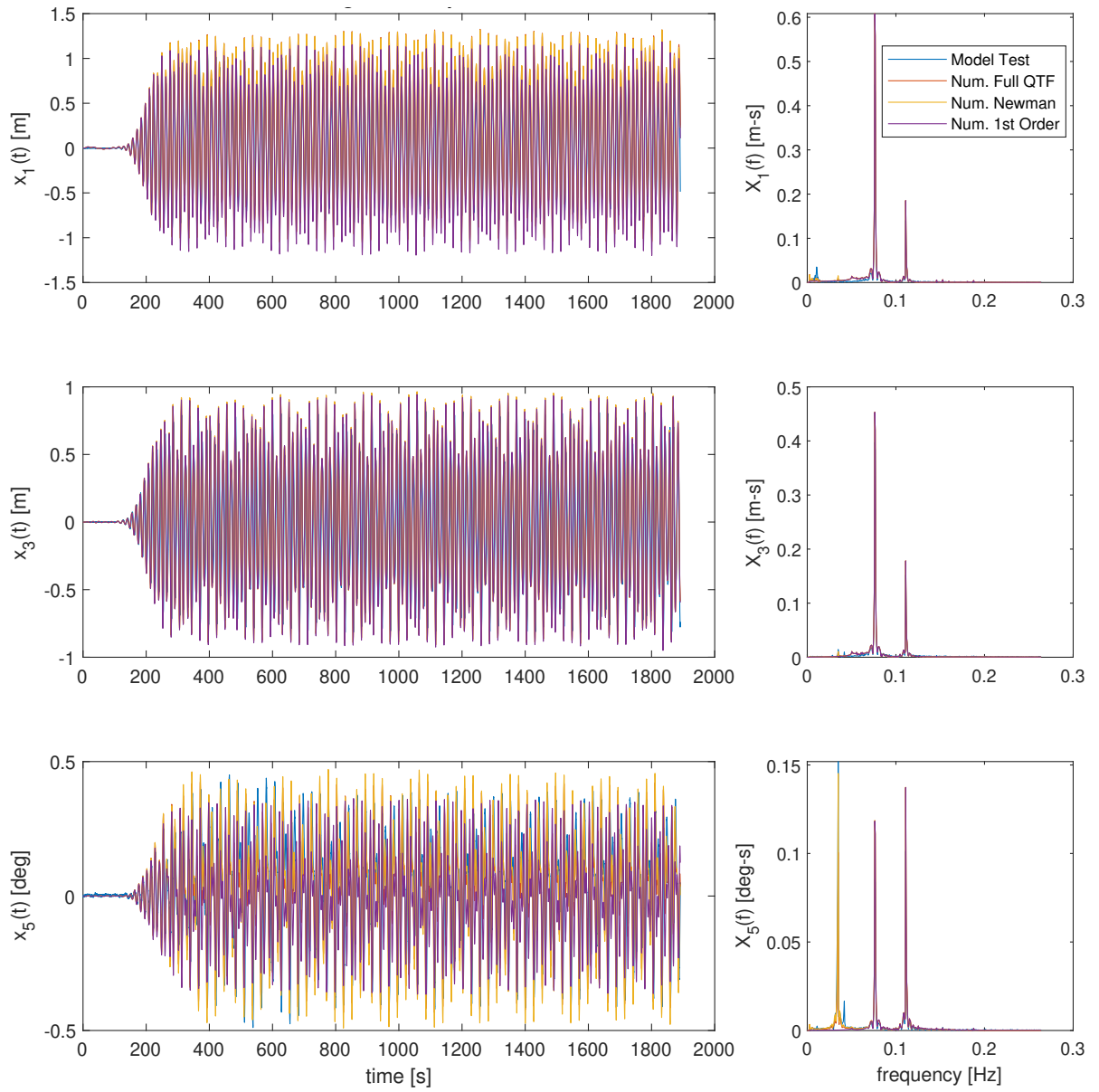


Figure D.8: Test 8 bichromatic wave motion reconstruction

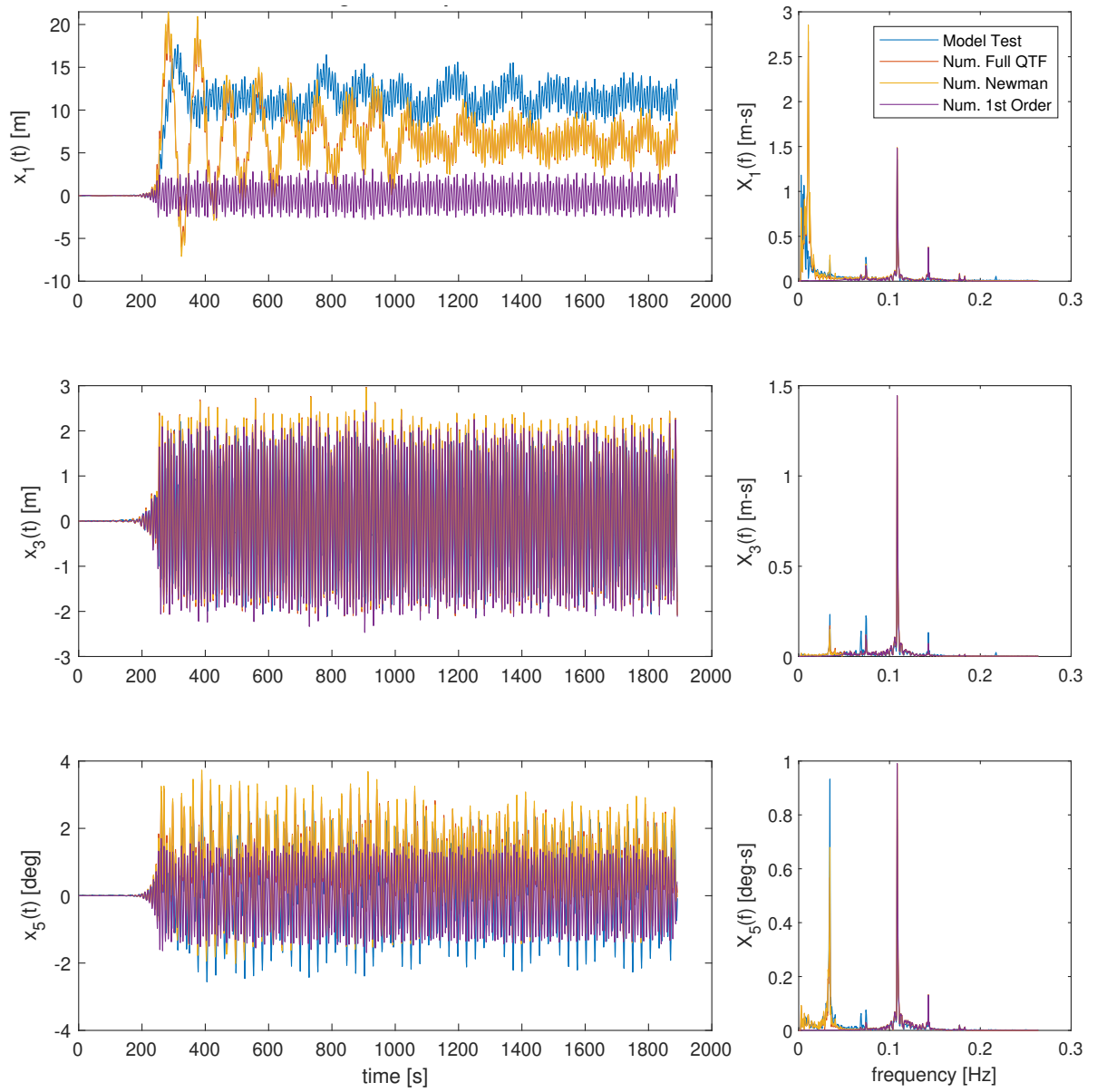


Figure D.9: Test 9 bichromatic wave motion reconstruction

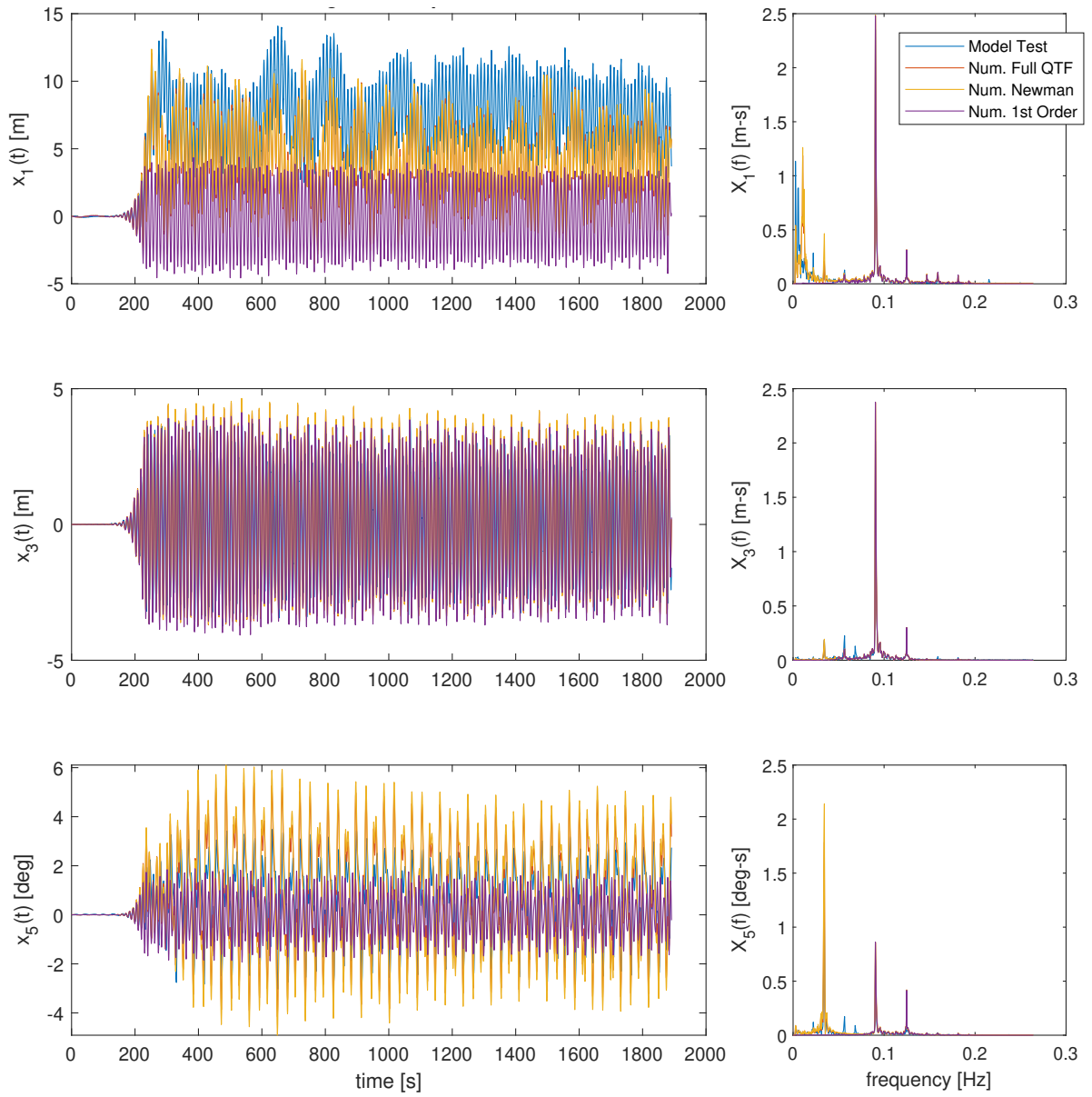
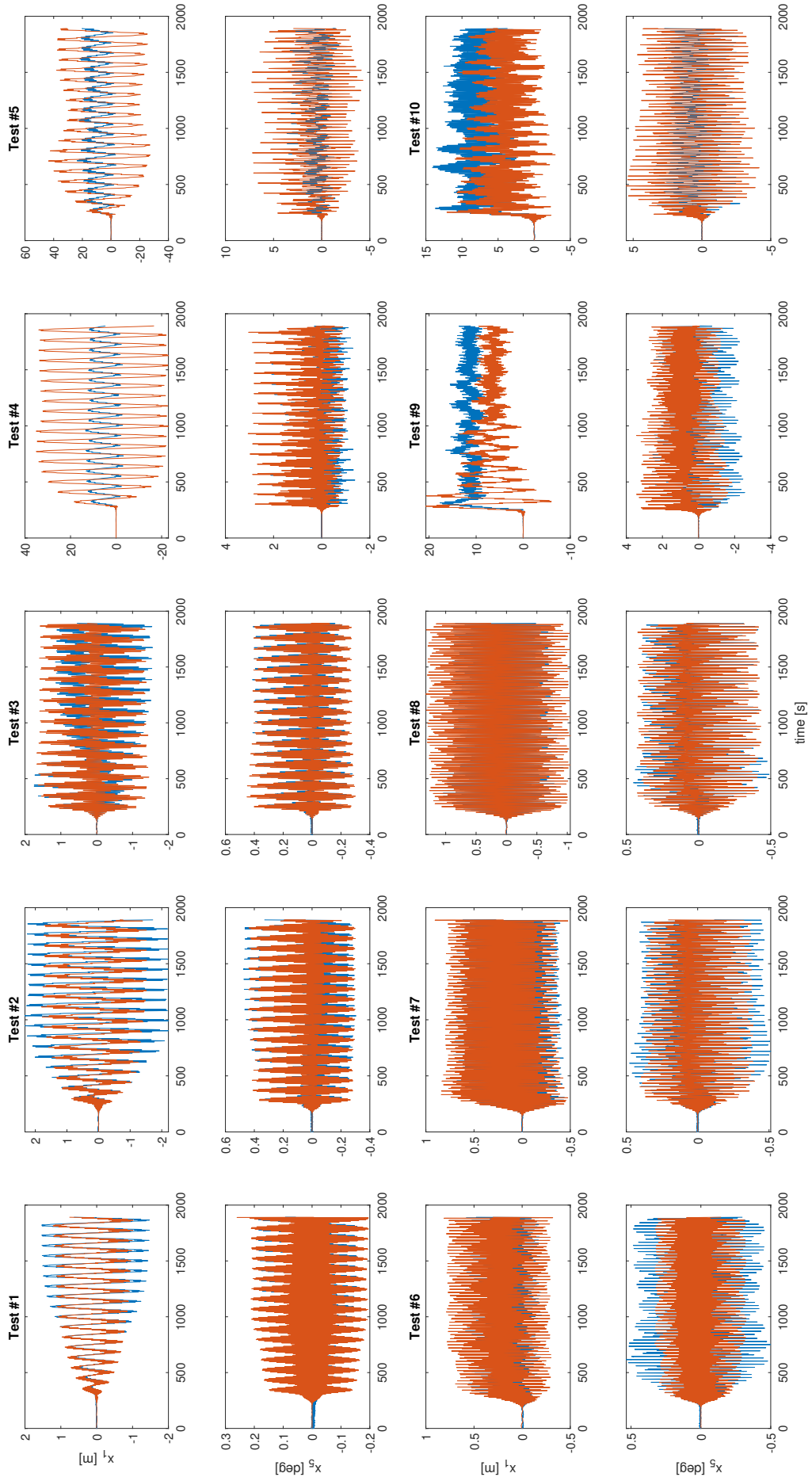


Figure D.10: Test 10 bichromatic wave motion reconstruction

Figure D.11 shows the results of all 10 bichromatic wave motion reconstruction time series. This is done for easier comparison between the results of the different conditions. In all plots the blue line represents the measured model response and the orange line represents the numerical reconstruction. For each test the surge and pitch response are shown. Note that the five tests on the top have a difference frequency of the surge natural frequency and the five tests on the bottom have a difference frequency of the pitch natural frequency.



E Irregular Time Series Reconstruction - Potential Flow Only

The results of the numerical reconstruction are shown below for the irregular wave model tests. For each group the wave elevation time series of the first test in the group was used. The group numbers correlate to the significant wave heights and peak frequencies referenced in table 4.3. For each group number plots are shown for surge, heave, and pitch. The legend shows the four values that are compared: the measured data from model tests, the numerical results using the constant average acceleration method and the full QTF, the numerical results using Newman's approximation, and the numerical results including only the first order excitation. Both time domain and frequency domain plots are shown.

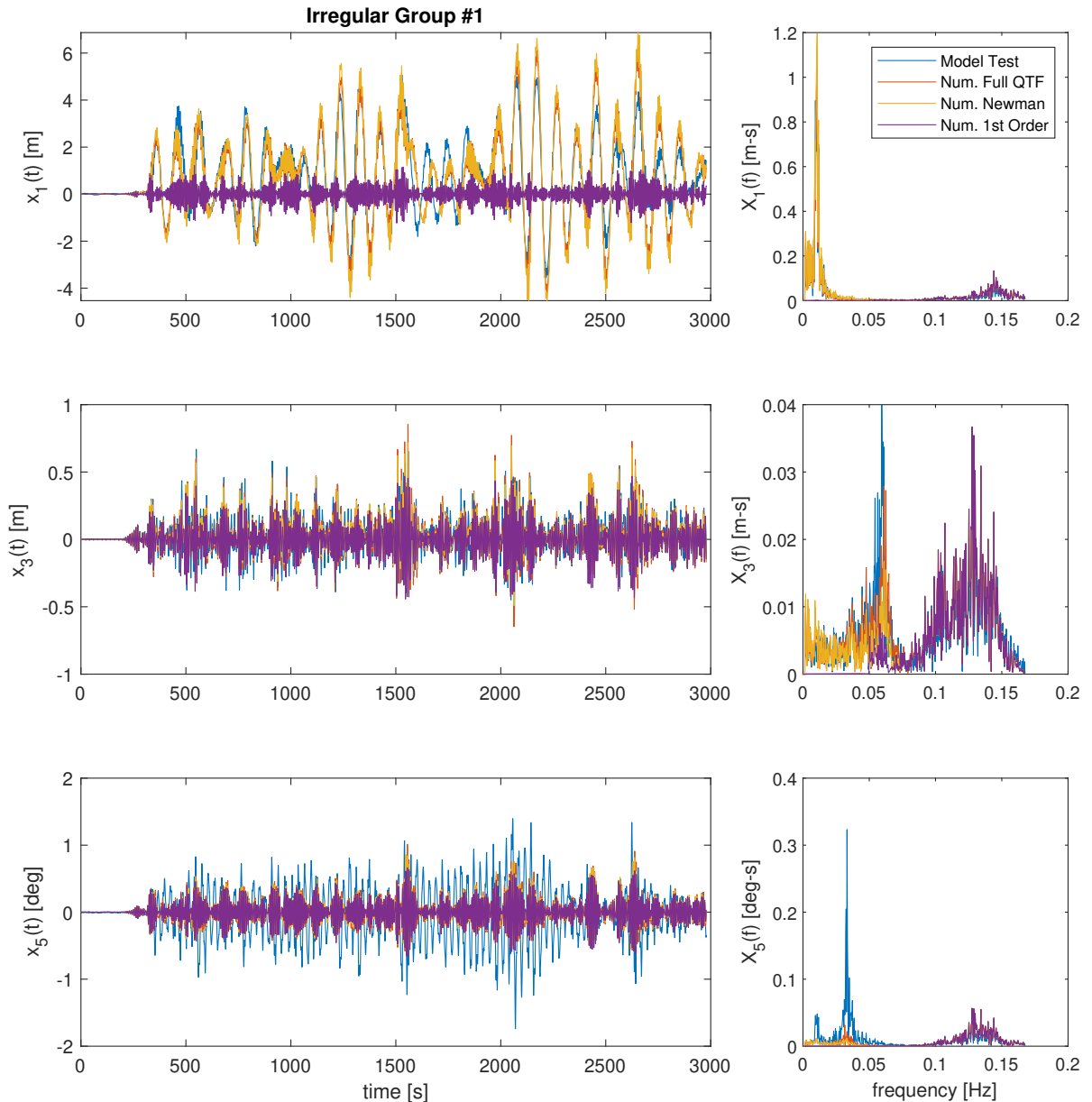


Figure E.1: Group 1 irregular wave motion reconstruction

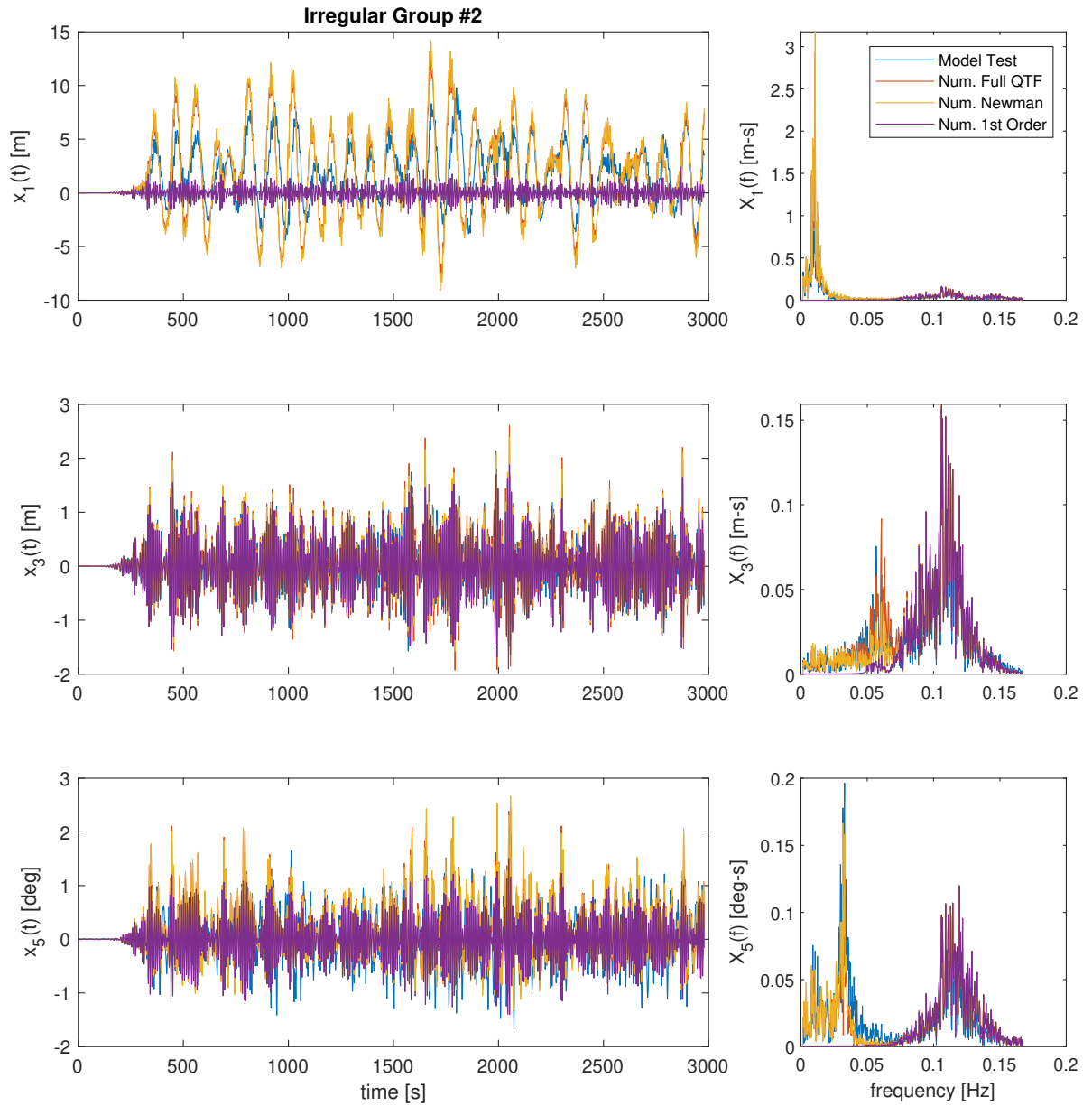


Figure E.2: Group 2 irregular wave motion reconstruction

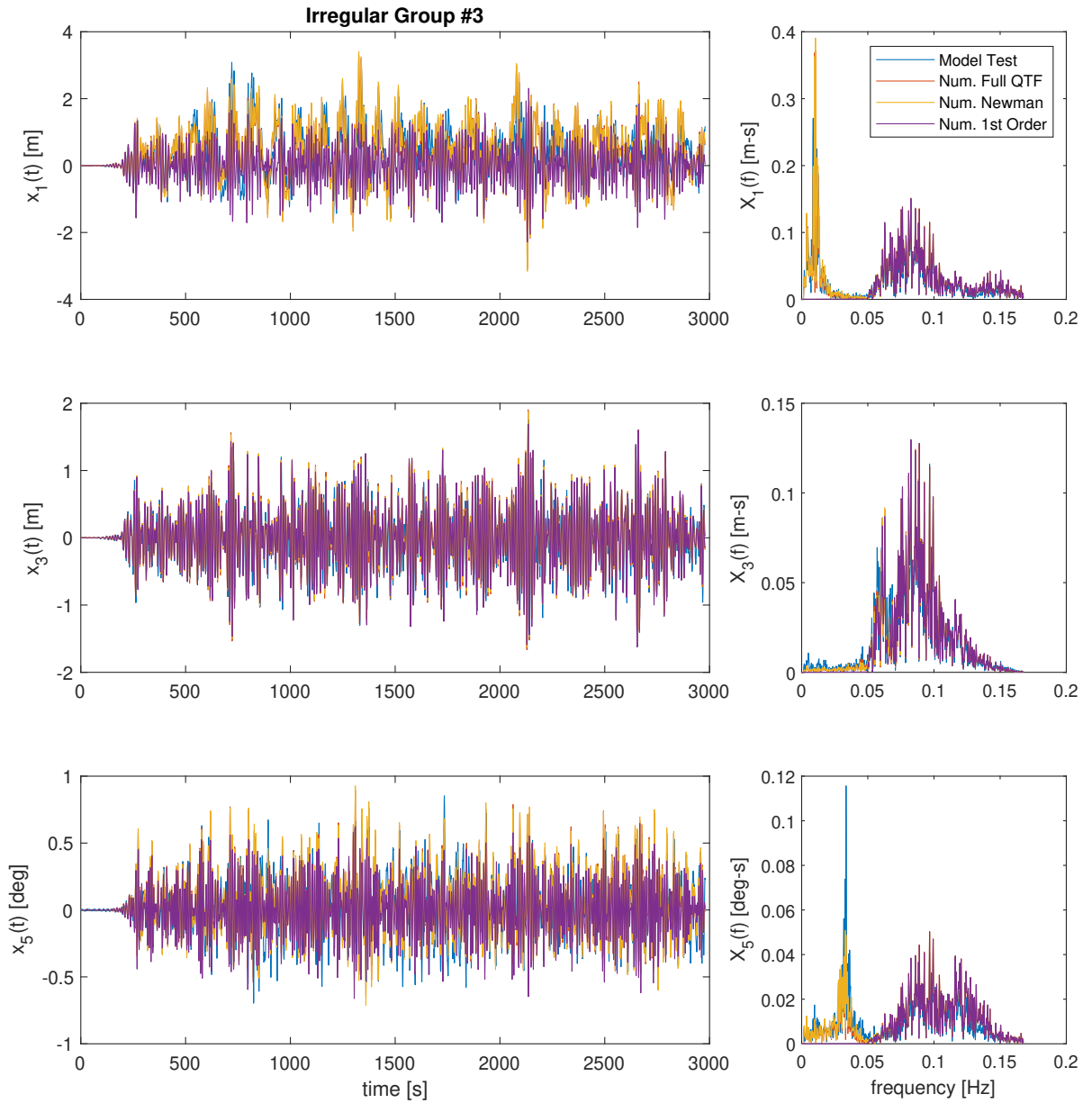


Figure E.3: Group 3 irregular wave motion reconstruction

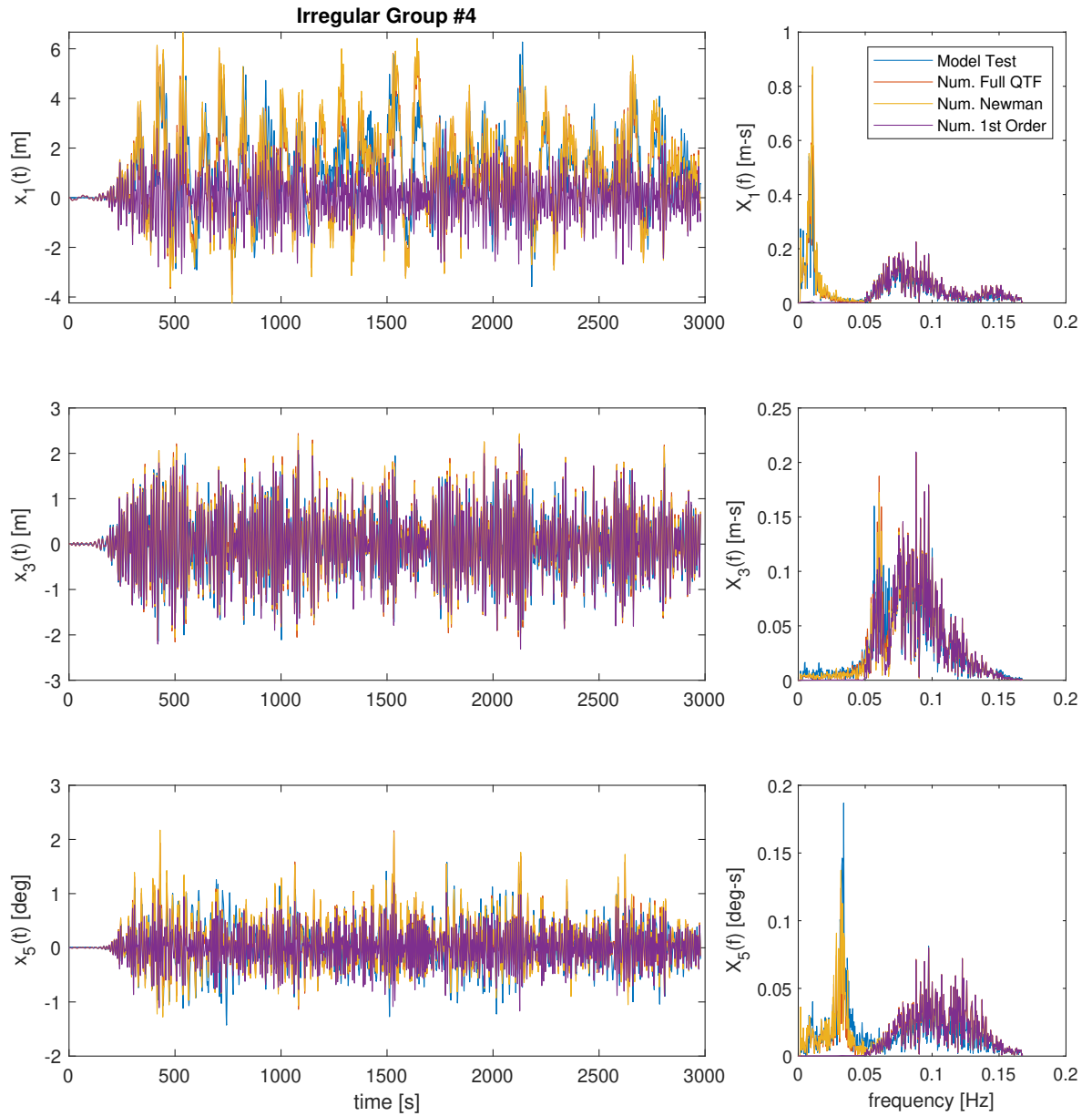


Figure E.4: Group 4 irregular wave motion reconstruction

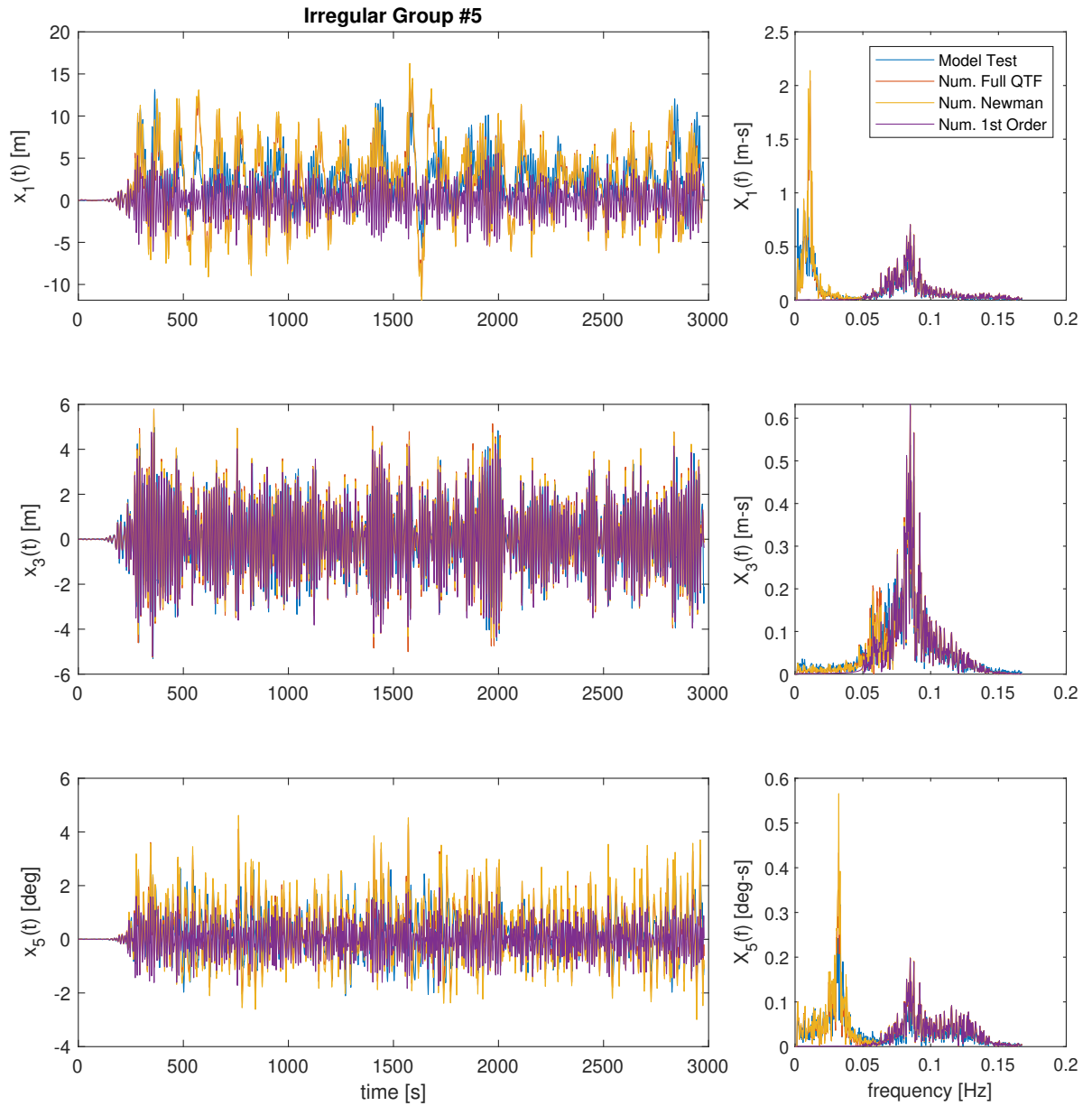


Figure E.5: Group 5 irregular wave motion reconstruction

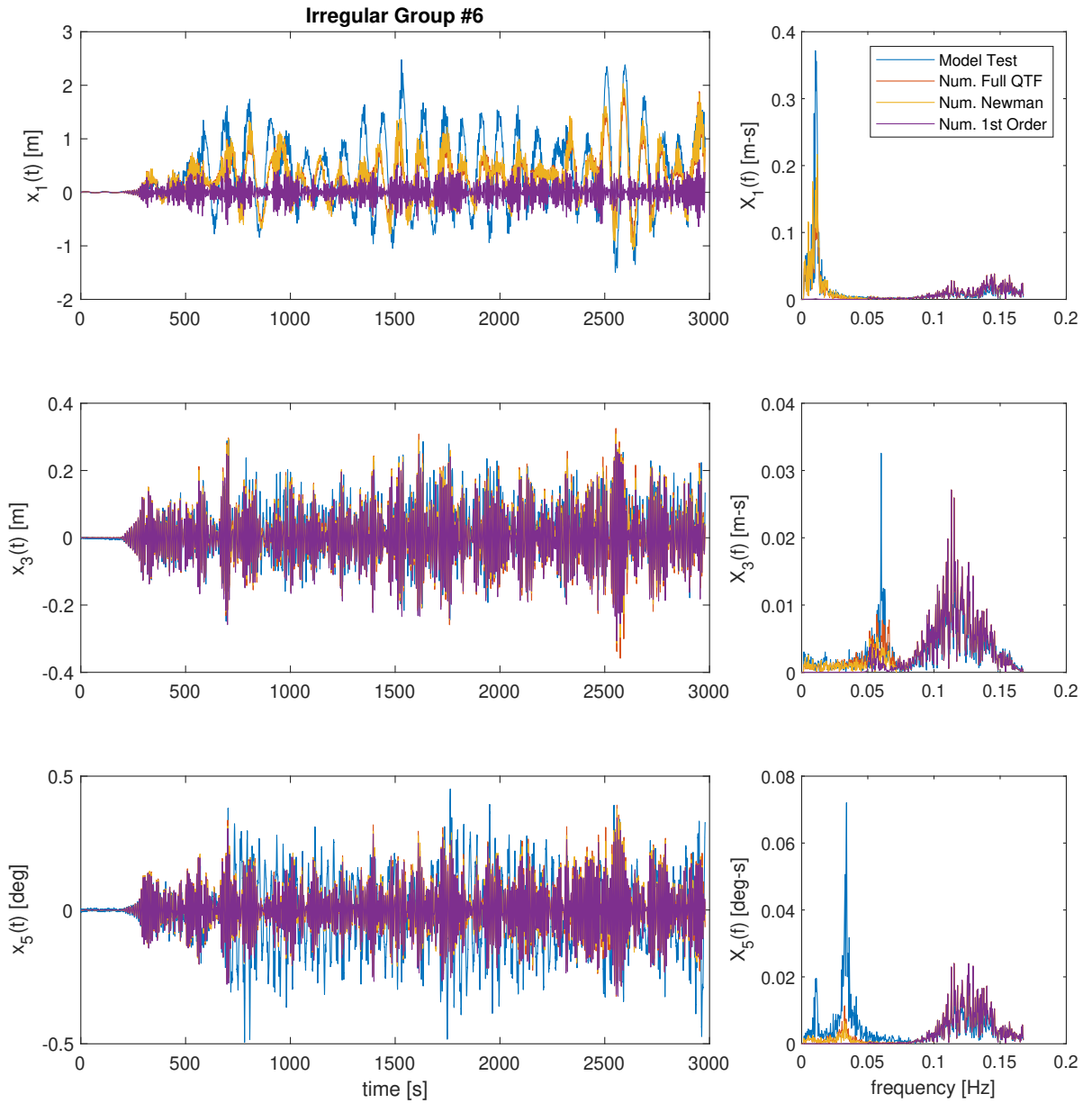


Figure E.6: Group 6 irregular wave motion reconstruction

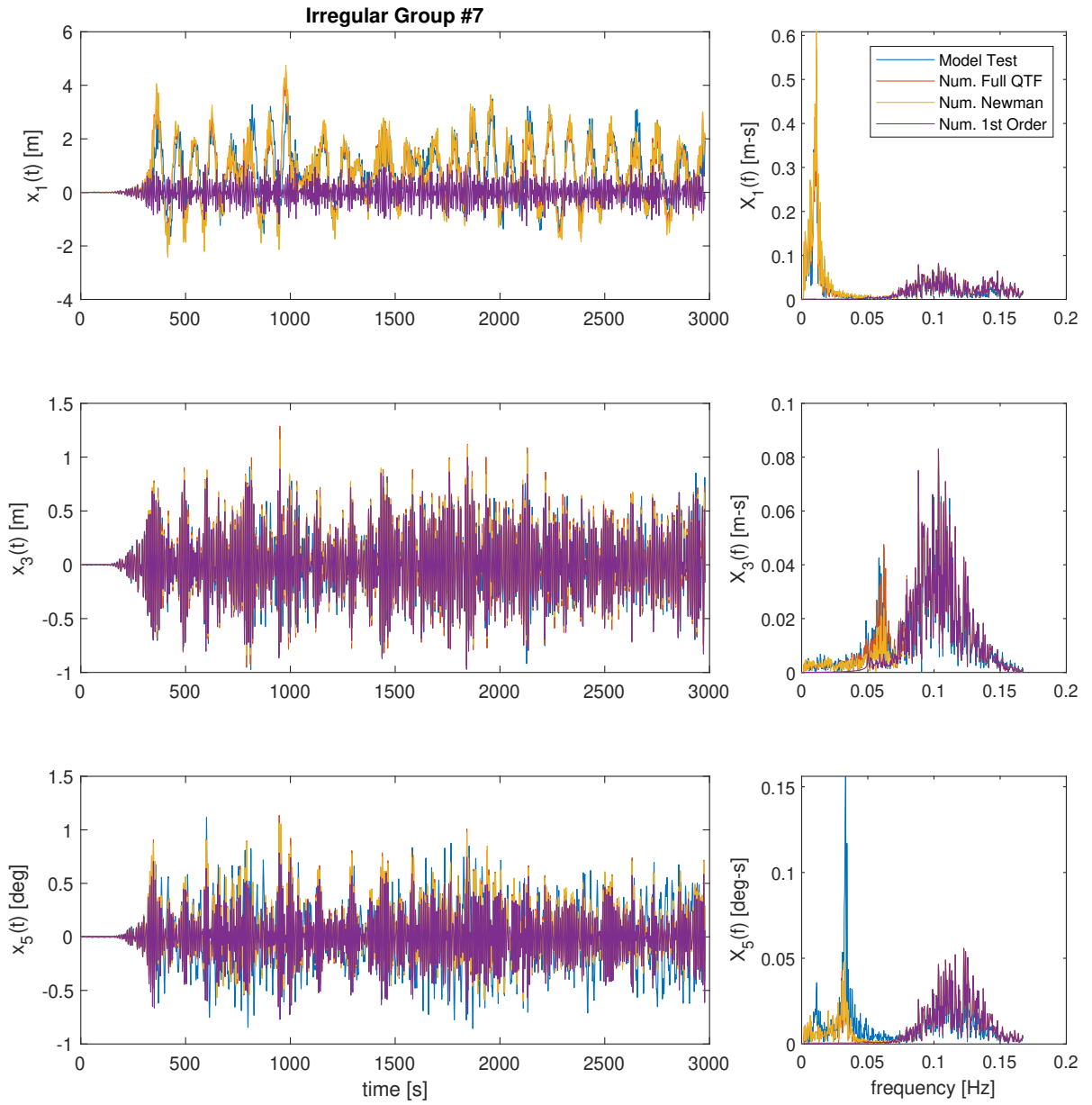


Figure E.7: Group 7 irregular wave motion reconstruction

F Empirical Transfer Functions

A second approach was used to validate the results of the potential flow analysis with the model test data. Instead of creating time series from the potential flow coefficients and comparing to the model data, the model data was used to create empirical coefficients to be compared with the numerically generated coefficients. The cross spectral analysis methods used in this project follow those proposed by Stansberg [27]. For this method only the irregular wave tests were considered as they provide information across a range of frequencies.

F.0.1 First Order Empirical Coefficients

First the linear relationship was determined. This process was only done to determine the linear motion transfer functions, and not to determine the first order forcing. It is assumed that the distribution of both the input (the free surface elevation) and the output (the motion response) are Gaussian distributed and that each frequency component is independent of the other frequency components [27]. It is also assumed that the response in each degree of freedom is uncoupled from the response in the other degrees of freedom. With these assumptions the two-sided auto spectrum of the free surface elevation, η , is given as in (71). In this equation and those to follow $\langle \rangle$ signifies statistical averaging. The implementation of this process will be discussed. Functions of frequency, (f) , are functions in the frequency domain. The free surface elevation and body motions were brought into the frequency domain by use of a fast Fourier transform.

$$S_{\eta\eta}(f) = \frac{1}{T_{span}} \langle |\eta(f)|^2 \rangle \quad (71)$$

The complex cross spectrum of the free surface elevation and the response motion, x , is described by (72). Again, $*$ represents the complex conjugate.

$$S_{\eta x}(f) = \frac{1}{T_{span}} \langle x(f)\eta(f)^* \rangle \quad (72)$$

After both of these spectra have been calculated the first order transfer function between the variables will follow from (73). Stansberg describes how this process will work even if noise is present in the signal which could include some nonlinear effects [27].

$$H_{x\eta}^{(1)}(f) = \frac{S_{\eta x}(f)}{S_{\eta\eta}(f)} \quad (73)$$

The statistical averaging was performed by averaging the results of multiple spectra. The irregular model test data described in table 4.3 includes multiple tests for a given statistical sea state description. First the transient was removed from each of the tests. For the irregular tests this left time series of over three hours. Each of these time series were then divided into shorter time series. It is important to still have time series long enough to track the low frequency motions. The length of the divided series was set to be at least 1000 s, which correlates to roughly 10 natural surge oscillations. Each of the original time series was then considered 11 separate time series, which allowed for more averaging of the spectra, which should provide smoother results. The broken time series also provide a significant advantage in the second order analysis. The storage size needed for the quadratic transfer function grows quadratically with the length of the time series. By shortening the time series, the amount of stored information needed to calculate the quadratic transfer function becomes manageable, and still allows for a better averaging process.

The means of the spectra described by (71) and (72) were taken across all tests of the same statistical parameters. A separate linear transfer function was found for each group of wave conditions for each of the six degrees of freedom. Given the head sea direction only the functions of surge, heave, and pitch provide meaningful information.

Coherence is a value that quantifies the linear correlation of the input and output. The complex amplitude coherence is described by Stansberg and is calculated following (74).

$$C_{\eta x}(f) = \frac{S_{\eta x}(f)}{\sqrt{S_{\eta\eta}(f)S_{xx}(f)}} \quad (74)$$

The absolute value of the coherence is typically used as a measure of how well a linear model can describe a relationship. Figure F.1 shows the linear motion transfer functions in surge, heave, and pitch. Also included are plots of the absolute value of the coherence, C_x , along the same frequency range. The frequency range where C_x is close to one is the frequency range that is well modeled by the linear transfer function. As expected C_x is

closest to 1 in the frequency range where there is wave energy; the irregular wave groups with the higher peak periods see better coherence at lower frequencies and vice versa.

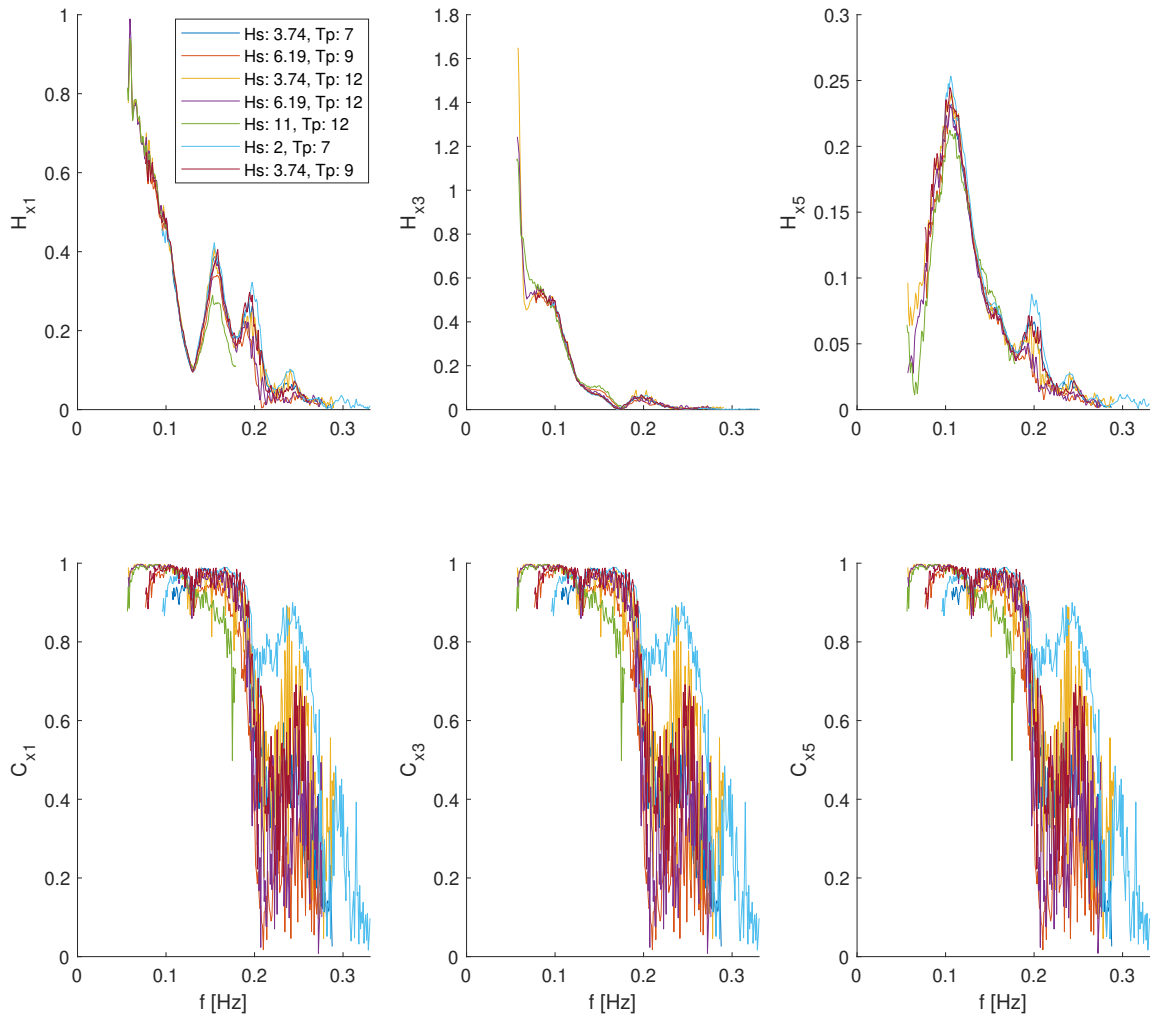


Figure F.1: Empirical first order transfer functions and linear coherence from irregular wave tests

These transfer empirical transfer functions show relatively good agreement to the first order potential flow transfer functions, shown for comparison in figure F.2.

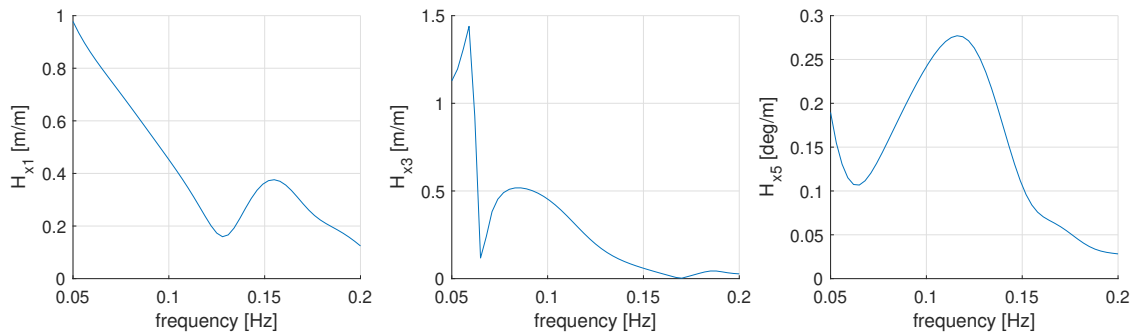


Figure F.2: Potential flow first order transfer functions for comparison

F.0.2 Second Order Empirical Coefficients

Next calculations were performed to find the empirical difference frequency force quadratic transfer function. In order to perform a cross bi-spectral analysis of wave elevation and low frequency force, a time series of the low frequency force is needed. This was not recorded in the model tests, so it needs to be estimated from the time series of the response. The methodology described by Fonseca was used for this task. Fonseca estimates that the low frequency surge motion of the platform in head seas can be thought of as fully decoupled from the other degrees of freedom without large errors [10]. With this assumption the surge motion is described as a one degree of freedom oscillator, and the force can be calculated following (75) as described in [10]. In this equation only the low frequency surge motion is desired to find the low frequency force. To achieve this the data was run through a band-pass filter with a frequency range of 0.0 Hz - 0.05 Hz. The frequency range was chosen to avoid any wave frequency energy, and thus any first order motion. This method assumes that the motion can be linearly decomposed into motions of different orders.

$$g^{(2)}(t) = m(\ddot{x}_1(t) + 2\xi\omega_n\dot{x}_1(t) + \omega_n^2x_1(t)) \quad (75)$$

The above equation makes use of the mass, natural frequency, and damping. The mass is a known value, but the natural frequency and damping need to either be iteratively estimated, or assumed based on a different test. Fonseca describes that in his work the natural frequency was obtained from the model tests while the damping ratio was iteratively changed to tune the results of the analysis. In this project it was attempted to obtain both values from the decay tests performed in the model basin described in [29].

The natural frequencies and damping ratios were estimated for surge, heave, and pitch from the model decay tests. A decay test is when no external forcing is present, and the model is initially displaced in one degree of freedom. The model is then released and allowed to oscillate freely. If the degree of freedom is under damped the model will oscillate with its damped natural frequency with amplitudes that logarithmically decay. The time and amplitude of successive peaks were measured from the decay tests. The undamped natural frequencies and damping ratios were then calculated. The results are shown in table F.1.

	Surge	Heave	Pitch
f_n [Hz]	0.011	0.061	0.033
ξ	0.083	0.057	0.031

Table F.1: Empirical natural frequencies and damping ratios from model decay tests

The complex cross bi-spectrum was calculated from the wave elevation and the low frequency excitation force as described by Stansberg [27] and Equation (76). Again $\langle \rangle$ means statistical averaging; this was performed in the same manner as described for the linear analysis by grouping the broken time series by peak period and significant wave height, and averaging spectra among the group.

$$S_{\eta\eta g^{(2)}}(f_n, f_m) = \langle g^{(2)}(f_n - f_m)\eta(f_n)\eta(f_m)^* \rangle \quad (76)$$

The same approach as used in the time series construction was used here for the limits of the frequency range considered. The upper and lower bounds of f_n and f_m were taken as the frequencies where 1.0% of the maximum wave energy was found. Given the small step size in frequency ($\frac{1}{T_{span}}$) the two dimensional matrix for the cross bi-spectrum and the quadratic transfer function to follow become very large and difficult to compute and store. Sparse arrays are used to account for this, where information is only stored between the upper and lower frequency bounds. Still, breaking the time series as described for statistical averaging, shortens the T_{span} , increasing the frequency step size, which leads to significant benefits in the size of the two dimensional arrays.

Next the quadratic transfer function is calculated following Equation (77) again described by Stansberg.

$$H^{(2)}(f_n, f_m) = \frac{S_{\eta\eta g^{(2)}}(f_n, f_m)}{S_{\eta\eta}(f_n)S_{\eta\eta}(f_m)} \quad (77)$$

The quadratic transfer function was calculate for surge, heave, and pitch, for each of the seven statistically averaged irregular wave groups. At the time of writing there is a problem with the calculations. The results do not show the expected trend and the order of magnitude of the results is also not as expected. As an example of this problem figure F.3 shows a diagonal of the real component of the quadratic transfer function at a difference frequency of the surge natural frequency. In the plot the blue line with a positive trend is the result of the potential flow study. The other seven lines along the bottom of the plot are the empirical functions from each irregular wave group. It is clear that at this stage there is a significant problem with the calculations.

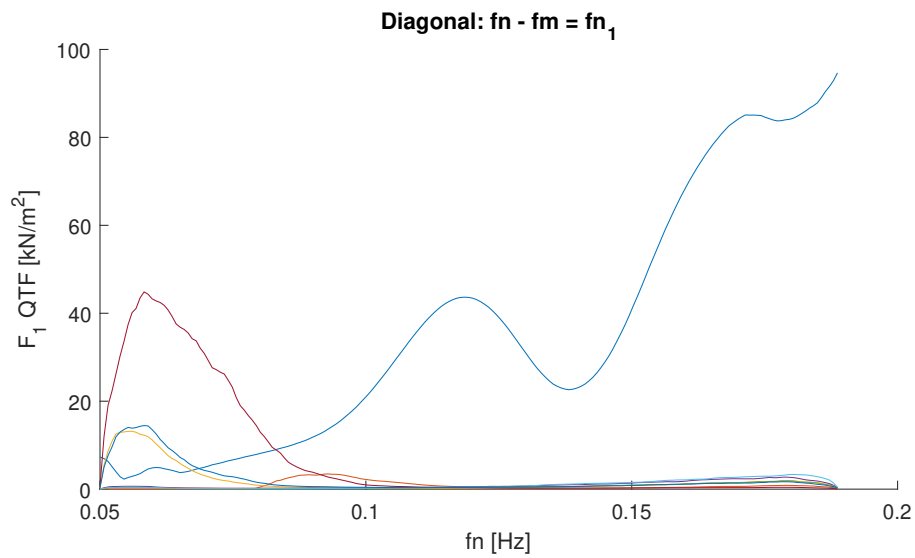


Figure F.3: Empirical and potential flow quadratic transfer function diagonal comparison

Fonseca et al. were able to obtain good results from the same data and with a similar approach [10]. This indicates that the method can be effective and it could be worked on more in the future.

G CFD Model Setup

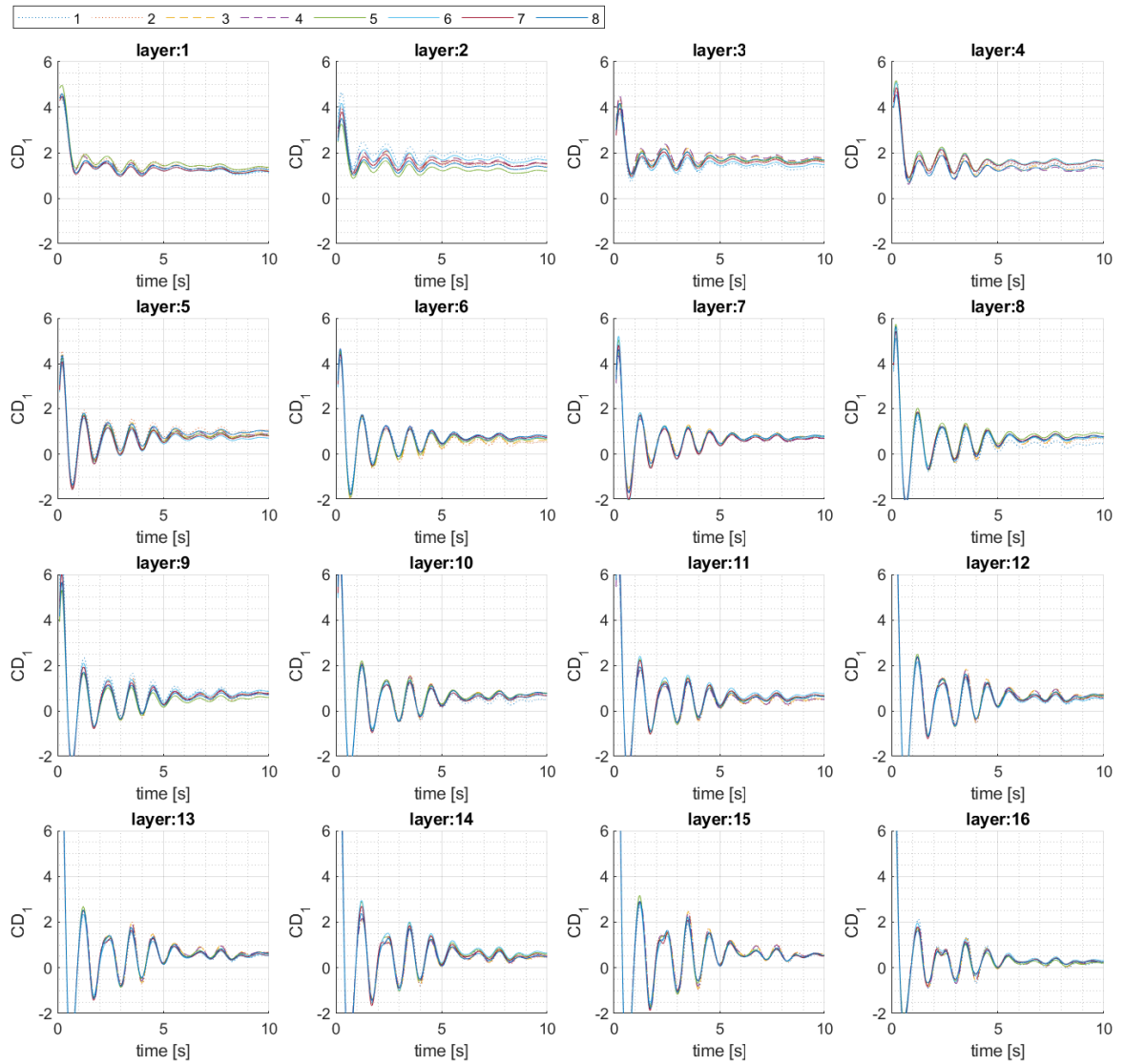


Figure G.1: Mesh convergence study with distributed force full time series using varying mesh densities

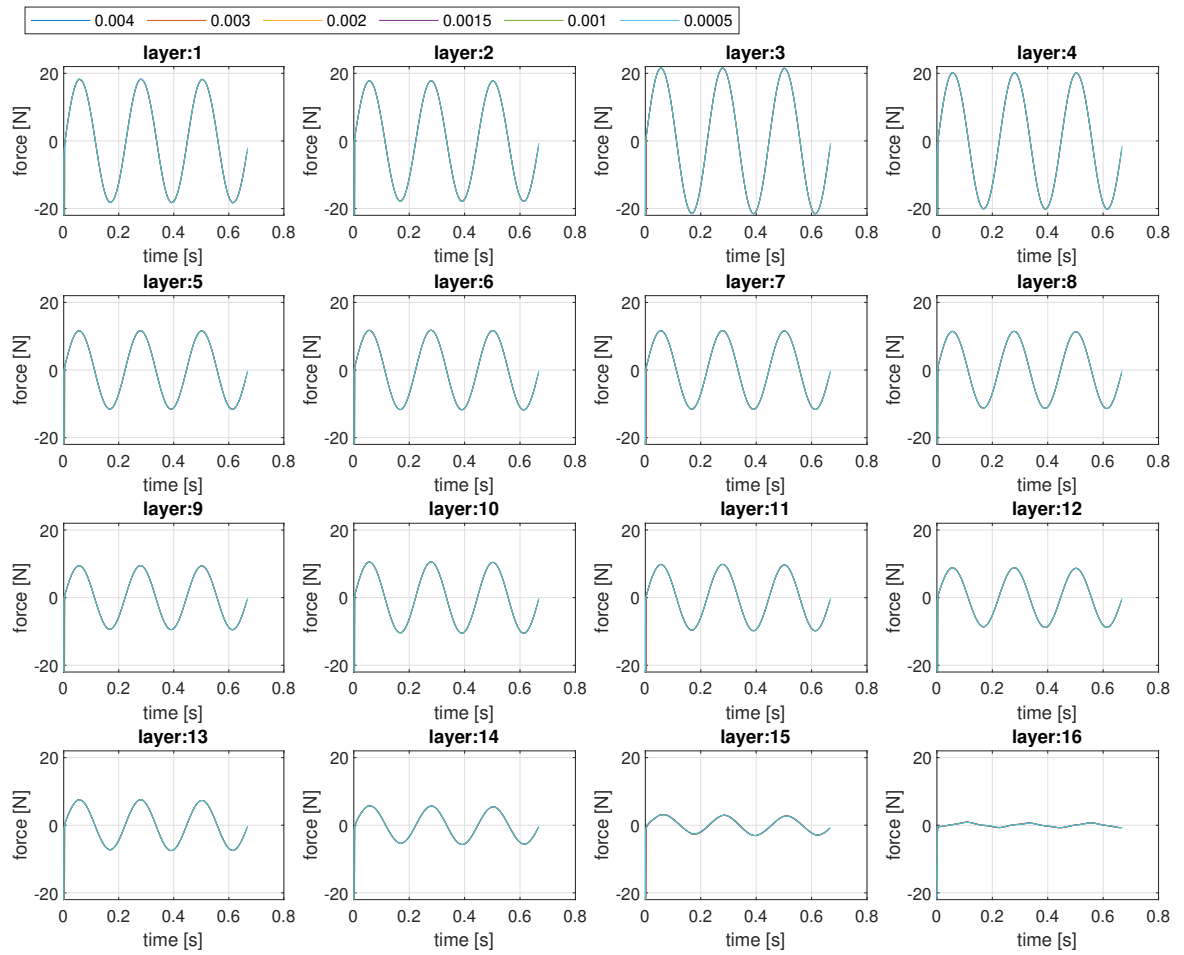


Figure G.2: Time step convergence study with distributed force time series using varying time steps

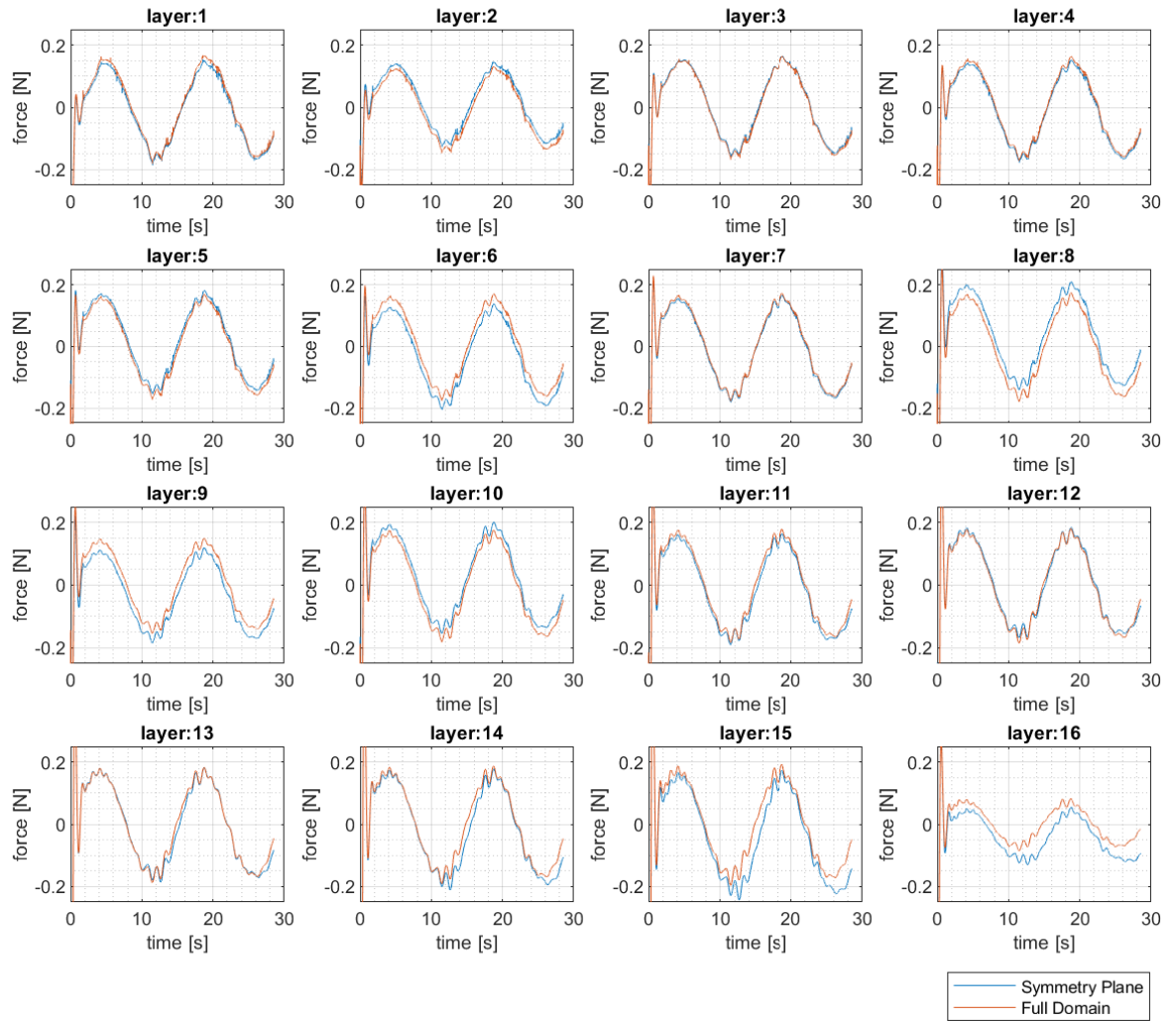


Figure G.3: Symmetry plane validation with distributed force time series

G.1 Initial and Boundary Conditions

Initial and boundary conditions are described for all field values used in the CFD simulations:

- “alpha.water” defines the volume fraction of water used for each cell in the VOF method. Initially every cell with a z coordinate lower than 0.0 is assigned a value of 1.0 and every cell with a z coordinate higher than 0.0 is assigned a value of 0.0. At all boundaries excluding the top of the domain a constraint of zero gradient is imposed. At the top, or the atmosphere, a uniform value of 0.0 is imposed.
- “gammaInt” is the value of intermittency used in the transition turbulence model. Every cell is initially assigned a value of 1.0, indicating fully turbulent flow. This value is fixed at the three sides of the domain (not including the symmetry plane) and at seafloor and atmosphere. At the symmetry plane a symmetry plane condition is imposed meaning that the cells on this boundary view artificial cells mirrored to them with the same values. On the surface of the platform a zero gradient condition is imposed.
- “k” is the value of turbulent kinetic energy used in the turbulence model. Its initial condition is based on recommendations found in the OpenFOAM user manual based on a maximum velocity and turbulence intensity of 5%. This value is fixed at the extents of the domain, and a special wall function is used as the boundary condition at the platform surface.
- “nut” is the value of turbulent viscosity used in the turbulence model. Its initial and boundary conditions are similar to those of k (turbulent kinetic energy).
- “omega” is the value of dissipation rate of turbulence used in the turbulence model. Its initial and boundary conditions are also similar to those of k (turbulent kinetic energy).
- “p_rgh” is the dynamic pressure. It is initially set to 0.0. At the symmetry plane a symmetry plane condition is used. At all other boundaries excluding the atmosphere but including the platform surface a condition is set which fixes the flux of the pressure. At the atmosphere the pressure is adjusted to make sure that the total pressure is equal to atmospheric pressure.
- “pointDisplacement” is a variable that states where each cell is displaced due to the mesh motion in the overset method. This is initially 0.0 everywhere. The boundaries of the background domain are fixed to remain at 0.0. The boundaries of the overset domain including the surface of the platform are calculated based on the overset method at each time step.
- “ReThetat” is the turbulent transition Reynolds number used in the transition turbulence model. Its initial condition is based on OpenFOAM user manual recommendations based on the initial turbulent kinetic energy and the characteristic size of the body. This value is fixed at the extents of the domain, and is zero gradient is allowed on the platform surface. A symmetry plane condition is again used for the symmetry plane.
- “U” is the velocity and is initially set to 0.0 in each direction for all cells other than on the surface of the platform. On the surface of the platform a velocity in the x-direction is imposed which is based on the calculation of the initial velocity of the platform in its oscillatory motion. The oscillating motion of the platform is sinusoidal and starts with zero displacement, meaning maximum velocity. If the velocity is not initialized correctly the solution struggles to develop and can diverge. The extents of the domain and the seafloor are assigned slip type boundary conditions, meaning that the velocity can move along the surface without any viscous shear. The atmosphere uses a pressure inlet outlet velocity type condition which similar to the pressure condition helps maintain atmospheric pressure at the boundary.
- “zoneID” is a variable used in the overset method to assign each cell to a particular domain. All cells from the background domain have a value of 0.0 and all cells of the overset domain have a value of 1.0. This does not change throughout the simulation.

H Single Forced Oscillation Post-Processing

Time series of the force on each elevation layer are shown for each of the eight single forced oscillation cases. The plots show the total force in blue, labeled “OpenFOAM”, the potential flow predicted force in orange, labeled “Potential Flow”, and the difference between the two in yellow, labeled “Viscous Difference”. The extraction of the viscous correction coefficients is based on the viscous difference component for each layer.

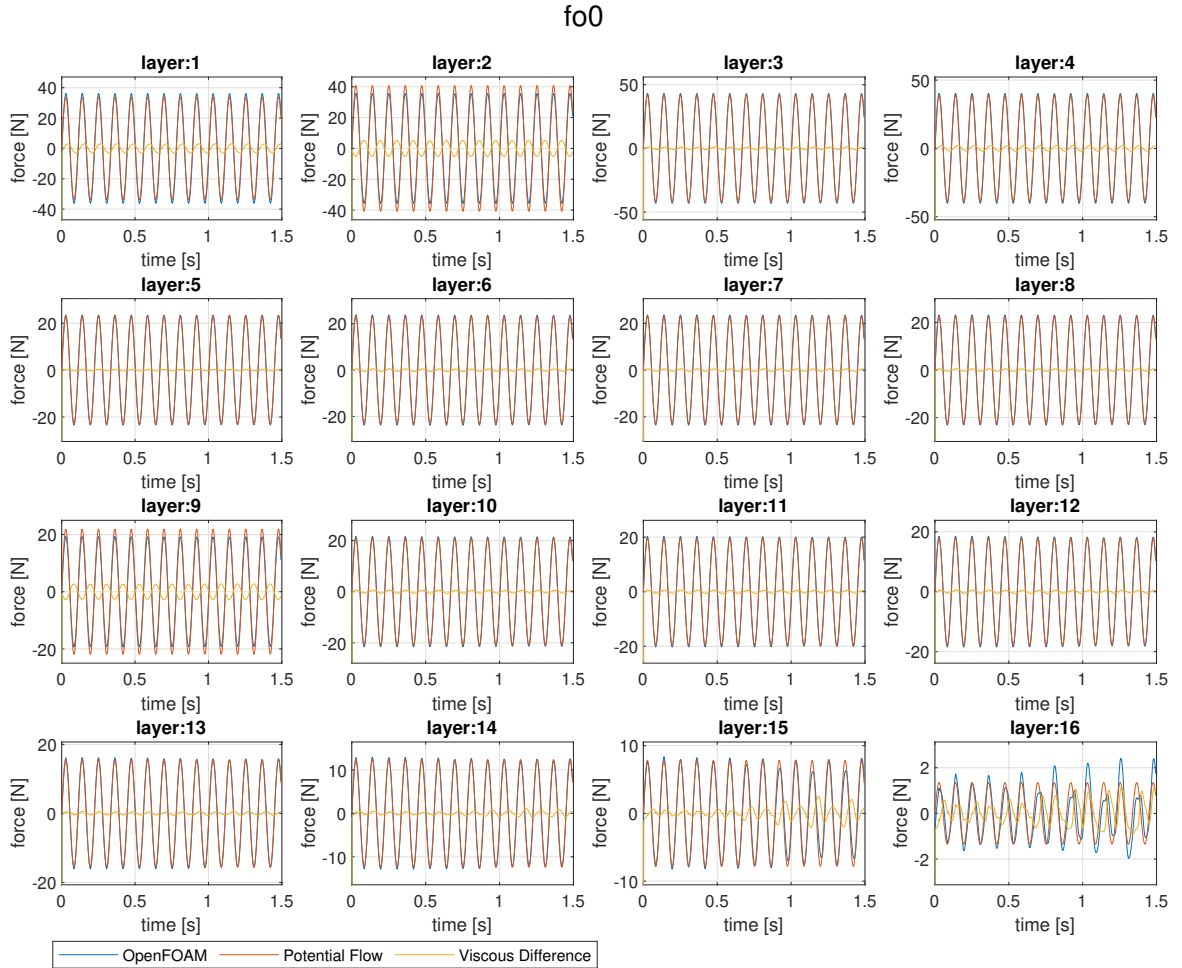


Figure H.1: Decomposed distributed force time series for case: *fo0*

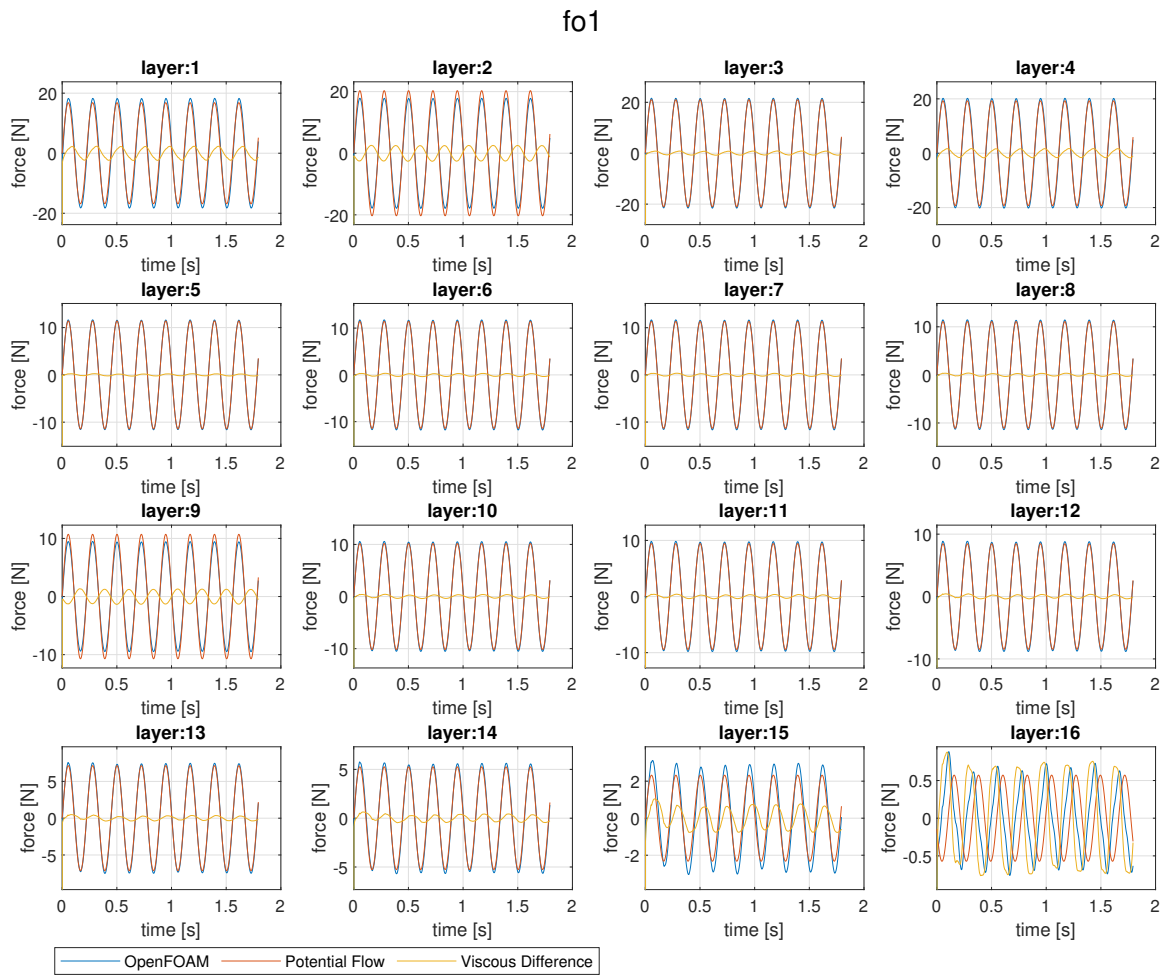


Figure H.2: Decomposed distributed force time series for case: *fo1*

fo2

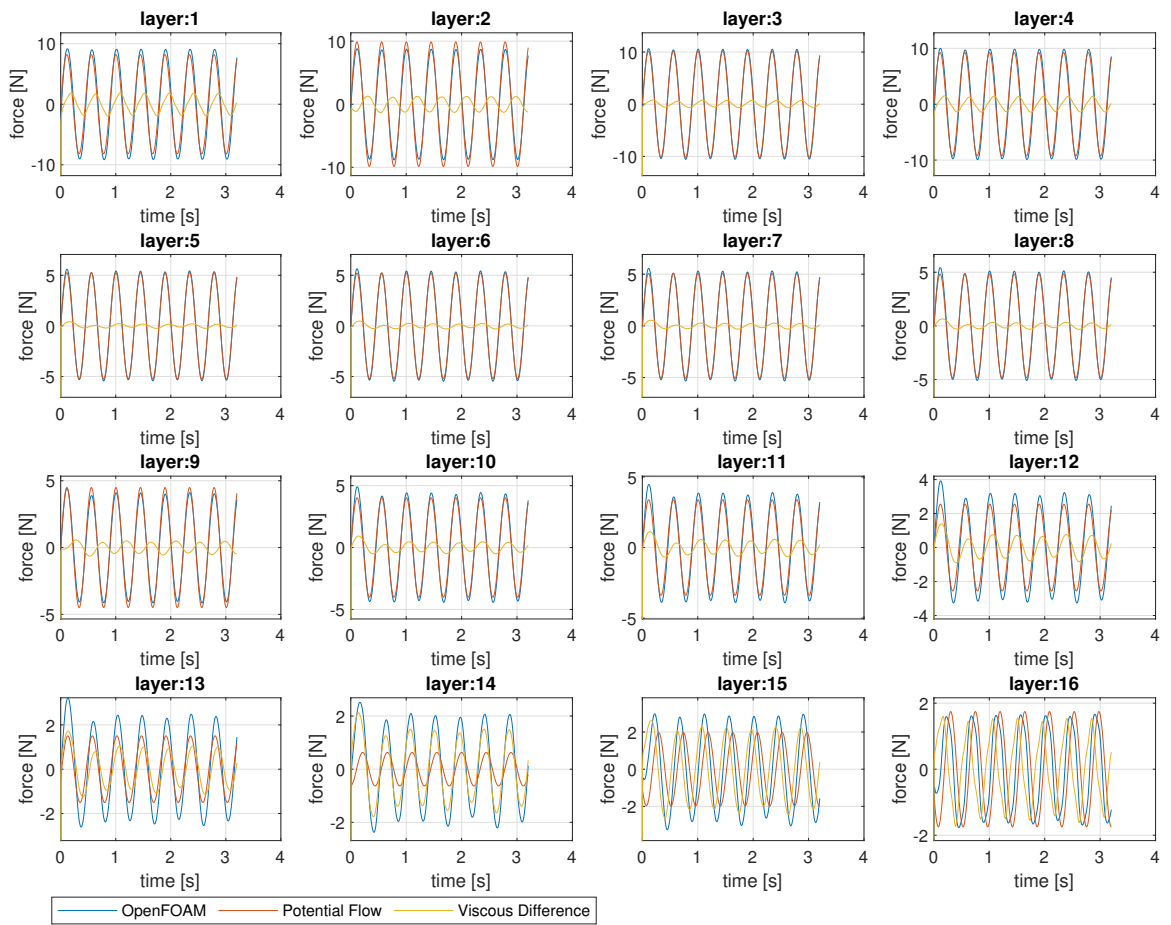


Figure H.3: Decomposed distributed force time series for case: *fo2*

fo3

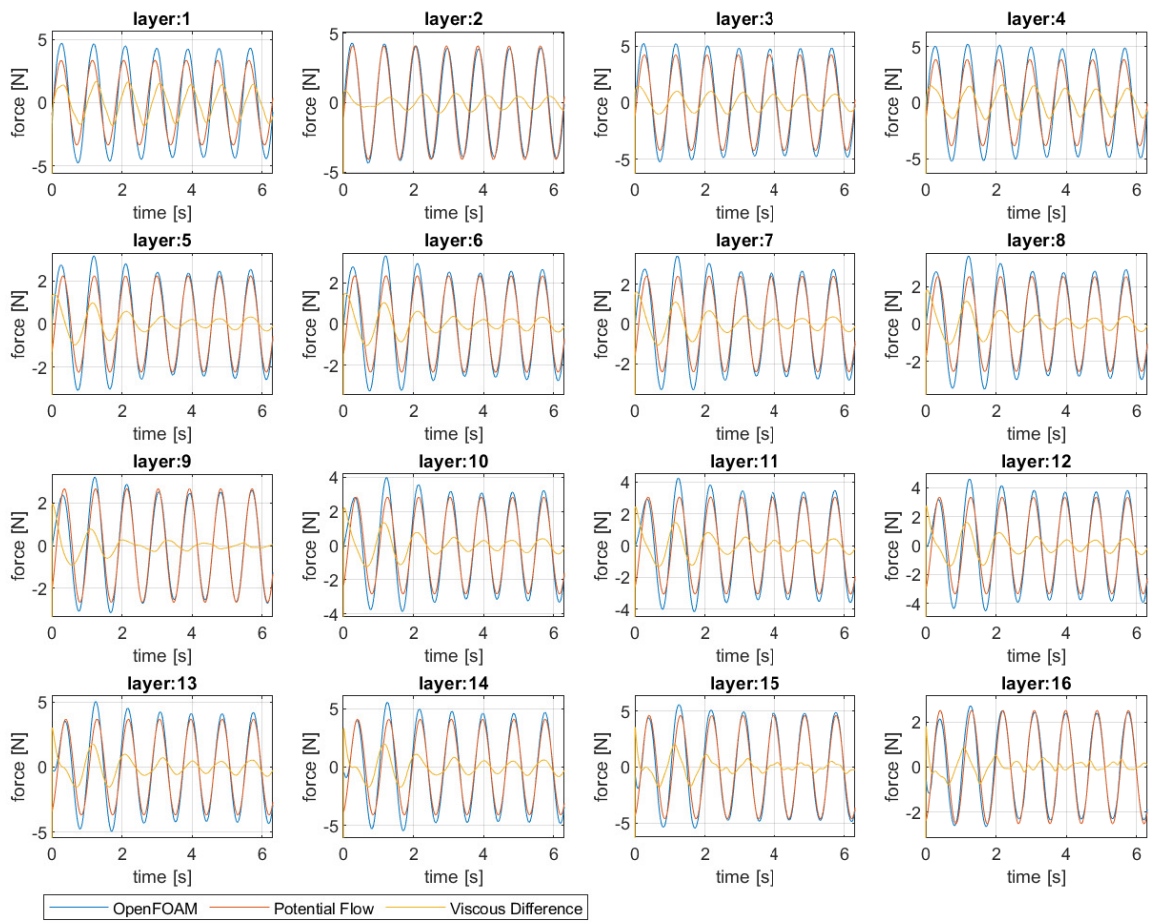


Figure H.4: Decomposed distributed force time series for case: *fo3*

fo4

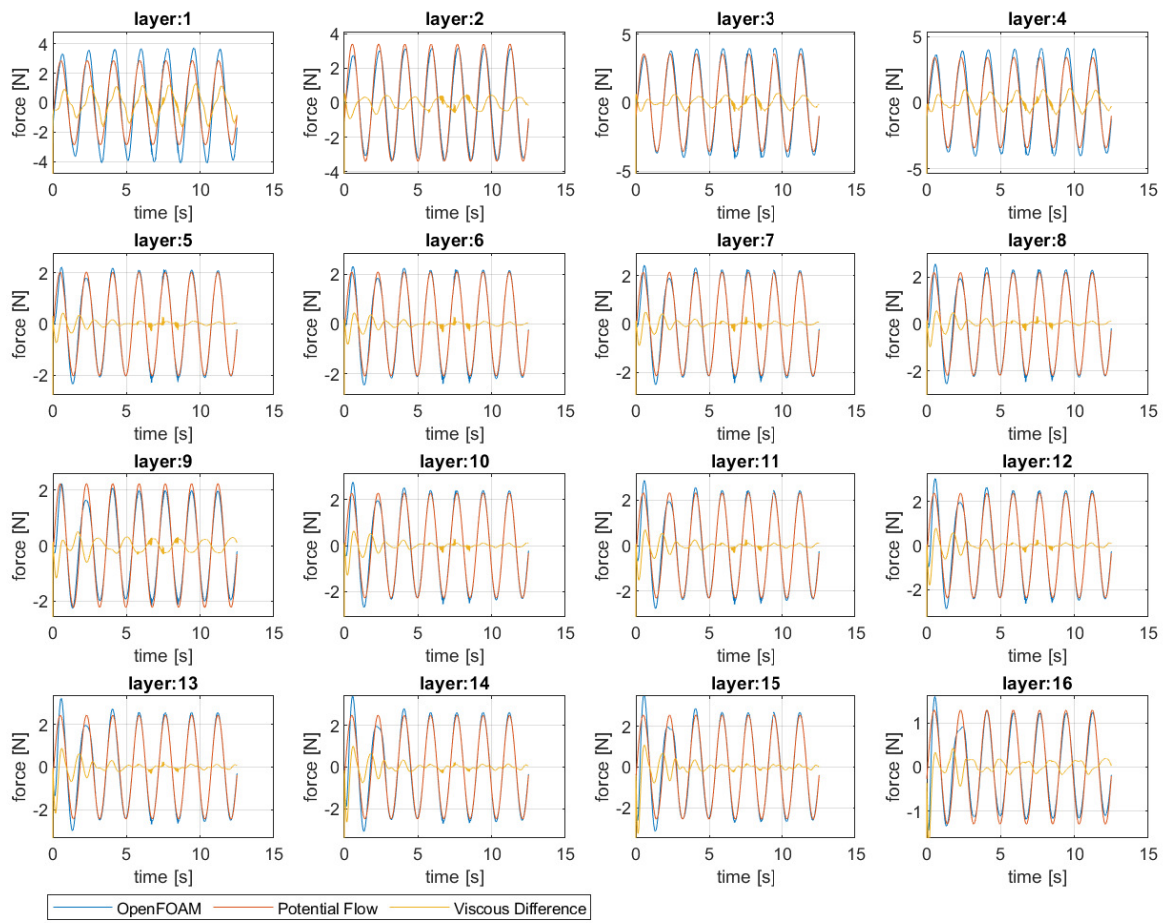


Figure H.5: Decomposed distributed force time series for case: *fo4*

fo5

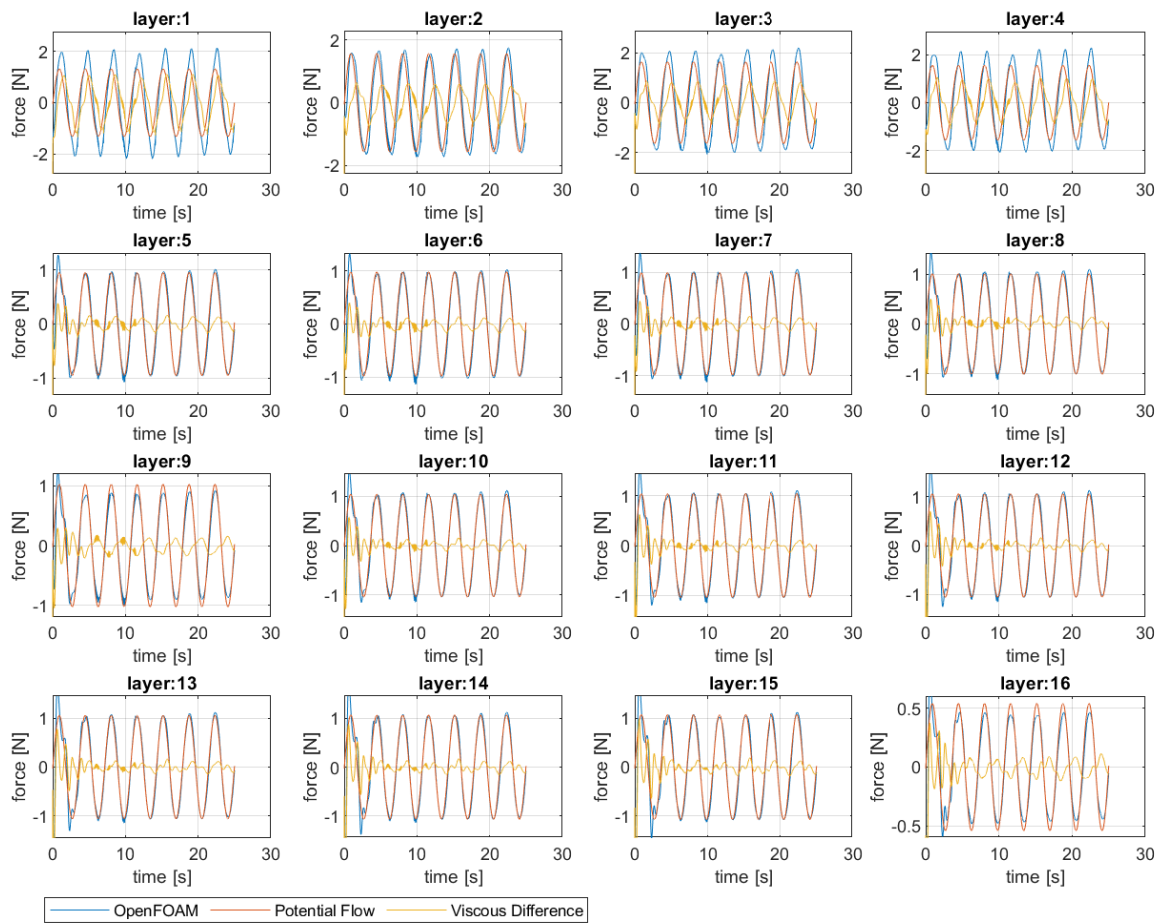
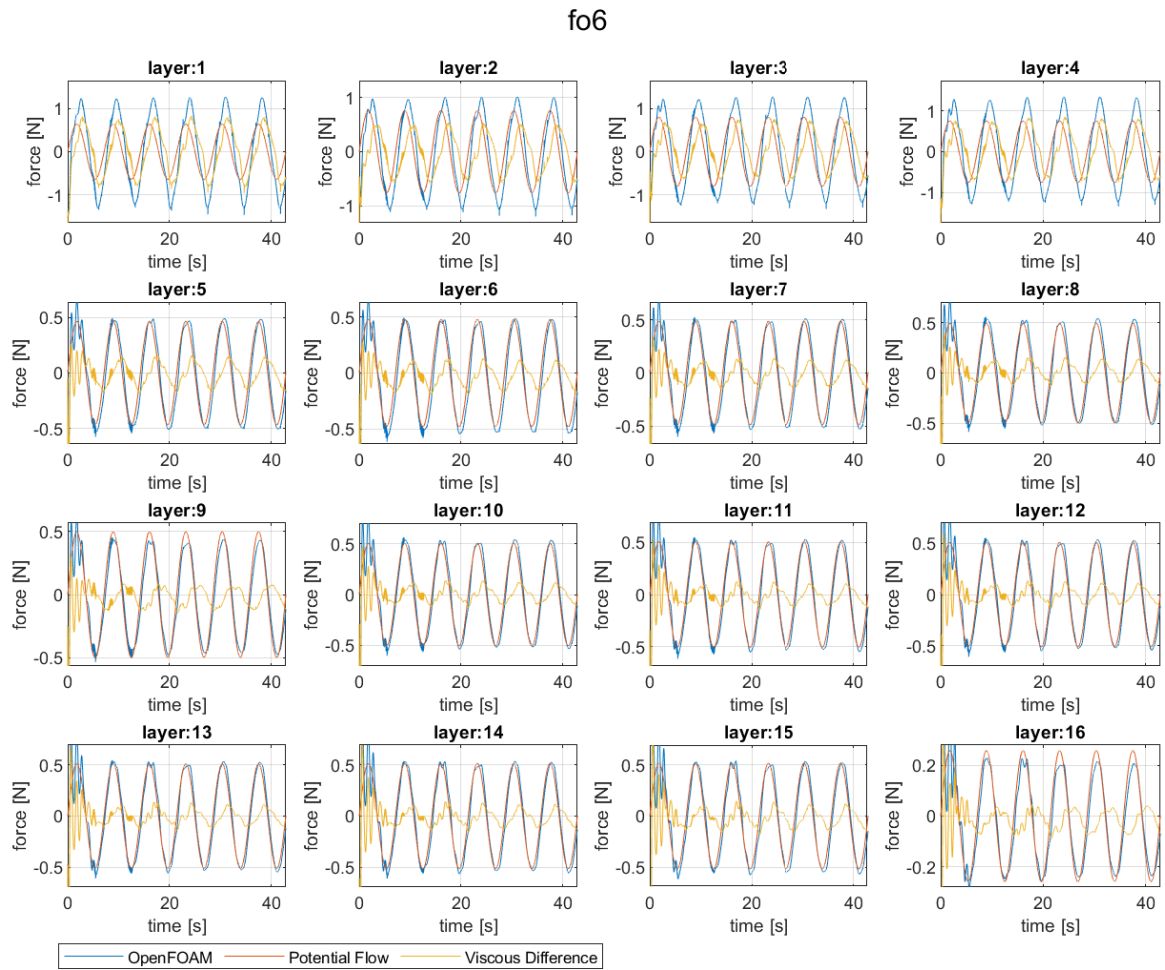


Figure H.6: Decomposed distributed force time series for case: *fo5*

Figure H.7: Decomposed distributed force time series for case: *fo6*

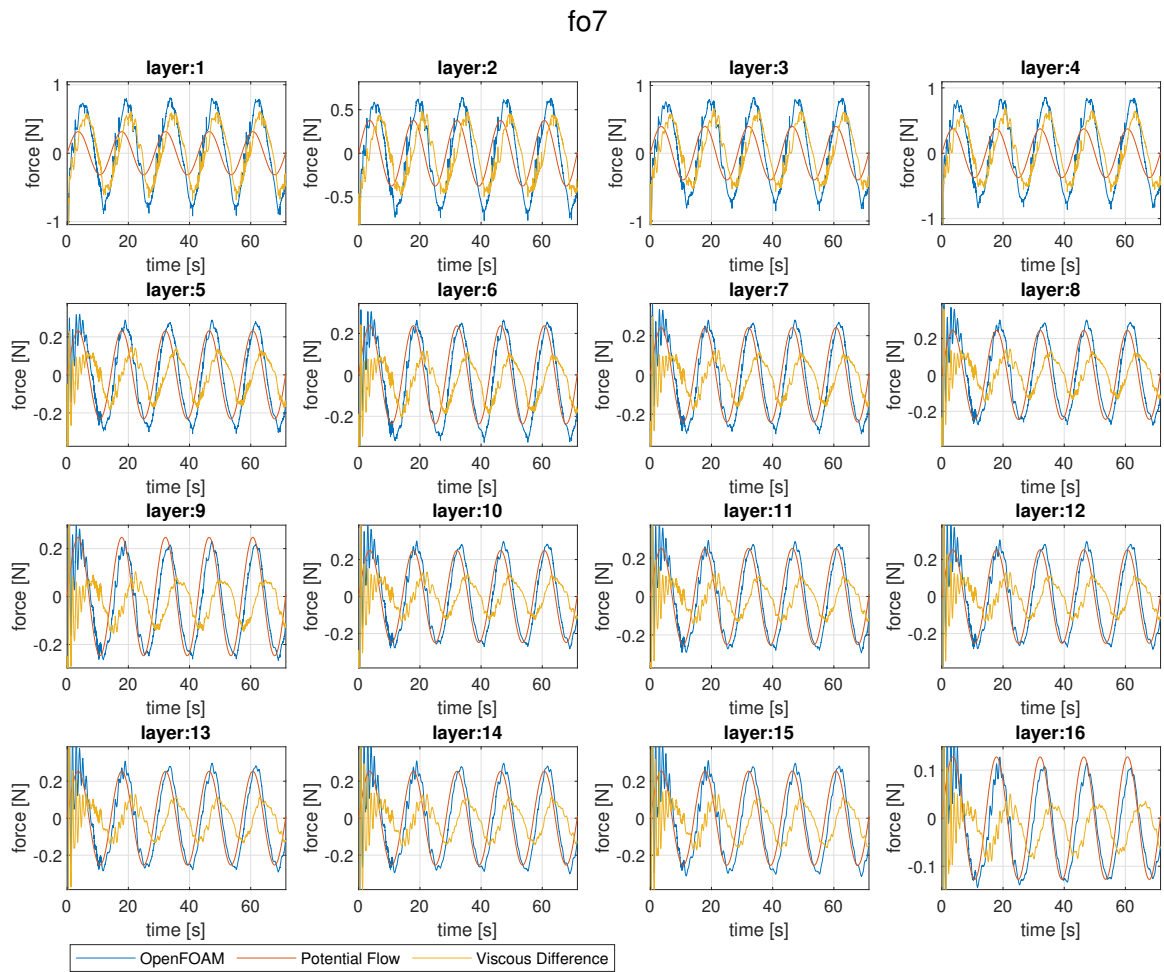


Figure H.8: Decomposed distributed force time series for case: *fo7*

Convergence of the calculated coefficients are shown for each of the single forced oscillation cases. The coefficients are calculated for each successive period of oscillation according to two methods. The resulting coefficients are shown as a function of the period of oscillation to demonstrate stabilized results. The dashed lines with “x” marks are for the method where the part in phase with velocity is either attributed wholly to quadratic or linear damping. The solid lines with “o” marks are for the method where the quadratic and linear portions of the damping are separated using the third and fifth frequencies.

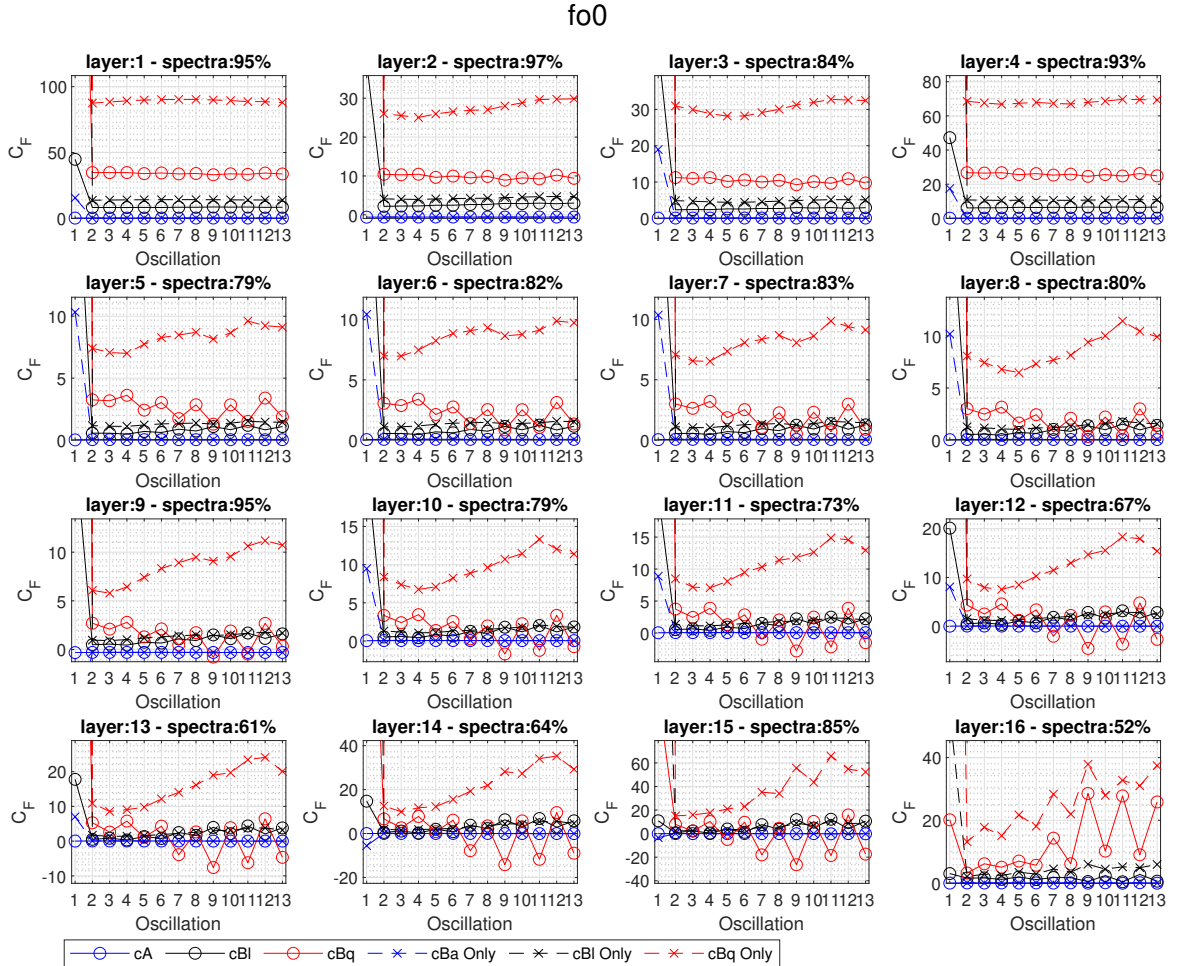


Figure H.9: Coefficient convergence with successive oscillations for case: f_{o0}
 c_A [N-s²/m]; c_{Bl} [N-s/m]; c_{Bq} [N-s²/m²]

fo1

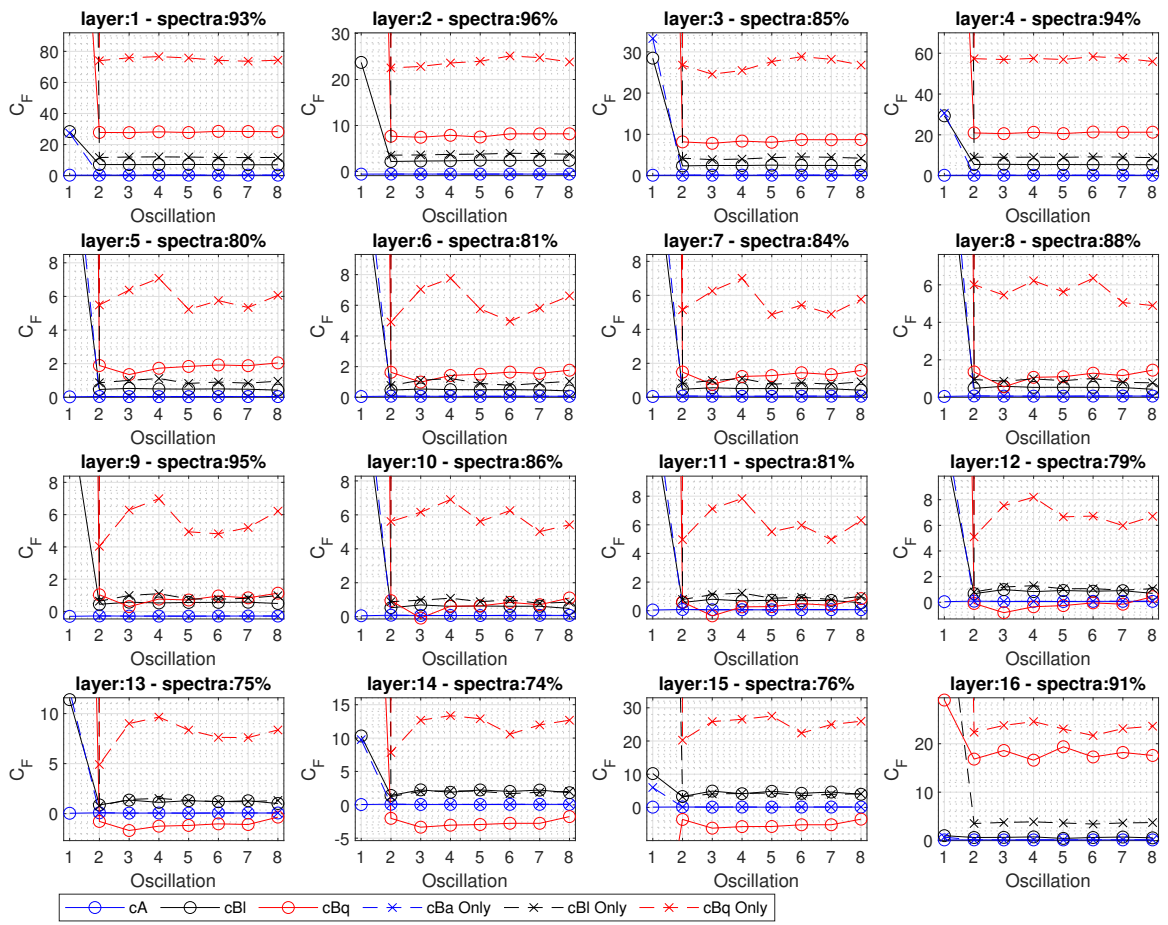


Figure H.10: Coefficient convergence with successive oscillations for case: *fo1*
 cA [N-s²/m]; cBl [N-s/m]; cBq [N-s²/m²]

fo2

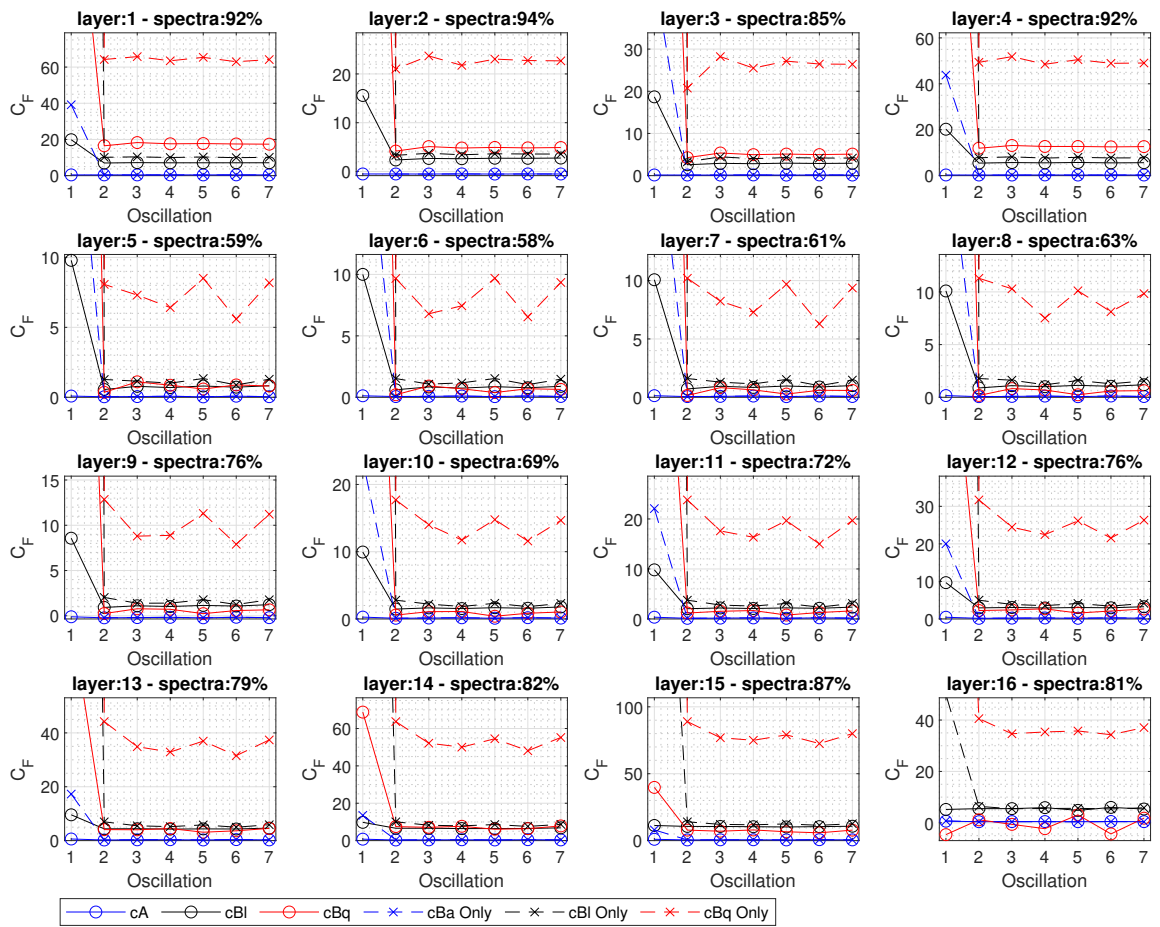


Figure H.11: Coefficient convergence with successive oscillations for case: *fo2*
 cA [N-s²/m]; cBl [N-s/m]; cBq [N-s²/m²]

fo3

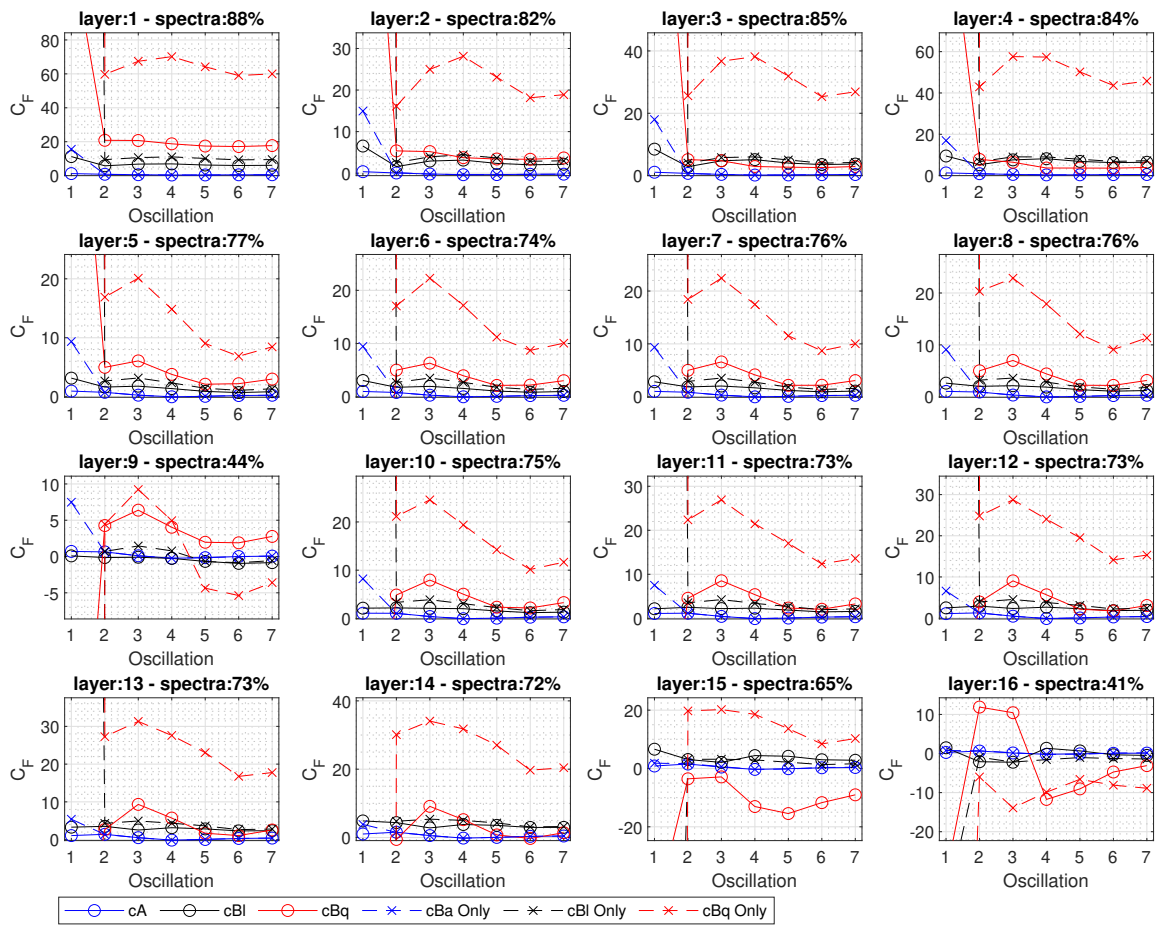


Figure H.12: Coefficient convergence with successive oscillations for case: $fo3$
 cA [N-s²/m]; cBl [N-s/m]; cBq [N-s²/m²]

fo4

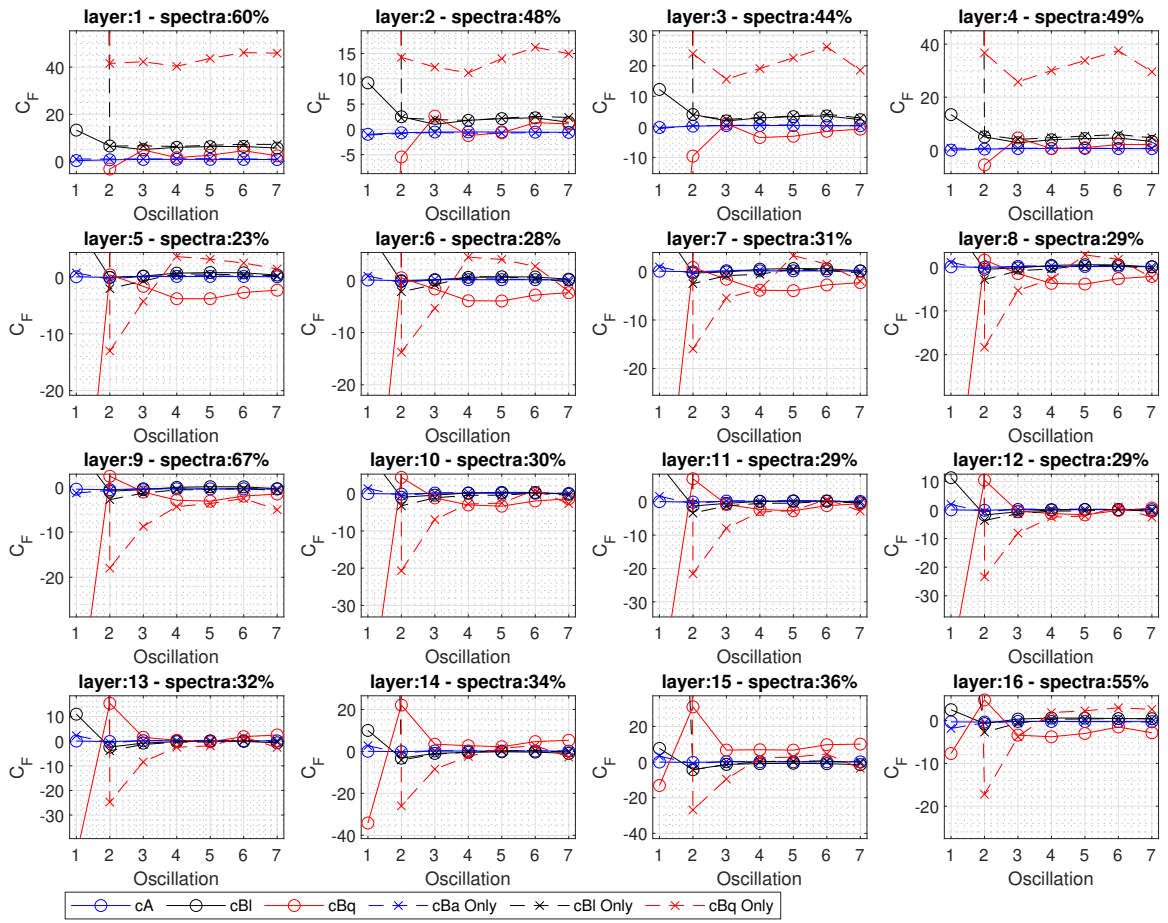


Figure H.13: Coefficient convergence with successive oscillations for case: $fo4$
 cA [N-s²/m]; cBl [N-s/m]; cBq [N-s²/m²]

fo5

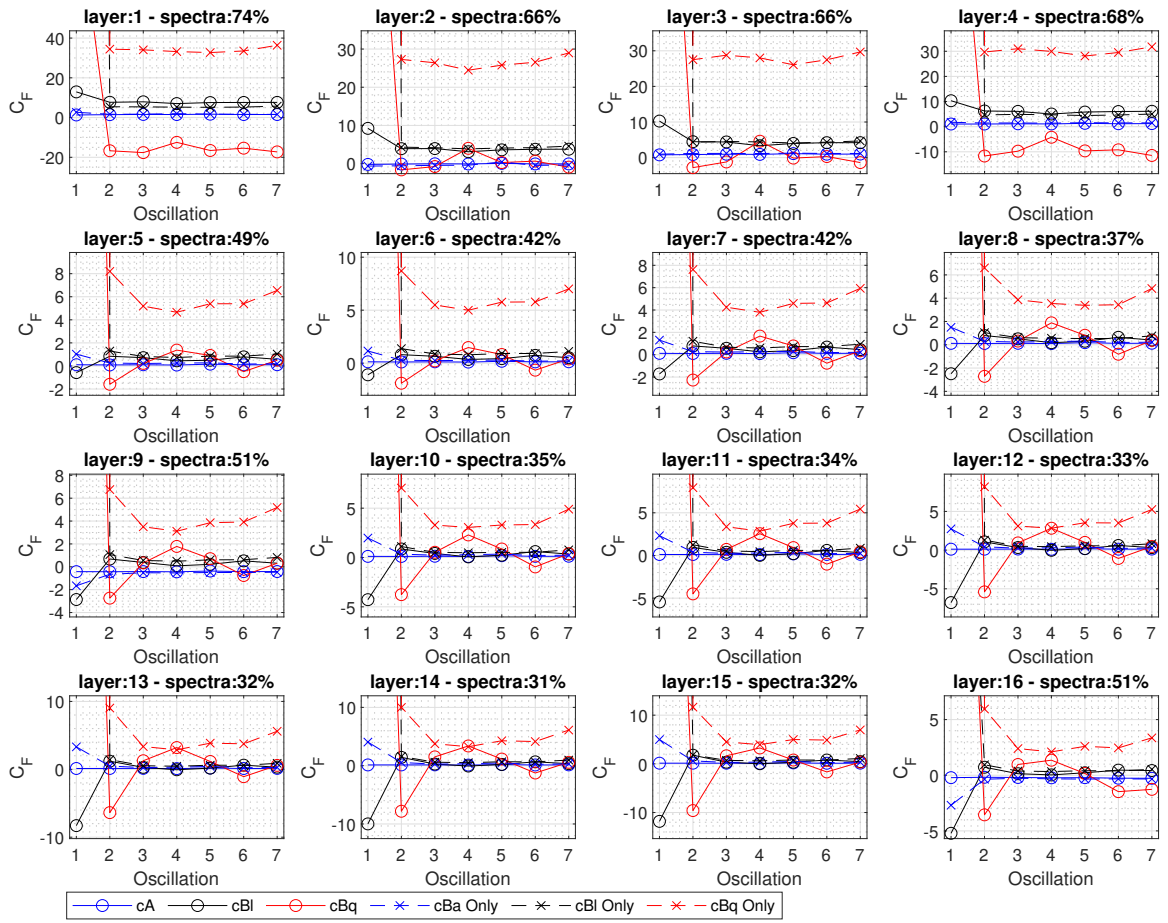


Figure H.14: Coefficient convergence with successive oscillations for case: fo5
 cA [N-s²/m]; cBl [N-s/m]; cBq [N-s²/m²]

fo6

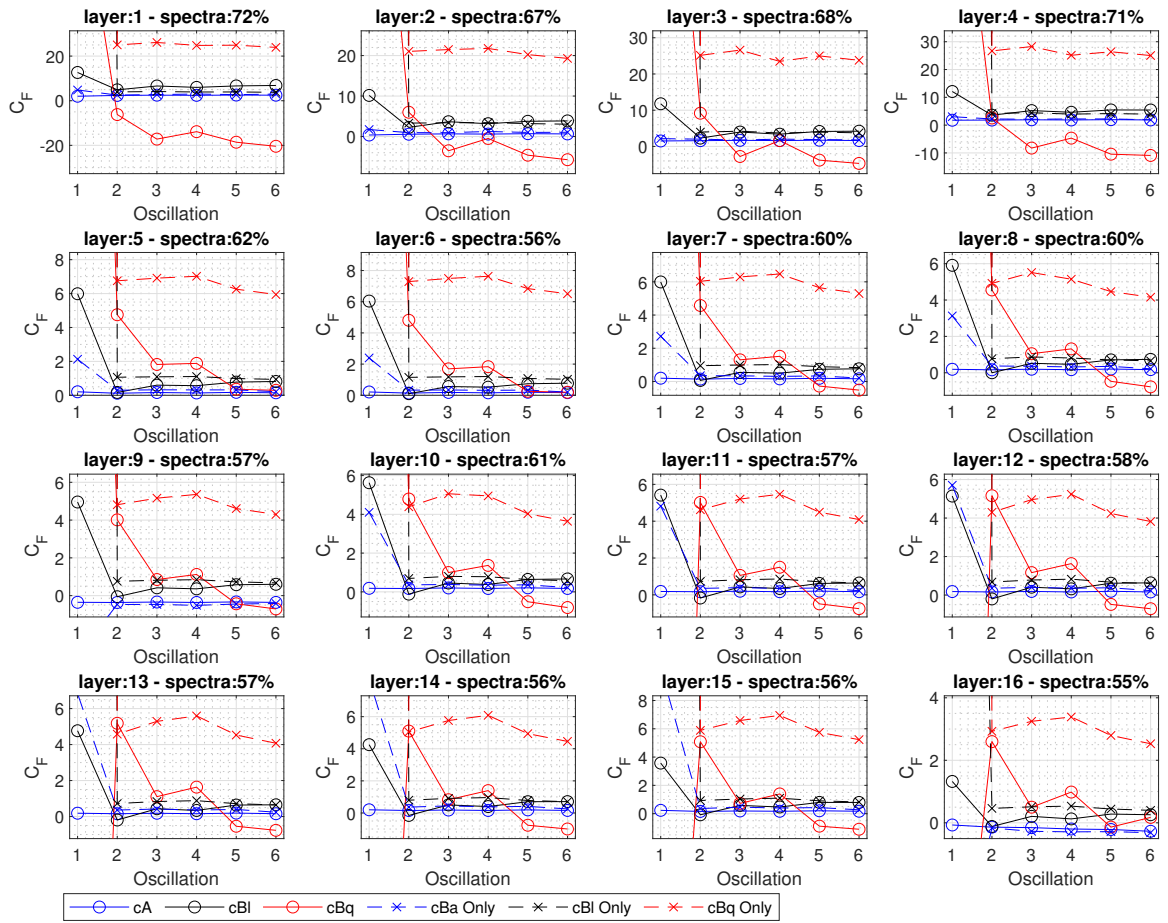


Figure H.15: Coefficient convergence with successive oscillations for case: *fo6*
 cA [N-s²/m]; cBl [N-s/m]; cBq [N-s²/m²]

fo7

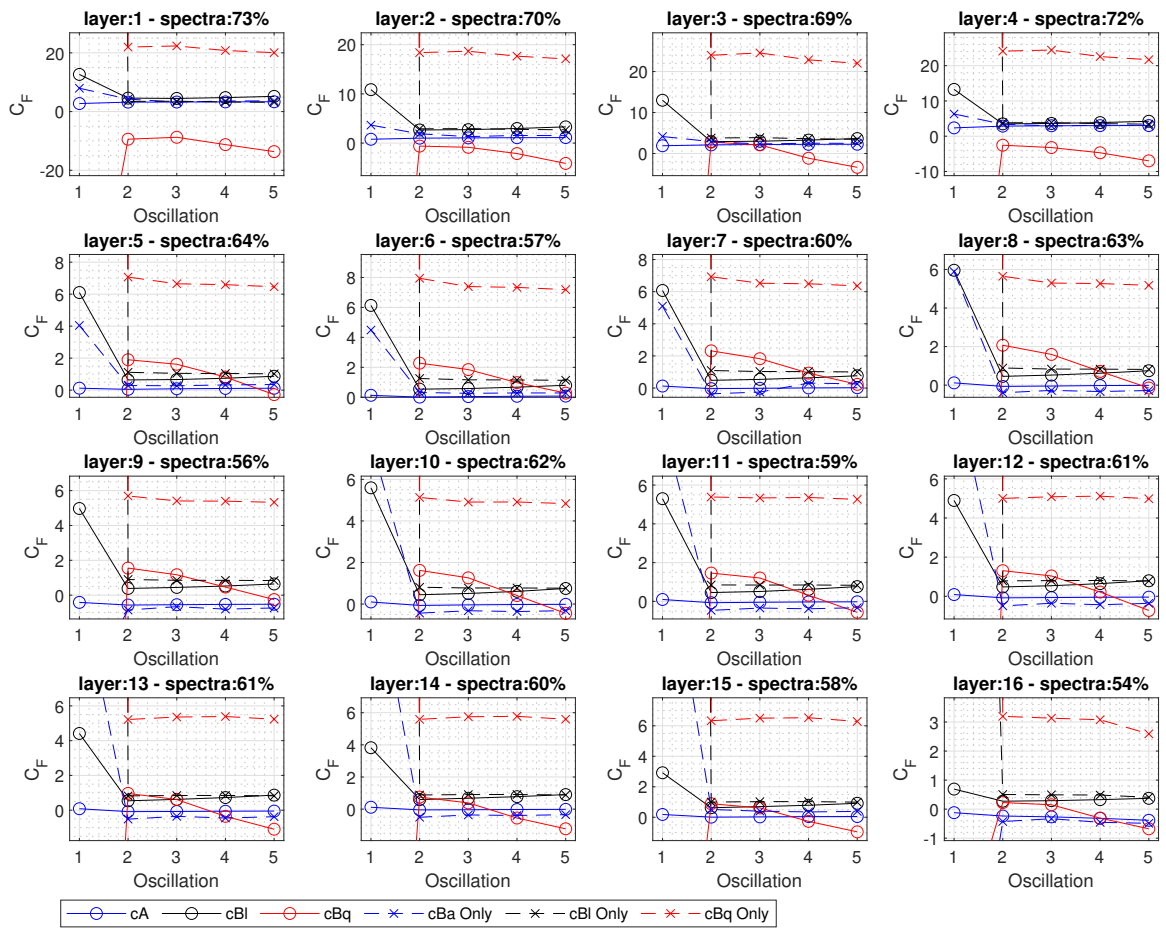


Figure H.16: Coefficient convergence with successive oscillations for case: fo7
 cA [N-s²/m]; cBl [N-s/m]; cBq [N-s²/m²]

I Combined Forced Oscillations Post-Processing: Coefficient Extraction

Time series of the force on each elevation layer are shown for each of the six combined forced oscillation cases. The plots show the total force in blue, labeled “OpenFOAM”, the potential flow predicted force in orange, labeled “Potential Flow”, and the difference between the two in yellow, labeled “Viscous Difference”. The extraction of the viscous correction coefficients is based on the viscous difference component for each layer.

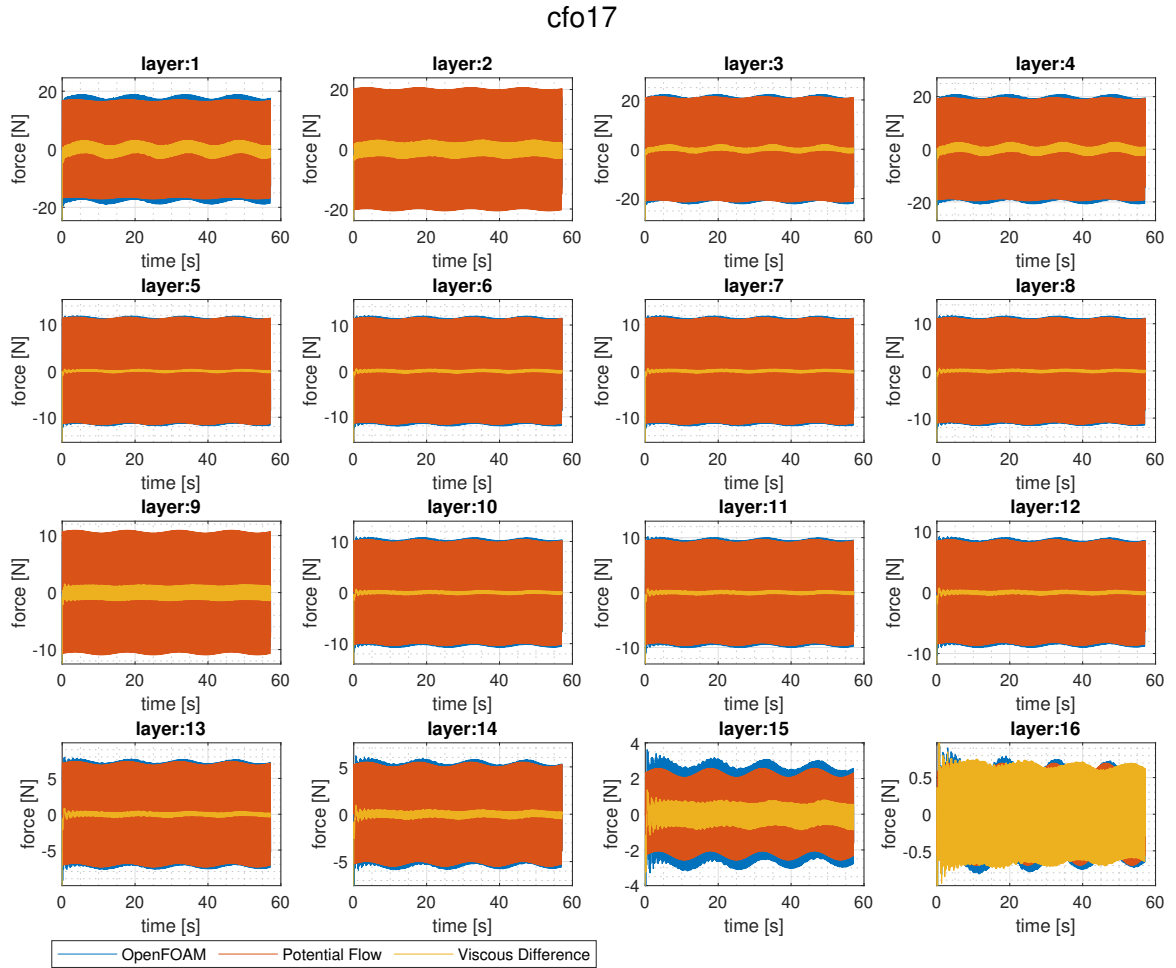


Figure I.1: Decomposed distributed force time series for case: *cfo17*

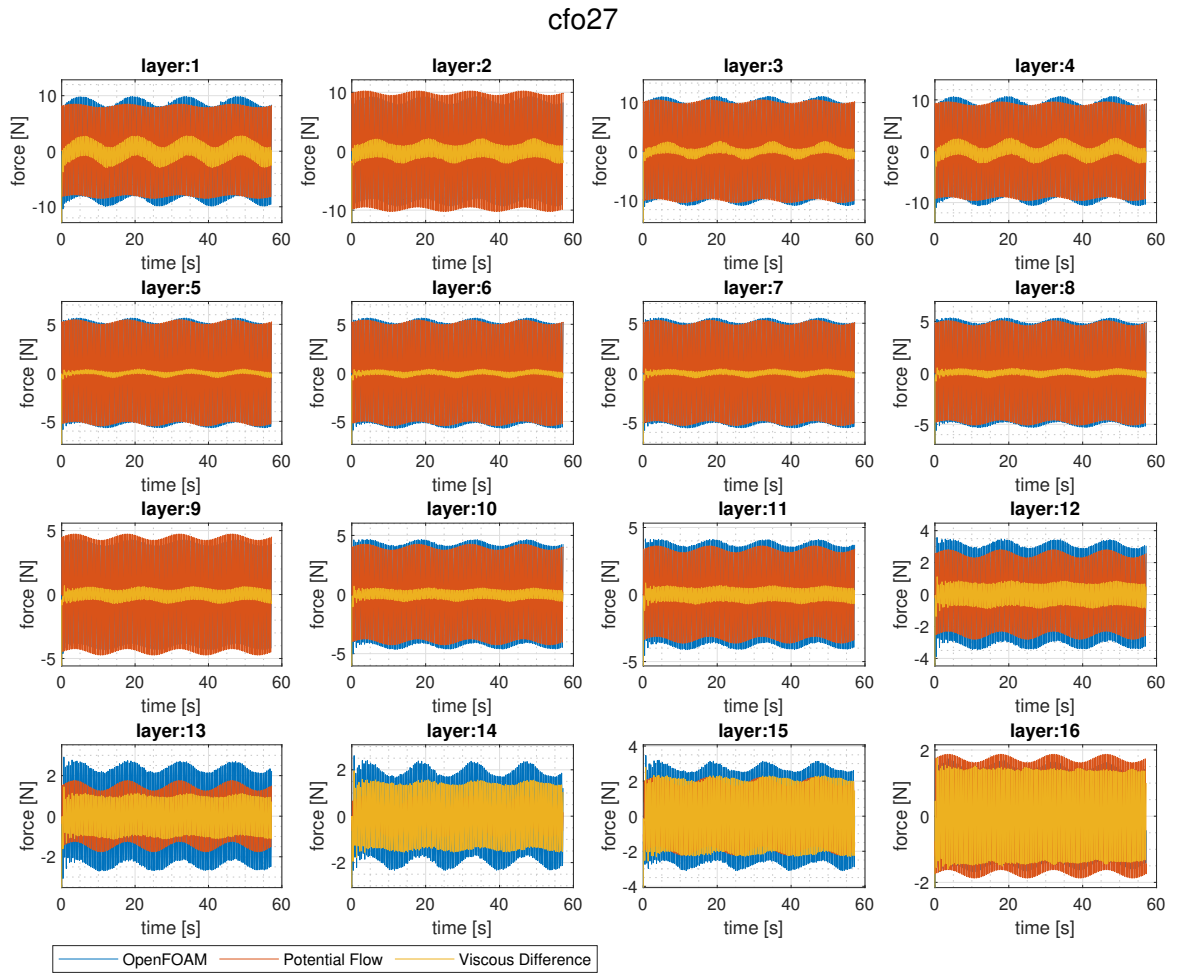


Figure I.2: Decomposed distributed force time series for case: *cfo27*

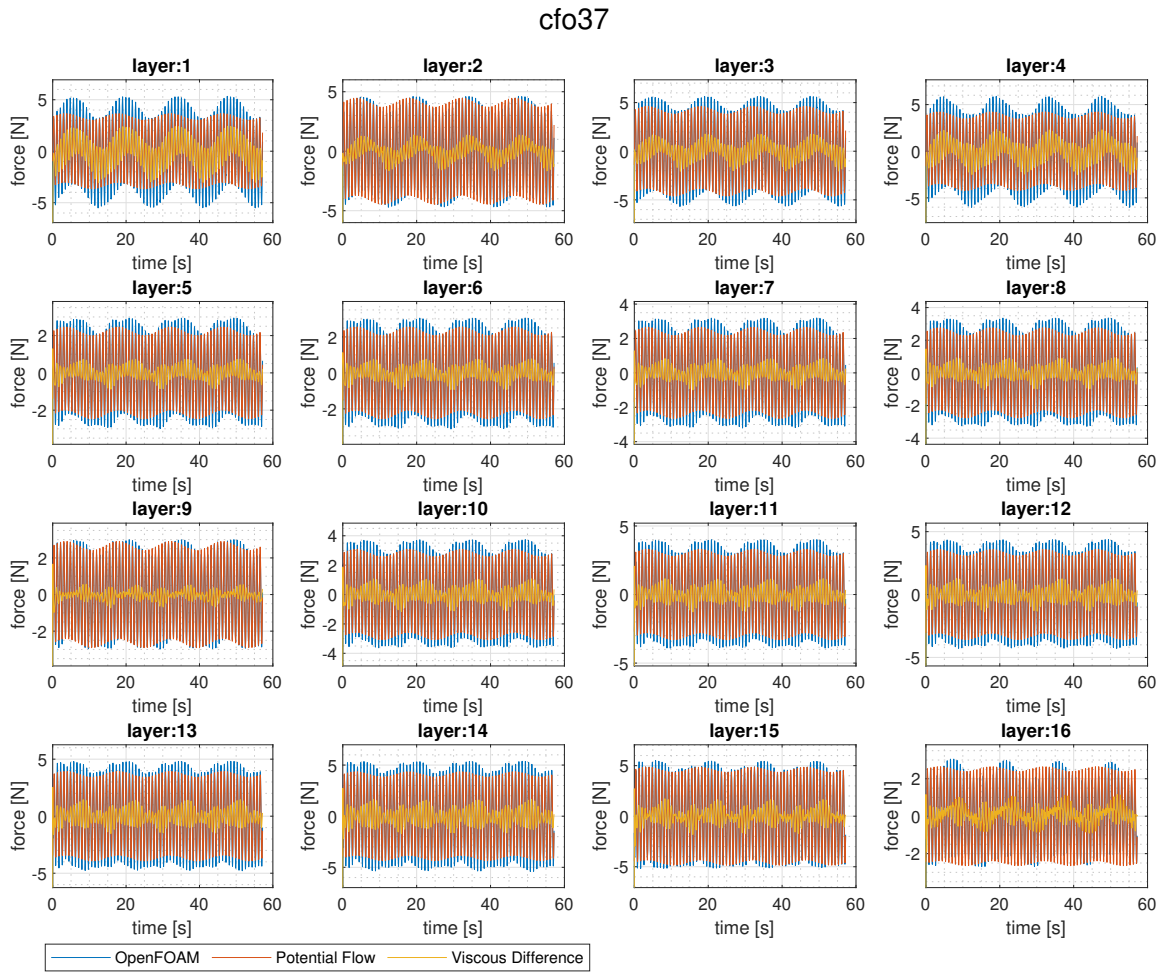


Figure I.3: Decomposed distributed force time series for case: *cfo37*

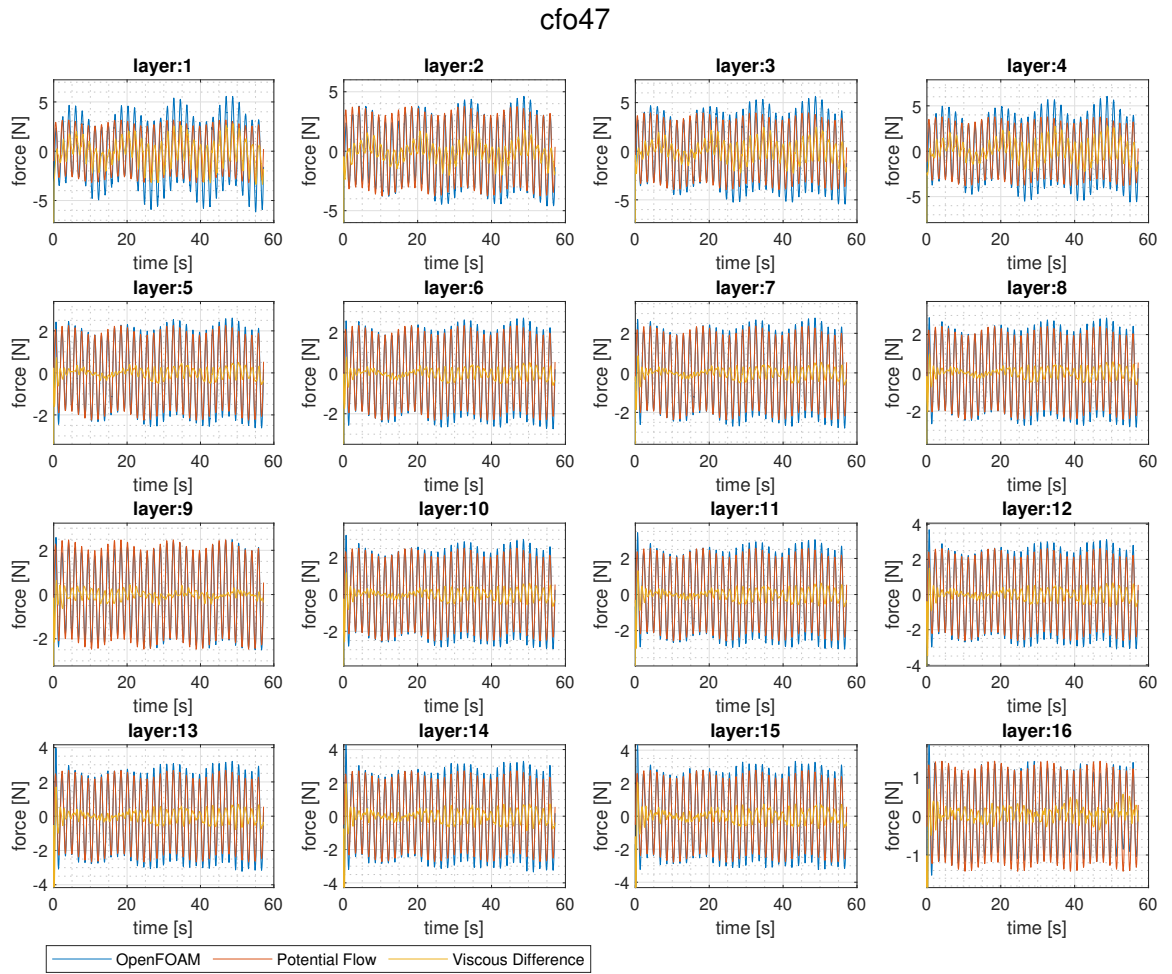


Figure I.4: Decomposed distributed force time series for case: *cfo47*

cfo57

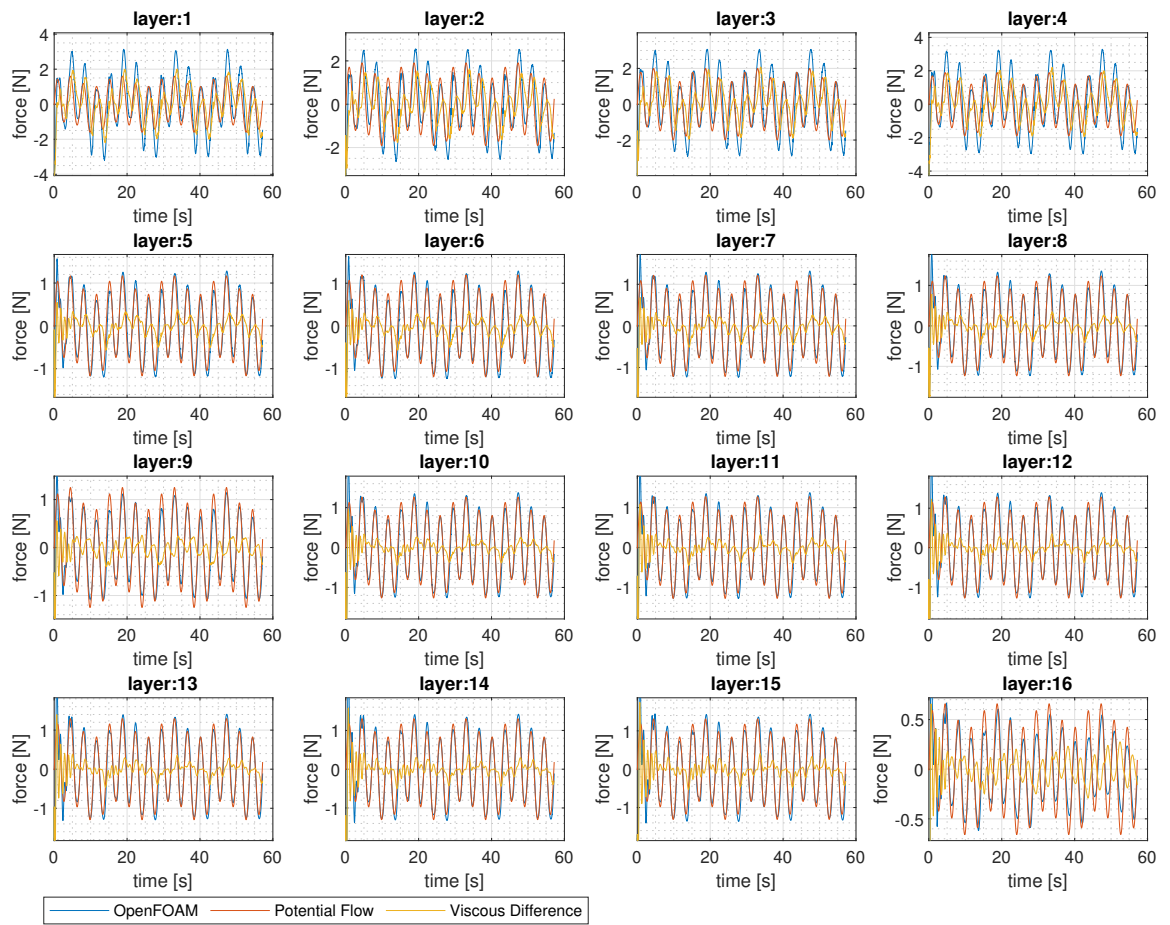


Figure I.5: Decomposed distributed force time series for case: *cfo57*

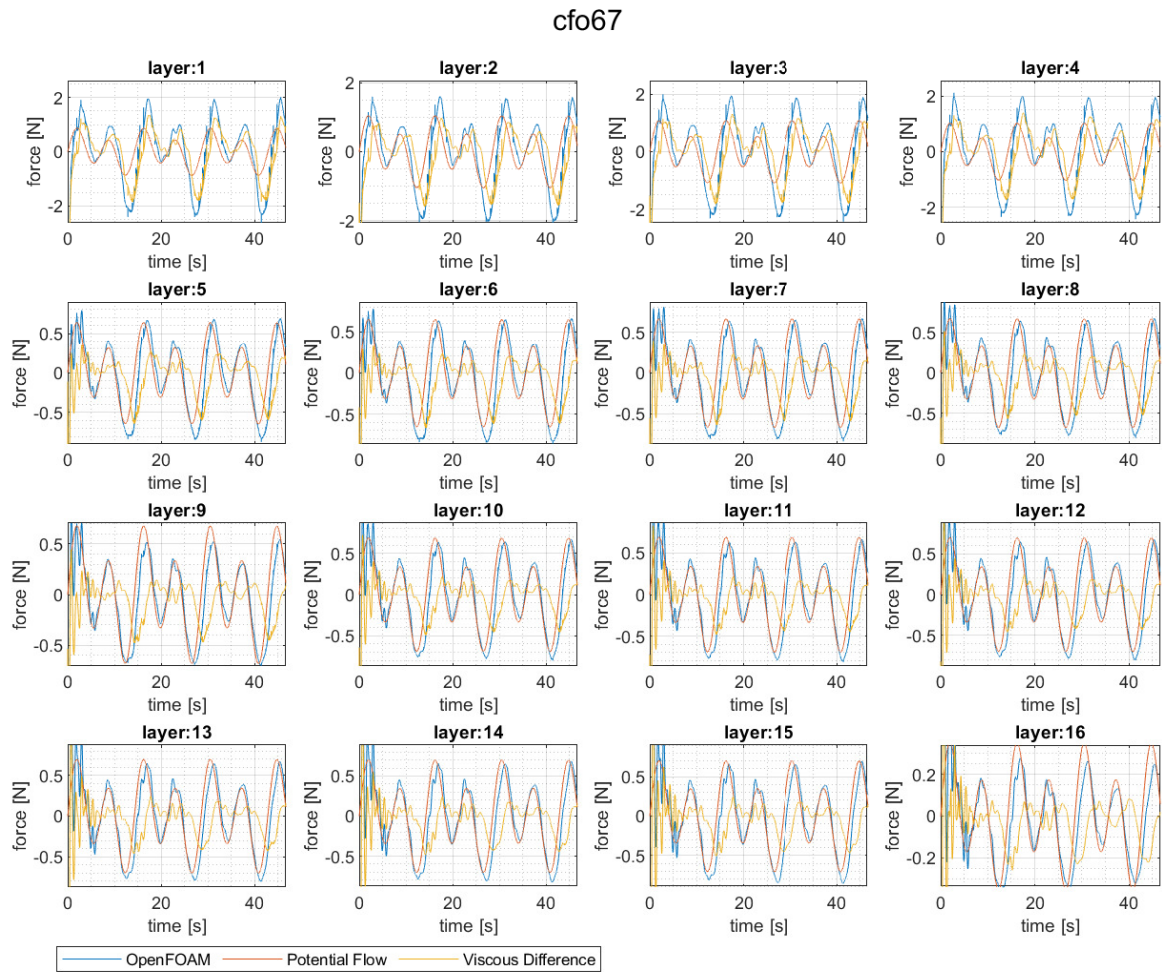


Figure I.6: Decomposed distributed force time series for case: *cfo67*

Convergence of the calculated coefficients are shown for each of the combined forced oscillation cases. The coefficients are calculated for each successive period of oscillation according to two methods. The resulting coefficients are shown as a function of the period of oscillation to demonstrate stabilized results. The dashed lines represent the method where the part in phase with velocity is either attributed wholly to quadratic or linear damping. The solid lines represent the method where the quadratic and linear portions of the damping are separated using the third and fifth frequencies. For both line types the “o” marks are for the coefficients of the first KC number of the combination (lower KC number) and the “x” marks are for the coefficients of the second KC number of the combination (higher KC number).

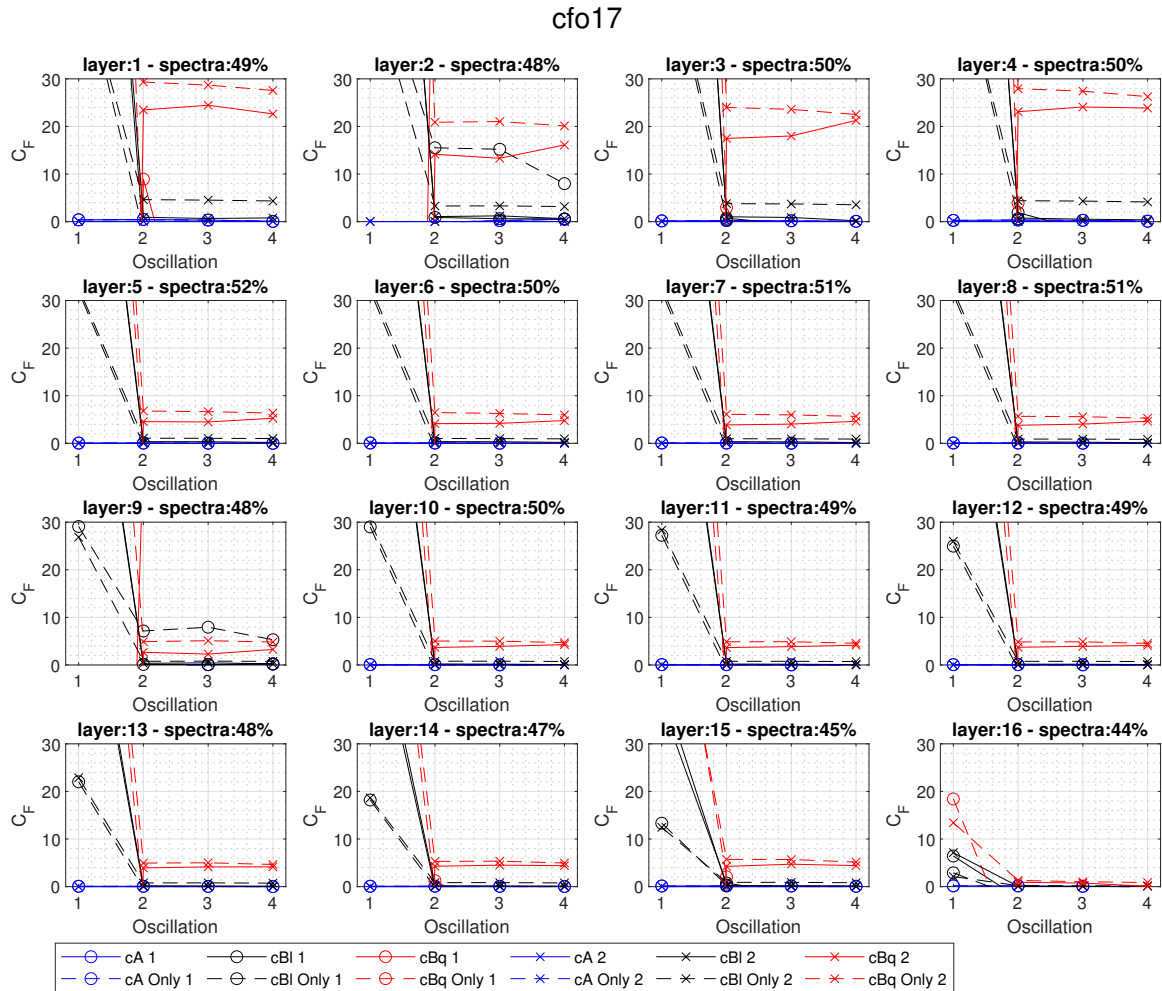


Figure I.7: Coefficient convergence with successive oscillations for case: *cfo17*
 cA [N-s²/m]; cBl [N-s/m]; cBq [N-s²/m²]

cfo27

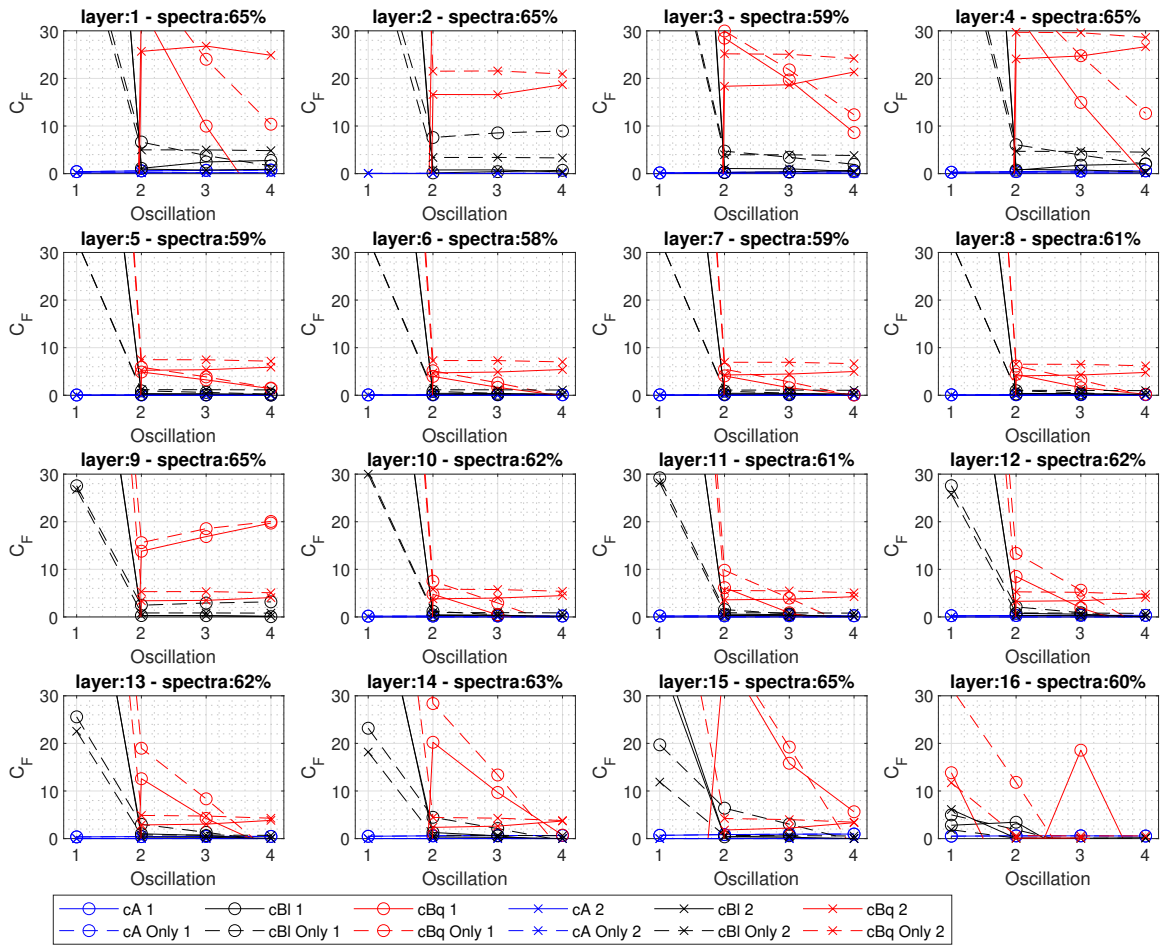


Figure I.8: Coefficient convergence with successive oscillations for case: *cfo27*
 cA [N-s²/m]; cBI [N-s/m]; cBq [N-s²/m²]

cfo37

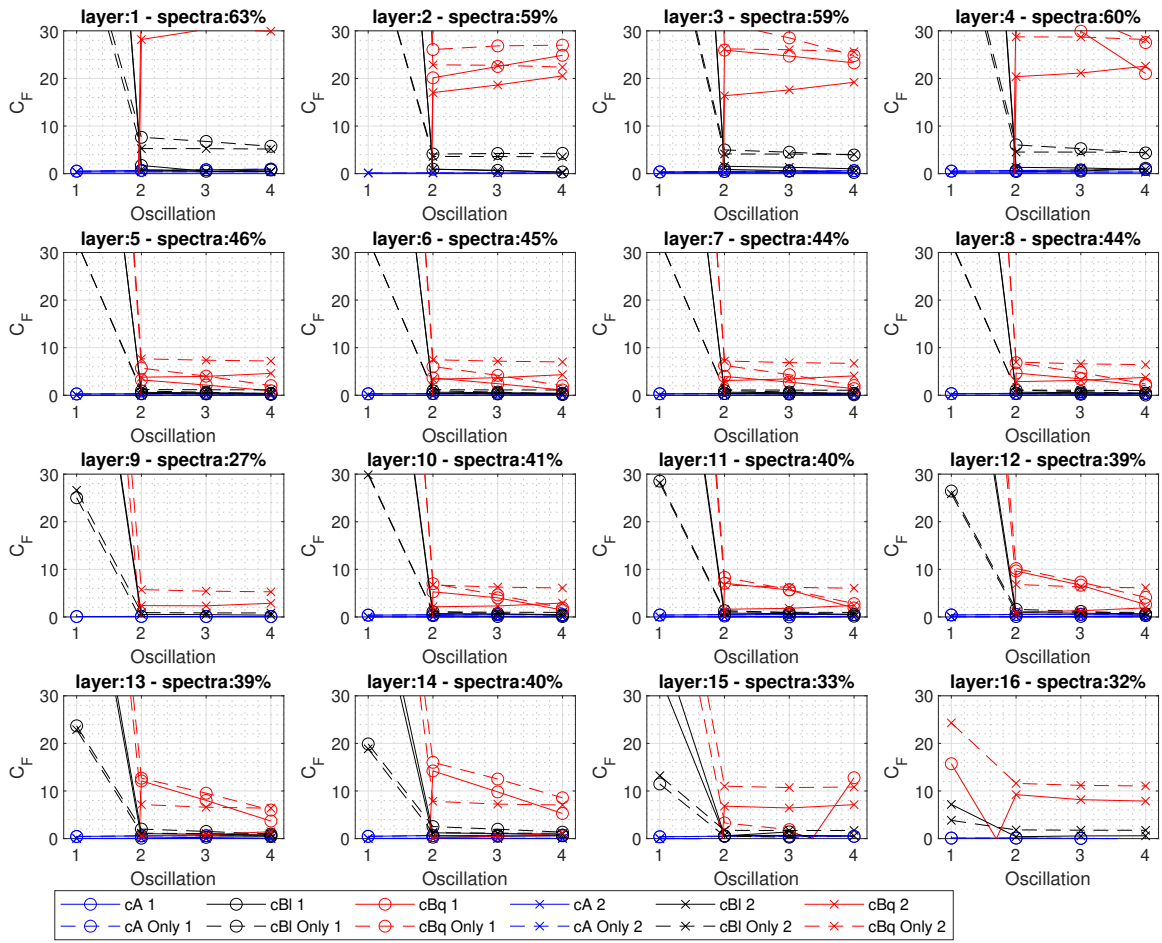


Figure I.9: Coefficient convergence with successive oscillations for case: *cfo37*
 cA [N-s²/m]; cBI [N-s/m]; cBq [N-s²/m²]

cfo47

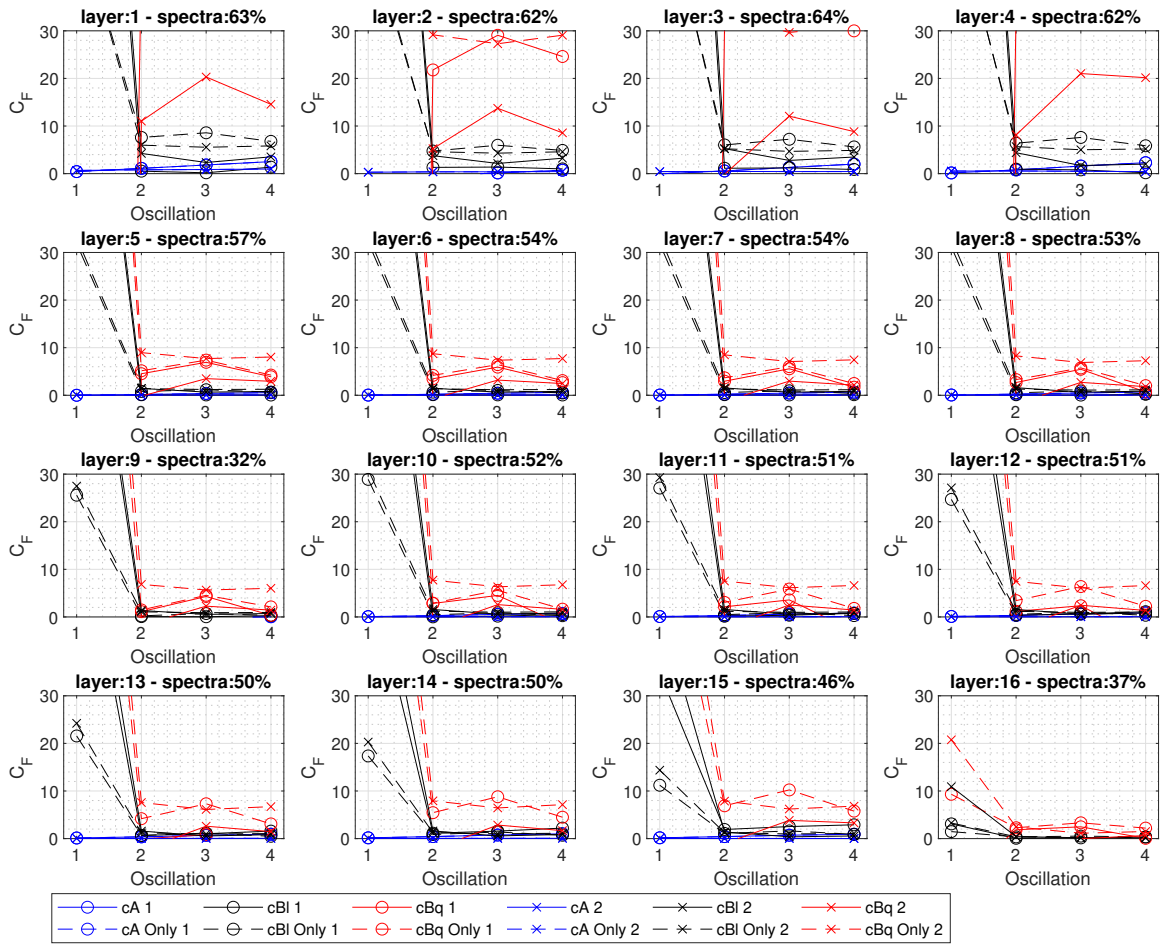


Figure I.10: Coefficient convergence with successive oscillations for case: *cfo47*
 cA [N-s²/m]; cBl [N-s/m]; cBq [N-s²/m²]

cfo57

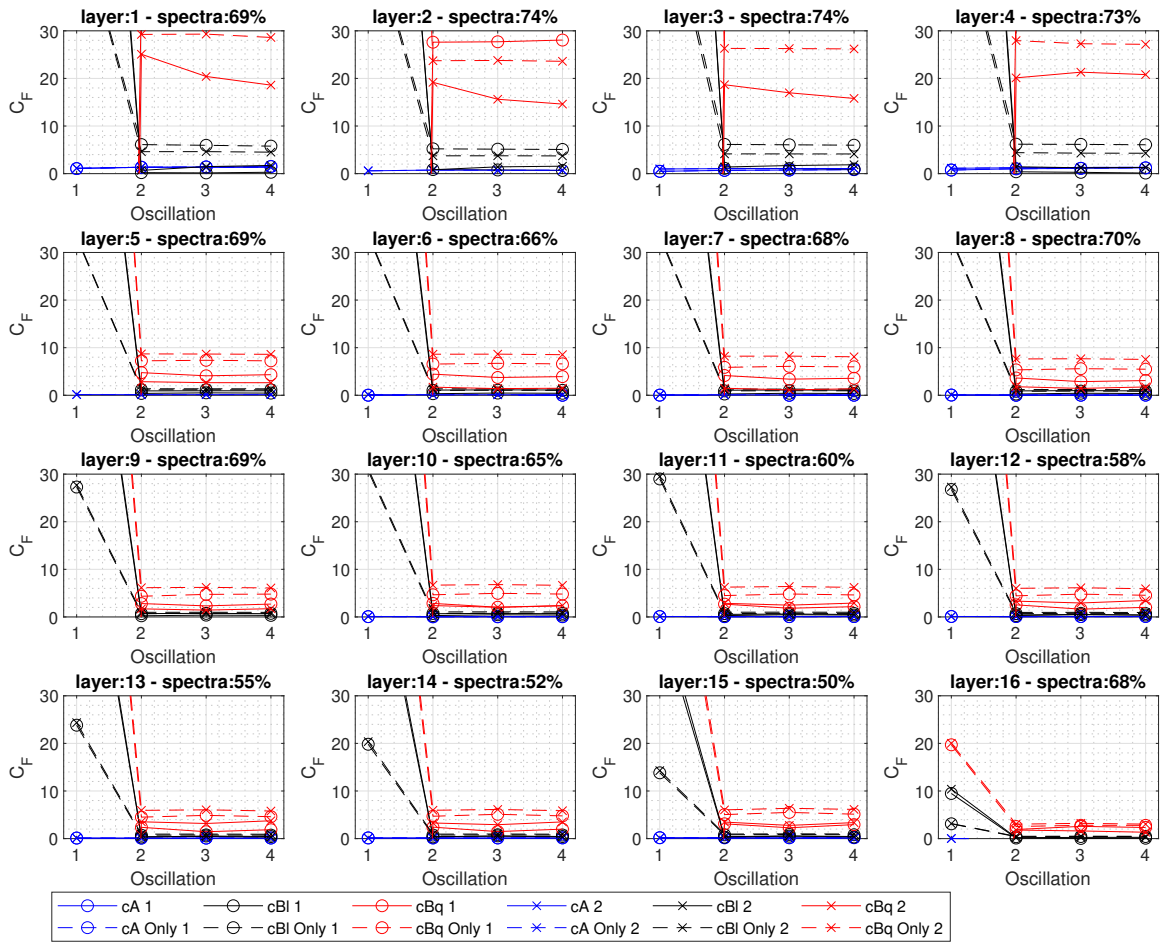


Figure I.11: Coefficient convergence with successive oscillations for case: *cfo57*
 cA [N-s²/m]; cBI [N-s/m]; cBq [N-s²/m²]

cfo67

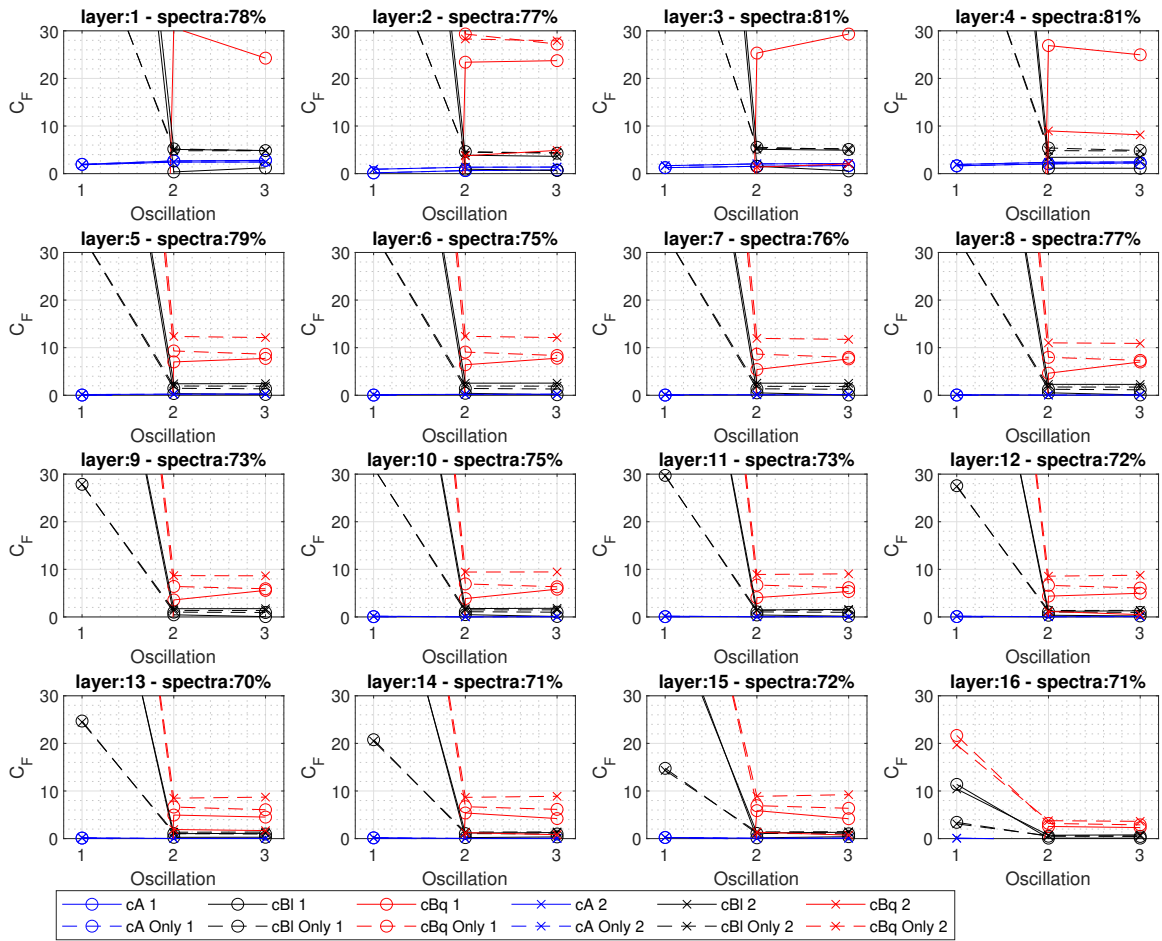


Figure I.12: Coefficient convergence with successive oscillations for case: *cfo67*
 cA [N-s²/m]; cBl [N-s/m]; cBq [N-s²/m²]

Force Coefficients: cfo27

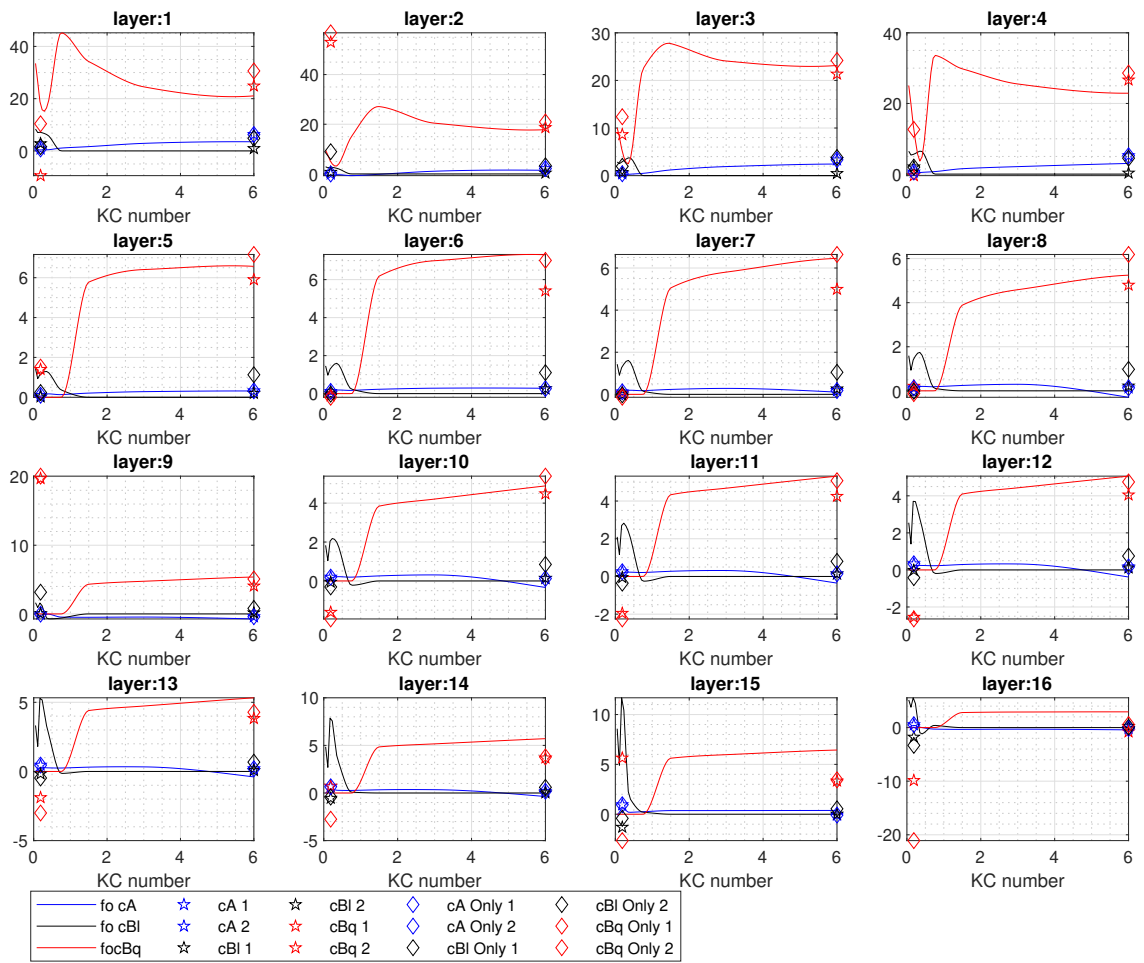


Figure I.14: Combined case coefficient comparison with chosen functions for case: *cfo27*
 cA [N-s²/m]; cBl [N-s/m]; cBq [N-s²/m²]

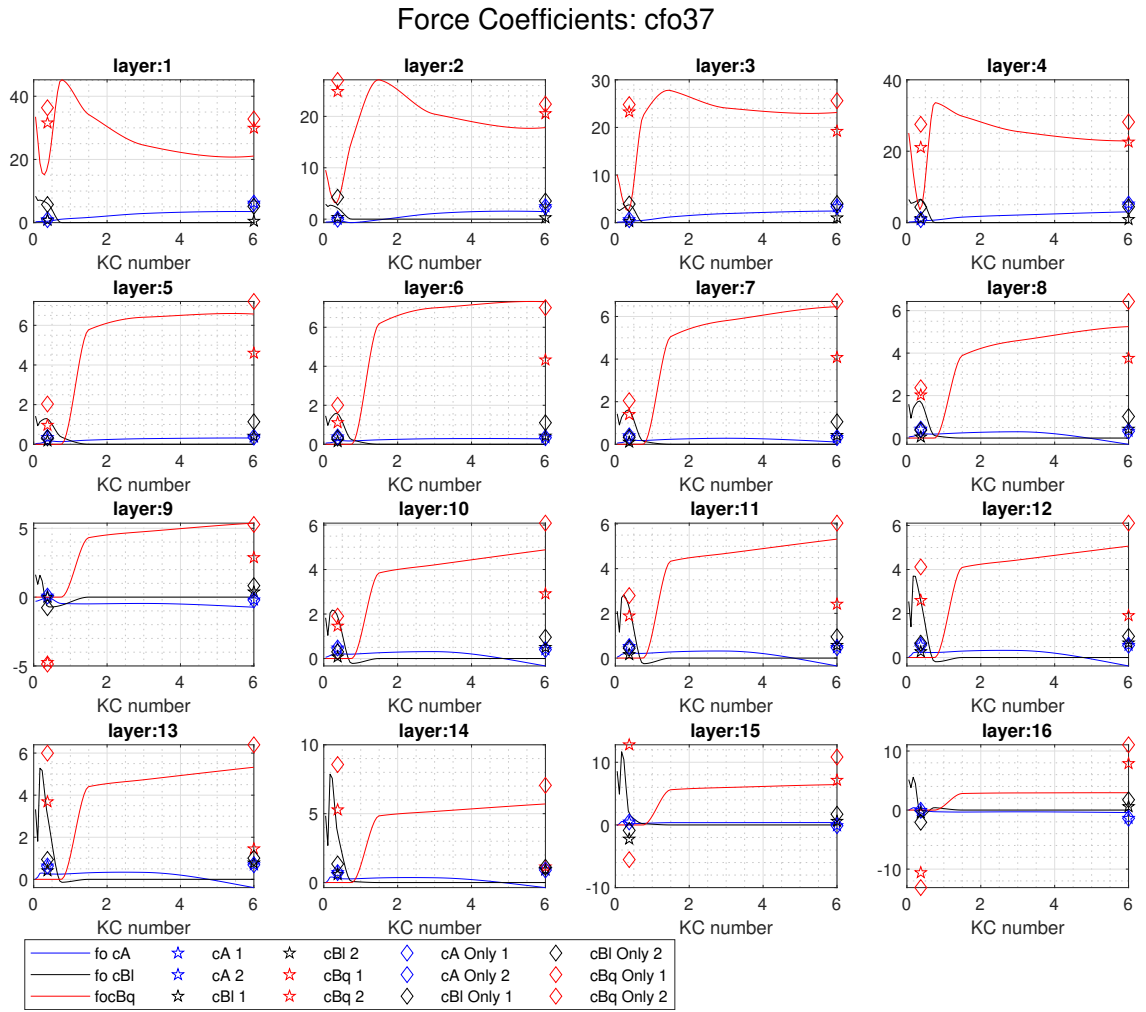


Figure I.15: Combined case coefficient comparison with chosen functions for case: *cfo37*
 cA [N-s²/m]; cBl [N-s/m]; cBq [N-s²/m²]

Force Coefficients: cfo47

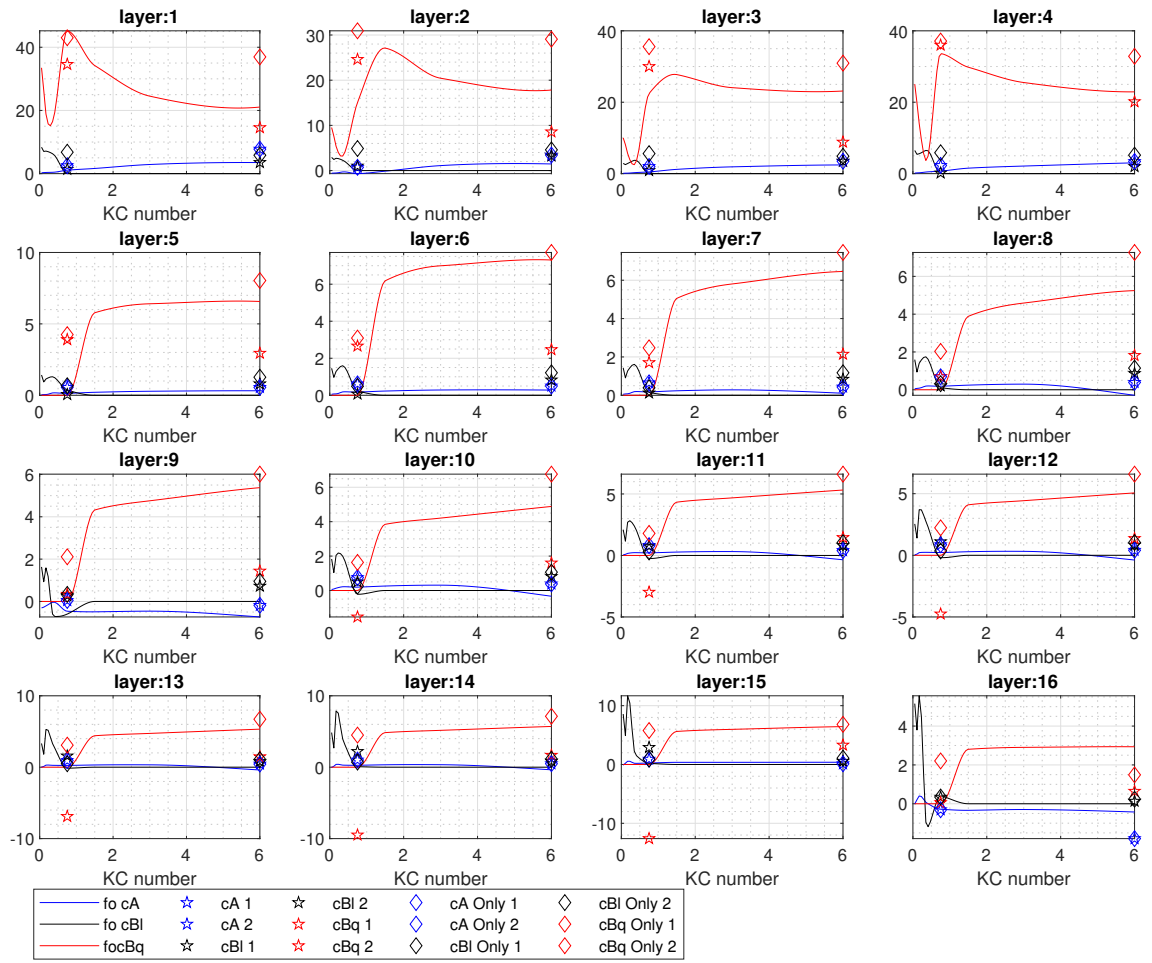


Figure I.16: Combined case coefficient comparison with chosen functions for case: *cfo47*
 cA [N-s²/m]; cBl [N-s/m]; cBq [N-s²/m²]

Force Coefficients: cfo57

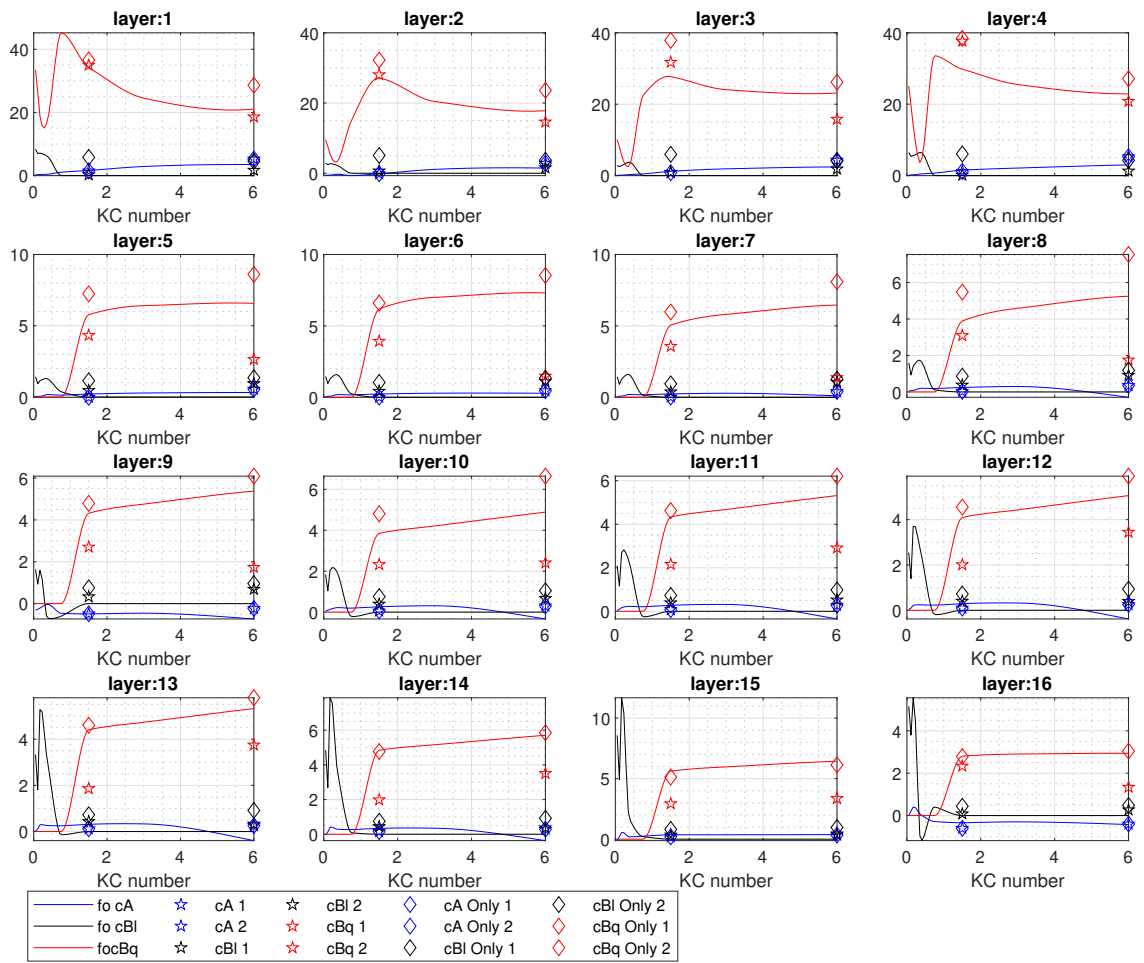


Figure I.17: Combined case coefficient comparison with chosen functions for case: *cfo57*
 cA [N-s²/m]; cBl [N-s/m]; cBq [N-s²/m²]

Force Coefficients: cfo67

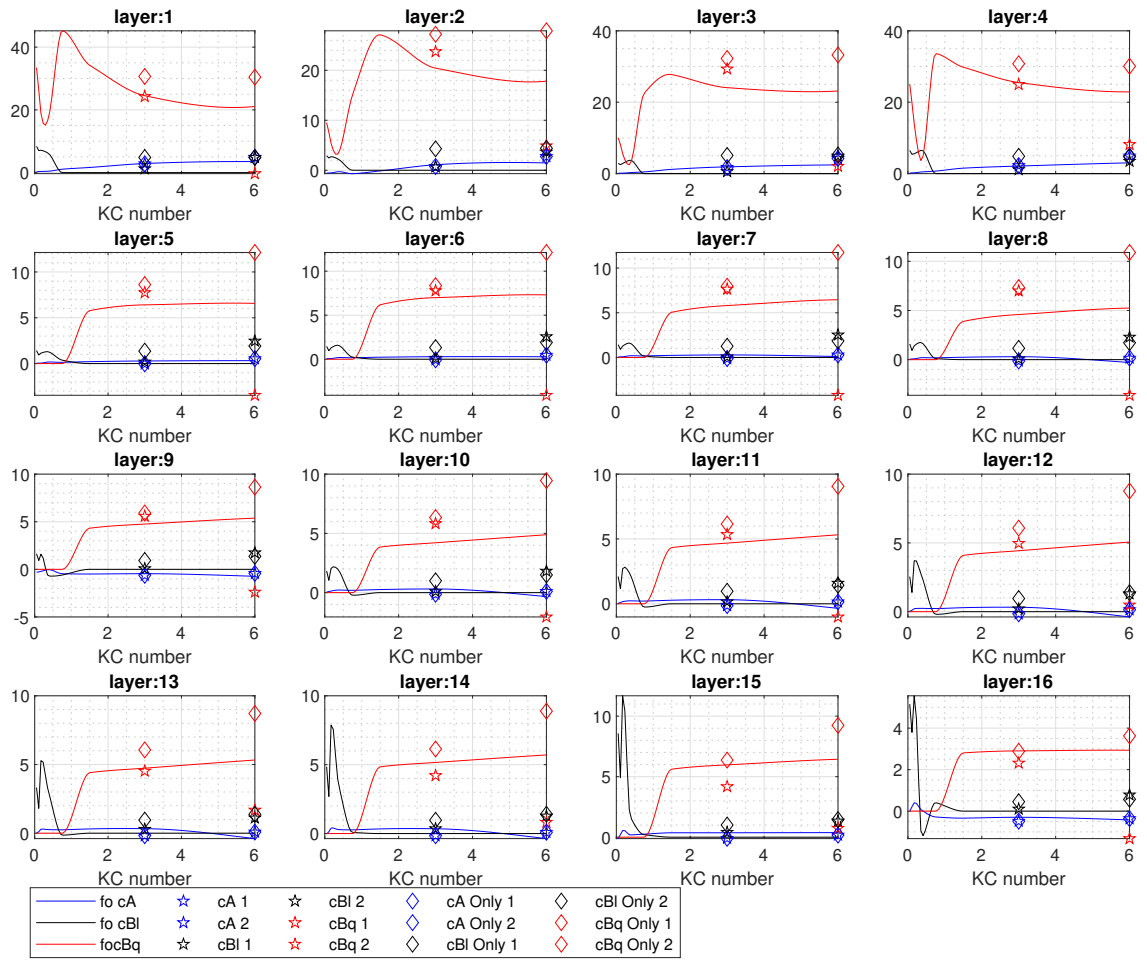


Figure I.18: Combined case coefficient comparison with chosen functions for case: *cfo67*
 cA [N-s²/m]; cBl [N-s/m]; cBq [N-s²/m²]

J Combined Forced Oscillations Post-Processing: Force Series Reconstruction

The implementation of the viscous correction functions is tested and tuned by recreating the force time series of the combined forced oscillations. The resulting reconstructed force time series are shown for three different methods. The first, “IF”, uses the instantaneous frequency method. The second, “Amp”, uses the distance traveled amplitude method. The third, “Spec”, uses the frequency spectrum to KC number spectrum method.

The first plot shows the total force recorded in OpenFOAM as well as the predicted potential flow force and their difference, which would be the correct viscous correction force. The three attempts at recreating the viscous correction force are included on the same axes.

The second plot shows the summation of the potential flow prediction with the three viscous corrections and compares them with the original OpenFOAM force.

The third plot shows what the first two models view the KC number as throughout the simulation. The third spectral method does not select a single KC number, so it is not included in this plot.

These three plots are shown for each of the six combined forced oscillation cases.

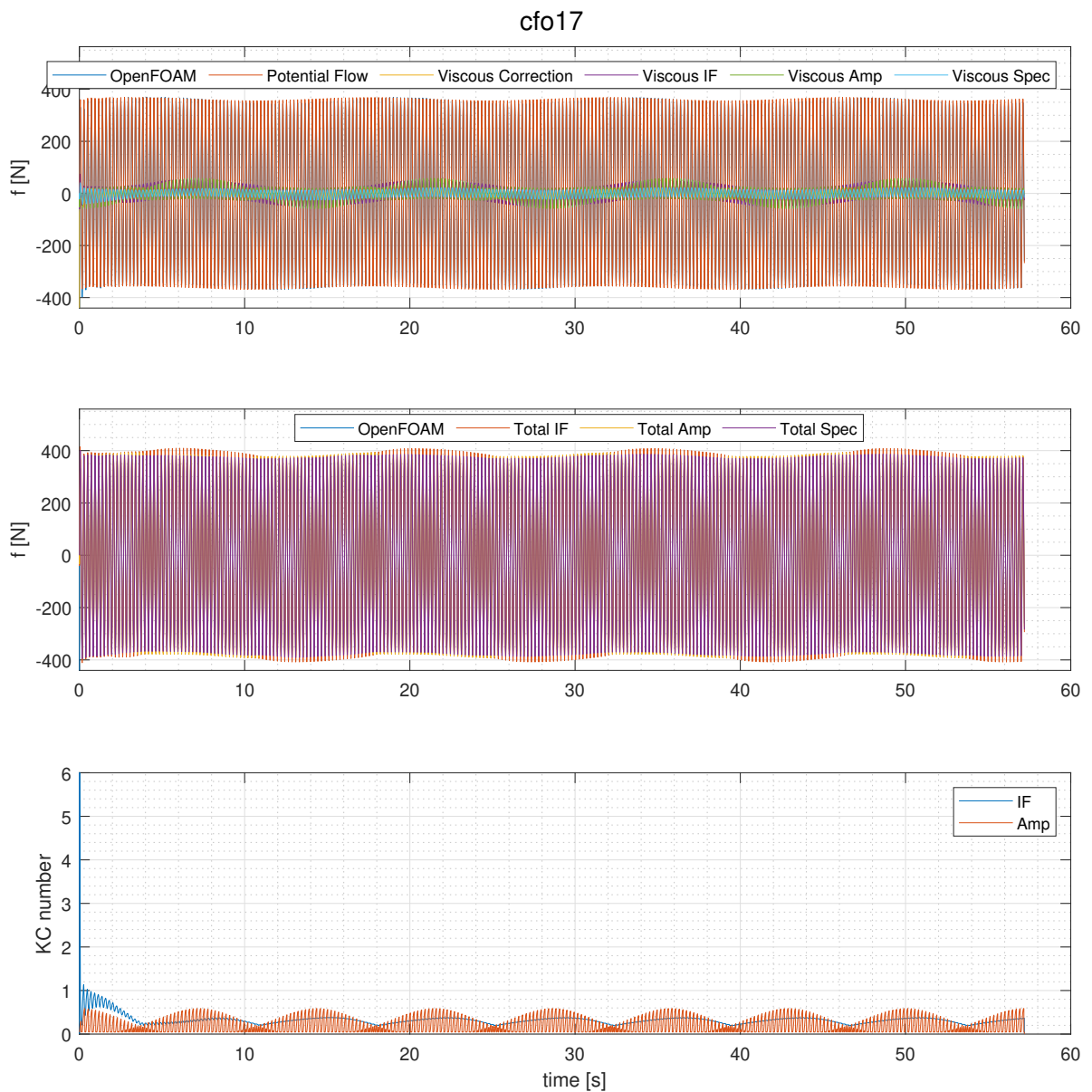


Figure J.1: Reconstruction of case: *cfo17*

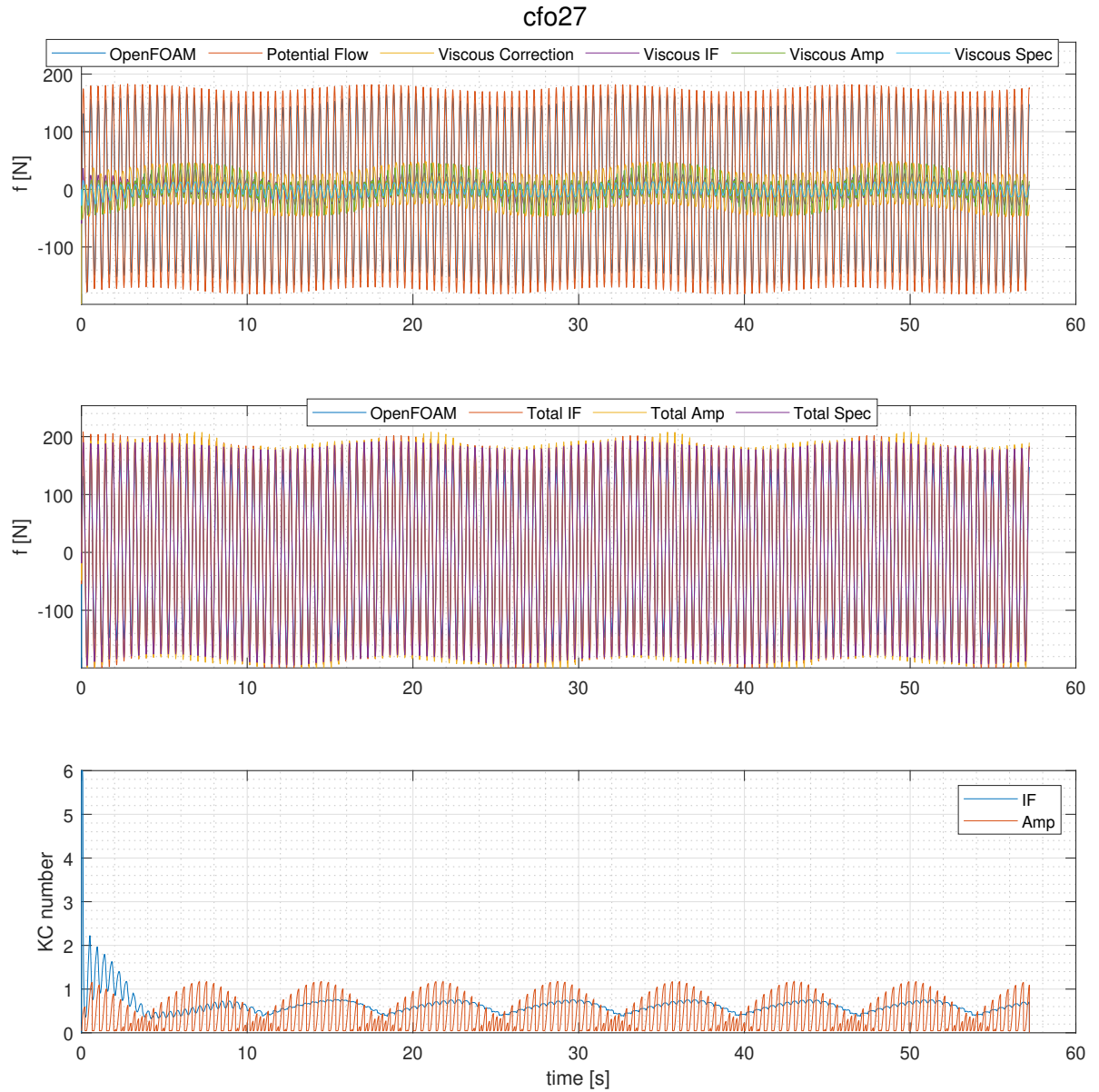


Figure J.2: Reconstruction of case: *cfo27*

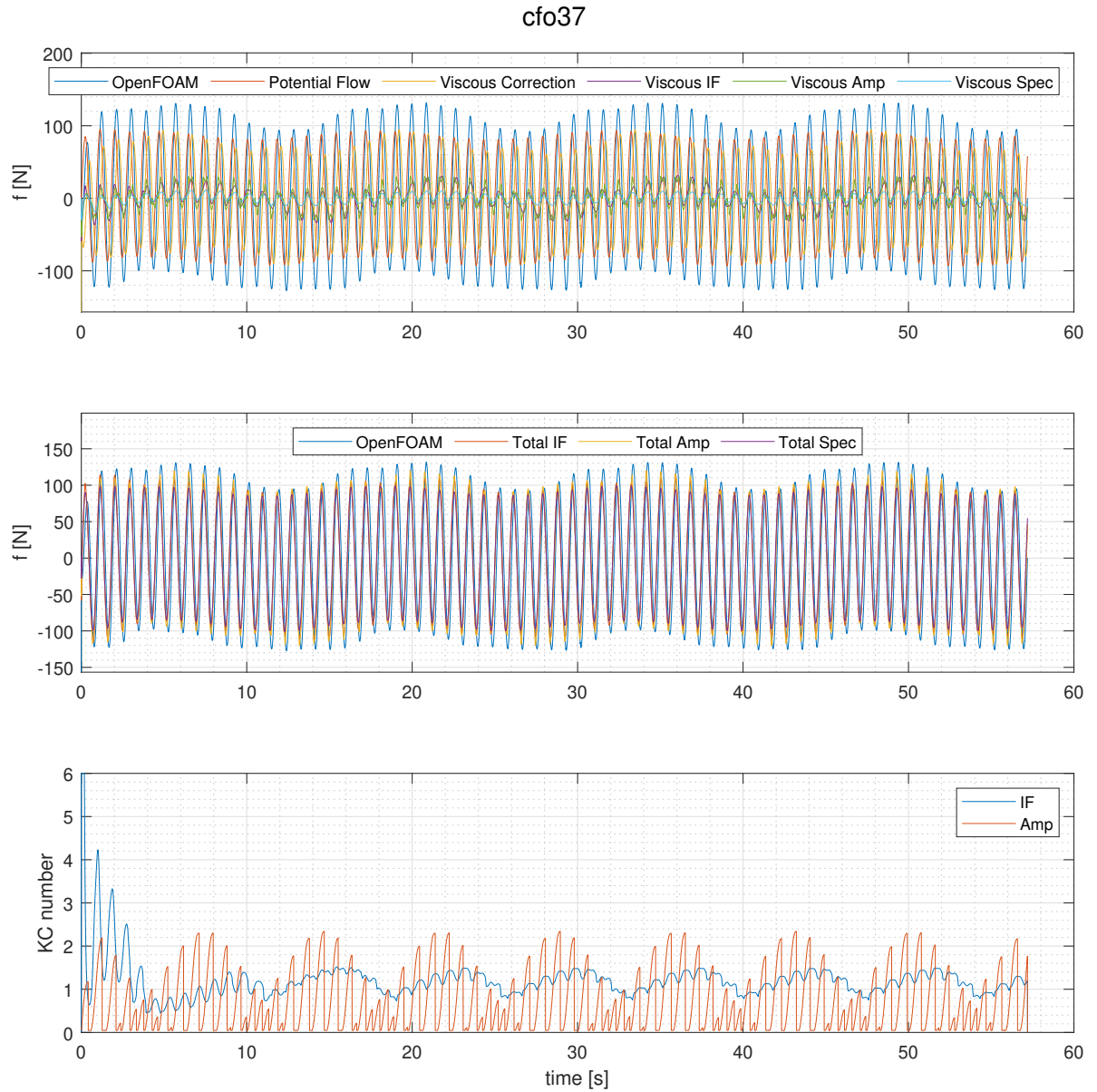


Figure J.3: Reconstruction of case: *cfo37*

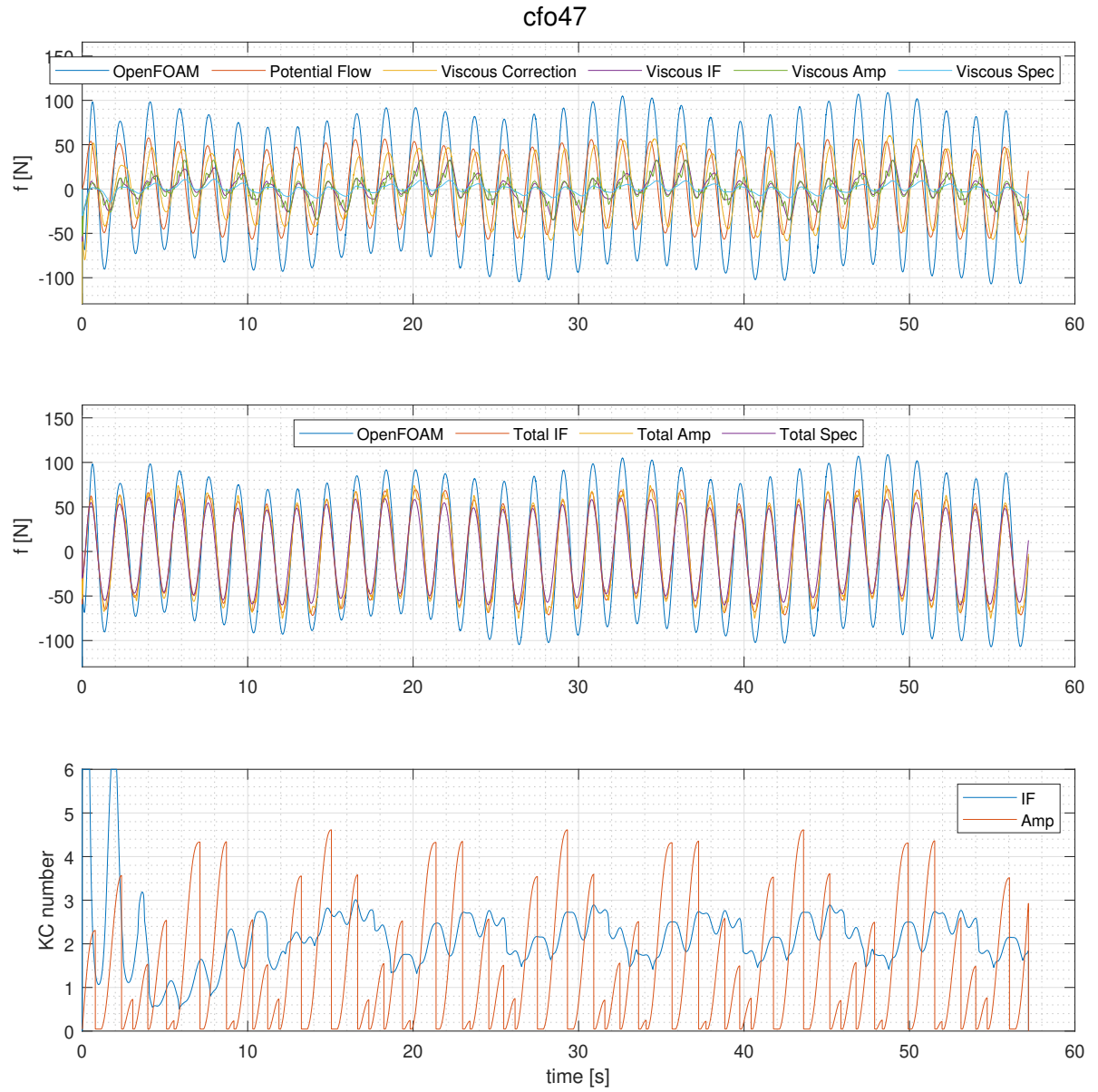


Figure J.4: Reconstruction of case: *cfo47*

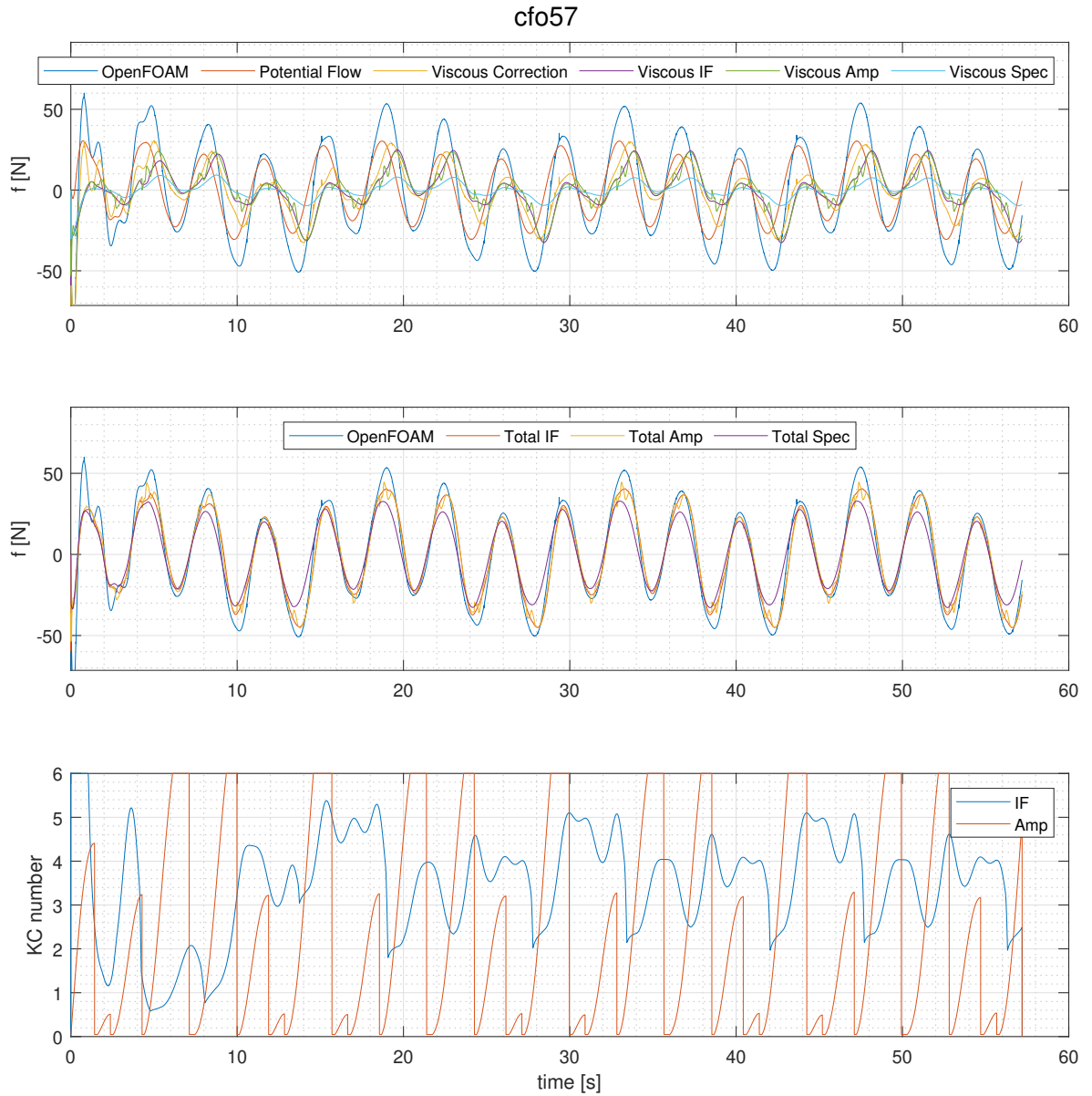


Figure J.5: Reconstruction of case: *cfo57*

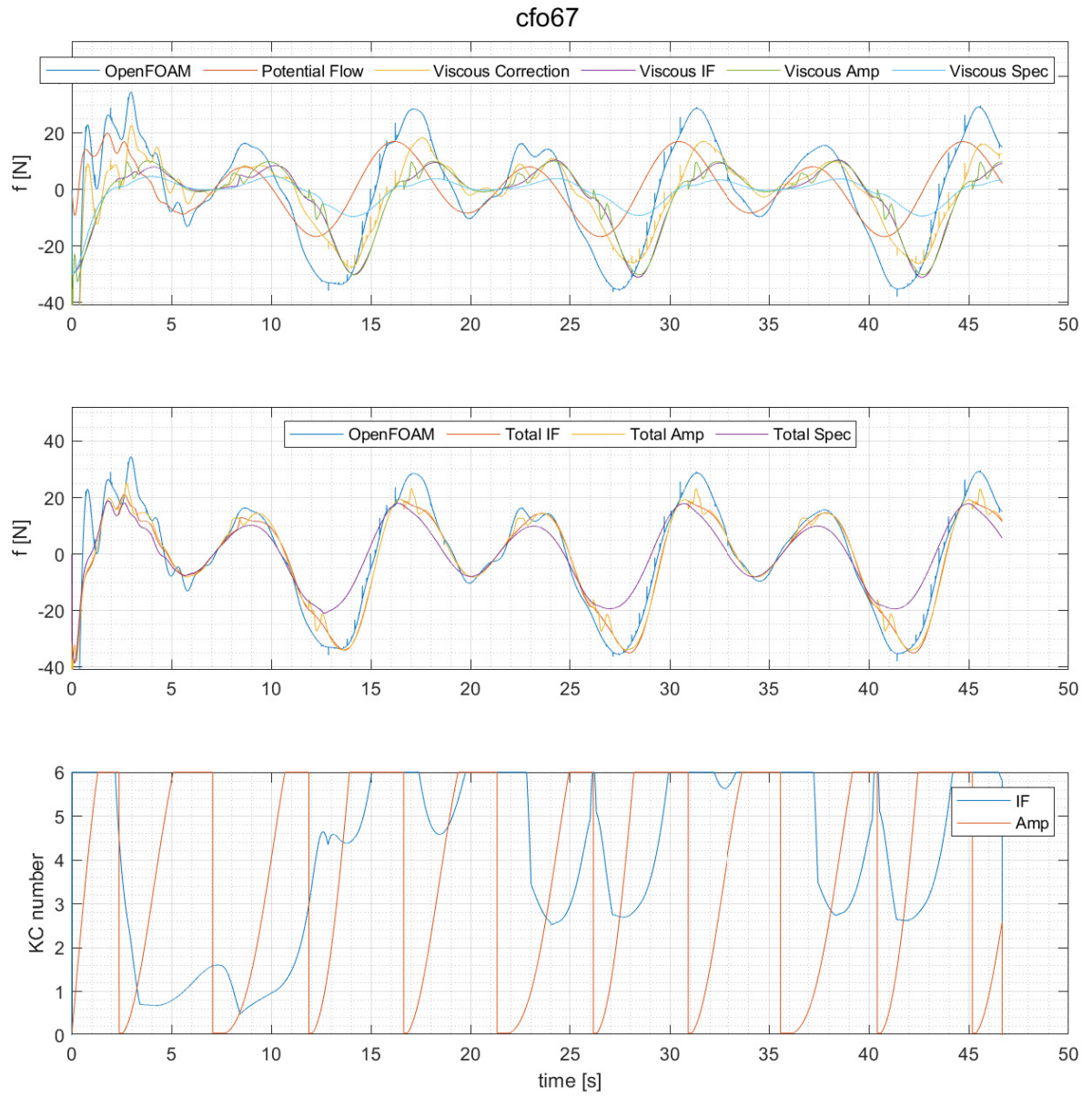


Figure J.6: Reconstruction of case: *cfo67*

K Time Series Reconstruction with Viscous Correction Functions

The following plots show time series reconstruction of the motions of the platform in the model tests. The results from three different modeling techniques are shown. The first is a potential flow only model with a constant value of critical damping. The second incorporates the full viscous correction model. The third incorporates only the quadratic portion of the viscous correction model.

K.1 Mono-Chromatic Cases

The first set of time series are for the mono-chromatic wave cases.

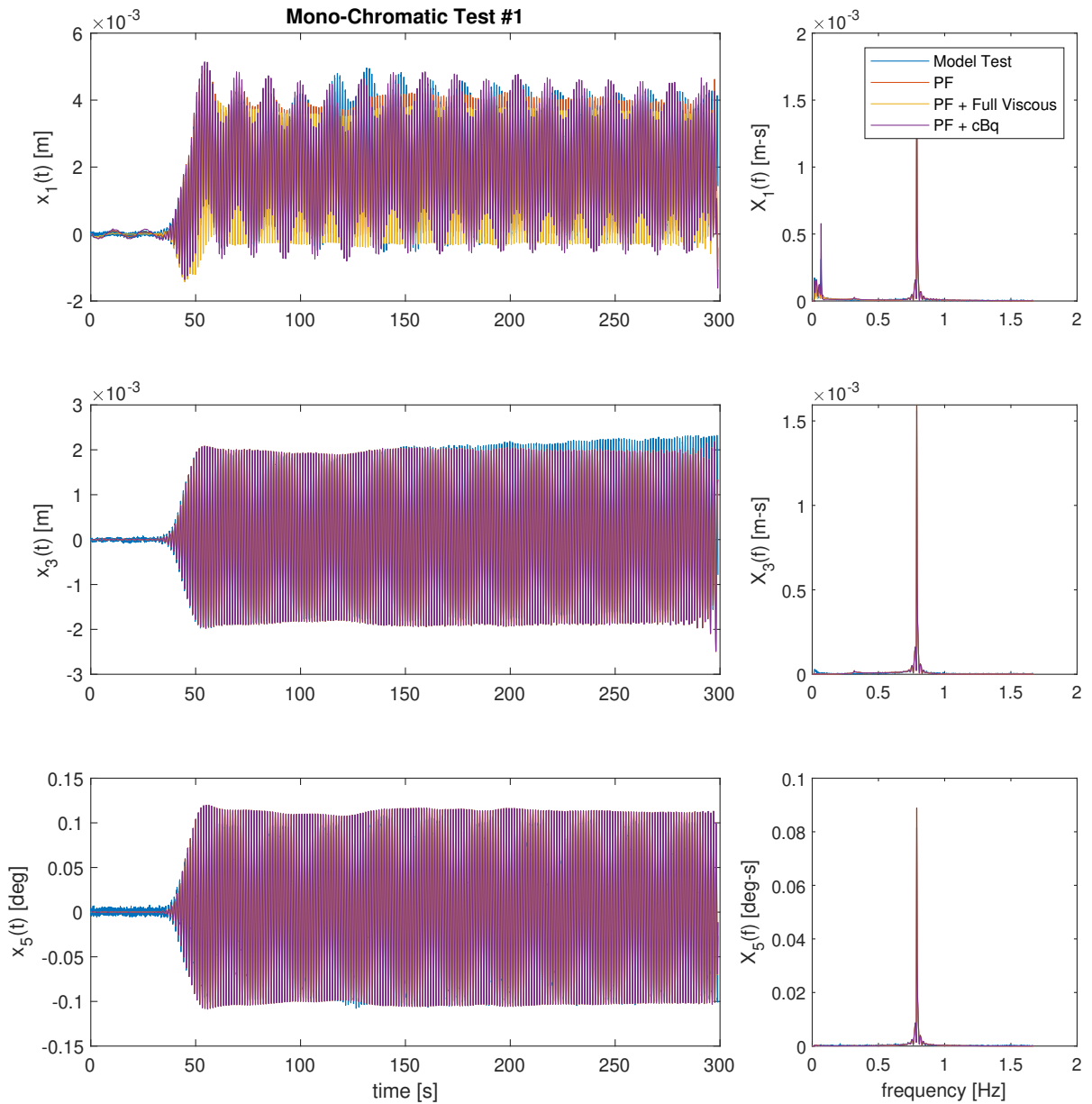


Figure K.1: Time series reconstruction of mono-chromatic test #1 with viscous corrections

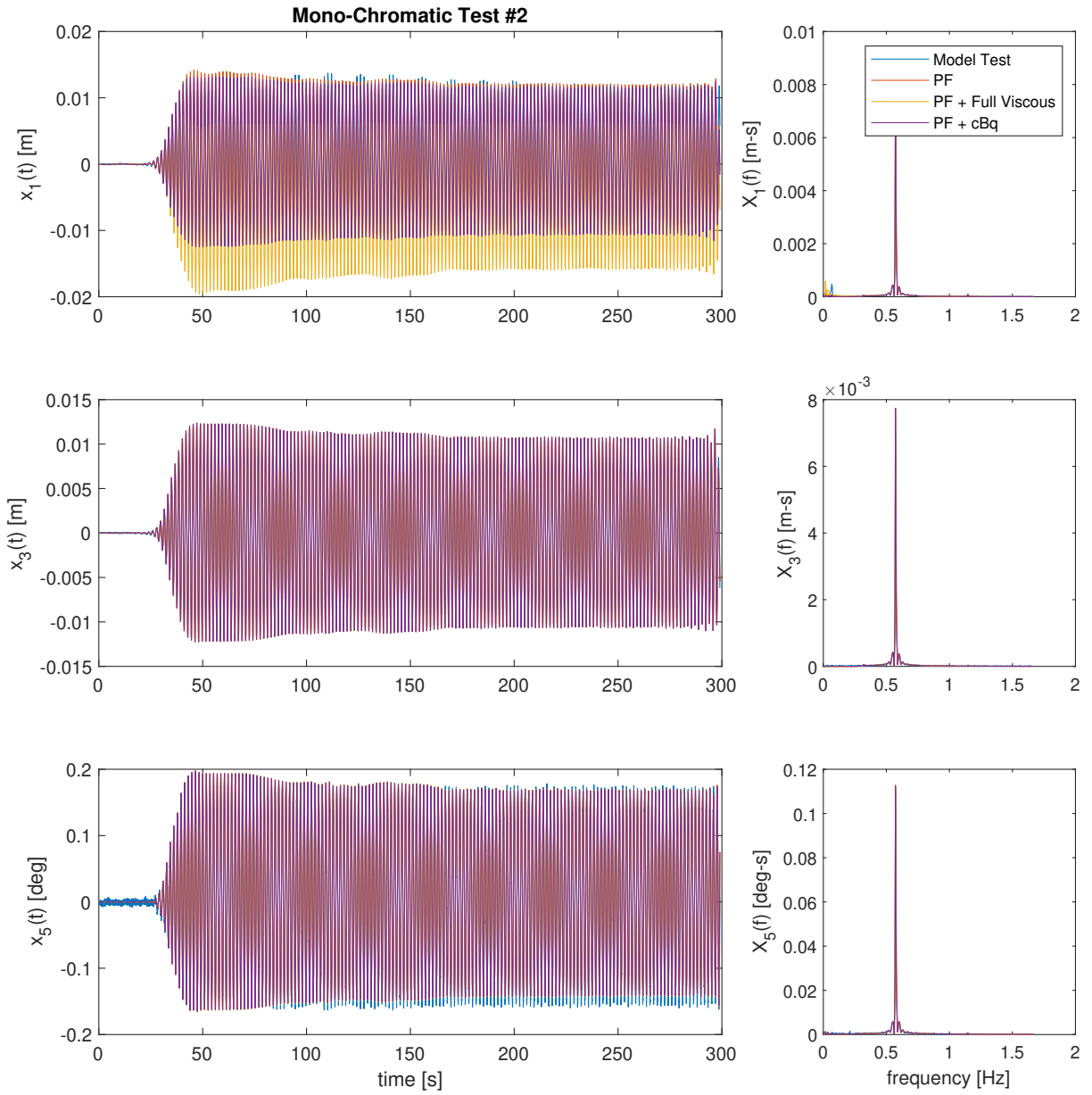


Figure K.2: Time series reconstruction of mono-chromatic test #2 with viscous corrections

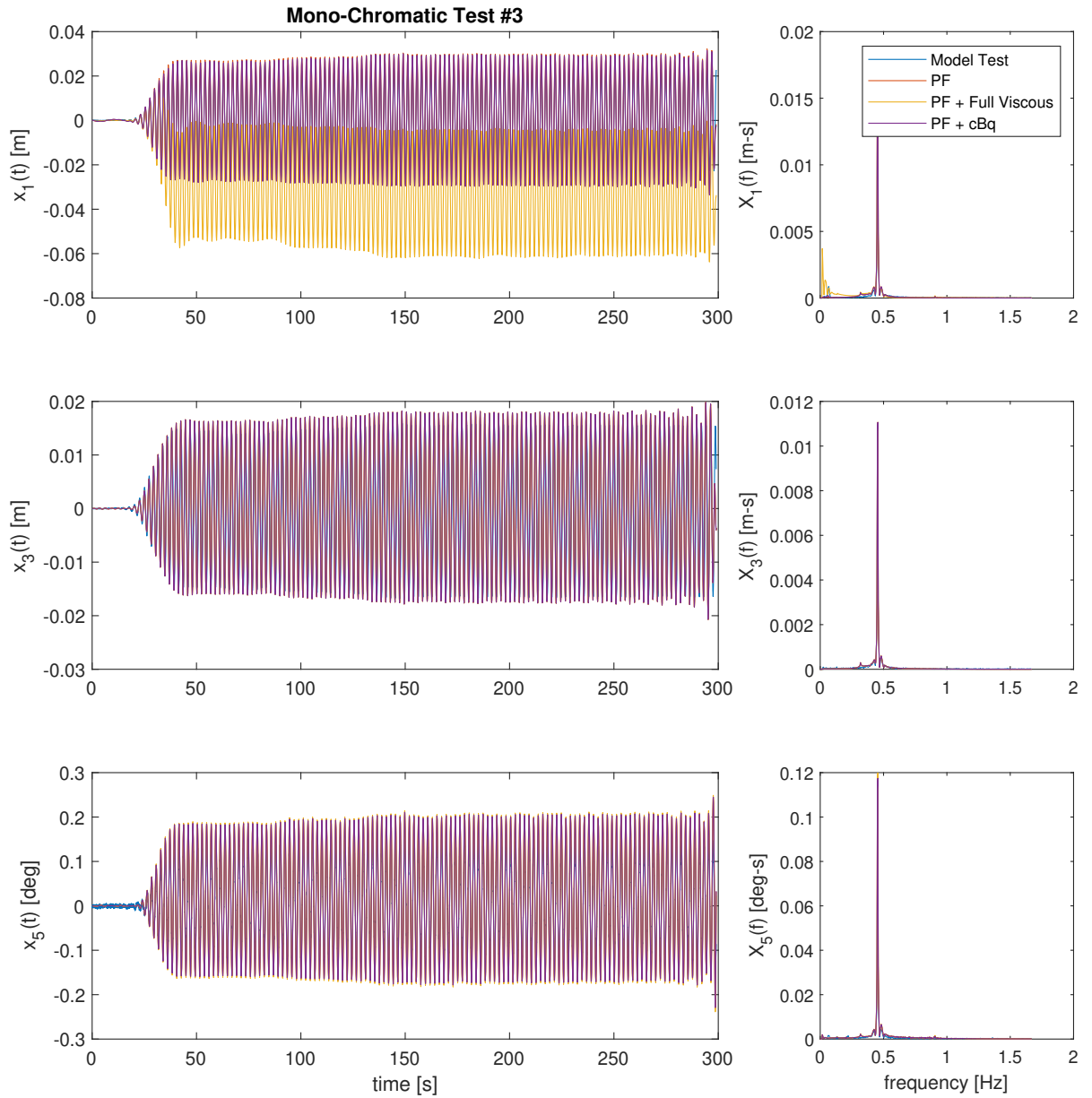


Figure K.3: Time series reconstruction of mono-chromatic test #3 with viscous corrections

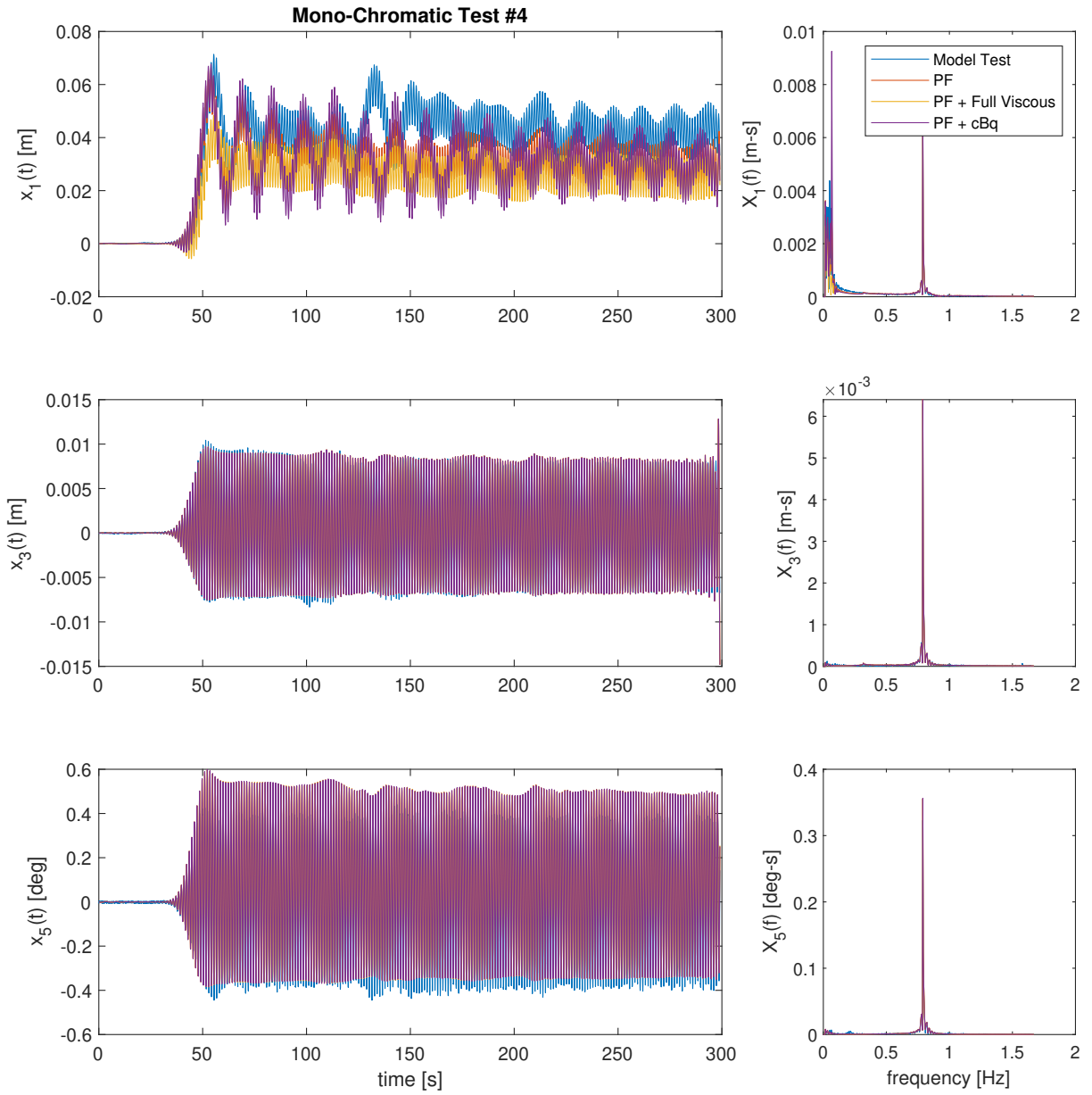


Figure K.4: Time series reconstruction of mono-chromatic test #4 with viscous corrections

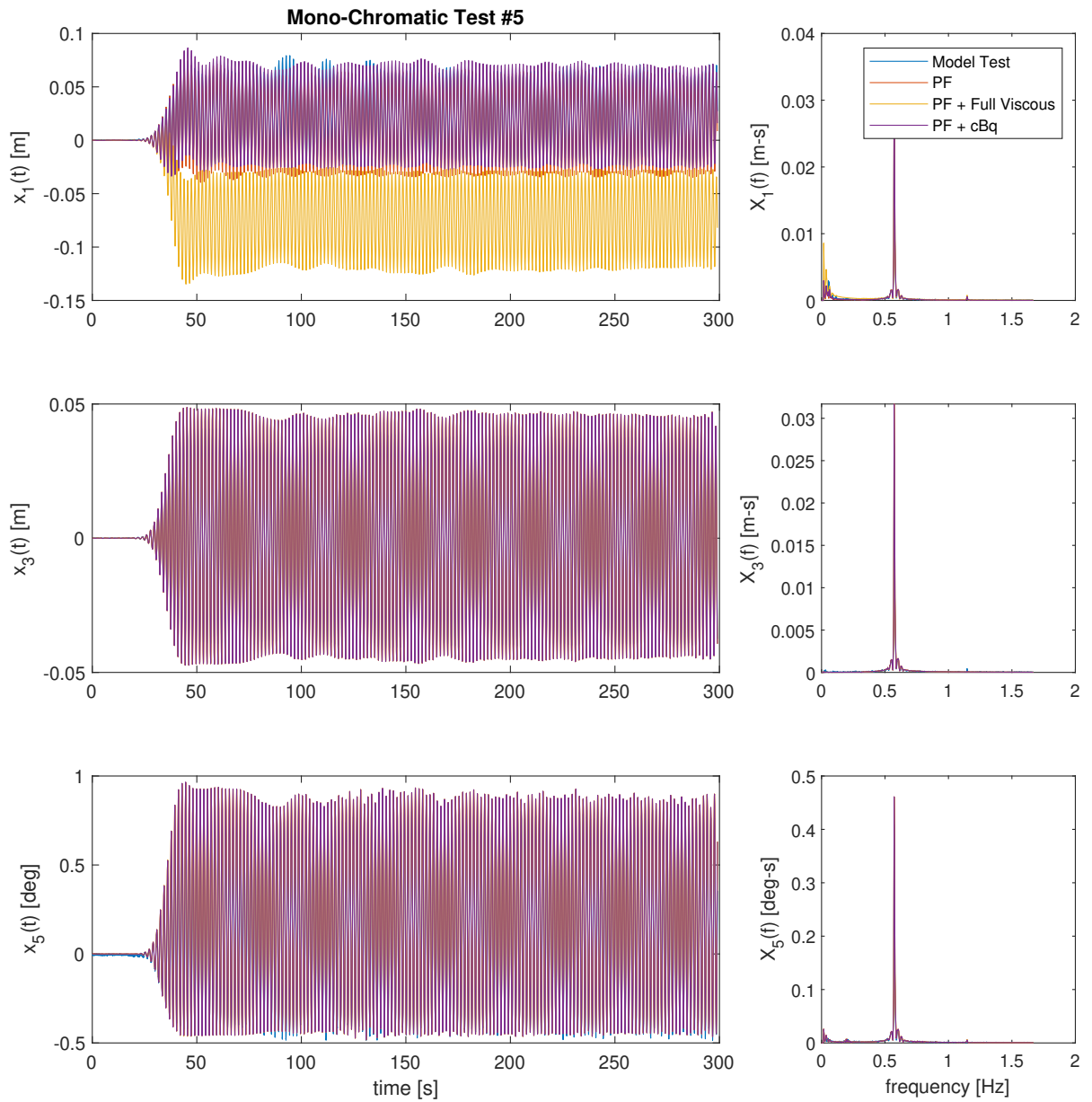


Figure K.5: Time series reconstruction of mono-chromatic test #5 with viscous corrections

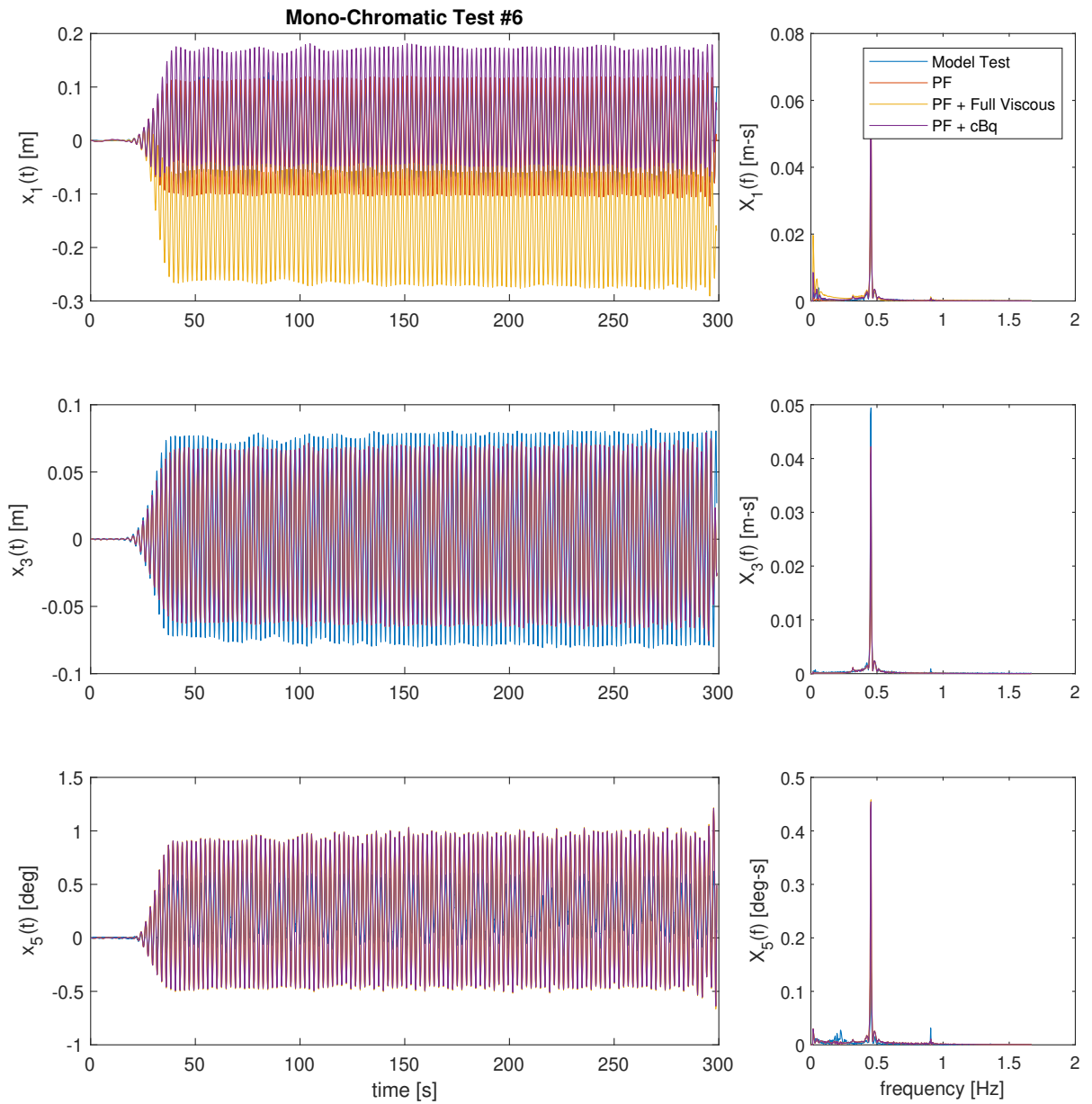


Figure K.6: Time series reconstruction of mono-chromatic test #6 with viscous corrections

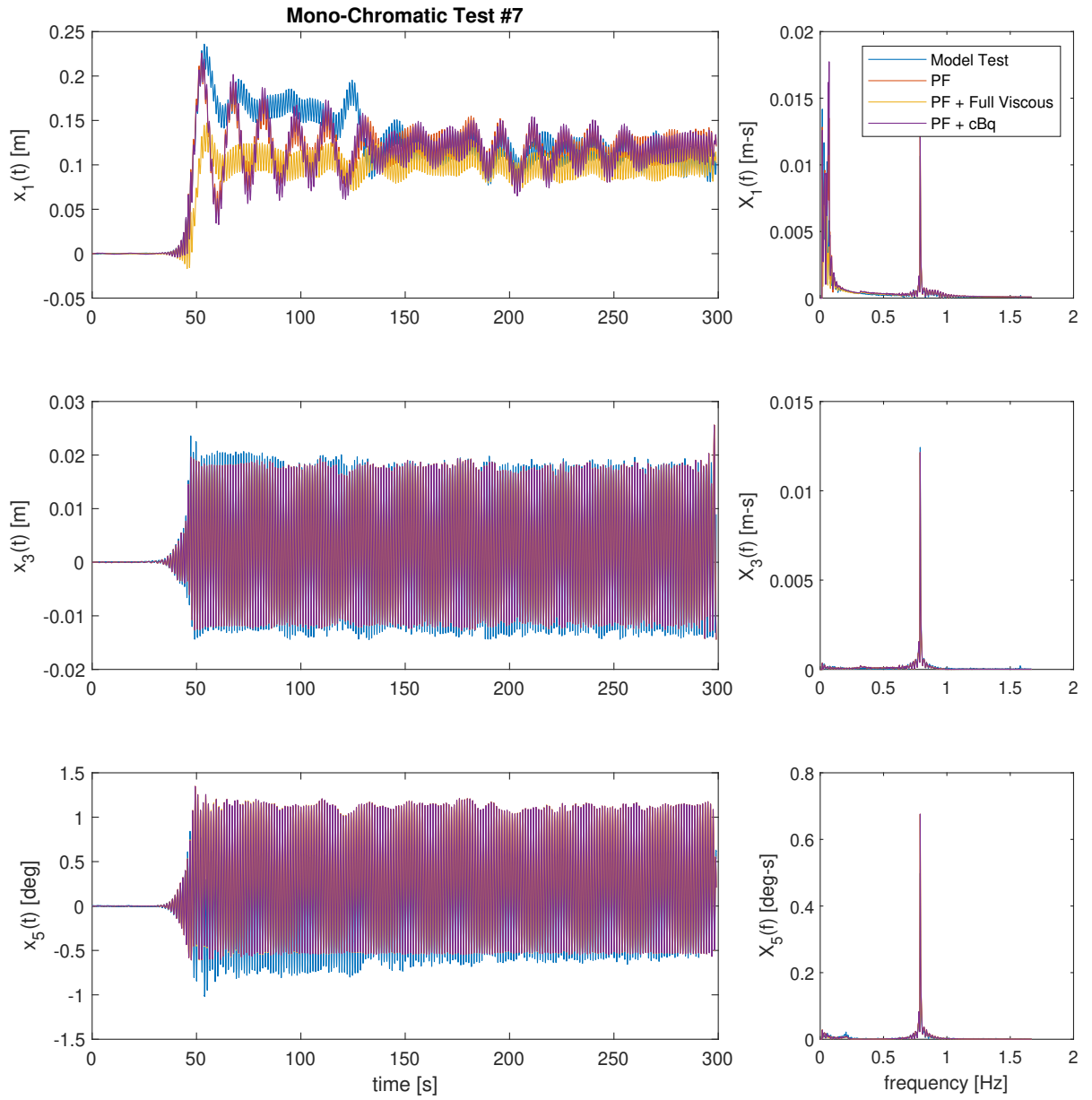


Figure K.7: Time series reconstruction of mono-chromatic test #7 with viscous corrections

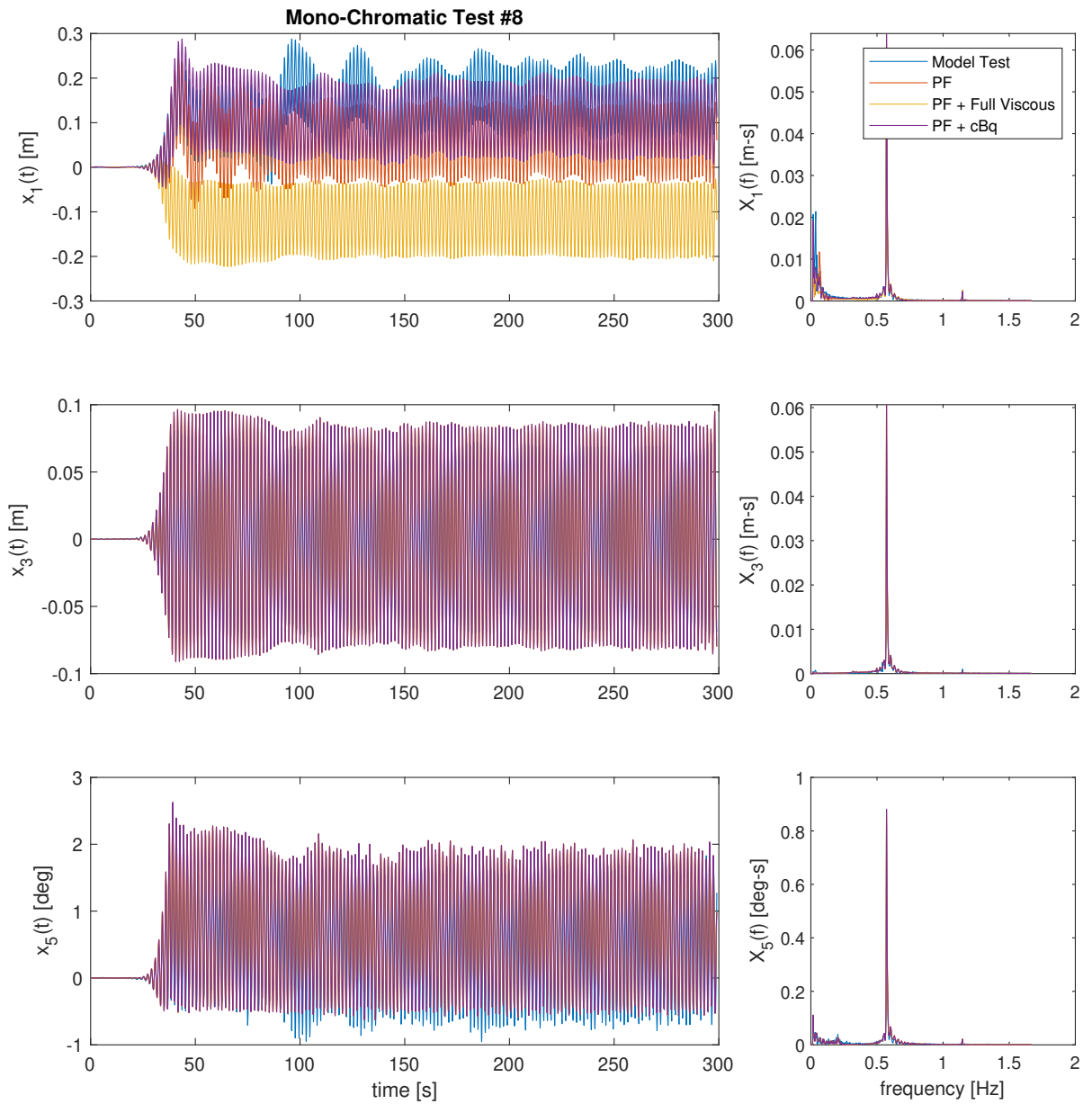


Figure K.8: Time series reconstruction of mono-chromatic test #8 with viscous corrections

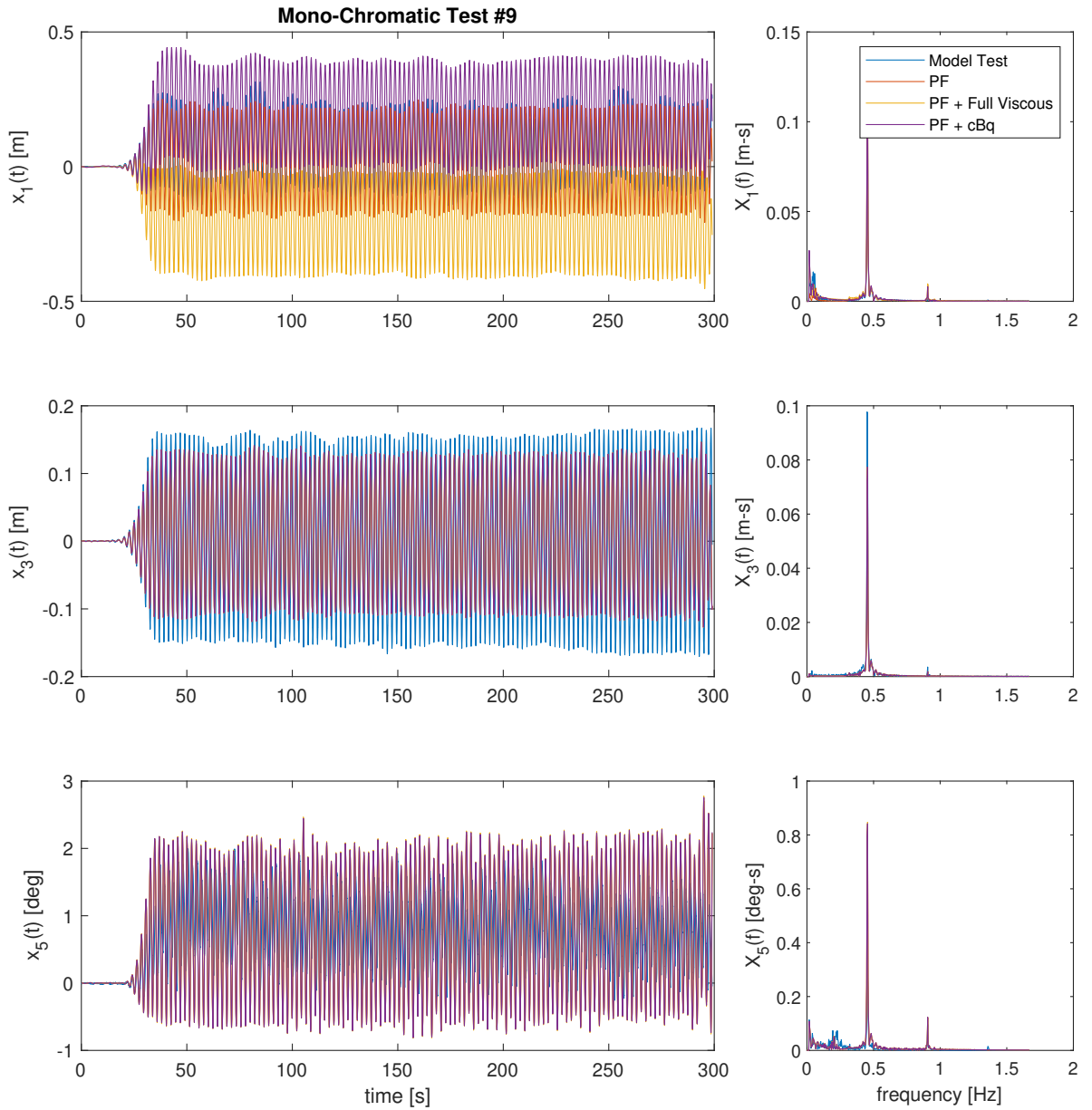


Figure K.9: Time series reconstruction of mono-chromatic test #9 with viscous corrections

K.2 Bi-Chromatic Cases

The second set of time series are for the bichromatic wave cases. Tests 1-5 have a difference frequency of the surge natural frequency and tests 6-10 have a difference frequency equal to the pitch natural frequency.

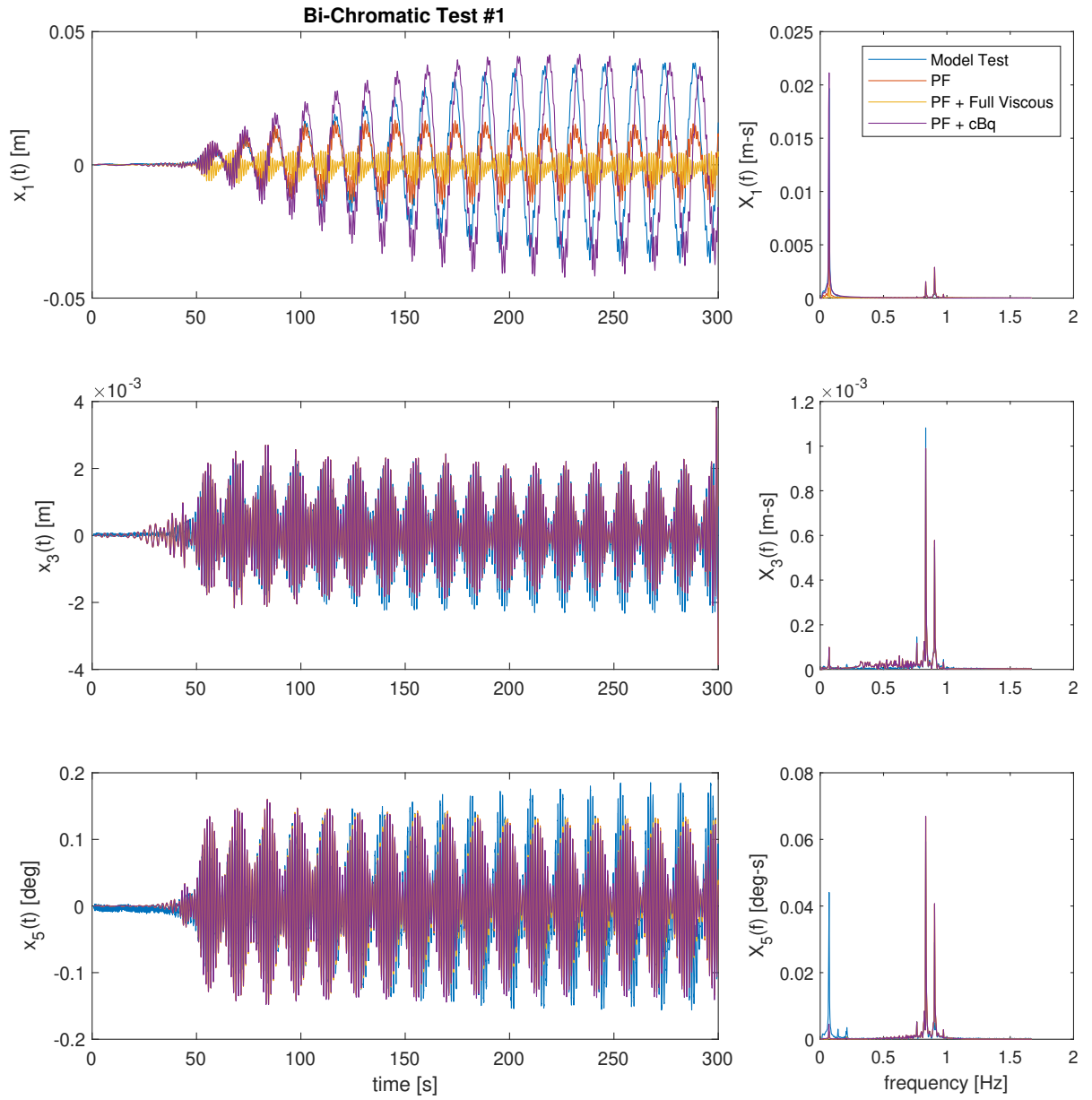


Figure K.10: Time series reconstruction of bi-chromatic test #1 with viscous corrections

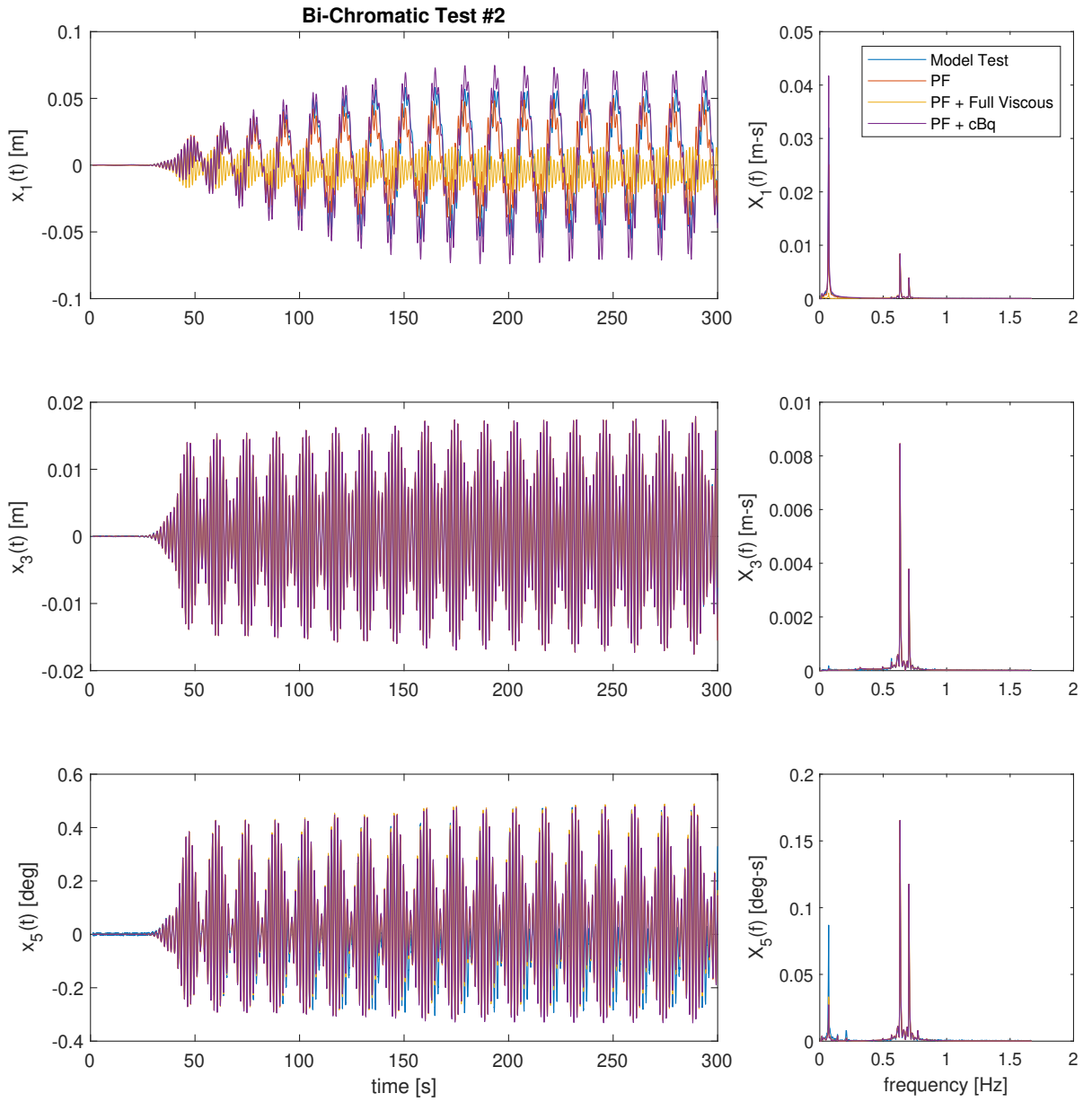


Figure K.11: Time series reconstruction of bi-chromatic test #2 with viscous corrections

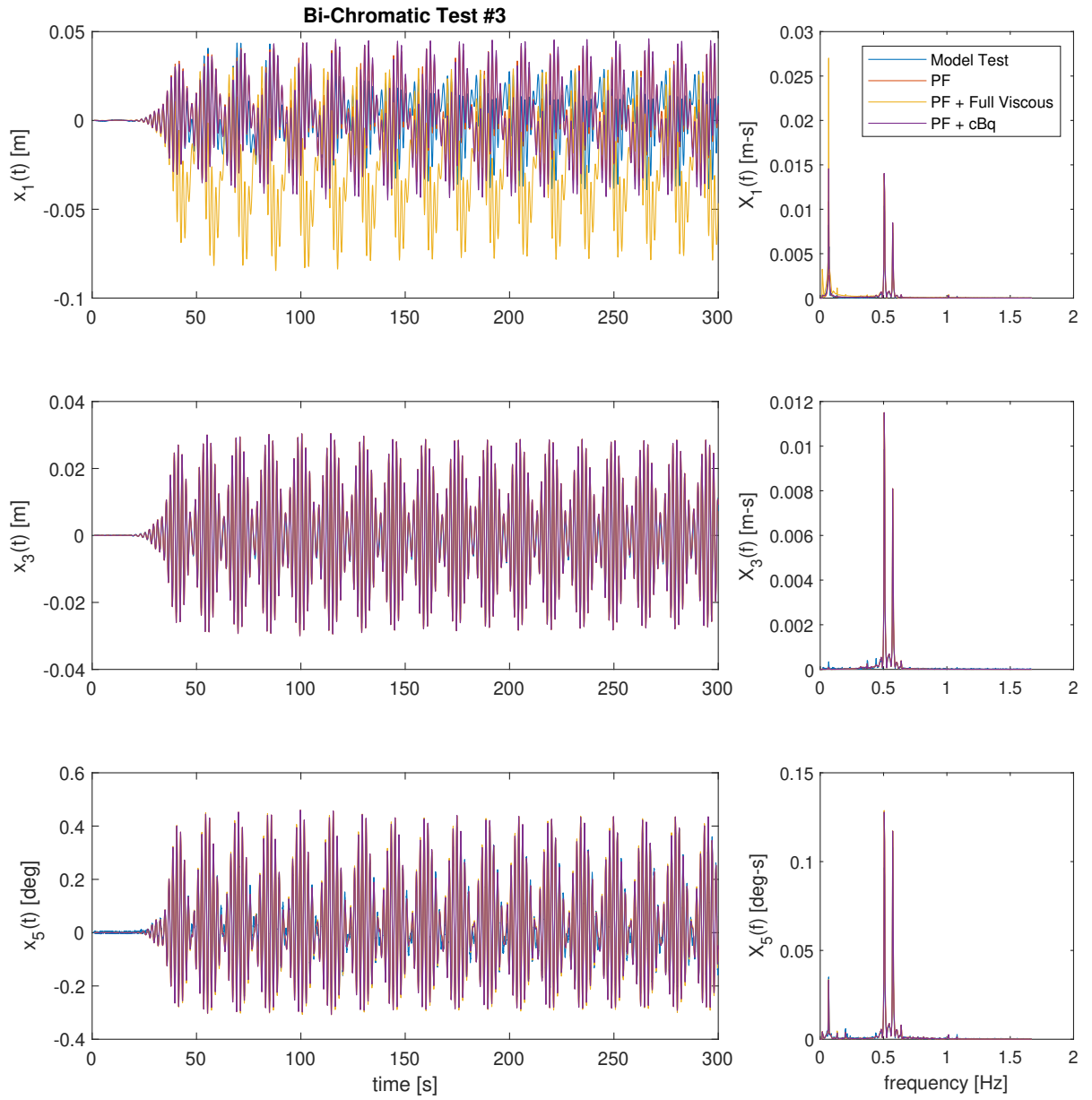


Figure K.12: Time series reconstruction of bi-chromatic test #3 with viscous corrections

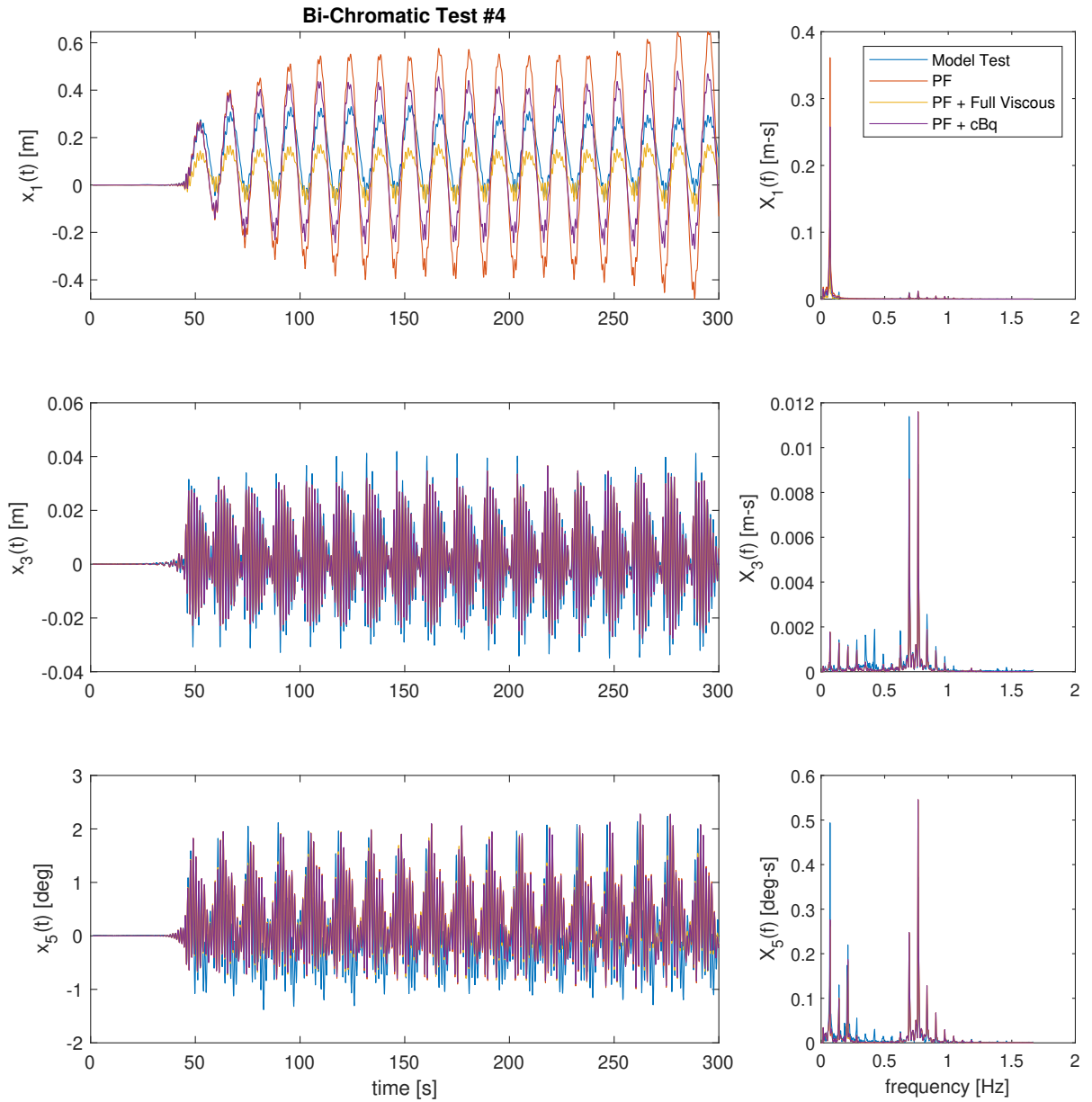


Figure K.13: Time series reconstruction of bi-chromatic test #4 with viscous corrections

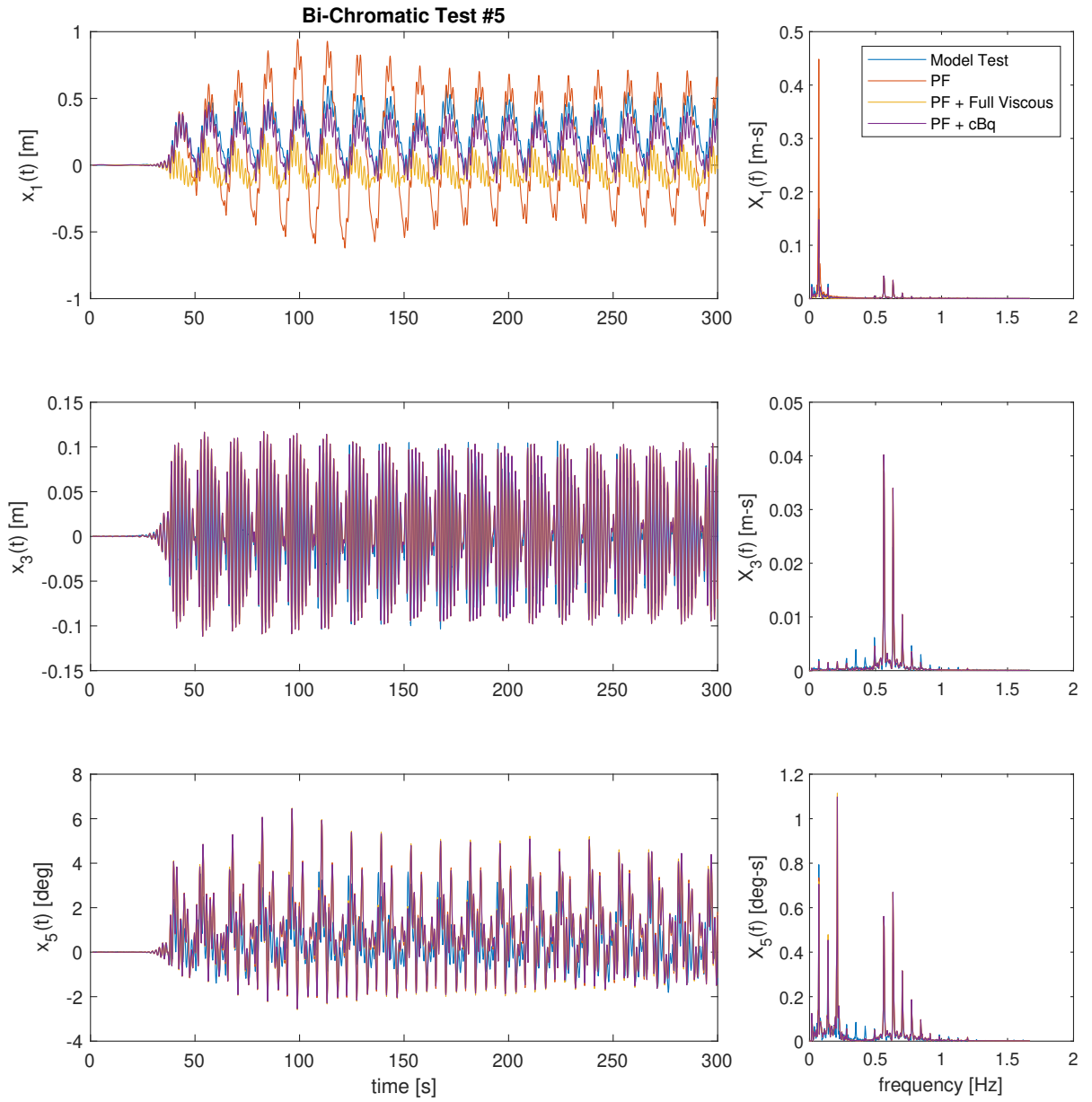


Figure K.14: Time series reconstruction of bi-chromatic test #5 with viscous corrections

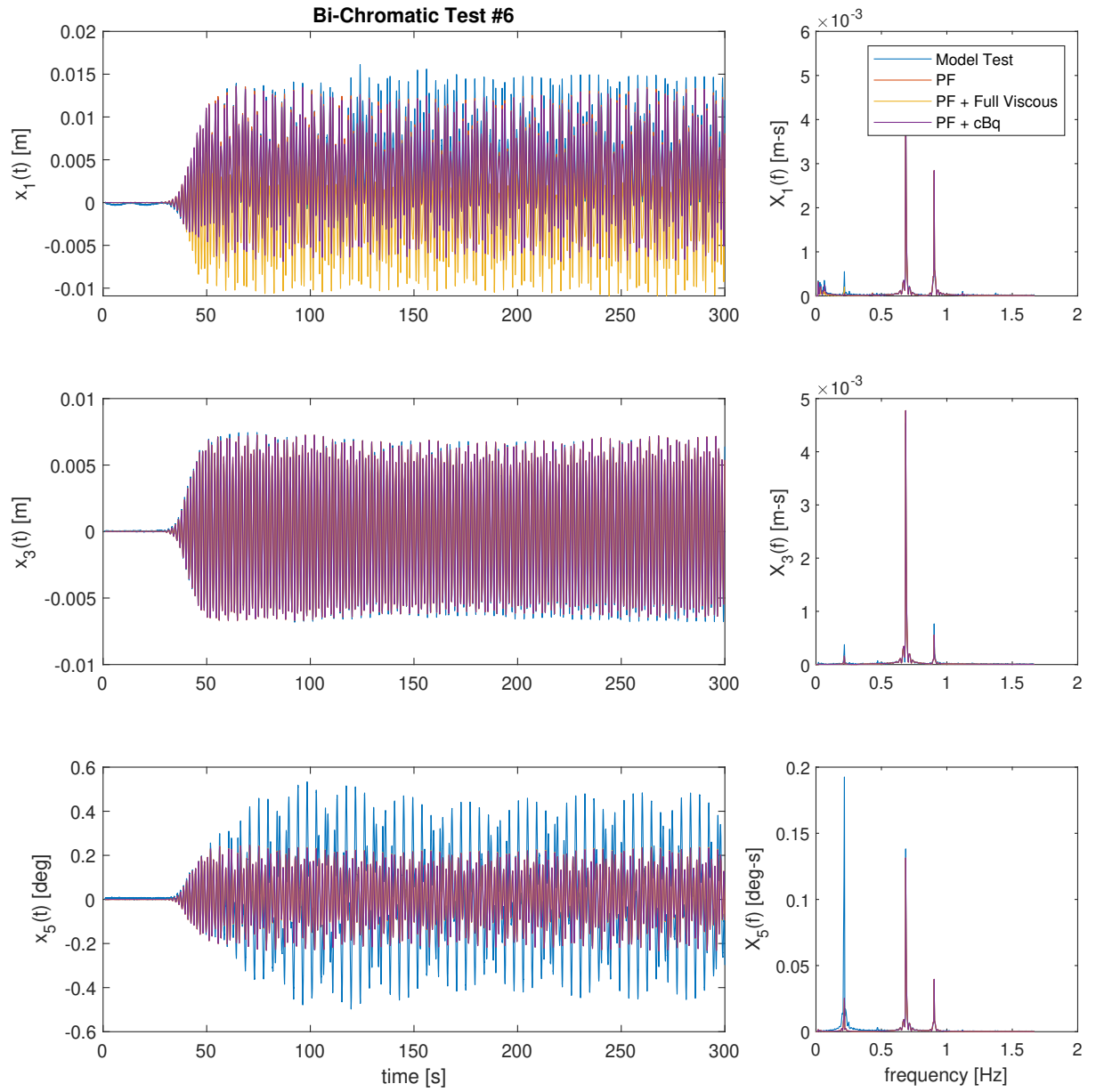


Figure K.15: Time series reconstruction of bi-chromatic test #6 with viscous corrections

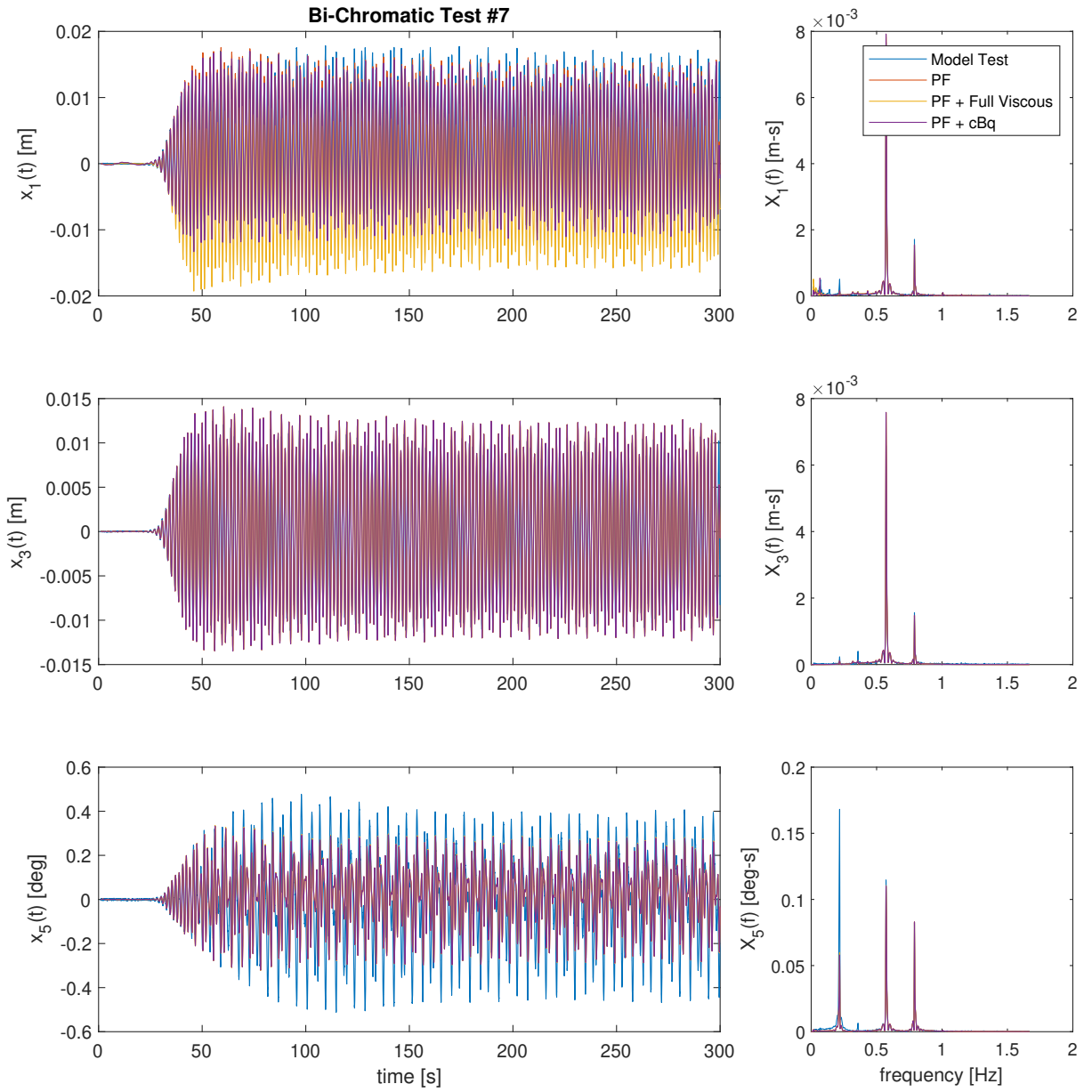


Figure K.16: Time series reconstruction of bi-chromatic test #7 with viscous corrections

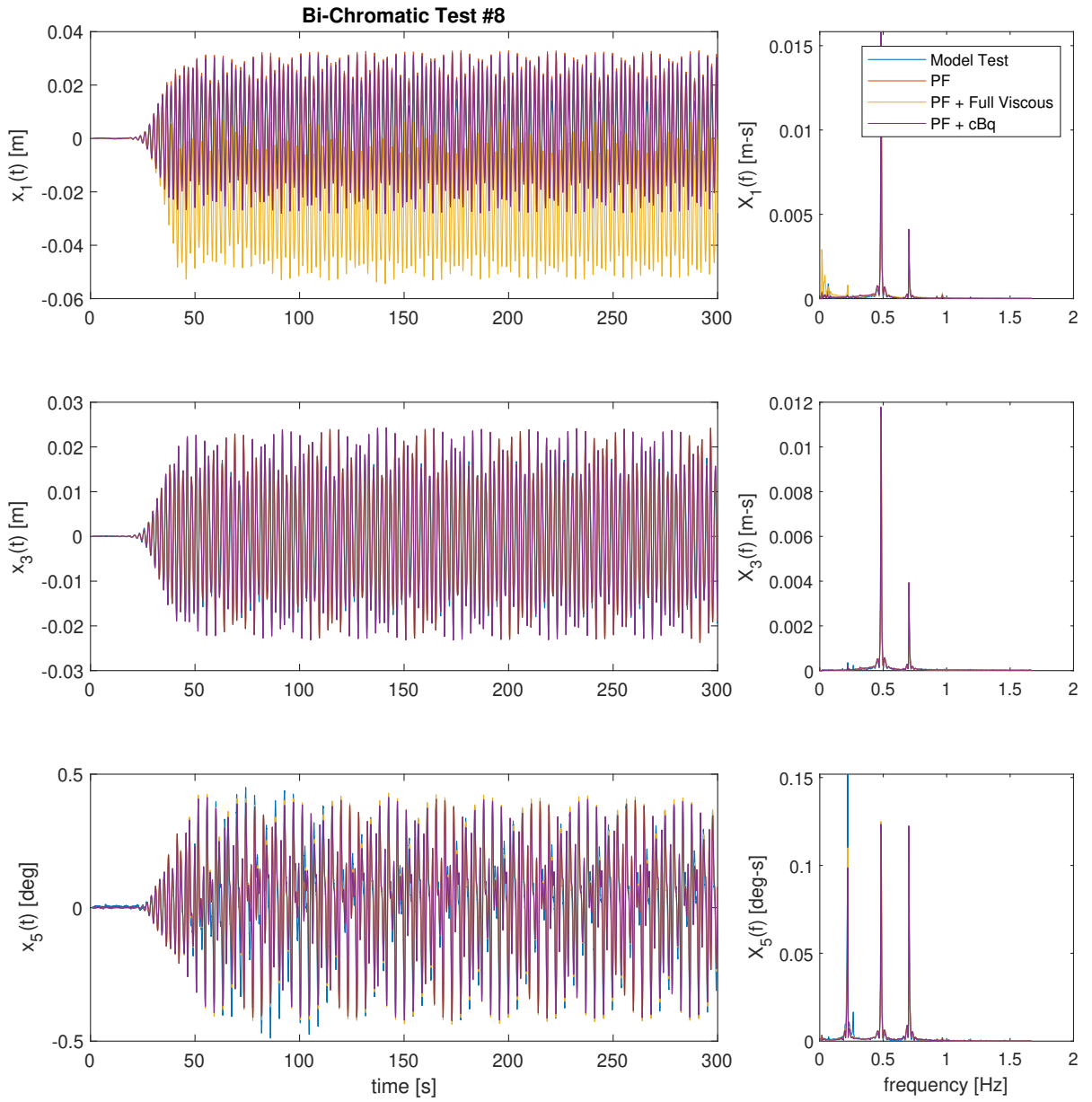


Figure K.17: Time series reconstruction of bi-chromatic test #8 with viscous corrections

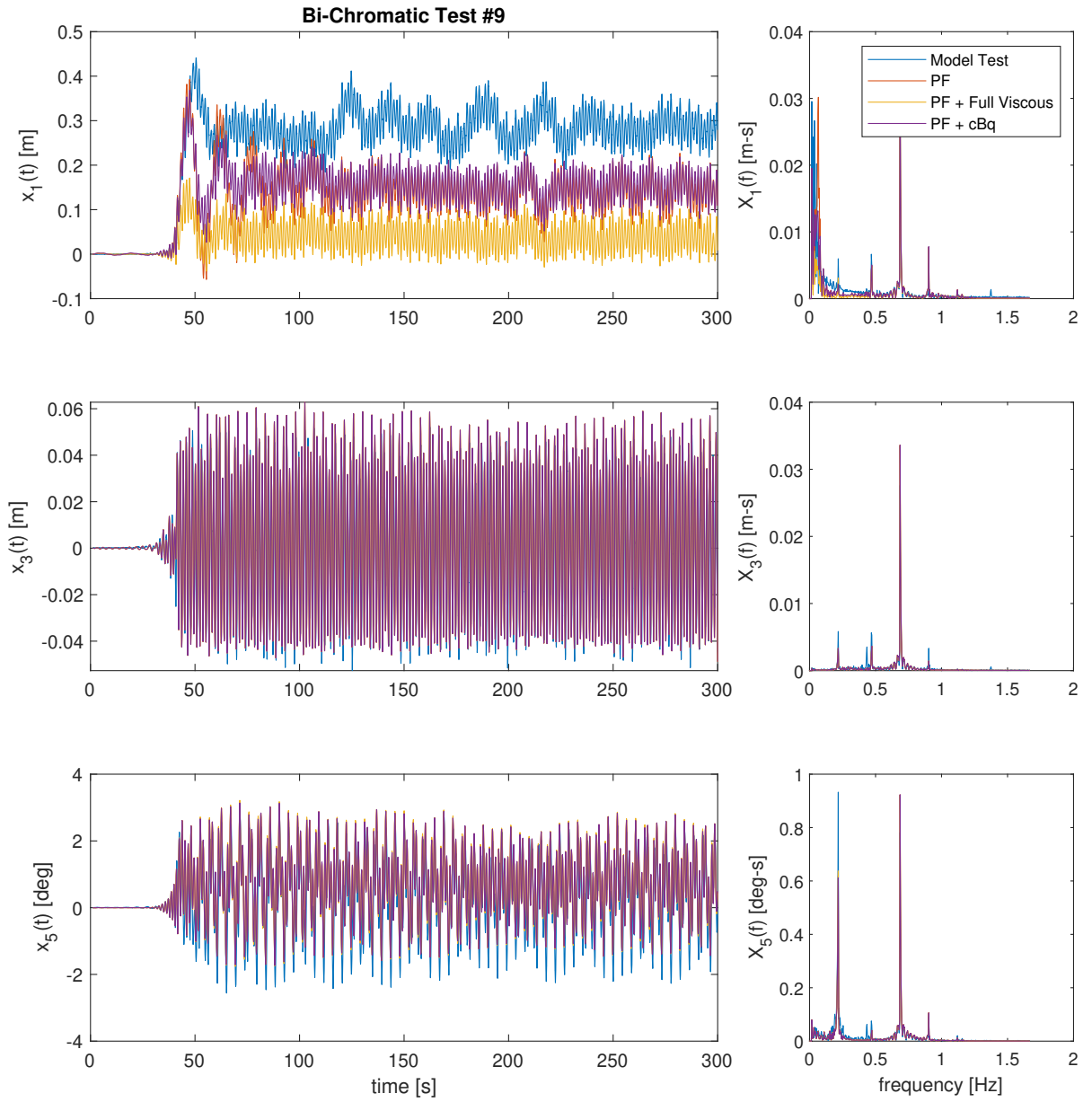


Figure K.18: Time series reconstruction of bi-chromatic test #9 with viscous corrections

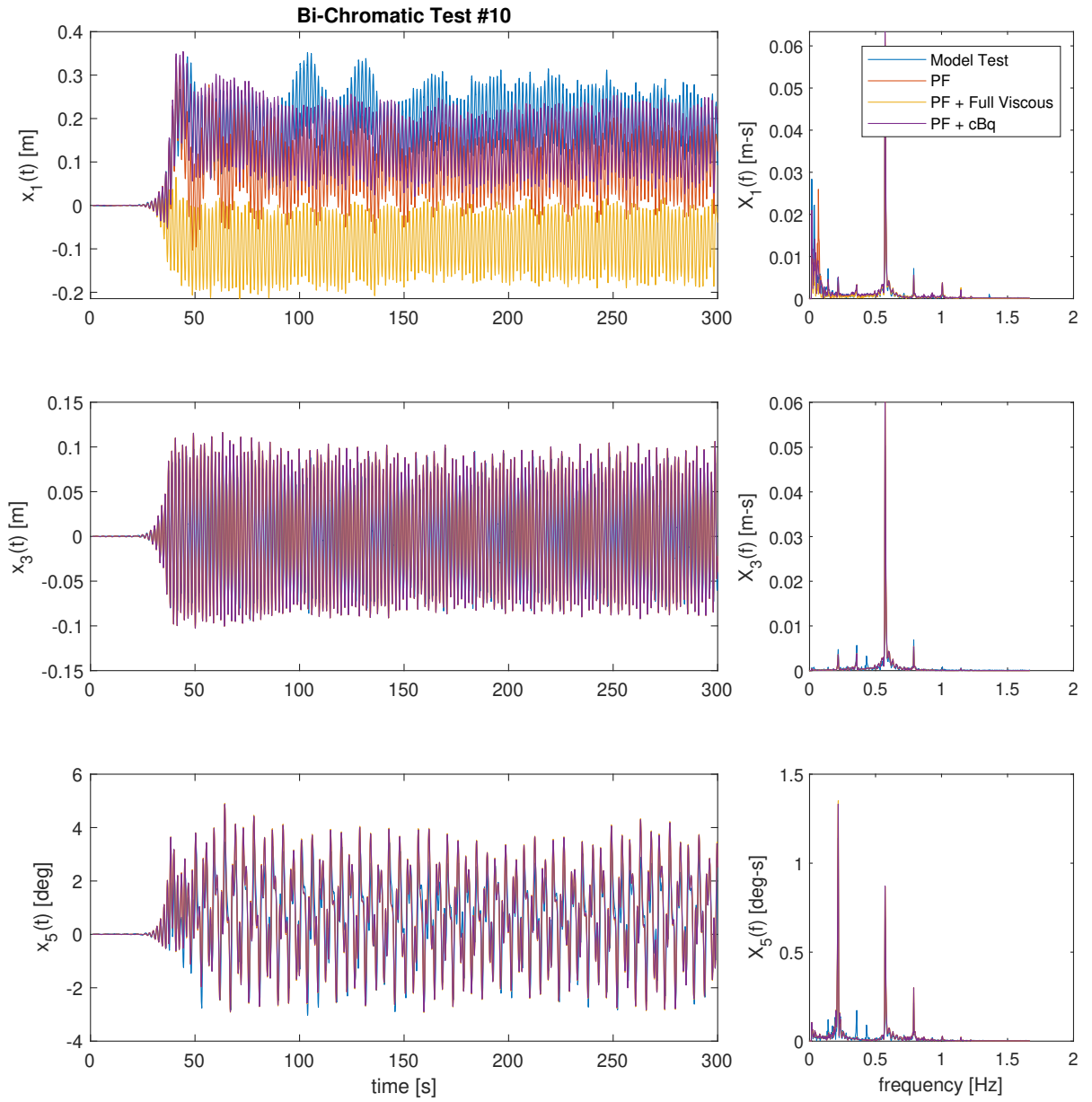


Figure K.19: Time series reconstruction of bi-chromatic test #10 with viscous corrections

K.2.1 Direction Dependent Coefficients

Figure K.20 shows the surge motion for the first five bi-chromatic wave cases ($f_{diff} = fn_1$) when the direction dependent coefficients are used. Based on the sign of the relative velocity the corresponding viscous correction coefficients are selected. This incorporates changes in the drag forces due to the asymmetric geometry.

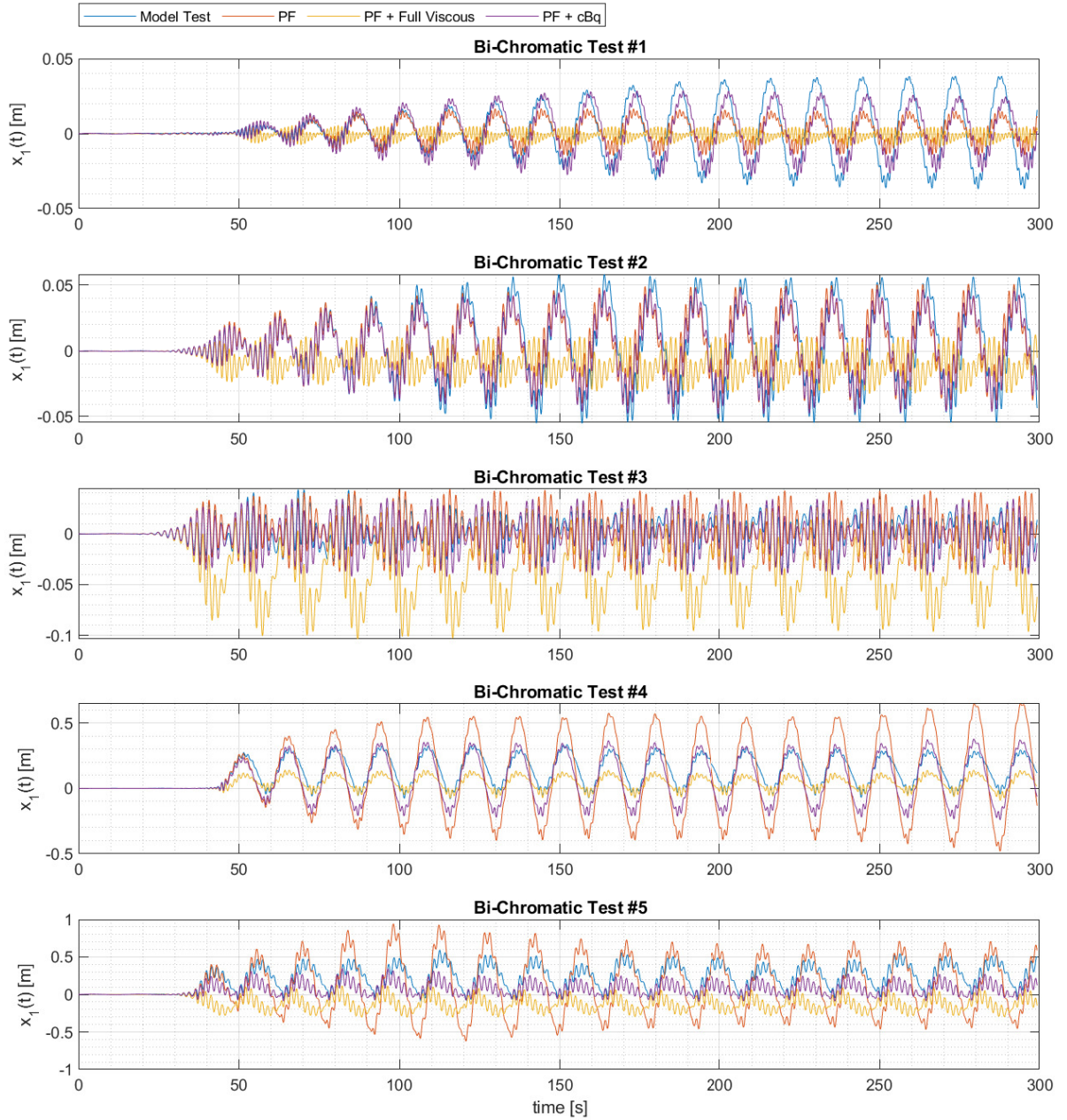


Figure K.20: Time series reconstruction of bi-chromatic wave model test with direction split viscous corrections

K.3 Irregular Cases

The third set of reconstructed time series are for the irregular wave tests.

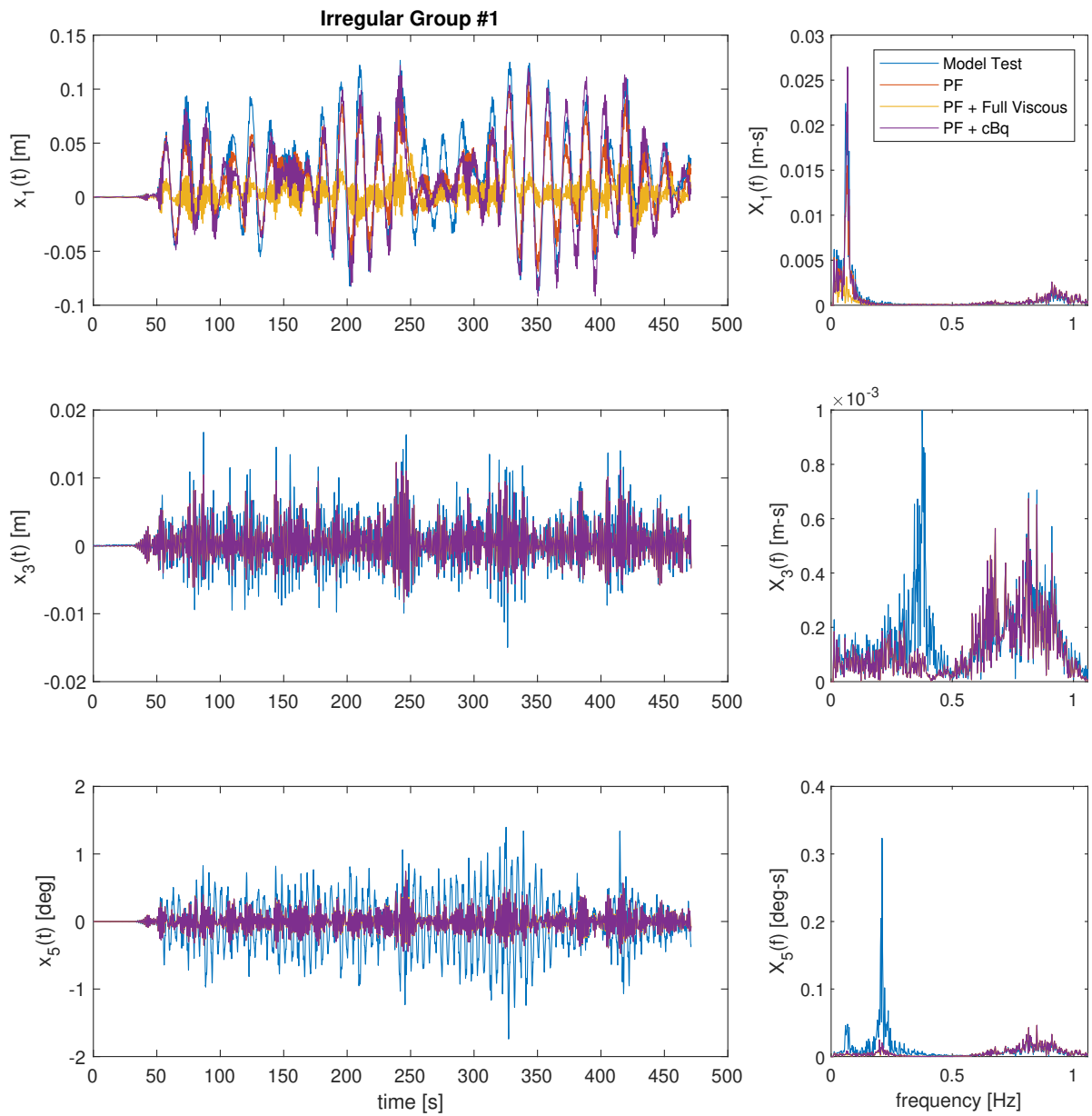


Figure K.21: Time series reconstruction of irregular test #1 with viscous corrections

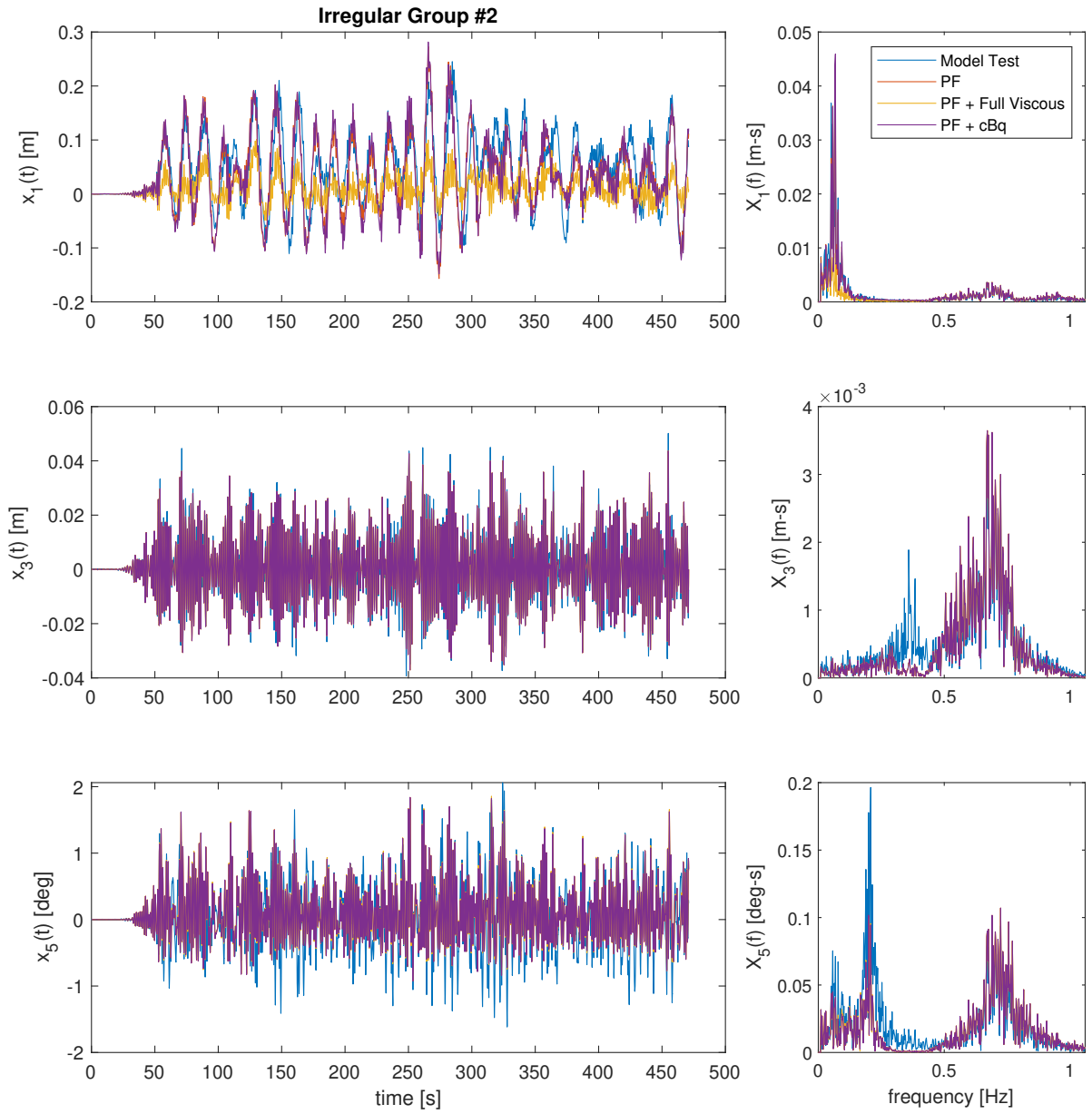


Figure K.22: Time series reconstruction of irregular test #2 with viscous corrections

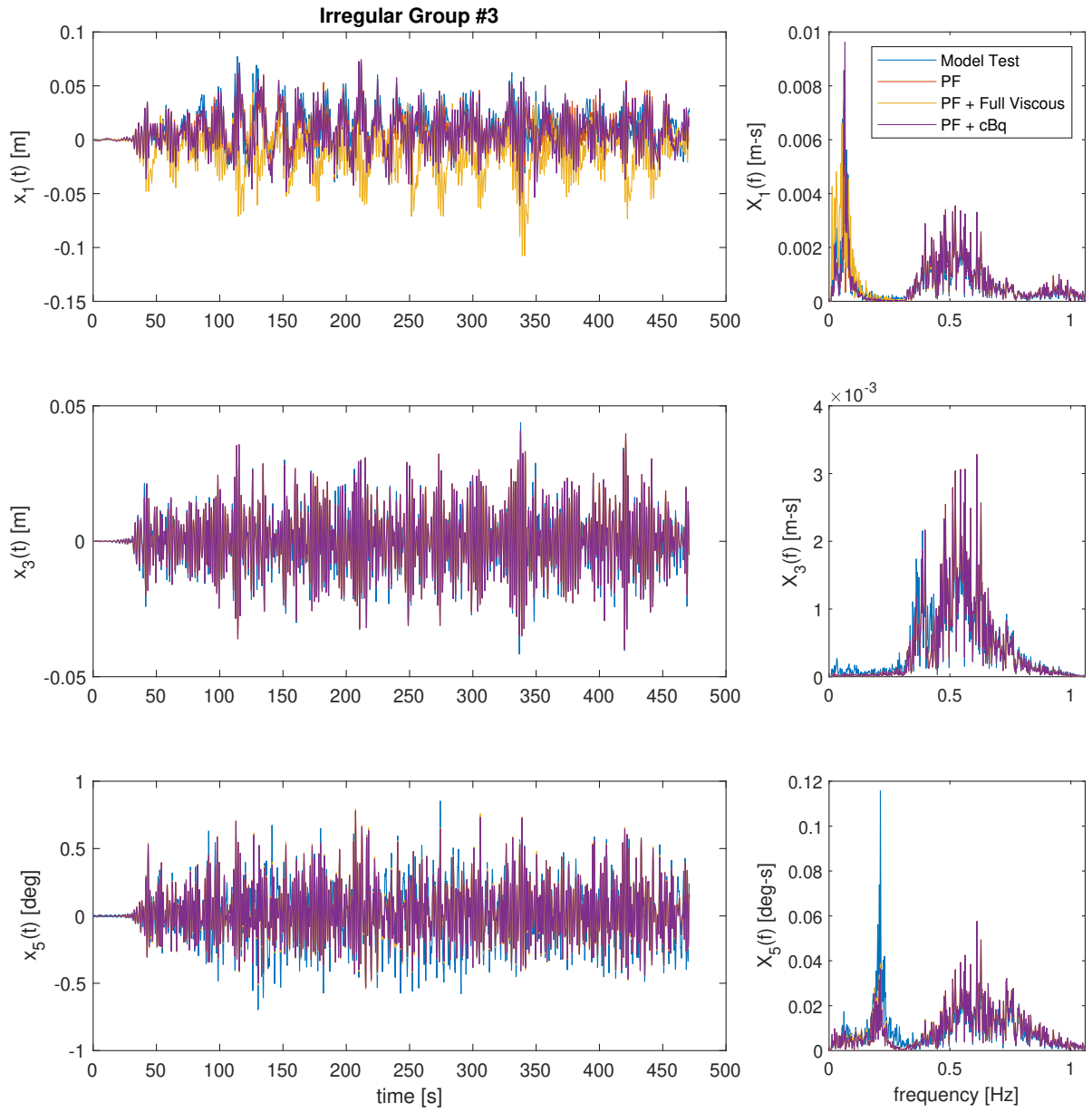


Figure K.23: Time series reconstruction of irregular test #3 with viscous corrections

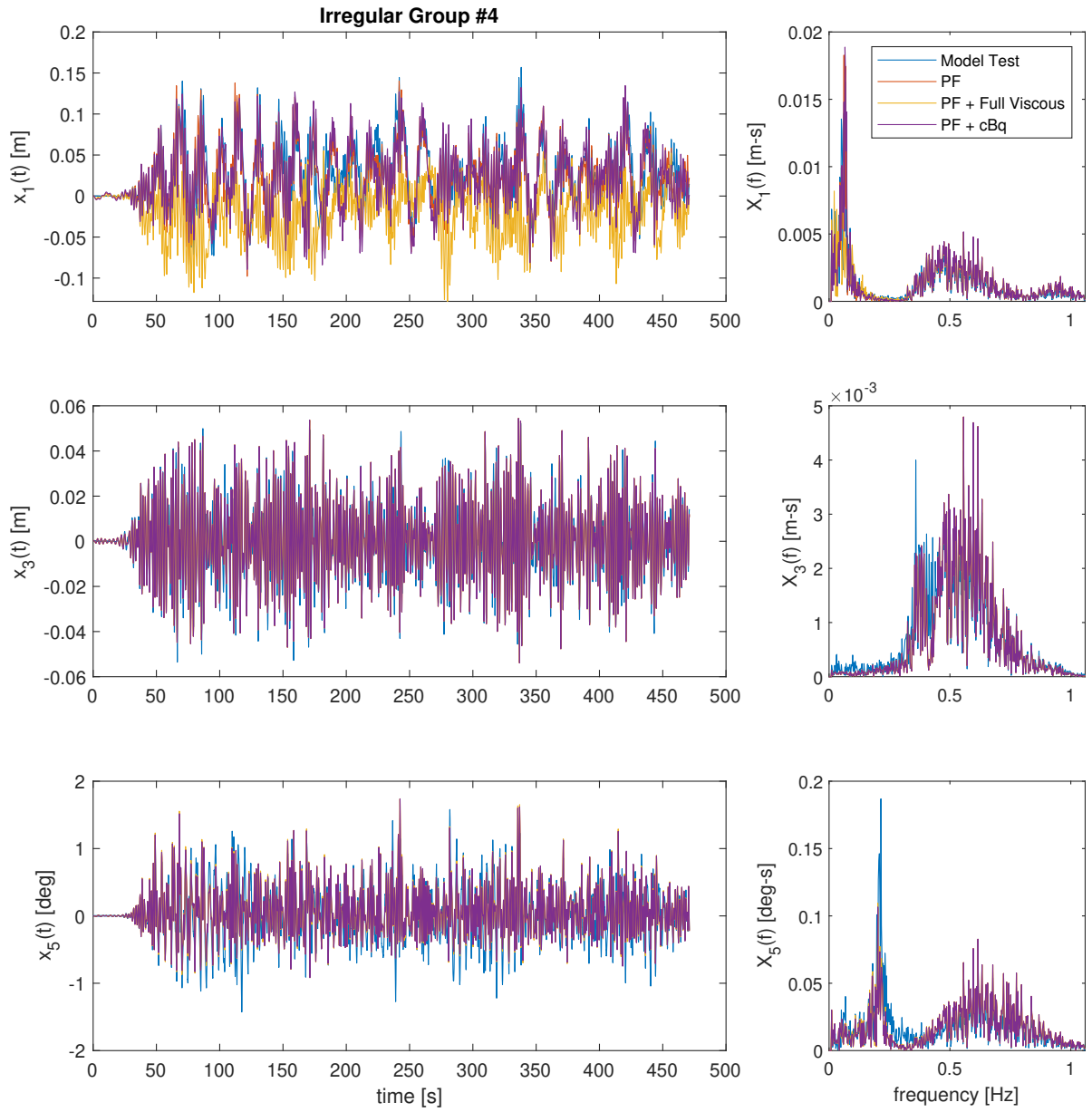


Figure K.24: Time series reconstruction of irregular test #4 with viscous corrections

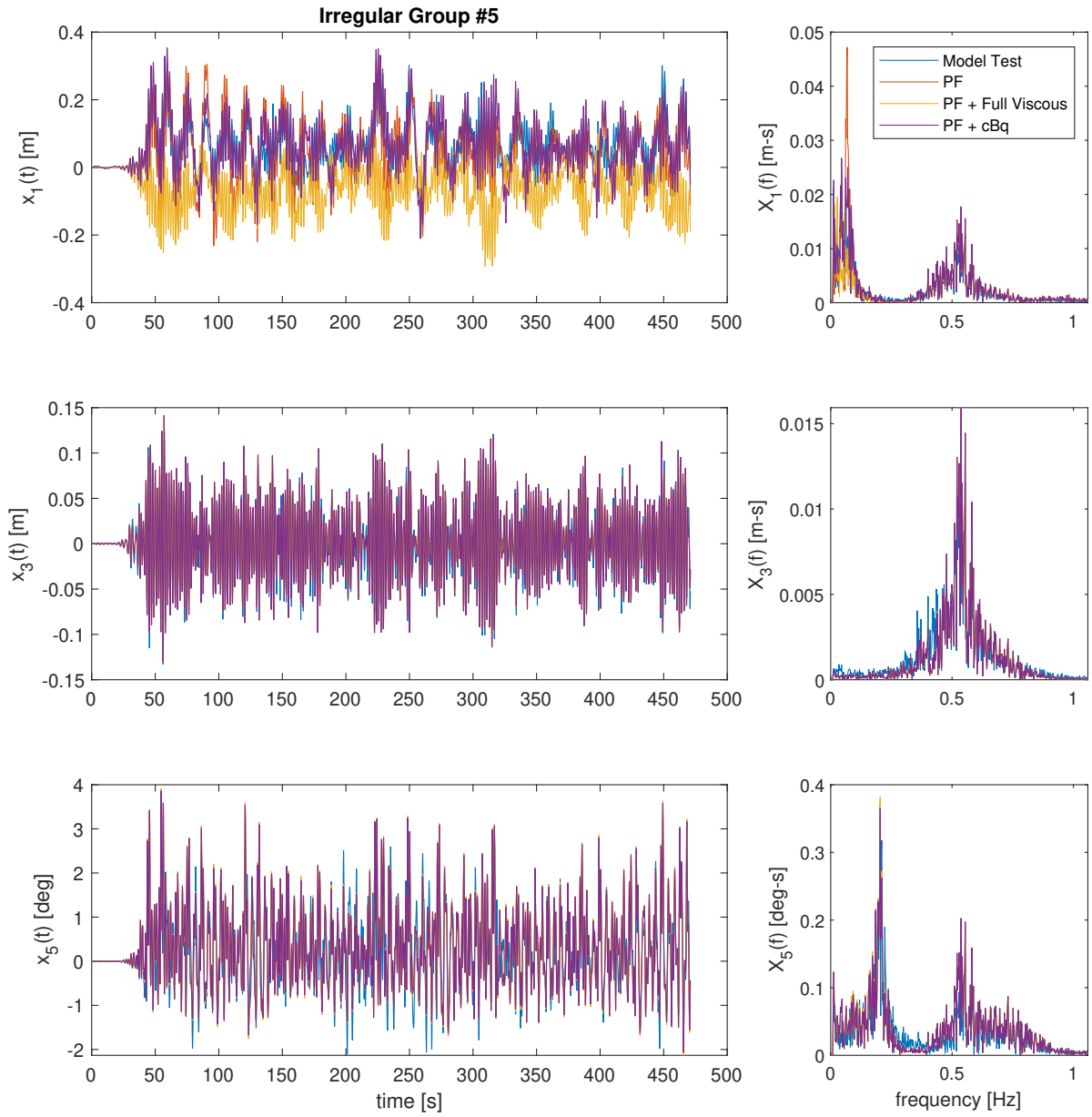


Figure K.25: Time series reconstruction of irregular test #5 with viscous corrections

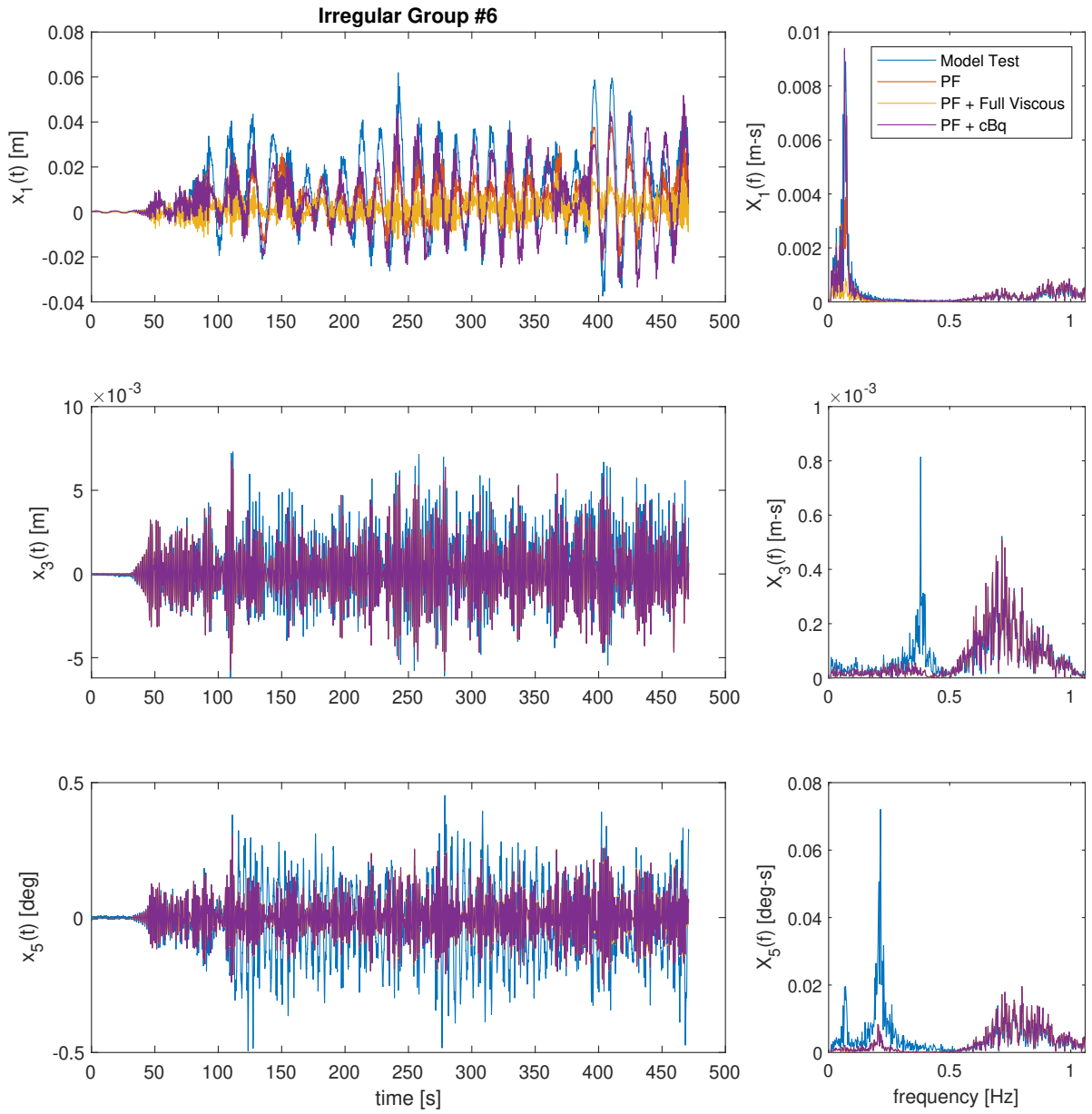


Figure K.26: Time series reconstruction of irregular test #6 with viscous corrections

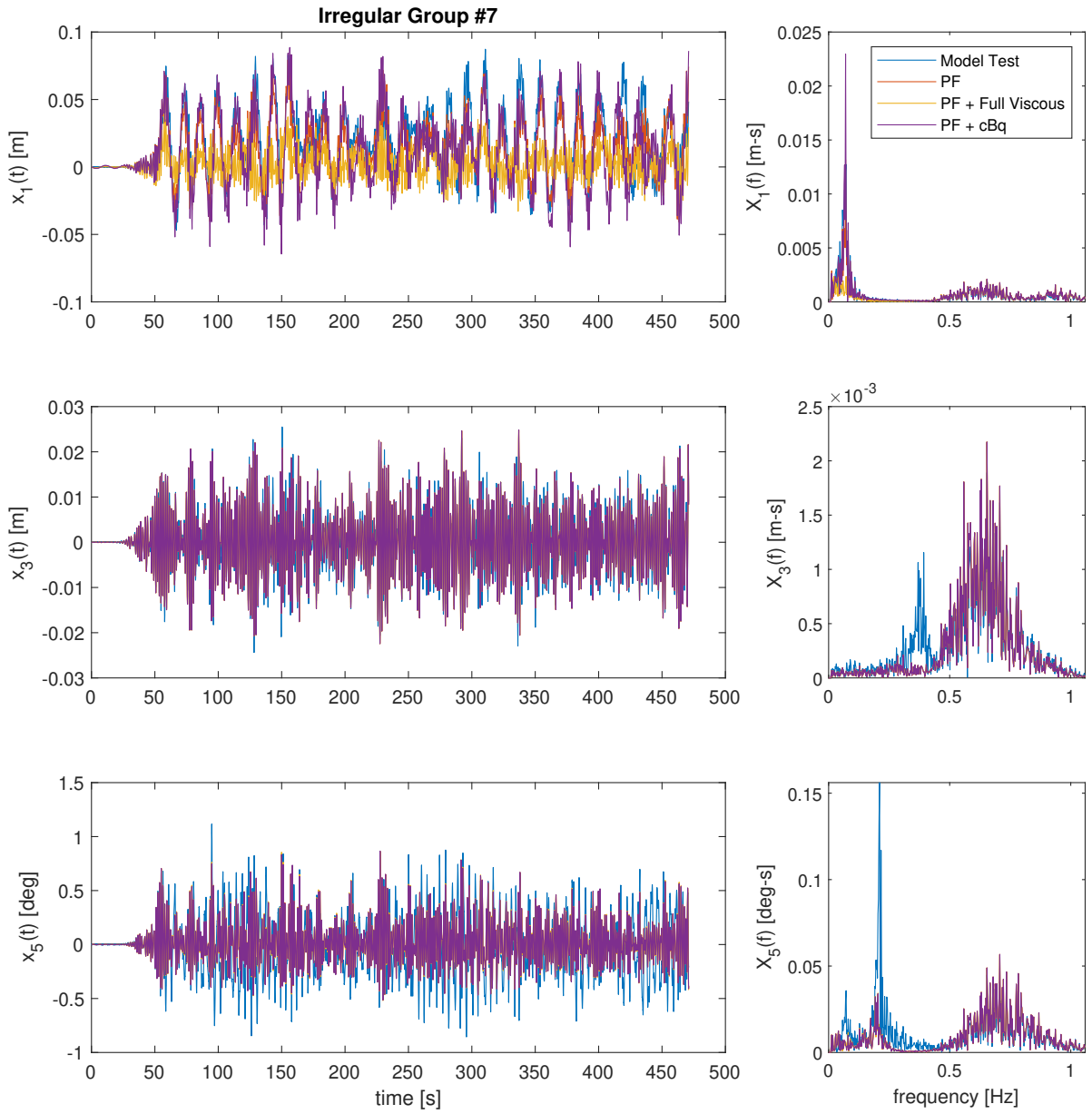


Figure K.27: Time series reconstruction of irregular test #7 with viscous corrections